Contrast Media & Molecular Imaging

Imaging Diagnostic and Pathology in the Management of Oncological-Patients

Lead Guest Editor: Elena Bonanno
Guest Editors: Orazio Schillaci, Alessandro Bombonati, Nicola Toschi, and Pietro Muto

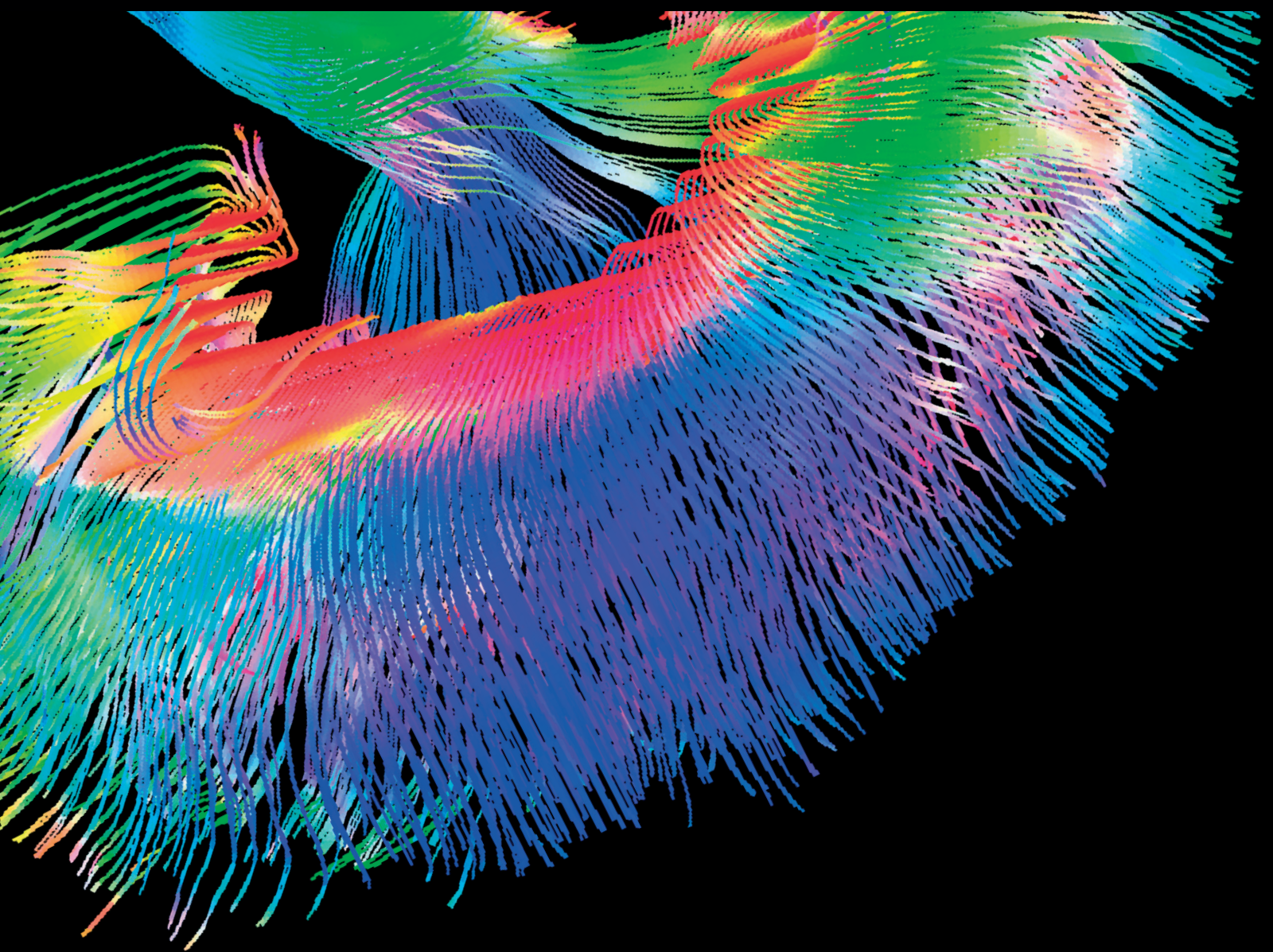

Imaging Diagnostic and Pathology in the Management of Oncological-Patients

Contrast Media & Molecular Imaging

Imaging Diagnostic and Pathology in the Management of Oncological-Patients

Lead Guest Editor: Elena Bonanno
Guest Editors: Orazio Schillaci, Alessandro Bombonati, Nicola Toschi, and Pietro Muto

Editorial Board

Contents

Hindawi
Contrast Media & Molecular Imaging
Volume 2019, Article ID 2513680, 2 pages
https://doi.org/10.1155/2019/2513680

Editorial

Imaging Diagnostic and Pathology in the Management of Oncological-Patients

Elena Bonanno,[1,2] **Nicola Toschi**,[3,4,5] **Alessandro Bombonati**,[6] **Pietro Muto**,[7] **and Orazio Schillaci**[3,8]

[1]*Anatomic Pathology, Department of Experimental Medicine, University of Rome "Tor Vergata", Via Montpellier 1, 00133 Rome, Italy*
[2]*"Diagnostica Medica" and "Villa Dei Platani", Avellino, Italy*
[3]*Department of Biomedicine and Prevention, University of Rome "Tor Vergata", Via Montpellier 1, 00133 Rome, Italy*
[4]*Martinos Center for Biomedical Imaging, Boston, MA, USA*
[5]*Harvard Medical School, Boston, MA, USA*
[6]*Department of Pathology and Laboratory Medicine, Einstein Medical Center, Philadelphia, PA, USA*
[7]*Radiation Oncology, Istituto Nazionale Tumori-IRCCS-G. Pascale Foundation, Naples, Italy*
[8]*IRCCS Neuromed, Pozzilli, IS, Italy*

Correspondence should be addressed to Elena Bonanno; elena.bonanno@uniroma2.it

Received 28 May 2019; Accepted 28 May 2019; Published 16 June 2019

Personalized medicine is one of the main objectives of both basic and translational cancer research. Nevertheless, it has become clear that the creation of personalized therapeutic protocols requires synergistic, transdisciplinary competencies. Indeed, novel approved therapies rarely take into account both the interindividual variability and the aptitude of cancer cells to undergo those genetic and molecular adaptation involved in the drug resistance phenomenon. In spite of recent and promising biomedical and biomarker discoveries, individually tailored medical care is still far from reality, and molecules which are output by preclinical trials are very rarely translatable to evaluation for the diagnostic or therapeutical potential. The discrepancy between experimental data on new anticancer molecules and the opportunity to actually employ them in both diagnosis and therapy is due to multiple factors such as biological differences between human diseases and animal models, inconsistence of experimental plans, and/or incorrect interpretation of experimental results. For example, several preclinical studies lack data validation performed by pathologists with long-term experience in cancer animal models. In view of the above, it appears evident that working towards personalized medicine in oncology requires the synergic combination of several disciplines such as nuclear medicine and anatomic pathology, which represent two complementary approaches to diagnosis, prognosis, and evaluation of therapeutic response.

The focus of this special issue is the alliance between Imaging Diagnostic (i.e., Nuclear Medicine and Radiology) and Anatomic Pathology, in the belief that a structured collaboration model between these disciplines can speed up the achievement of a medical paradigm that takes into account the uniqueness of every human being.

Out of a total of nineteen submissions, after two rounds of rigorous review, fifteen contributions were accepted for publications. Among them, four papers are focused on the breast cancer, four on lung cancer, three on prostate cancer, and three on the early detection of lymphoma. In addition, in several studies, the authors reported artificial intelligence applications for the diagnosis of tumor lesions; for example, a deep neural network architecture is able to discriminate malignant breast cancer lesions in mammographic images.

In conclusion, we felt that the novelties highlighted in this special issue can provide the scientific rationale for further investigations in translational medicine based on the

combination between Pathology and Diagnostic Imaging data.

Conflicts of Interest

The editors declare that they have no conflicts of interest.

Acknowledgments

The guest editors are thankful to all authors who submitted their contributions to this special issue, as well as to the reviewers for their precious input on how to improve initial (re)submissions.

Elena Bonanno
Nicola Toschi
Alessandro Bombonati
Pietro Muto
Orazio Schillaci

Hindawi
Contrast Media & Molecular Imaging
Volume 2019, Article ID 5982834, 9 pages
https://doi.org/10.1155/2019/5982834

Research Article

An Ad Hoc Random Initialization Deep Neural Network Architecture for Discriminating Malignant Breast Cancer Lesions in Mammographic Images

Andrea Duggento,[1] **Marco Aiello**,[2] **Carlo Cavaliere**,[2] **Giuseppe L. Cascella**,[3,4] **Davide Cascella**,[5] **Giovanni Conte**,[5] **Maria Guerrisi**,[1] **and Nicola Toschi**[1,6,7]

[1]*Department of Biomedicine and Prevention, University of Rome Tor Vergata, Rome, Italy*
[2]*IRCCS SDN, Naples, Italy*
[3]*Idea 75 s.r.l., Bari, Italy*
[4]*DEI-Politecnico di Bari, BARI, Italy*
[5]*GEM ICT s.r.l., Bari, Italy*
[6]*Department of Radiology, "Athinoula A. Martinos" Center for Biomedical Imaging, Boston, MA, USA*
[7]*Harvard Medical School, Boston, MA, USA*

Correspondence should be addressed to Andrea Duggento; duggento@med.uniroma2.it

Received 1 August 2018; Accepted 2 May 2019; Published 22 May 2019

Academic Editor: Alexander R. Haug

Breast cancer is one of the most common cancers in women, with more than 1,300,000 cases and 450,000 deaths each year worldwide. In this context, recent studies showed that early breast cancer detection, along with suitable treatment, could significantly reduce breast cancer death rates in the long term. X-ray mammography is still the instrument of choice in breast cancer screening. In this context, the false-positive and false-negative rates commonly achieved by radiologists are extremely arduous to estimate and control although some authors have estimated figures of up to 20% of total diagnoses or more. The introduction of novel artificial intelligence (AI) technologies applied to the diagnosis and, possibly, prognosis of breast cancer could revolutionize the current status of the management of the breast cancer patient by assisting the radiologist in clinical image interpretation. Lately, a breakthrough in the AI field has been brought about by the introduction of deep learning techniques in general and of convolutional neural networks in particular. Such techniques require no a priori feature space definition from the operator and are able to achieve classification performances which can even surpass human experts. In this paper, we design and validate an ad hoc CNN architecture specialized in breast lesion classification from imaging data only. We explore a total of 260 model architectures in a train-validation-test split in order to propose a model selection criterion which can pose the emphasis on reducing false negatives while still retaining acceptable accuracy. We achieve an area under the receiver operatic characteristics curve of 0.785 (accuracy 71.19%) on the test set, demonstrating how an ad hoc random initialization architecture can and should be fine tuned to a specific problem, especially in biomedical applications.

1. Introduction

Breast cancer is one of the most common cancers in women, with more than 1,300,000 cases and 450,000 deaths each year worldwide [1]. In the era of precision medicine [2], the identification and stratification of breast lesions in the early stage of cancer development is an essential starting point for increasing the probability of therapeutic success. In this context, early detection of breast lesions through mammography has been seen to be associated with an extremely high probability of cure, with a 97% survival in five years [3]. To date, however, identification of breast cancer lesions is affected by an unsatisfactory rate of false-positive results.

Currently, X-ray mammography represents the standard breast screening technique. The false-positive and false-negative rates resulting by mammography are relatively high, especially for patients with very dense breasts [4, 5]. The sensitivity of mammography is further influenced by age and ethnicity of patients, personal history, implementation and (especially) expertise, and experience of the radiologist performing the exam. In addition, the mammographic exam does not provide any indication about probable disease evolution and/or outcome (and neither does it provide clues about possibly appropriate therapeutic choices). In this context, it is not surprising that the rate of false-negative or -positive results for mammography described in the literature is extremely variable. While it is evident that possibly high rates of false-negative results are critical, false positives also carry significant consequences. A recent retrospective investigation of registry data concerning 405,191 women aged 40 to 89 years, screened with digital mammography between 2003 and 2011, reported a rate of 12.12% of false-positive results. However, others studies indicate a rate of false positive of up to 20% in specific centers [6]. While a single study computed a very low rate of false-negative results (0.1 to 0.5%) regardless of the patient's age, several retrospective analyses indicated that mammographic examinations are associated with a high false-negative rate (between 8 and 16%), which is often quoted as an average 15%. These results, apparently controversial, can be explained by the numerous factors that influence the interpretation of mammographic images such as quality of instrumentation, radiologist's experience, and the availability of a second opinion [7–11]. Also, false-positive mammograms are often associated with increased short-term anxiety but no long-term anxiety and no measurable health utility decrement [11]. In a recent study, a false-positive result increased women's motivation to undergo future breast cancer screening, whilst it did not increase their self-reported motivation to travel to avoid a false-positive mammogram [12]. Also, in presence of false-positive cases, patients are frequently subjected to repeated invasive (bioptic examination) and/or stringent follow-up programs, such as additional mammography exams mammography or equivalent medical procedures which, on top of possibly generating health detriment on their own, also carry significant financial burden. The direct breast-care costs in the year following a false-positive screening mammogram are approximately 500$ higher than in the case of a true-negative result [13].

In view of the above, the introduction of novel artificial intelligence (AI) technologies applied to the diagnosis and possibly prognosis of breast cancer could revolutionize the current status of the management of the breast cancer patient. The support of AI in the diagnostic path of breast cancer patients can potentially both reduce the healthcare costs due to misdiagnosis and promote the achievement of new precision medicine protocols [14]. In this context, the disruptive innovation in computer vision brought about through what is known as deep learning [15–17], and in particular, a class of methods known as deep convolutional neural networks (CNNs) [18] is very quickly making its way into the world of medical imaging. Accordingly, in a preliminary study, Chougrad et al. [13] described a CAD based on deep CNN able to discriminate between malignant and benignant breast mass in mammographic images with high accuracy. Likewise, other papers employed massive transfer learning approaches (GoogleNet and AlexNet) [19–21] and compared them to in-house, random initialization models showing that the latter achieves fairly poor performance. Other authors focused on a relatively small dataset and an "in-house" architecture measuring the relationship between network depth and model performance [22]. Still, published results are often hard to validate and replicate also due to the lack of a shared, standard curated dataset of informative mammographic images, and transfer learning approaches may not perform equally well when applied to datasets which are too distant in nature from the application at hand.

The main aim of this study was to design an ad hoc random initialization "in-house" deep neural network architecture to classify/detect breast lesion and explore whether satisfactory performance can be obtained without having to include the inaccurately trained, albeit powerful, public models currently available for transfer learning. Given the strong dependence of CNN performance on the specific task, we aimed to distill what are the key characteristics of a CNN suitable for breast lesion classification. We based our investigation on the recently released Curated Breast Imaging Subset of the Digital Database for Screening Mammography, which is curated by trained radiologists as well as pathologists.

2. Methods

2.1. Dataset. The training and testing of our CNN is done over the Curated Breast Imaging Subset of DDSM Digital Database for Screening Mammography (CBIS-DDSM) [23, 24], which is a collection of mammograms from several sources (Massachusetts General Hospital, Wake Forest University School of Medicine, Sacred Heart Hospital, and Washington University of St. Louis School of Medicine). The database collects both mediolateral oblique (MLO) and craniocaudal (CC) views of each breast. Each breast view is annotated with regions of interest (ROIs) for masses manually drawn (freehand) by expert radiologists and automatically included in a rectangular section of the image. Other annotations include the Breast Imaging Reporting and Data System (BI-RADS) descriptors for mass shape, mass margin, and breast density; overall BI-RADS assessment ranged from 0 to 5; rating of the subtlety of the abnormalities ranged from 1 to 5. Table 1 provides summary of the annotations available for each image.

2.2. Workflow and Architecture Overview. Our model was developed by combining the TensorFlow [25] and Keras [26] libraries; the whole workflow (Figure 1) consists of the following: (i) image preprocessing as described above; (ii) data augmentation; (iii) CNN training; (iv) performance evaluation with respect to a validation set, which allows to compare models trained on the training set; and (v) final

Table 1: Summary of the annotations available for each image in the CBIS-DDSM dataset. As all these annotations are derived from the image, none of these features were imputed into our classifier.

Patient_id	Anonymous alphanumeric code
Breast_density	4 (153), 2 (757), 3 (449), 1 (337)
Left or right breast	Left (817), right (879)
Image view	CC(784), MLO(912)
Abnormality id	1 (1570), 2 (84), 4 (10), 3 (28), 5 (2), 6 (2) (integer index used to label multiple lesions within the same image)
Abnormality type	Mass (1696)
Mass shape	Irregular (526), round (169), lobulated (399), oval (423), architectural_distortion(158), asymmetric_breast_tissue(26), lymph_node(45)
Mass margins	Focal_asymmetric_density (27), n/a (4), spiculated (407), circumscribed (455), ill_defined (472), obscured (308), microlobulated (143), n/a (60)
Assessment	5 (374), 4 (702), 0 (162), 3 (364), 2 (91), 1 (3)
Pathology	Malignant (784), benign (771), benign_without_callback (141)
Subtlety	5 (687), 4 (453), 2 (141), 3 (358), 1 (55), 0 (2)

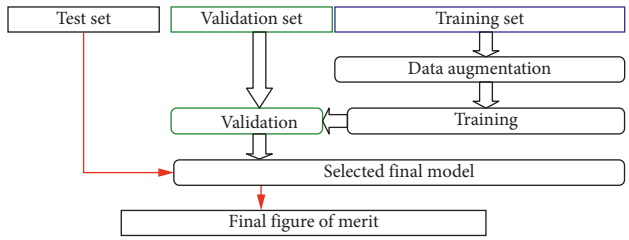

Figure 1: Workflow of our method. The original training set provided by CBIS-DDSM is further divided into a new "training set" and a "validation set." The new training set is employed to fit the model parameters, and the validation set is employed to validate and compare the performance of each model on an unbiased set of images. The final model is chosen accordingly to its performance of the validation set and its performance quantified in an unbiased manner on the test set. Overall, the split was as follows: training set (1158 images), validation set (160 images), and test set (378 images).

evaluation of the best model on the test set. The CNN training is further composed of several steps (which also depends on the specific CNN architecture which can be grouped in (1) convolutional layers and (2) neural layers). Each step is described in the following paragraphs.

2.2.1. Image Preprocessing. Every mass/ROI (Figure 2) is labeled either as "benign" or "malignant" according to pathological findings. As input, we employed all the pre-segmented ROIs containing images of masses, retaining only the "benign"-"malignant" label and hence stripping any other information (Figure 1). Starting from a training set of 1318 images and a test set of 378 images, we created a training set of 1158 images, a validation set of 160 images, and retained the original test set of 378 images.

2.2.2. Data Augmentation. It is common practice to synthetically increase the information available to the CNN by applying multiple transformations to the training set [27]. This practice is called "augmentation" and serves the purpose of providing the learning algorithm with as many informative images as possible in order to prevent overfitting (i.e., an excessive specialization of the CNN to the data at hand, which occurs when the training dataset is not sufficiently large to allow for generalization). Accordingly, for each extracted ROI, we perform data augmentation by transforming the training images employing random rotations, rescalings, and shear deformations (it is important to note that since CNNs are not invariant for affine transformation, this process is actually able to inject new training information into the dataset). Figure 3 shows an example of a batch of images resulting from the augmentation process.

2.2.3. Training. The process of training consists in tuning the weights of the model (see following paragraphs), to maximize the loss function of the model and hence the accuracy of the automatic classification/diagnosis formulated by the model. Batches of images from the CNN training set are fed into the algorithm, and the weights of the model are found by a trial and error in the attempt to improve its accuracy. Each "attempt" is commonly called "epoch". After each epoch, the weights of the model are updated.

(1) Convolutional Layers. Convolutional layers are the first stages of the actual image processing pipeline (Figure 4), and their role is to distill information regarding spatially correlated features of the input image. Convolutional layers function in a way that resembles the physiology of early pathways of the visual cortical areas in humans, where neurons respond to simple tuning—e.g., a neuron might be sensitive to vertical contrasts while another to horizontal contrasts. For example, convolution processes may highlight edges, or smooth the image, or make contrasts in a specific direction more prominent. At each layer, convolved images are subsampled to reduce resolution and passed to the next layer. Each convolutional layer extracts features using as input a linear combination of the outputs of the previous layer. Recursively, more and more (but smaller and smaller) images are produced, each containing information about an intricate combination of features. To the human eye, the images produced after the last layers typically look completely unrelated to the original input. A more technical description of this process can found in [29]. The convolutional part of the CNN is described by the number of convolutional layers, the number of convolutional kernels in each layer and their sizes, the details of the activation functions, and other image processing steps (e.g., how the subsampling is done and whether there is a global-normalization step).

(2) Neural Layers. The output of the last convolutional layer is the input to a series of one or few layers of neuronal arrays. A neuronal array is a set of weighted switch-like

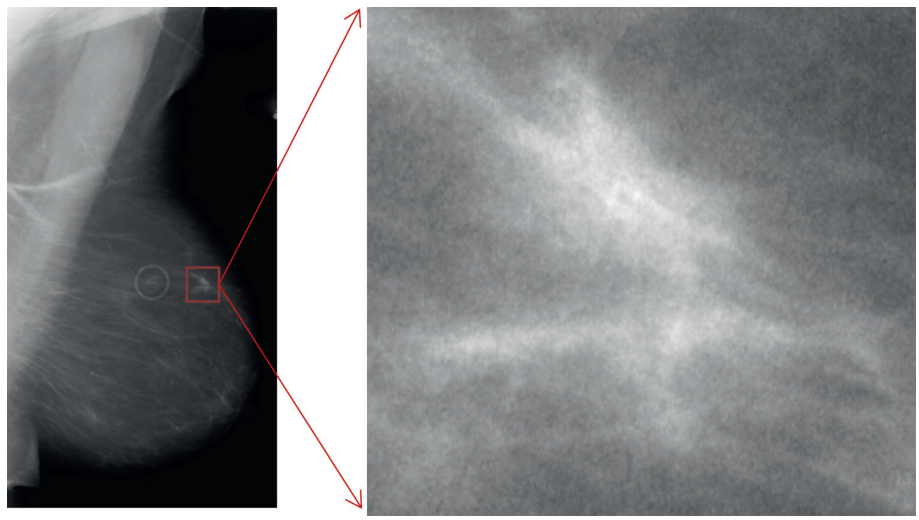

Figure 2: Example whole raw images and ROI extraction to be passed to image augmentations.

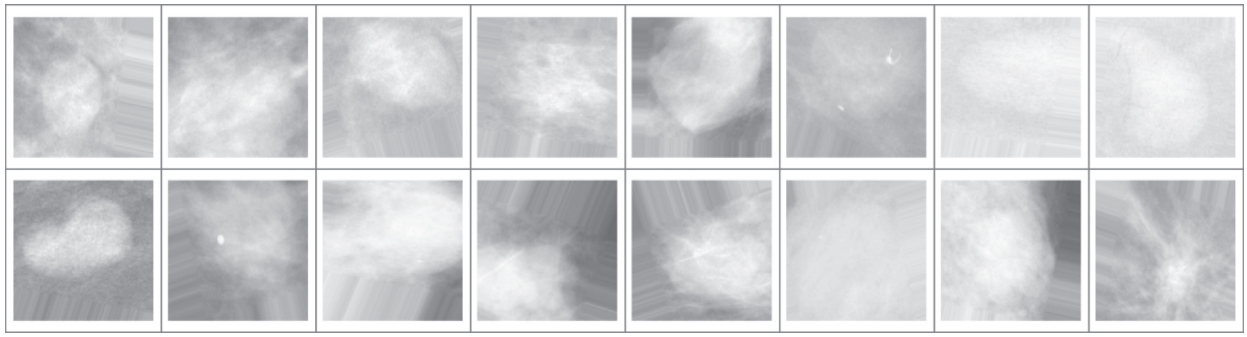

Figure 3: Example of a batch of 16 images from the training set. The ROI from which each image has been generated has been randomly rescaled (independently over the two axes), rotated by a random angle, randomly flipped, and resampled to fit into a pixel frame with aspect ratio 1. Any remaining area not filled by the image is padded with an array of pixels drawn from the edge of the image.

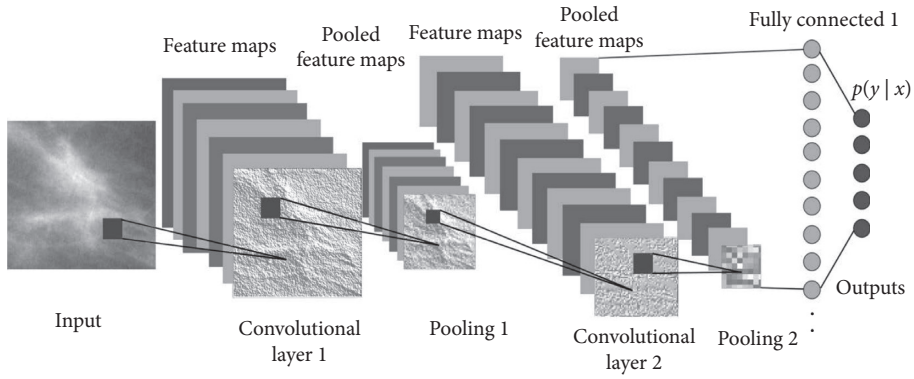

Figure 4: Overall architecture of the model (adapted from [28]).

discriminators that, much like to the firing of a neuron excited by a suprathreshold stimulus, activate when a certain combination of features is active. Again, stacking two or more neuronal layers allows to extract more and more sophisticated combinations of features. Such neural layers are called "fully-connected" because each neuron is linked *a priori* with any element (a voxel in an image or a neuron) of the previous layer. The weights of those links are tuned during the training process. In our model, the very last layer is composed by a single neuron with a sigmoid activation, i.e., its output is a number between 0 and 1, which describes the algorithm's educated guess regarding the malignancy of (the mass depicted in) the image (0: completely benign, 1: completely malignant). Varying the threshold on this

continuous sigmoid function allows the construction of receiver operating characteristic (ROC) curves.

2.2.4. Performance Evaluation during Model Training and Model Selection. At each epoch, we test the diagnostic accuracy of the model on a separate validation set (see above) which, importantly, is not used (i.e., it is completely "unseen") for training, thus providing an unbiased evaluation tool. For example, a high accuracy on the training set coupled with a low accuracy on the validation set is a good indication of overfitting has occurred.

It is important to note that, for real-life problems, there is no simple way to choose the best model architecture. Very similar architectures can perform differently, while very different architectures in terms of depth, number of layers, or number of parameters perform could perform almost equally. In this paper, we heuristically explored the space of number of possible architectures and trained them in order to gain insights into what an optimal CNN architecture for classification of breast lesions may be. In particular, we explored (though not exhaustively) the space of the following parameters: number of convolutional layers (2–5), size of the input image (from 78 to 612 pixels, depending on architecture and dimensions of images after the last convolutional layer, which in turn ranged from 1 to 8 pixels), number of convolutional kernels per each layer (from 4 to 64, not necessary identical on every layer), size of the convolutional kernel (from 3 to 11, not necessary identical on every layer), size of pooling (from 2 to 4, depending on the image size and kernel size), method for the last layer vectorization (global mean, global max, or flattening), number of fully connected layers before the last single-neuron layer (from 1 to 3), and numbers of neurons in each fully connected layer (from 200 to 5, typically decreasing with depth of the layer), for a total of 260 tested architectures. Every architecture was evaluated according to its performance on the validation set according to two separate criteria: (a) highest area under the ROC curve (AUC) ("model 1") and (b) best $F2$ score amongst all best $F2$ statistics attained by every single architecture ("model 2"). The $F2$ score is defined as $F2 = 5 * \text{precision} * \text{recall}/4 * \text{precision} + \text{recall}$. Within each model, the optimal operating point was chosen according to the $F1$ score (i.e., maximizing the harmonic average of precision and sensitivity, a commonly adopted criterion which compromises between sensitivity and the ability to discriminate a true positive result) for model 1 and $F2$ score for model 2.

3. Results

Both "model 1" and "model 2" happened to share the same convolutional architecture: 3 convolutional layers with 64 kernels each; size of kernels in each layer was 7×7, 5×5, and 3×3, respectively; the parameter dropout factor on each convolution was 25%; after rectified linear unit (ReLU) activation, on each layer, a max pooling method with size 4×4, 3×3, and 2×2 (and same stride) was employed. "Model 1" and "model 2" differed only in terms of the size of the input images and of the neuronal architecture: "model 1" had an input image of 238×238 pixels and fully connected neuronal layers composed by 50 and 10 neurons each before the last single-neuron layer. "Model 2" had an input image of 286×286 pixels and fully connected neuronal layers composed by 50 and 20 neurons each before the last single-neuron layer. Training the models took approximately 78 hours (4000 training epochs) on a 40-CPU dedicated HP bladesystem. Examples of our result on the validation set as well as final performance of our best models on the test set are shown in Figure 5. Examples of images which are "easy" to classify correctly are shown in Figure 6. Examples of images which are "difficult" to classify correctly are shown in Figure 7.

Our final "model 1" achieved an AUC of 0.785. Detailed performance statistics for this model when selecting an optimal operating point according to the best $F1$ score method are presented in Table 2. Our final "model 2" achieved an AUC curve of 0.774. Detailed performance statistics for this model when selecting an optimal operating point according to the best $F2$ score (which is a weighted average between sensitivity—which is emphasized 4-fold—and positive predictive value (PPV)) method are also presented in Table 2.

4. Discussion

While the classical machine learning (ML) paradigm is based on providing a result (i.e., a classification) given a human-defined set of features extracted from input data, CNNs are able to capture intricate relations between image features that are typically invisible to the human eye. Moreover, CNN architectures need not to be problem specific. However, their adaptability with respect to the image classification tasks, and their complete independence from the burden as well as possible bias of human-defined features, comes with the cost of a vast number of parameters which, in turns, require a large amount of training data. Given a certain CNN architecture, if the demand of training data is not met, the performance of the algorithm in terms of classification accuracy might plunge to chance levels. In this pilot study, we have explored the possibility of designing ad hoc CNN architecture with random initialization while studying heuristically which characteristics, out of the multitude of CNN varieties, may be important for breast lesion classification and may warrant further investigation. We employed rigorous validation and test set splits and achieved an area under the ROC curve of 0.78. Additionally, the optimal cutoff point as calculated with an $F1$ statistics was associated with 62.44% specificity and 84.4% sensitivity. Given the health as well as psychological implications of a false-negative diagnosis in breast cancer (see Introduction), we also strived to select a model which could pose more emphasis on avoided false negatives while still being selected rigorously. We therefore evaluated our model performance at an operating point determined by maximizing the $F2$ statistic, obtaining a sensitivity of 99.7%. While the specificity of this model may seem low, it is important to note

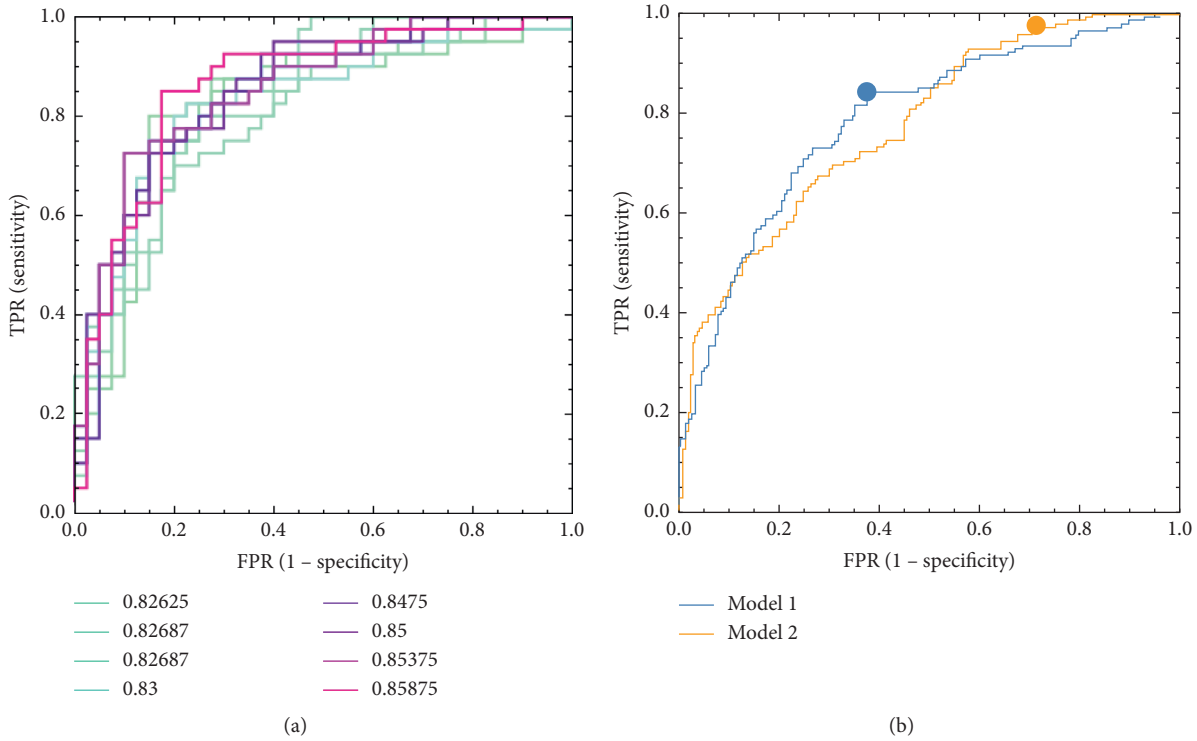

Figure 5: (a) Receiver operating characteristic (ROC) curves for a subsample of the architectures tested on the validation set (AUCs obtained on the validation set are shown in the legend). (b) ROC curve related to our best performing model (model 1: selected according to AUC on the validation set and model 2: selected according to $F2$ statistics on the validation set) when evaluated on the test set.

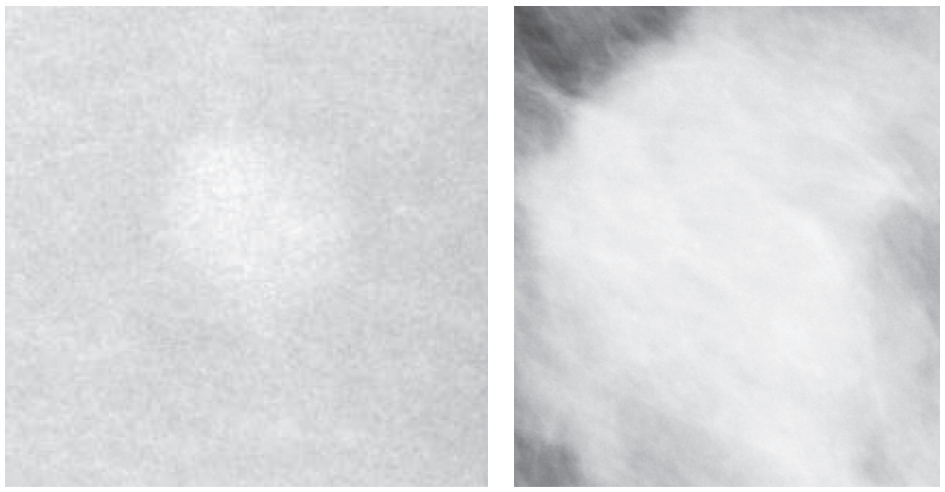

Figure 6: Example images that are easy to classify: (a) image of a benign lesion that is easily categorized as a benign lesion (score 2.2×10^{-9} from model 1 on a scale from 0 to 1); (b) image of a malignant lesion that is easily categorized as a malignant lesion (score 1.0 from model 1 on a scale from 0 to 1).

that, when performing model as well as operating point (i.e., cutoff) selection, it is critical to keep the end-user's needs and priorities in mind. We therefore put forward that, in a condition like breast cancer where a false negative may have devastating consequences which are overall much more burdensome than those of a false positive, a criterion like the $F2$ statistic (or similar) may be the instrument of choice.

As noted in the introduction, a few papers based almost exclusively on transfer learning have obtained comparable or higher performance on breast cancer classification as compared to our results. While transfer learning can provide steeper learning rates and asymptotically higher performance when approaching a new classification task and a small training set, it is likely that a

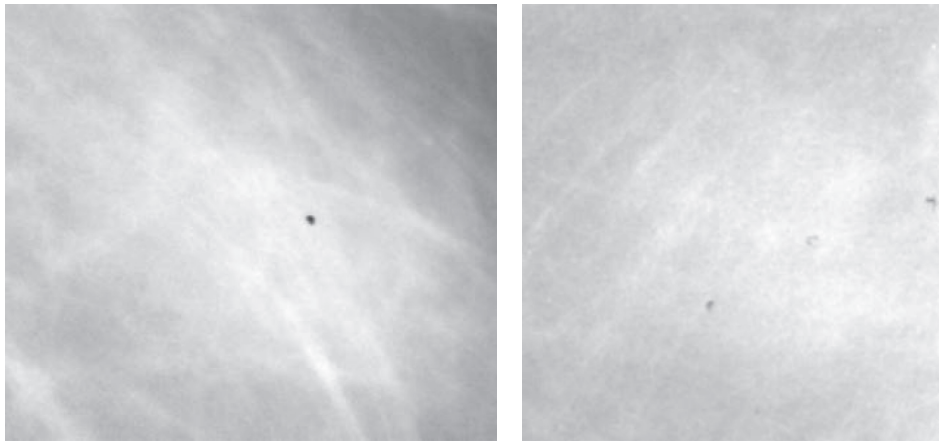

(a) (b)

Figure 7: Example images that are very difficult to classify: (a) image of a benign lesion that is falsely categorized as a malignant lesion (score 0.99992 from model 1 on a scale from 0 to 1); (b) image of a malignant lesion that is falsely categorized as a benign lesion (score .0133 from model 1 on a scale from 0 to 1).

Table 2: Performance statistics for our best performing models as evaluated on the test set.

Model 1 (best AUC overall on tde validation set, point witd best F1 score on tde test set)									
Accuracy	PPV (precision)	FDR	TPR (recall, sensitivity)	FNR (missrate)	FPR (fall out)	TN (specificity)	*F*1 score	*F*2 score	*F*5 score
71.19%	59.80%	40.20%	84.40%	15.60%	37.56%	62.44%	70.00%	77.98%	63.50%
Model 2 (best F2 score overall on the validation set, point with best F2 score on the test set)									
Accuracy	PPV (precision)	FDR	TPR (recall, sensitivity)	FNR (missrate)	FPR (fallout)	TN (specificity)	*F*1 score	*F*2 score	*F*5 score
55.93%	47.40%	52.60%	97.16%	2.84%	71.36%	28.64%	63.72%	80.30%	52.81%

dedicated learning framework would reach asymptotically higher performance when a large enough training set is made available. Further, one might speculate that the type of background knowledge and the realm of the application are also influential: for a lesion detection problem in mammograms, an architecture well-trained to distinguish (say) cars from the pedestrian might make a worse transfer learning source than, for example, an equally well-trained architecture to distinguish benign from malignant lung nodules.

Of note, the capabilities of a CNN in particular, and of deep learning in general, can, e.g., also be extended to predict molecular alterations (e.g., genetic changes) as long as the training data has been annotated both clinically and genomically in an accurate manner [30]. This could greatly enhance the management of breast cancer patients, in which the choice of therapeutic strategy is currently based on molecular characteristics of breast tumors, which in turn established by histological analysis of biopsies or surgical samples. Specifically, immunohistochemical reactions allow to evaluate the expression of targets for biological (cerB2), antihormonal (estrogen receptor), or radiochemical therapies (Ki67) [31–33]. Therefore, one can envisage an algorithm able to predict the molecular features of breast cancer tissues by the analysis of digital mammographic images, which could be conceivably realized by training a CNN jointly with histopathological and molecular data. The introduction of this type of diagnostic approaches has the potential to introduce radical changes in the organization of imaging diagnostic, anatomic pathology, as well as oncology departments. Specifically, the possibility to provide oncologists with possible molecular profiles and/or treatment options at the time of mammography could significantly reduce the need for bioptic investigation, hence optimizing the overall resources available to the healthcare facility. Most importantly, such CAD frameworks could ameliorate the patient's quality of life by reducing both the number of invasive procedures such as (often repeated) biopsies as well as the average wait before therapy inception. Also, deep learning has the potential to seamlessly integrate data from multimodal imaging of breast cancer, such as mammography and molecular imaging (PET, CT, and MR), with digitalized histological images. The algorithms could be trained to emphasize and highlight morphological signs whose identification is commonly time-consuming to the naked eye but may result in diagnostically actionable items (e.g., microvessel density, neoangiogenesis, lymphovascular invasion, chromatin alteration, or mitotic figures). This type of workflow would not only render pathology and imaging work quick and more accurate but also redefine the role of pathologists to experts able to agglomerate and interpret genetic/molecular, morphological, and imaging information to produce a more integrated and accurate diagnosis [34, 35].

In summary, our pilot study can lay the foundation for the development of new multimodal and multidisciplinary diagnostic tools able to move yet another step towards the goal of realizing a true personalized medicine approach able to take into account the unique peculiarities of every human being.

Data Availability

The images from the Curated Breast Imaging Subset data used for training the algorithms are from previously reported studies and datasets, which have been cited. The processed data are described in (DOI: 10.1038/sdata.2017.177) and currently available at https://wiki.cancerimagingarchive.net/display/Public/CBIS-DDSM.

Conflicts of Interest

The authors declare that they have no conflicts of interest.

Acknowledgments

The authors wish to acknowledge the Bari ReCaS Data Center (University of Bari "Aldo Moro" and National Institute of Nuclear Physics), coordinated by Prof. G. P. Maggi, for providing access to the high-performance computing resources necessary to conduct this study. The authors also wish to thank Dr. Manuel Scimeca and Dr. Nicoletta Urbano for their expert advice and helpful discussion.

References

[1] D. C. Koboldt, R. S. Fulton, M. D. McLellan et al., "Comprehensive molecular portraits of human breast tumours," *Nature*, vol. 490, no. 7418, pp. 61–70, 2012.

[2] R. L. N. Godone, G. M. Leitão, N. B. Araújo, C. H. M. Castelletti, J. L. Lima-Filho, and D. B. G. Martins, "Clinical and molecular aspects of breast cancer: targets and therapies," *Biomedicine & Pharmacotherapy*, vol. 106, pp. 14–34, 2018.

[3] J. A. Malmgren, J. Parikh, M. K. Atwood, and H. G. Kaplan, "Improved prognosis of women aged 75 and older with mammography-detected breast cancer," *Radiology*, vol. 273, no. 3, pp. 686–694, 2014.

[4] E. D. Pisano, C. Gatsonis, E. Hendrick et al., "Diagnostic performance of digital versus film mammography for breast-cancer screening," *New England Journal of Medicine*, vol. 353, no. 17, pp. 1773–1783, 2005.

[5] H. D. Nelson, K. Tyne, A. Naik et al., "Screening for breast cancer: an update for the U.S. Preventive services task force," *Annals of Internal Medicine*, vol. 151, no. 10, pp. 727–737, 2009.

[6] S. Hofvind, A. Ponti, J. Patnick et al., "False-positive results in mammographic screening for breast cancer in Europe: a literature review and survey of service screening programmes," *Journal of Medical Screening*, vol. 19, no. 1, pp. 57–66, 2012.

[7] M. G. Wallis, M. T. Walsh, and J. R. Lee, "A review of false negative mammography in a symptomatic population," *Clinical Radiology*, vol. 44, no. 1, pp. 13–15, 1991.

[8] E. C. Coveney, J. G. Geraghty, R. O'Laoide, J. B. Hourihane, and N. J. O'Higgins, "Reasons underlying negative mammography in patients with palpable breast cancer," *Clinical Radiology*, vol. 49, no. 2, pp. 123–125, 1994.

[9] O. Graf, T. H. Helbich, G. Hopf, C. Graf, and E. A. Sickles, "Probably benign breast masses at US: is follow-up an acceptable alternative to biopsy?," *Radiology*, vol. 244, no. 1, pp. 87–93, 2007.

[10] I. G. Murphy, M. F. Dillon, A. O. Doherty et al., "Analysis of patients with false negative mammography and symptomatic breast carcinoma," *Journal of Surgical Oncology*, vol. 96, no. 6, pp. 457–463, 2007.

[11] C. H. F. Hill, S. B. Coopey, P. E. Freer, and K. S. Hughes, "False-negative rate of combined mammography and ultrasound for women with palpable breast masses," *Breast Cancer Research and Treatment*, vol. 153, no. 3, pp. 699–702, 2015.

[12] A. N. A. Tosteson, D. G. Fryback, C. S. Hammond et al., "Consequences of false-positive screening mammograms," *JAMA Internal Medicine*, vol. 174, no. 6, pp. 954–961, 2014.

[13] H. Chougrad, H. Zouaki, and O. Alheyane, "Deep convolutional neural networks for breast cancer screening," *Computer Methods and Programs in Biomedicine*, vol. 157, pp. 19–30, 2018.

[14] H. Hampel, N. Toschi, C. Babiloni et al., "Revolution of alzheimer precision neurology. Passageway of systems biology and neurophysiology," *Journal of Alzheimer's Disease*, vol. 64, no. s1, pp. S47–S105, 2018.

[15] Y. Bengio, A. Courville, and P. Vincent, "Representation learning: a review and new perspectives," *IEEE Transactions on Pattern Analysis and Machine Intelligence*, vol. 35, no. 8, pp. 1798–1828, 2013.

[16] Y. LeCun, Y. Bengio, and G. Hinton, "Deep learning," *Nature*, vol. 521, no. 7553, pp. 436–444, 2015.

[17] J. Schmidhuber, "Deep learning in neural networks: an overview," *Neural Networks*, vol. 61, pp. 85–117, 2015.

[18] Y. LeCun, K. Kavukcuoglu, and C. Farabet, "Convolutional networks and applications in vision," in *Proceedings of the 2010 IEEE International Symposium on Circuits and Systems*, pp. 253–256, Paris, France, May 2010.

[19] L. Shen, "End-to-end Training for Whole Image Breast Cancer Diagnosis using An All Convolutional Design," 2017, http://arxiv.org/abs/170809427.

[20] D. Lévy and A. Jain, "Breast mass classification from mammograms using deep convolutional neural networks," 2016, http://arxiv.org/abs/161200542.

[21] W. Hang, Z. Liu, and A. Hannun, *GlimpseNet: Attentional Methods for Full-Image Mammogram Diagnosis*, Stanford AI Lab Internal Report, Stanford University, Stanford, CA, USA, 2017, http://cs231n.stanford.edu/reports/2017/pdfs/517.pdf.

[22] J. Arevalo, F. A. González, R. Ramos-Pollán, J. L. Oliveira, and M. A. Guevara Lopez, "Representation learning for mammography mass lesion classification with convolutional neural networks," *Computer methods and programs in biomedicine*, vol. 127, pp. 248–257, 2016.

[23] M. Heath, K. Bowyer, D. Kopans et al., *Current Status of the Digital Database for Screening Mammography. Digital Mammography*, pp. 457–460, Springer, Berlin, Germany, 1998.

[24] M. Heath, K. Bowyer, D. Kopans, R. Moore, and W. P. Kegelmeyer, "The digital database for screening mammography," in *Proceedings of the 5th International Workshop on Digital Mammography*, Medical Physics Publishing, Toronto, Canada, June 2000.

[25] M. Abadi, P. Barham, J. Chen et al., *Tensorflow: A System For Large-Scale Machine Learning*, OSDI, Savannah, GA, USA, 2016.

[26] F. Chollet, "Keras," 2015, https://keras.io.

[27] O. Ronneberger, P. Fischer, and T. Brox, "U-net: convolutional networks for biomedical image segmentation," *Lecture Notes in Computer Science*, vol. 9351, pp. 234–241, 2015.

[28] S. Albelwi and A. Mahmood, "A framework for designing the architectures of deep convolutional neural networks," *Entropy*, vol. 19, no. 6, 2017.

[29] M. D. Zeiler and R. Fergus, "Visualizing and understanding convolutional networks," in *Proceedings of the European Conference on Computer Vision—ECCV 2014*, D. Fleet, T. Pajdla, B. Schiele, and T. Tuytelaars, Eds., vol. 8689, Lecture Notes in Computer Science, Zurich, Switzerland, September 2014.

[30] M. K. Leung, A. Delong, B. Alipanahi, and B. J. Frey, "Machine learning in genomic medicine: a review of computational problems and data sets," *Proceedings of the IEEE*, vol. 104, no. 1, pp. 176–197, 2016.

[31] Y. Peng, Y. M. Butt, B. Chen, X. Zhang, and P. Tang, "Update on immunohistochemical analysis in breast lesions," *Archives of Pathology & Laboratory Medicine*, vol. 141, no. 8, pp. 1033–1051, 2017.

[32] D. Wang, J. Xu, G. Shi, and G. Yin, "Molecular markers' progress of breast cancer treatment efficacy," *Journal of Cancer Research and Therapeutics*, vol. 11, no. 1, pp. C11–C15, 2015.

[33] A. C. Wolff, M. E. H. Hammond, D. G. Hicks et al., "Recommendations for human epidermal growth factor receptor 2 testing in breast cancer: American Society of Clinical Oncology/College of American Pathologists clinical practice guideline update," *Archives of Pathology & Laboratory Medicine*, vol. 138, no. 2, pp. 241–256, 2014.

[34] M. Scimeca, N. Urbano, R. Bonfiglio, O. Schillaci, and E. Bonanno, "Management of oncological patients in the digital era: anatomic pathology and nuclear medicine teamwork," *Future Oncology*, vol. 14, no. 11, pp. 1013–1015, 2018.

[35] O. Schillaci and N. Urbano, "Personalized medicine: a new option for nuclear medicine and molecular imaging in the third millennium," *European Journal of Nuclear Medicine and Molecular Imaging*, vol. 44, no. 4, pp. 563–566, 2017.

Hindawi
Contrast Media & Molecular Imaging
Volume 2019, Article ID 5081909, 10 pages
https://doi.org/10.1155/2019/5081909

Research Article

Associations between Histogram Analysis Parameters Derived from DCE-MRI and Histopathological Features including Expression of EGFR, p16, VEGF, Hif1-alpha, and p53 in HNSCC

Hans Jonas Meyer,[1] **Leonard Leifels**,[1] **Gordian Hamerla**,[1] **Anne Kathrin Höhn**,[2] **and Alexey Surov**[1]

[1]*Department of Diagnostic and Interventional Radiology, University of Leipzig, Leipzig, Germany*
[2]*Department of Pathology, University of Leipzig, Leipzig, Germany*

Correspondence should be addressed to Hans Jonas Meyer; jonas90.meyer@web.de

Received 5 July 2018; Accepted 5 December 2018; Published 2 January 2019

Guest Editor: Elena Bonanno

Background. Our purpose was to elucidate possible correlations between histogram parameters derived from dynamic contrast-enhanced MRI (DCE-MRI) with several histopathological features in head and neck squamous cell carcinomas (HNSCC). *Methods*. Thirty patients with primary HNSCC were prospectively acquired. Histogram analysis was derived from the DCE-MRI parameters: K_{trans}, K_{ep}, and V_e. Additionally, in all cases, expression of human papilloma virus (p16) hypoxia-inducible factor-1-alpha (Hif1-alpha), vascular endothelial growth factor (VEGF), epidermal growth factor receptor (EGFR), and tumor suppressor protein p53 were estimated. *Results*. K_{ep} kurtosis was significantly higher in p16 tumors, and V_e min was significantly lower in p16 tumors compared to the p16 negative tumors. In the overall sample, K_{ep} entropy correlated well with EGFR expression ($p = 0.38$, $P = 0.04$). In p16 positive carcinomas, K_{trans} max correlated with VEGF expression ($p = 0.46$, $P = 0.04$), K_{trans} kurtosis correlated with Hif1-alpha expression ($p = 0.46$, $P = 0.04$), and K_{trans} entropy correlated with EGFR expression ($p = 0.50$, $P = 0.03$). Regarding K_{ep} parameters, mode correlated with VEGF expression ($p = 0.51$, $P = 0.02$), and entropy correlated with Hif1-alpha expression ($p = 0.47$, $P = 0.04$). In p16 negative carcinomas, K_{ep} mode correlated with Her2 expression ($p = -0.72$, $P = 0.03$), V_e max correlated with p53 expression ($p = -0.80$, $P = 0.009$), and V_e p10 correlated with EGFR expression ($p = 0.68$, $P = 0.04$). *Conclusion*. DCE-MRI can reflect several histopathological features in HNSCC. Associations between DCE-MRI and histopathology in HNSCC depend on p16 status. K_{ep} kurtosis and V_e min can differentiate p16 positive and p16 negative carcinomas.

1. Introduction

Head and neck squamous cell carcinoma (HNSCC) is a frequently occurring malignancy [1]. Previously, the role of imaging modalities was to locate the primary tumor and detect infiltration of bordering body structures and distant metastasis [2]. However, modern imaging modalities can also provide valuable information regarding tumor microstructure and might be able to predict several histopathological features in tumors [3, 4].

Dynamic contrast-enhanced MRI (DCE-MRI) is a functional imaging technique, which is able to assess tumor vascularization by measurement of sequential changes of signal intensity over time after contrast media application [5, 6]. In DCE-MRI, quantitative parameters like K_{trans} (volume transfer constant in min^{-1}), V_e (volume fraction of the extravascular extracellular space which is dimensionless), and K_{ep} (rate constant in min^{-1}) can be obtained [6].

Previous reports suggested that DCE-MRI can reflect tumor vessel density [6]. However, besides perfusion, DCE-MRI is also linked to cellularity, as well as to proliferation index [7, 8]. Furthermore, it has been shown that DCE-MRI can predict survival and treatment response to radiochemotherapy in HNSCC [5, 9–11]. Additionally, it can predict tumor

recurrence [12] and metastatic spread [13]. Besides the prognostic information, DCE-MRI can also aid in discrimination between benign and malignant head and neck tumors [14].

Histogram analysis is used to analyze radiological images. By using this technique, every voxel of a region of interest (ROI) is issued into a histogram. Thereby, a broad spectrum of new parameters can be estimated: minimum, mean, maximum, median, mode, percentiles, kurtosis, skewness, and entropy. According to the literature, heterogeneity of the histogram might also display heterogeneity of the tumor [15].

Several histopathological parameters play an important role in HNSCC. For example, p16 expression, associated with human papilloma virus, is one of the most important prognostic factors in HNSCC [16]. Other parameters, such as vascular endothelial growth factor (VEGF), hypoxia-inducible factor-1-alpha (Hif1-alpha), epidermal growth factor receptor (EGFR), and tumor suppressor protein p53 expression, are also of prognostic relevance and might aid in treatment response prediction in HNSCC [17, 18]. Presumably, imaging might also be able to reflect these expression profiles, especially by using the more advanced histogram-based analysis. Recently, a first promising study identified statistical differences between p16 positive and p16 negative carcinomas using histogram-based parameters derived from diffusion-weighted imaging [19]. Previously, only two studies analyzed relationships between DCE-MRI and histopathological parameters like the proliferation index Ki 67 and/or tumor cellularity in HNSCC using conventional ROI-based analysis [7, 20]. Presumably, histogram-based DCE parameters may show more associations with histopathology.

Therefore, the aim of this study was to estimate whole lesion histogram parameters derived from DCE-MRI and to elucidate possible correlations with several clinically relevant histopathological features in HNSCC.

2. Materials and Methods

This prospective study was approved by the institutional review board (Ethics committee of the University of Leipzig, study codes 180-2007, 201-10-12072010, and 341-15-05102015). All methods were performed in accordance with the relevant guidelines and regulations. All patients gave their written informed consent.

2.1. Patients. For this study, 30 patients (22 men and 8 women; mean age 57.0 ± 10.6 years; range 33–77 years) with histopathological proven primary HNSCC were included into the present study. Different tumor localizations were identified: the oropharynx in 46.7% of cases, tongue in 23.3%, hypopharynx in 10%, larynx in 16.7%, and nasopharynx in 3.3% of cases. There were T3 staged cancers in 33.3% and T4 in 40% cases and only 26.7% with T1 and T2 cancers. 90% of cases were nodal positive and 10% of patients without any nodal metastases. Well and moderately differentiated tumors were identified in 36.7% of patients and poorly differentiated in 63.3%. All patients did not receive any form of cancer treatment before the investigation.

2.2. DCE-MRI. In all patients, dynamic contrast-enhanced (DCE) imaging was performed using T1w DCE sequences according to a imaging protocol, as reported previously (TR/TE 2.47/0.97 ms, flip angle 8°, voxel size 1.2 × 1.0 × 5.0 mm, and slice thickness 5 mm) [7, 21]. The sequence included forty scans at 6 seconds. The contrast application of 0.1 mmol gadobutrol per kg of bodyweight (Gadovist®, Bayer Healthcare, Leverkusen, Germany) started after the fifth scan with a rate of 3 ml per second (Spectris Solaris, Medrad, Bayer Healthcare, Leverkusen, Germany). The acquired images were further analyzed with Tissue 4D (Siemens Medical Systems, Erlangen, Germany), which uses a population-based technique for the arterial input function (AIF). The AIF was modelled to the gadolinium dose and according to the biexponential model of Tofts and Kermode. Finally, K_{trans}, V_e, and K_{ep} were calculated (for exemplary parameter images, see Figures 1 and 2).

2.3. Histogram Analysis. The acquired DCE-MRI data were processed with a Matlab-based application (Mathworks, Natick, MA, USA). On the K_{trans}, K_{ep}, and V_e maps, a volume of interest was drawn inside the tumor boundary using all slices with visible tumor areas and thus providing a whole lesion measurement. All measures were performed by one experienced author (AS, 15 years of general radiological experience). The following parameters were estimated for K_{trans}, K_{ep}, and V_e: mean, maximum, minimum, median, mode, 10^{th}, 25^{th}, 75^{th}, and 90^{th} percentiles, as well as kurtosis, skewness, and entropy.

2.4. Histopathological Findings. In every patient, the diagnosis was confirmed by tumor biopsy. The histological specimens were deparaffinized, rehydrated, and cut into 5 μm slices. Moreover, the histological slices were stained by the epidermal growth factor receptor (EGFR, EMERGO Europe, clone 111.6, dilution 1 : 30), vascular endothelial growth factor (VEGF, EMERGO Europe, clone VG1, dilution 1 : 20), tumor suppressor protein p53 (DakoCytomation, Glostrup, Denmark; clone DO-7, dilution 1 : 100), hypoxia-inducible factor-1 (Hif1-alpha) (Biocare Medical, 60 Berry Dr Pacheco, CA 94553; clone EP1215Y, dilution 1 : 100), and p16 (p16 expression, CINtec Histology, Roche, Germany), as performed in our previous study [22].

Pannoramic microscope scanner (Pannoramic SCAN, 3DHISTECH Ltd., Budapest, Hungary) with Carl Zeiss objectives up to 41x bright field magnification by default was used to digitalize all specimens. In the used bottom-up technique, the whole sample was acquired at a high resolution. All slides were analyzed with Pannoramic Viewer 1.15.4 (open source software, 3D HISTECH Ltd., Budapest, Hungary), and three representative images with a magnification of ×200 were extracted from each patient.

The histopathological images were further investigated by using the ImageJ software 1.48v (National Institutes of Health Image program). The tumors were divided according to the p16 status.

Finally, expression of EGFR, VEGF, HIF1-alpha, and p53 (Figures 1 and 2) was semiautomatically estimated as a

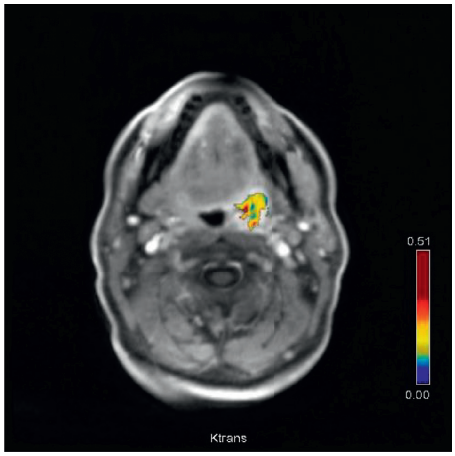

(a)

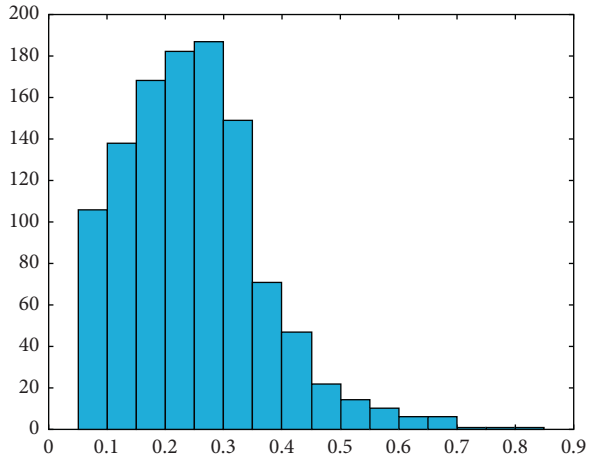

(b)

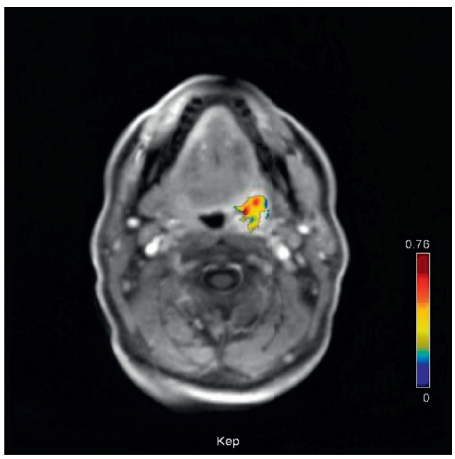

(c)

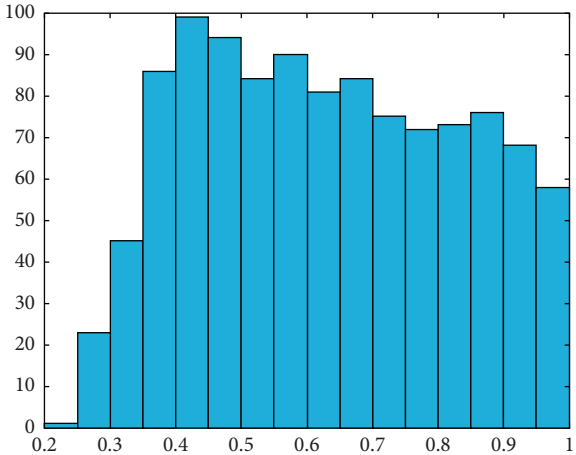

(d)

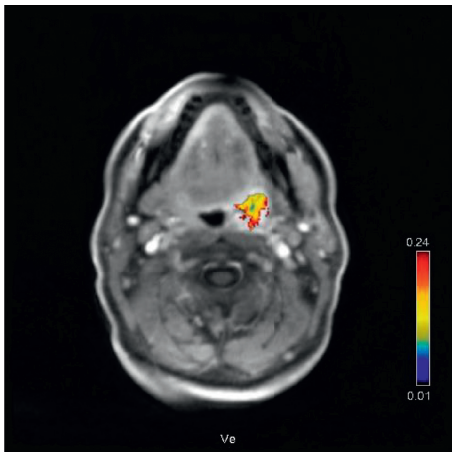

(e)

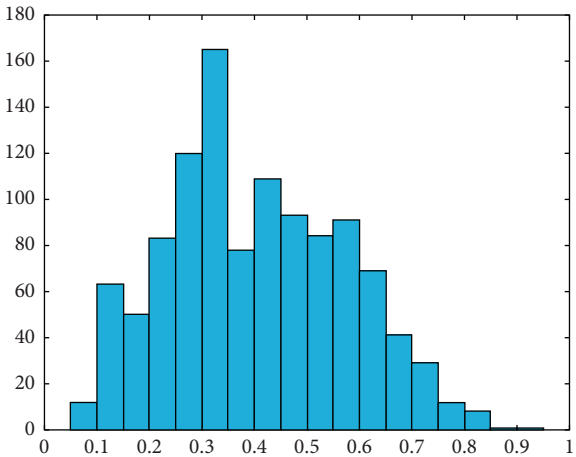

(f)

Figure 1: Continued.

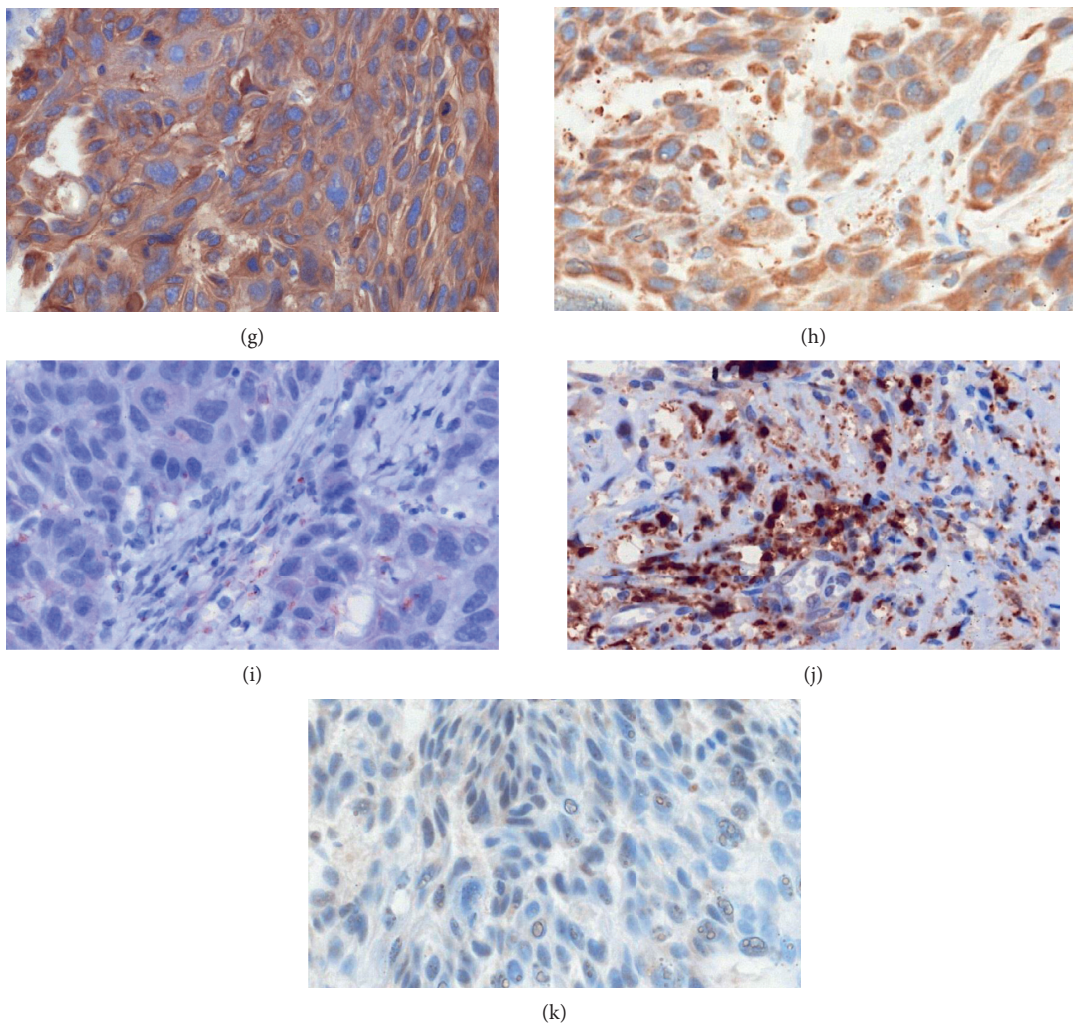

Figure 1: DCE-MRI and histopathological findings in a patient with histologically proven squamous cell carcinoma of the oropharynx. The p16 status is negative for this patient. (a) K_{trans} map of the tumor. (b) Histogram of K_{trans} values. The histogram analysis parameters (min^{-1}) are as follows: mean = 0.25, min = 0.05, max = 0.80, p10 = 0.10, p25 = 0.16, p75 = 0.32, p90 = 0.40, median = 0.24, mode = 0.27, kurtosis = 4.5, skewness = 0.93, and entropy = 3.17. (c) K_{ep} map of the tumor. (d) Histogram of K_{ep} values. Estimated histogram analysis parameters (min^{-1}) are as follows: mean = 0.63, min = 0.23, max = 1.0, p10 = 0.38, p25 = 0.46, p75 = 0.80, p90 = 0.92, median = 0.62, mode = 0.57, kurtosis = 1.89, skewness = 0.11, and entropy = 3.86. (e) V_e map of the tumor. (f) Histogram of V_e values. Estimated histogram analysis parameters are as follows: mean = 0.40, min = 0.08, max = 0.91, p10 = 0.18, p25 = 0.27, p75 = 0.53, p90 = 0.64, median = 0.39, mode = 0.25, kurtosis = 2.37, skewness = 0.29, and entropy = 3.72. (g) EGFR staining, 106866 μm^2 stained area. (h) Her2 staining, 57694 μm^2 stained area. (i) VEGF staining, 1177 μm^2 stained area. (j) Hif1-alpha staining, 27708 μm^2 stained area. (k) P53 staining, no staining is detectable in the carcinoma.

sum of stained areas (in μm^2) by using a brightness threshold. Figure 1 displays a p16 negative, and Figure 2 shows a p16 positive carcinoma.

2.5. Statistical Analysis. Statistical analysis was performed using GraphPad Prism (GraphPad Software, La Jolla, CA, USA). Collected data were evaluated by means of descriptive statistics.

Spearman's correlation coefficient (ρ) was used to analyze associations between investigated imaging and histopathology parameters. Mann–Whitney U test was used for discrimination between p16 groups. P values below 0.05 were considered statistically significant.

3. Results

There were 10 (33.3%) p16 negative and 20 (66.7%) p16 positive tumors. K_{ep} kurtosis was significantly higher in p16 tumors, and V_e min was significantly lower in p16 positive tumors compared to the p16 negative tumors, $P = 0.049$ and $P = 0.044$, respectively (Figure 3).

In the overall sample, the correlation analysis revealed only one statistically significant correlation between K_{ep} entropy and EGFR expression ($\rho = 0.38$, $P = 0.04$) (Figure 4).

In the p16 positive carcinomas, K_{trans} max correlated with VEGF expression ($\rho = 0.46$, $P = 0.04$), K_{trans} kurtosis correlated with Hif1-alpha expression ($\rho = 0.46$, $P = 0.04$) and K_{trans} entropy correlated with EGFR expression ($\rho =$

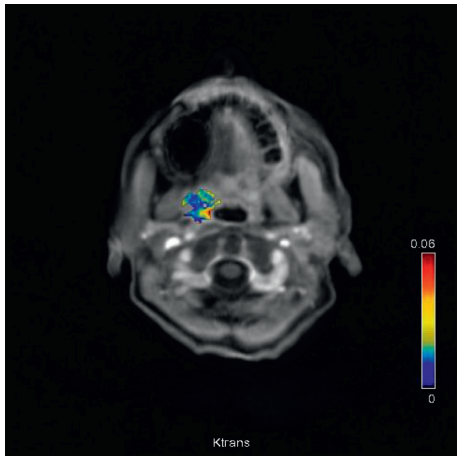

(a)

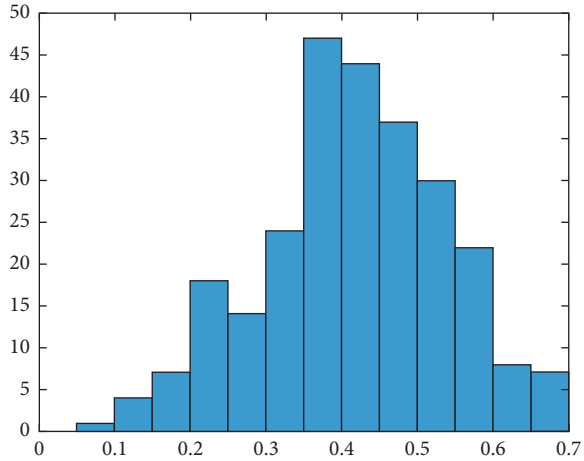

(b)

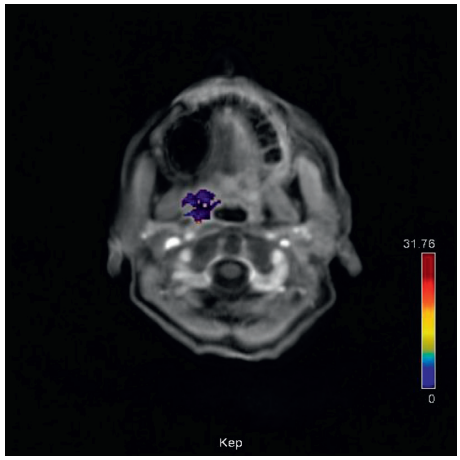

(c)

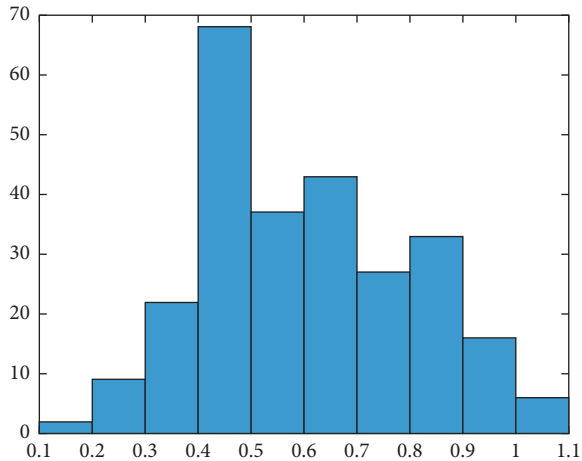

(d)

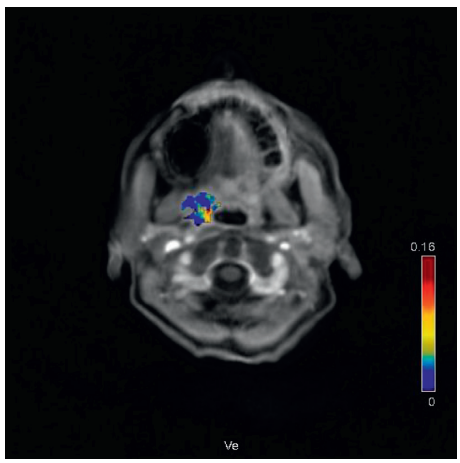

(e)

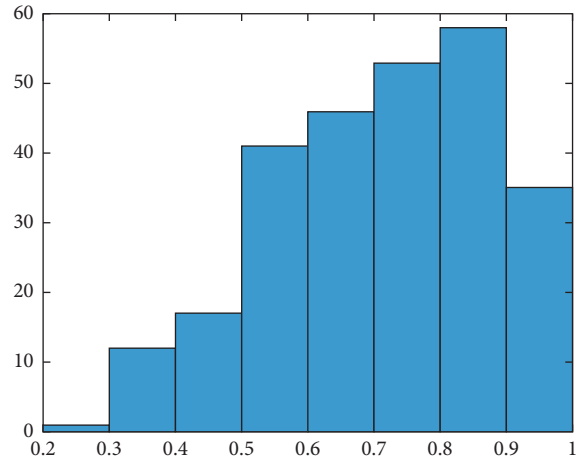

(f)

Figure 2: Continued.

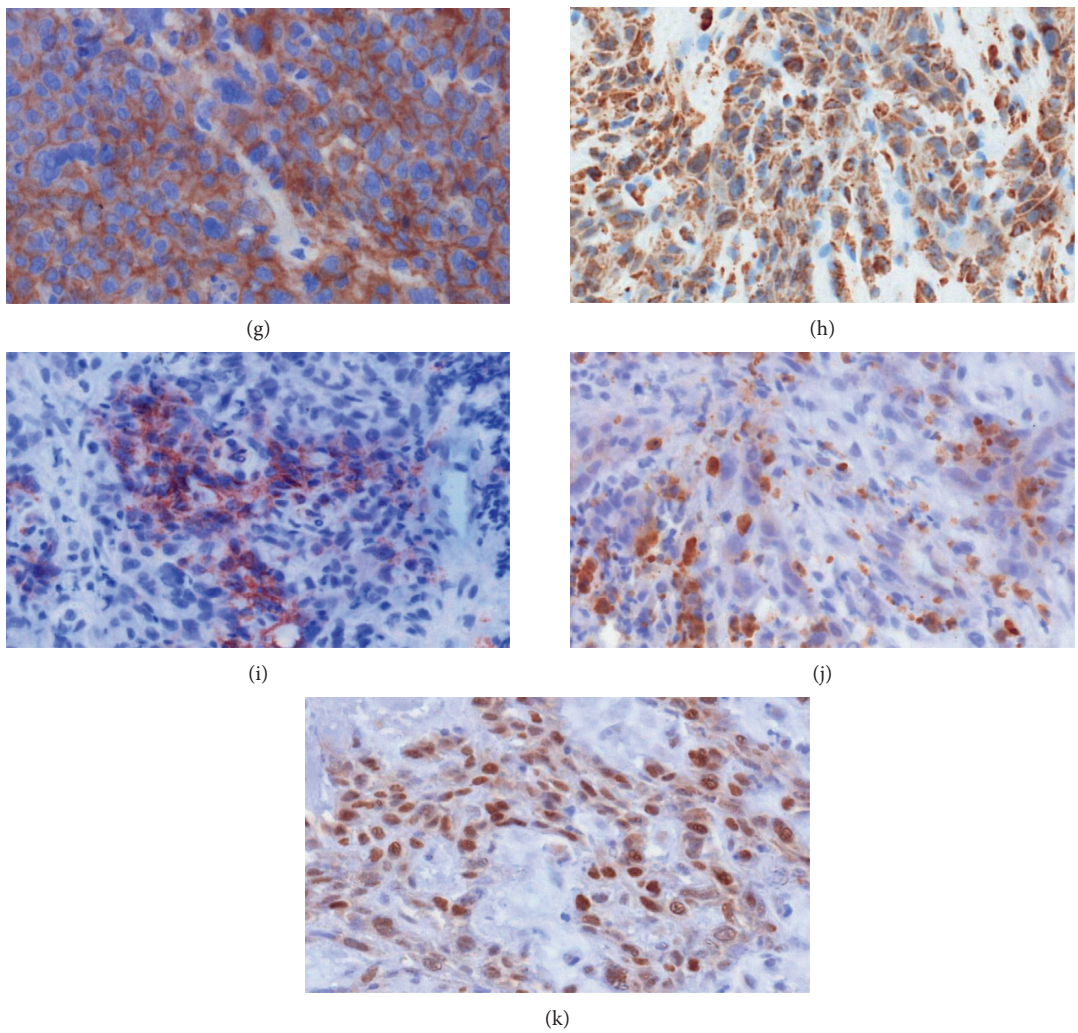

Figure 2: A p16 positive oropharyngeal HNSCC. (a) K_{trans} map of the tumor. (b) Histogram of K_{trans} values. The histogram analysis parameters (min^{-1}) are as follows: mean = 0.42, min = 0.09, max = 0.70, p10 = 0.24, p25 = 0.35, p75 = 0.50, P90 = 0.57, median = 0.42, mode = 0.47, kurtosis = 2.78, skewness = −0.18, and entropy = 3.29. (c) K_{ep} map of the tumor. (d) Histogram of K_{ep} values. Estimated histogram analysis parameters (min^{-1}) are as follows: mean = 0.60, min = 0.18, max = 1.04, p10 = 0.38, p25 = 0.45, p75 = 0.75, p90 = 0.88, median = 0.58, mode = 0.45, kurtosis = 2.20, skewness = 0.24, and entropy = 2.93. (e) V_e map of the tumor. (f) Histogram of V_e values. Estimated histogram analysis parameters are as follows: mean = 0.71, min = 0.22, max = 0.99, p10 = 0.49, p25 = 0.58, p75 = 0.86, p90 = 0.92, median = 0.73, mode = 0.63, kurtosis = 2.33, skewness = −0.38, and entropy = 2.68. (g) EGFR staining, 49020 μm^2 stained area. (h) Her2 staining, 56207 μm^2 stained area. (i) VEGF staining, 42720 μm^2 stained area. (j) Hif1-alpha staining, 11134 μm^2 stained area. (k) P53 staining, 45011 μm^2 stained area.

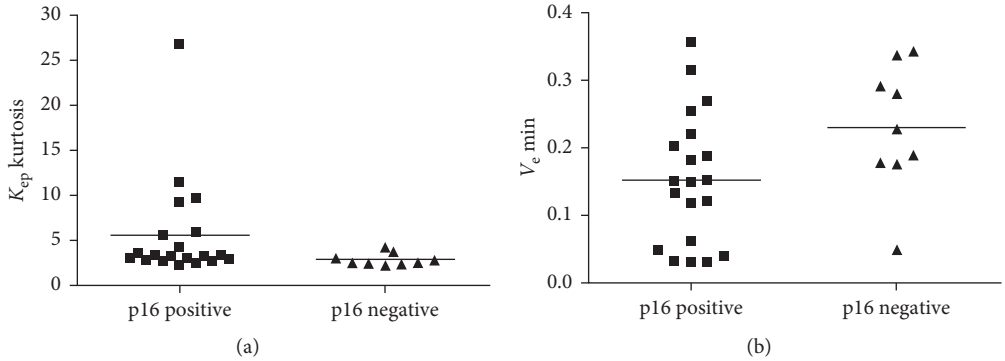

Figure 3: (a) Comparison between p16 and p16 negative tumors. K_{ep} kurtosis was significantly higher in p16 positive tumors (Mann–Whitney U test, $p = 0.049$). (b) V_e min was significantly lower in p16 positive tumors (Mann–Whitney U test, $p = 0.044$).

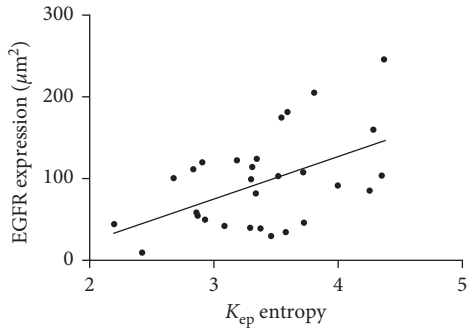

Figure 4: Correlation analysis between K_{ep} entropy and EGFR expression in the overall patient sample. Spearman's correlation coefficient ($p = 0.38$, $P = 0.04$).

0.50, $P = 0.03$). Regarding K_{ep} parameters, mode correlated with VEGF expression ($\rho = 0.51$, $P = 0.02$), and entropy correlated with Hif1-alpha expression ($\rho = 0.47$, $P = 0.04$). None of the V_e values were associated with the analyzed histochemical parameters.

In the p16 negative group, the following associations could be identified: K_{ep} mode correlated with Her2 expression ($\rho = -0.72$, $P = 0.03$), V_e max correlated with p53 expression ($\rho = -0.80$, $P = 0.009$), and V_e p10 correlated with EGFR expression ($\rho = 0.68$, $P = 0.04$).

4. Discussion

This present study identified statistically significant associations between histogram parameters derived from DCE-MRI and different histopathological features in HNSCC. Furthermore, it showed that these relationships depended on the p16 status.

There is increasing evidence that MRI, especially using functional imaging modalities, is able to reflect tumor microstructure and to predict tumor behavior [3, 7, 8, 20]. It is widely acknowledged that DCE-MRI is associated with vascularity in tissues, especially with microvessel density as the most investigated parameter. For example, significant associations between DCE-MRI and microvessel density have been reported in experimental [23] as well as in clinical investigations [7, 24, 25].

Notably, it has been shown that different DCE parameters might also reflect different aspects of tumor microstructure [7]. So, V_e might also be strongly associated with cellularity because it reflects the amount of extracellular space, as it was exemplarily shown in a glioma model [8]. This might be one reason for the different correlations identified in the present study.

Several studies elucidated possible correlations between imaging and histopathology in HNSCC. For example, it has been shown that diffusion-weighted imaging (DWI) correlated with Ki 67 expression as well with nucleic areas [3, 26]. In another study, K_{trans} correlated inversely with Ki 67 expression ($r = -0.62$), whereas V_e tended to correlate with the cell count [7]. Furthermore, Jansen et al. showed that K_{ep} correlated statistically significant with VEGF expression ($r = 0.808$) [20].

In the present study, K_{ep} mode correlated with VEGF expression in p16 positive patients. Interestingly, also K_{trans} max correlated in a similar fashion with VEGF expression. Furthermore, K_{trans} max also showed a significant association with Hif1-alpha. Presumably, the maximum value of K_{trans} may reflect tumor areas with the highest vessel density. Therefore, the observed correlation between K_{trans} max and expression of VEGF is logical. Our results are in agreement with some previous reports. For example, in gliomas, also a positive correlation between VEGF and K_{trans} was observed [27–29].

However, some studies did not find significant associations between DCE-MRI and histopathology. For example, in breast cancer, no correlations between histogram parameters derived from DCE-MRI and VEGF expression could be identified [24].

Rasmussen et al. found associations between standardized uptake values (SUV) derived from positron emission tomography (PET) with 2-deoxy-2-[18F]fluoro-D-glucose (FDG) and histopathology in HNSCC [30]. There were negative correlations for Bcl-2 and p16 and positive with β-tubulin-1 index. Moreover, in another study, SUV was only associated with VEGF expression, whereas no association was found for GLUT-1, Ki 67, P53, CD68, Hif1-alpha, and CD31 [31]. Our results indicate that DCE-MRI might be more sensitive than FDG PET for prediction of histopathological features.

It is believed that the histogram-based analysis of radiological images can better reflect tumor than conventional ROI-based analysis [15]. For example, it was shown that histogram analysis of DCE and DWI can identify more correlations between parameters of these imaging modalities [32].

The present study showed that kurtosis values derived from K_{ep} and V_e min were significantly different in p16 positive compared to p16 negative tumors. This novel finding might be caused by several underlying tissue characteristics. In a recent study by de Perrot et al., histogram analysis derived from the ADC map was used to differentiate between p16 positive and p16 negative HNSCSS [19]. V_e is a parameter, which might be related to ADC values and cellularity [8, 30]. Interestingly, V_e min that represents voxels with the lowest extracellular space, and, presumably, areas with the highest cell density, was lower in p16 positive lesions. This finding may suggest that p16 positive tumors may show a higher cell density than p16 negative tumors. In the study by de Perrot et al., also kurtosis derived from ADC maps could distinguish p16 positive and p16 negative carcinomas [19].

These findings might be related to several causes. As reported previously, p16 positive cancers were more often nonkeratinizing and had a high Ki 67 expression [19]. Moreover, expression profiles of p16 positive and p16 negative cancers might differ significantly emphasizing their different tumor behavior. So, it was shown that expression of Eps8 is different in these subtypes of HNSCC [33]. This EGFR substrate contributes to the carcinogenesis and might be involved in invasiveness in HNSCC [31]. Interestingly, the expression of Eps8 correlated with the tumor stage and p16 status but not with anatomical localization of tumors [33]. Moreover, the expression of other histopathological parameters such as EGFR, VEGF,

and NOTCH1 differ between p16 positive and negative tumors, which suggest differences in tumor angiogenesis in these entities [34]. This might be also a reason for the identified influence of p16 expression on association between imaging and histopathology.

Furthermore, it is known that p16 expression is one of the most important prognostic factors in HNSCC with a more favorable outcome for p16 positive cancers [16]. The other investigated histopathological features are also of clinical importance. So, EGFR is involved in the regulation of many cellular pathways, including cell proliferation, apoptosis, and cellular differentiation [35]. It was identified that EGFR expression is a good prognostic parameter in HNSCC [35, 36]. Furthermore, p53 regulates the activity of pathways, which lead to cell cycle arrest, senescence, or apoptosis [37]. Another parameter, namely, VEGF predicts outcome in HNSCC. VEGF overexpression has been reported as a poor indicator for patients with head and neck cancer [38]. Finally, Hif1-alpha characterizes cellular responses to hypoxic stress and is related to the neoangiogenesis [39]. Overexpression of Hif1-alpha was also significantly associated with poor survival in HNSCC [39]. Therefore, the possibility to characterize HNSCC based on imaging is very important. The identified associations between DCE-MRI parameters and several histopathological markers can be used in clinical practice.

There are several limitations of this study to address. Firstly, our patient sample size is small yet good comparable to similar studies. Secondly, we performed a whole tumor measurement for the DCE-MRI images, whereas the histopathology was investigated only on a small part of the tumor, which might limit our correlation results. Further prospective studies are needed to confirm our preliminary results.

In conclusion, the present study identified statistically significant correlations between histogram parameters derived from DCE-MRI and expression of VEGF, EGFR, p53, and Hif1-alpha in HNSCC. Associations between DCE-MRI and histopathology in HNSCC depend on the p16 status. Furthermore, K_{ep} kurtosis and V_e minimum can differentiate p16 positive and p16 negative carcinomas.

Data Availability

The data used to support the findings of this study are available from the corresponding author upon request.

Ethical Approval

The study was approved by the institutional review board of the University of Leipzig. All procedures performed in the study were in accordance with the ethical standards of the institutional research committee and with the 1964 Helsinki Declaration and its later amendments or comparable ethical standards.

Conflicts of Interest

The authors declare that there are no conflicts of interest.

Authors' Contributions

Conceptualization was done by Alexey Surov. Data curation was performed by Leonard Leifels, Alexey Surov, and Hans Jonas Meyer. Formal analysis was conducted by Leonard Leifels, Hans Jonas Meyer, and Anne Kathrin Höhn. Investigation was performed by Leonard Leifels, Alexey Surov, and Anne Kathrin Höhn. Methodology was contributed by Hans Jonas Meyer and Alexey Surov. Project administration was done by Alexey Surov. Resources were contributed by Alexey Surov and Hans Jonas Meyer. Software was contributed by Hans Jonas Meyer and Alexey Surov. Supervision was done by Alexey Surov. Validation was performed by Alexey Surov and Hans Jonas Meyer. Visualization was performed by Alexey Surov. Writing of the original draft was performed by Hans Jonas Meyer. Writing in terms of review and editing was performed by Leonard Leifels, Alexey Surov, Hans Jonas Meyer, and Anne Kathrin Höhn.

References

[1] B. J. M. Braakhuis, C. R. Leemans, and O. Visser, "Incidence and survival trends of head and neck squamous cell carcinoma in the Netherlands between 1989 and 2011," *Oral Oncology*, vol. 50, no. 7, pp. 670–675, 2014.

[2] T. A. Szyszko and G. J. R. Cook, "PET/CT and PET/MRI in head and neck malignancy," *Clinical Radiology*, vol. 73, no. 1, pp. 60–69, 2018.

[3] A. Surov, H. J. Meyer, and A. Wienke, "Correlation between apparent diffusion coefficient (ADC) and cellularity is different in several tumors: a meta-analysis," *Oncotarget*, vol. 8, no. 35, pp. 59492–59499, 2017.

[4] S. P. Li and A. R. Padhani, "Tumor response assessments with diffusion and perfusion MRI," *Journal of Magnetic Resonance Imaging*, vol. 35, no. 4, pp. 745–763, 2012.

[5] S.-H. Ng, C.-T. Liao, C.-Y. Lin et al., "Dynamic contrast-enhanced MRI, diffusion-weighted MRI and 18F-FDG PET/CT for the prediction of survival in oropharyngeal or hypopharyngeal squamous cell carcinoma treated with chemoradiation," *European Radiology*, vol. 26, no. 11, pp. 4162–4172, 2016.

[6] J. F. A. Jansen, J. A. Koutcher, and A. Shukla-Dave, "Non-invasive imaging of angiogenesis in head and neck squamous cell carcinoma," *Angiogenesis*, vol. 13, no. 2, pp. 149–160, 2010.

[7] A. Surov, H. J. Meyer, M. Gawlitza et al., "Correlations between DCE MRI and histopathological parameters in head and neck squamous cell carcinoma," *Translational Oncology*, vol. 10, no. 1, pp. 17–21, 2017.

[8] M. P. Aryal, T. N. Nagaraja, K. A. Keenan et al., "Dynamic contrast enhanced MRI parameters and tumor cellularity in a rat model of cerebral glioma at 7 T," *Magnetic Resonance in Medicine*, vol. 71, no. 6, pp. 2206–2214, 2014.

[9] D. Zheng, Q. Yue, W. Ren et al., "Early responses assessment of neoadjuvant chemotherapy in nasopharyngeal carcinoma by serial dynamic contrast-enhanced MR imaging," *Magnetic Resonance Imaging*, vol. 35, pp. 125–131, 2017.

[10] K. H. Wong, R. Panek, A. Dunlop et al., "Changes in multimodality functional imaging parameters early during chemoradiation predict treatment response in patients with locally advanced head and neck cancer," *European Journal of Nuclear Medicine and Molecular Imaging*, vol. 45, no. 5, pp. 759–767, 2017.

[11] S. C. Chan, N. M. Cheng, C. H. Hsieh et al., "Multiparametric imaging using ^{18}F-FDG PET/CT heterogeneity parameters and functional MRI techniques: prognostic significance in patients with primary advanced oropharyngeal or hypopharyngeal squamous cell carcinoma treated with chemoradiotherapy," *Oncotarget*, vol. 8, no. 37, pp. 62606–62621, 2017.

[12] E. J. Choi, H. Choi, S. A. Choi, and J. H. Youk, "Dynamic contrast-enhanced breast magnetic resonance imaging for the prediction of early and late recurrences in breast cancer," *Medicine*, vol. 95, no. 19, article e5330, 2016.

[13] D. P. Noij, M. C. de Jong, L. G. M. Mulders et al., "Contrast-enhanced perfusion magnetic resonance imaging for head and neck squamous cell carcinoma: a systematic review," *Oral Oncology*, vol. 51, no. 2, pp. 124–138, 2015.

[14] M. Sumi and T. Nakamura, "Head and neck tumours: combined MRI assessment based on IVIM and TIC analyses for the differentiation of tumors of different histological types," *European Radiology*, vol. 24, no. 1, pp. 223–231, 2013.

[15] N. Just, "Improving tumour heterogeneity MRI assessment with histograms," *British Journal of Cancer*, vol. 111, no. 12, pp. 2205–2213, 2014.

[16] C. A. Fischer, M. Kampmann, I. Zlobec et al., "p16 expression in oropharyngeal cancer: its impact on staging and prognosis compared with the conventional clinical staging parameters," *Annals of Oncology*, vol. 21, no. 10, pp. 1961–1966, 2010.

[17] J. E. Swartz, A. J. Pothen, I. Stegeman, S. M. Willems, and W. Grolman, "Clinical implications of hypoxia biomarker expression in head and neck squamous cell carcinoma: a systematic review," *Cancer Medicine*, vol. 4, no. 7, pp. 1101–1116, 2015.

[18] M. C. Solomon, M. S. Vidyasagar, D. Fernandes et al., "The prognostic implication of the expression of EGFR, p53, cyclin D1, Bcl-2 and p16 in primary locally advanced oral squamous cell carcinoma cases: a tissue microarray study," *Medical Oncology*, vol. 33, no. 12, p. 138, 2016.

[19] T. de Perrot, V. Lenoir, M. Domingo Ayllón, N. Dulguerov, M. Pusztaszeri, and M. Becker, "Apparent diffusion coefficient histograms of human papillomavirus-positive and human papillomavirus-negative head and neck squamous cell carcinoma: assessment of tumor heterogeneity and Comparison with histopathology," *American Journal of Neuroradiology*, vol. 38, no. 11, pp. 2153–2160, 2017.

[20] J. F. A. Jansen, D. L. Carlson, Y. Lu et al., "Correlation of a priori DCE-MRI and 1H-MRS data with molecular markers in neck nodal metastases: initial analysis," *Oral Oncology*, vol. 48, no. 8, pp. 717–722, 2012.

[21] A. Surov, H. J. Meyer, L. Leifels et al., "Histogram analysis parameters of dynamic contrast-enhanced magnetic resonance imaging can predict histopathological findings including proliferation potential, cellularity, and nucleic areas in head and neck squamous cell carcinoma," *Oncotarget*, vol. 9, no. 30, pp. 21070–21077, 2018.

[22] H. J. Meyer, L. Leifels, G. Hamerla, A. K. Höhn, and A. Surov, "ADC-histogram analysis in head and neck squamous cell carcinoma. Associations with different histopathological features including expression of EGFR, VEGF, HIF-1α, Her 2 and p53. A preliminary study," *Magnetic Resonance Imaging*, vol. 54, no. 12, pp. 214–217, 2018.

[23] A. Sterzik, P. M. Paprottka, P. Zengel et al., "DCE-MRI biomarkers for monitoring an anti-angiogenic triple combination therapy in experimental hypopharynx carcinoma xenografts with immunohistochemical validation," *Acta Radiologica*, vol. 56, no. 3, pp. 294–303, 2015.

[24] S. H. Kim, H. S. Lee, B. J. Kang et al., "Dynamic contrast-enhanced MRI perfusion parameters as imaging biomarkers of angiogenesis," *PLoS One*, vol. 11, no. 12, Article ID e0168632, 2016.

[25] Z. Z. Jia, H. M. Gu, X. J. Zhou et al., "The assessment of immature microvascular density in brain gliomas with dynamic contrast-enhanced magnetic resonance imaging," *European Journal of Radiology*, vol. 84, no. 9, pp. 1805–1809, 2015.

[26] A. Surov, P. Stumpp, H. J. Meyer et al., "Simultaneous 18F-FDG-PET/MRI: associations between diffusion, glucose metabolism and histopathological parameters in patients with head and neck squamous cell carcinoma," *Oral Oncology*, vol. 58, no. 2, pp. 14–20, 2016.

[27] N. Di, C. Yao, W. Cheng et al., "Correlation of dynamic contrast-enhanced MRI derived volume transfer constant with histological angiogenic markers in high-grade gliomas," *Journal of Medical Imaging and Radiation Oncology*, vol. 62, no. 4, pp. 464–470, 2018.

[28] M. M. Ali, B. Janic, A. Babajani-Feremi et al., "Changes in vascular permeability and expression of different angiogenic factors following anti-angiogenic treatment in rat glioma," *PLoS One*, vol. 5, no. 1, p. e8727, 2010.

[29] A. F. O'Neill, L. Qin, P. Y. Wen, J. F. de Groot, A. D. Van den Abbeele, and J. T. Yap, "Demonstration of DCE-MRI as an early pharmacodynamic biomarker of response to VEGF Trap in glioblastoma," *Journal of Neuro-oncology*, vol. 130, no. 3, pp. 495–503, 2016.

[30] G. B. Rasmussen, I. R. Vogelius, J. H. Rasmussen et al., "Immunohistochemical biomarkers and FDG uptake on PET/CT in head and neck squamous cell carcinoma," *Acta Oncologica*, vol. 54, no. 9, pp. 1408–1415, 2015.

[31] T. J. Grönroos, K. Lehtiö, K. O. Söderström et al., "Hypoxia, blood flow and metabolism in squamous-cell carcinoma of the head and neck: correlations between multiple immunohistochemical parameters and PET," *BMC Cancer*, vol. 14, no. 1, p. 876, 2014.

[32] H. J. Meyer, L. Leifels, S. Schob, N. Garnov, and A. Surov, "Histogram analysis parameters identify multiple associations between DWI and DCE MRI in head and neck squamous cell carcinoma," *Magnetic Resonance Imaging*, vol. 45, pp. 72–77, 2018.

[33] E. Nasri, L. B. Wiesen, J. A. Knapik, and K. M. Fredenburg, ""Eps8 expression is significantly lower in p16+ head and neck squamous cell carcinomas (HNSCC) compared to p16-HNSCC," *Human Pathology*, vol. 72, pp. 45–51, 2017.

[34] J. D. Troy, J. L. Weissfeld, A. O. Youk, S. Thomas, L. Wang, and J. R. Grandis, "Expression of EGFR, VEGF, and NOTCH1 suggest differences in tumor angiogenesis in HPV-positive and HPV-negative head and neck squamous cell carcinoma," *Head and Neck Pathology*, vol. 7, no. 4, pp. 344–355, 2013.

[35] P. Bossi, C. Resteghini, N. Paielli, L. Licitra, S. Pilotti, and F. Perrone, "Prognostic and predictive value of EGFR in head and neck squamous cell carcinoma," *Oncotarget*, vol. 7, no. 45, pp. 74362–74379, 2016.

[36] X. Ma, J. Huang, X. Wu et al., "Epidermal growth factor receptor could play a prognostic role to predict the outcome of nasopharyngeal carcinoma: a meta-analysis," *Cancer Biomarkers*, vol. 14, no. 4, pp. 267–277, 2014.

[37] S. Tandon, C. Tudur-Smith, R. D. Riley, M. T. Boyd, and T. M. Jones, "A systematic review of p53 as a prognostic factor of survival in squamous cell carcinoma of the four main anatomical subsites of the head and neck," *Cancer Epidemiology Biomarkers & Prevention*, vol. 19, no. 2, pp. 574–587, 2010.

[38] J. Zang, C. Li, L. N. Zhao et al., "Prognostic value of vascular endothelial growth factor in patients with head and neck cancer: a meta-analysis," *Head & Neck*, vol. 35, no. 10, pp. 1507–1514, 2013.

[39] L. Gong, W. Zhang, J. Zhou et al., "Prognostic value of HIFs expression in head and neck cancer: a systematic review," *PLoS One*, vol. 8, no. 9, Article ID e75094, 2013.

Hindawi
Contrast Media & Molecular Imaging
Volume 2018, Article ID 2136840, 9 pages
https://doi.org/10.1155/2018/2136840

Research Article

Spectral Photon-Counting Molecular Imaging for Quantification of Monoclonal Antibody-Conjugated Gold Nanoparticles Targeted to Lymphoma and Breast Cancer: An *In Vitro* Study

Mahdieh Moghiseh,[1] **Chiara Lowe**,[1] **John G. Lewis**,[2] **Dhiraj Kumar**,[3] **Anthony Butler**,[1] **Nigel Anderson**,[1] **and Aamir Raja**[1]

[1]*Department of Radiology, University of Otago, Christchurch School of Medicine, 2 Riccarton Avenue, Christchurch 8011, New Zealand*
[2]*Steroid & Immunobiochemistry Laboratory, Canterbury Health Laboratories, 524 Hagley Ave, Christchurch 8011, New Zealand*
[3]*Department of Obstetrics and Gynecology, University of Otago, Christchurch School of Medicine, 2 Riccarton Avenue, Christchurch 8011, New Zealand*

Correspondence should be addressed to Chiara Lowe; chiara.lowe@postgrad.otago.ac.nz

Received 20 July 2018; Accepted 18 November 2018; Published 18 December 2018

Guest Editor: Alessandro Bombonati

The purpose of the present study was to demonstrate an *in vitro* proof of principle that spectral photon-counting CT can measure gold-labelled specific antibodies targeted to specific cancer cells. A crossover study was performed with Raji lymphoma cancer cells and HER2-positive SKBR3 breast cancer cells using a MARS spectral CT scanner. Raji cells were incubated with monoclonal antibody-labelled gold, rituximab (specific antibody to Raji cells), and trastuzumab (as a control); HER2-positive SKBR3 breast cancer cells were incubated with monoclonal antibody-labelled gold, trastuzumab (specific antibody to HER2-positive cancer cells), and rituximab (as a control). The calibration vials with multiple concentrations of nonfunctionalised gold nanoparticles were used to calibrate spectral CT. Spectral imaging results showed that the Raji cells-rituximab-gold and HER2-positive cells-trastuzumab-gold had a quantifiable amount of gold, 5.97 mg and 0.78 mg, respectively. In contrast, both cell lines incubated with control antibody-labelled gold nanoparticles had less gold attached (1.22 mg and 0.15 mg, respectively). These results demonstrate the proof of principle that spectral molecular CT imaging can identify and quantify specific monoclonal antibody-labelled gold nanoparticles taken up by Raji cells and HER2-positive SKBR3 breast cancer cells. The present study reports the future potential of spectral molecular imaging in detecting tumour heterogeneity so that treatment can be tuned accordingly, leading to more effective personalised medicine.

1. Introduction

The current molecular imaging modalities, such as positron emission tomography (PET), single-photon emission-computed tomography (SPECT), magnetic resonance imaging (MRI), and optical coherence tomography (OCT), have come a long way towards the observation of biological processes at molecular and cellular levels. However, each of these modalities has its limitations that contribute to an inability in measuring specific biomarkers of cancer in patients [1–4]. PET and SPECT, although sensitive, are slow, nonspecific, and require radioactive tracers. MRI provides excellent soft tissue contrast but is slow, has poor spatial resolution, and cannot be used for patients with claustrophobia or metallic implants. OCT is sensitive and specific, but its limited penetration depth prevents it from being translated to most clinical tasks. To overcome the limitations associated with current biomedical imaging techniques, we aim to use new imaging technology at clinical X-ray energy ranges, with the inclusion of monoclonal antibody-functionalised gold nanoparticles.

The advent of the energy-discriminating photon-counting spectral detector [5] has opened the door to

radically new approaches to medical investigation and monitoring. Like a prism splitting white light into a rainbow, a spectral detector captures full information in multiple X-ray energy bins. Spectral CT imaging combines the high-resolution anatomical detail of standard CT with the ability to characterise and quantify components of the tissue. As each material has a specific measurable X-ray spectrum, spectroscopic imaging can simultaneously measure several biomarkers of biological processes at the cellular and molecular level, using simultaneously acquired data for multiple energy bins. The combination of high spatial and spectral resolution with specific identification and quantification of multiple tissue components, noninvasively, is unique to specific cells and molecules. This cellular and molecular-specific CT imaging is known as *spectral molecular CT imaging*. As an emerging revolution in X-ray-based imaging, spectral molecular CT promises to complement the existing molecular imaging modalities and to be a potential tool for delivering personalised medicine [6–10]. Preclinical results with spectral molecular CT have been very encouraging and indicate that the specific identification and quantification of tissue types and nanoparticles is possible, such as imaging of vulnerable plaque [11, 12], soft tissue quantification [13], reduction in metal-related CT artefacts [14, 15], crystal-induced arthropathies [16, 17], quantitative imaging of excised osteoarthritic cartilage [18], and K-edge imaging of high-Z (atomic number) biomedical nanoparticles [19, 20].

Laboratory and preclinical results with spectral molecular CT have been very encouraging, but the question of how spectral molecular CT imaging could be used in clinical practice still remains. Given the evidence so far, spectral CT has the capability of determining drug delivery and host immune response to cancer, a clinical area that is not yet met by current clinical imaging modalities. In recent years, advances in nanotechnology and nanomedicine have focussed on targeting tumours for diagnosis and therapy [21–23]. Nanoparticles possess desirable physiochemical properties for chemical and biological detection, including improving signal strength in imaging, high surface area to volume ratio, and easily tuneable surface chemistry [23–25]. Nanoparticle-based drug delivery systems for systemic applications have significant advantages and have the potential to be more effective compared to their nonformulated, free drug counterparts, as surface chemistry allows the attachment of functional groups which recognise biological cues for improved specificity [26].

Among metal nanoparticles, engineered gold nanoparticles (AuNPs) are increasingly utilised in various biomedical applications due to their inert nature, low size dispersity (size distribution), high stability, comparably easy synthesis, noncytotoxic nature, and biocompatibility [27]. AuNPs have ideal properties for use as a targeted nanocontrast material for imaging cancer [28–35]. Spectral molecular CT integrated with nanoparticle technology may solve limitations faced by current molecular imaging modalities and facilitate drug discovery. The present study will employ AuNPs to label monoclonal antibodies for the reasons stated.

The aim of the present research is to test the ability of spectral molecular CT to detect and quantify the delivery of drugs to tumours, using targeted gold-labelled monoclonal antibodies. We are reporting for the first time MARS spectral photon-counting CT imaging of Herceptin-modified AuNPs, specific to HER2-positive breast cancer cells, as a way of establishing a novel multifunctional platform that allows for the identification of pathology and assessment of treatment. Moreover, rituximab, specific to Raji lymphoma cancer cells, will provide a crossover experiment. A negative control is an ideal scenario for a preclinical "proof of principle" showing the ability of MARS spectral CT imaging technology to distinguish and quantify specifically labelled cells.

2. Materials and Methods

2.1. Spectral Photon-Counting CT Imaging

2.1.1. MARS Spectral CT Scanner Setup. MARS spectral CT is enabled by the properties of the photon-processing detector, Medipix3RX (Medipix3RX Collaboration, CERN), within the MARS spectral scanner [13]. Multiple energy windows or bins of the energy-resolving detector provide sufficient data to separate several materials in a single X-ray exposure [19]. The spectral CT technology has been reported to differentiate and quantify multiple different high-Z materials in a single scan by sampling the material-specific attenuation curves within multiple narrow energy bins, allowing the detection of element-specific K-edge discontinuities of the photoelectric cross section [36, 37].

Medipix3RX detector can be operated in either the single pixel mode (SPM) or charge summing mode (CSM) [38]. To cover the K-edge of Au, energy thresholds were set: 18, 30, 45, and 75 keV in CSM. Acquired data were reconstructed in four narrow CSM energy bins (18–30, 30–45, 45–75, and 75–118 keV) by a 3D algebraic reconstruction algorithm [39] (Table 1).

2.1.2. Image Processing. Prior to scanning the samples, the MARS system creates a pixel mask by acquiring 20 dark-field (without X-rays) and 200 flat-field (open beam) images. This mask was applied to remove noisy pixels, including non-functional and high and low sensitivity pixels [37, 40, 41]. For each study, the calibration vials (2, 4, and 8 mg/mL $AuCl_3{\cdot}xH_2O$) were placed within a phantom holder, along with the cell vials, and scanned. The assessment of the reconstructed images involved measuring the linear attenuation for each material and converting linear attenuation into Hounsfield units (HU). Using an in-house programme that uses the calculated effective mass attenuation of the calibration vials [20, 39], material decomposition (MD) was applied to the energy images and quantification of the trastuzumab and rituximab was performed by measuring the amount of gold in the cell clumps.

2.1.3. Cancer Cell Phantoms. 200 μL Eppendorf tubes of each material (Table 2) were placed in a polymethyl methacrylate (PMMA) phantom holder. One vial with SKBR3 was incubated with trastuzumab-gold nanoparticle complex (Her-AuNP). As a control, SKBR3 incubated with rituximab gold nanoparticle complex (Rit-AuNP) was

Table 1: Summary of MARS spectral CT scanner experimental setup.

Parameter	Value
Scan type	Continuous
Tube voltage	118 kVp
Tube current	12 μA
Exposure time	300 ms
Sample diameter	38 mm
Energy (CSM)	18, 30, 45, and 75 keV
Circular projections	720 over 360°
Flat fields	720
Voxel size	$1 \times 1 \times 1\,mm^3$
SDD, SOD	250 mm, 200 mm
Filtration	2 mm Al + 1.8 mm Al intrinsic

SDD: source-to-detector distance; SOD: source-to-object distance.

Table 2: Summary of phantom setup.

Raji phantom	SKBR3 phantom
AuNPs 2, 4, and 8 mg/mL AuNPs size by DLS: 50 nm (expected 40 nm) AuNPs absorbance: 530 nm	AuNPs 2, 4, and 8 mg/mL
Water, lipid	Water, lipid
Raji cells with Her-AuNP (control)	SKBR3 with Her-AuNP
Raji cells with Rit-AuNP	SKBR3 with Rit-AuNP (control)

Her, trastuzumab or Herceptin; Rit, rituximab.

included. Raji lymphoma cells were treated with the same protocol, incubated with Her-AuNP and Rit-AuNP, in a separate PMMA phantom holder. Water, lipid, and 3 concentrations of AuNPs (2, 4, and 8 mg/mL) were used for calibration purposes in both phantoms.

2.2. Gold Nanoparticles. The streptavidin-modified gold nanoparticles of size 40 nm were purchased from Fitzgerald Industries, Acton, MA, and characterised by the UV-visible spectrophotometer and dynamic light scattering (Malvern Nano Zetasizer ZS) to confirm the material, size, and size distribution.

The absorption spectrum of gold nanoparticles caused by surface plasmon absorption is directly related to the nanoparticle size. Surface plasmon resonance (SPR) is the coherent excitation of all free electrons within the conduction band. As particle size increases, the wavelength of SPR related to absorption shifts to longer, redder wavelengths [42, 43]. SPR is important as it allows the AuNP size to be specifically identified so that it is the gold added to the experiment which is being measured.

2.3. Antibodies and Labelling

2.3.1. Antibodies. Trastuzumab (Herceptin, Roche Pharmaceuticals, Mississauga, ON, Canada) binds exclusively to HER2-positive human breast cancer cells, and rituximab (Mabthera) binds to CD20 antigen on human B-cell lymphomas and are humanised chimeric therapeutic monoclonal antibodies with a human Fc domain. Both drugs were made and supplied by Roche Pharmaceuticals, Mississauga, ON, Canada. Goat antihuman IgGFc-biotin was from Fitzgerald Industries, Acton, MA, and streptavidin peroxidase was supplied by Jackson Immunoresearch Laboratories, West Grove, PA.

2.3.2. Biotinylation of Antibodies. Rituximab and trastuzumab were both dialysed, and then each were diluted to 2.5 mg/mL with 0.1 M borate buffer, pH 8.8, 1/20th volume of biotinamidocaproate N hydroxysuccinamide ester in DMSO (10 mg/mL) added (goat antihuman IgGFc-biotin, Fitzgerald Industries, Acton, MA) and then mixed for four hours at 200°C. Unreacted biotin ester was blocked by the addition of 1 M ammonium chloride. Following exhaustive dialysis against phosphate-buffered saline (PBS), the material was clarified by centrifugation and concentration adjusted to 2 mg/mL.

2.4. In Vitro Studies

2.4.1. Cell Lines. The HER2-positive human breast cancer line SKBR3 and the CD20-positive human B-cell line Raji cells were obtained from frozen stocks held by the Steroid and Immunobiochemistry Laboratory, Canterbury Health Laboratories, Christchurch, New Zealand. They were cultured in flasks in RPMI 1640 supplemented with 10% foetal calf serum (FCS) media and grown at 37°C in 5% CO_2. The SKBR3 cells were harvested at confluency and the Raji cells during log phase growth. Following harvest, the cells were centrifuged and washed twice with PBS. The cells were then used for cell-based ELISA experiments to optimise incubation and labelling conditions for subsequent labelling with antibody-AuNPs and analysis by spectral CT scanning. The use of both SKBR3 and Raji cells allowed crossover control experiments for each monoclonal antibody as SKBR3 HER2 positive but CD20 negative; and Raji cells are CD20 positive but HER2 negative.

2.4.2. Cell-Based Enzyme-Linked Immunosorbent Assay (ELISA). Washed cells were suspended into 11 mL of PBS and plated across the wells (100 μL/well containing 20,000 cells) of a 96-well, flat-bottomed, microtiter plate. The plate was centrifuged for 5 minutes to sediment the cells, and the PBS was carefully aspirated. Cells were fixed for 30 minutes at 20°C by adding 2% paraformaldehyde into the PBS (100 μL/well). The paraformaldehyde was then carefully aspirated, and the plate was dried under a gentle stream of air. The plate was then blocked with assay buffer containing 1% FCS for 30 minutes at 20°C (200 μL/well). Following blocking, the buffer was decanted, and the plate was blot dried by inversion. 2 mg/mL dilutions of either rituximab, trastuzumab, biotinylated rituximab, or biotinylated trastuzumab were added for 30 minutes at 20°C. The wells were then washed three times (200 μL/well). For the rituximab and trastuzumab series, antihuman IgGFc-biotin was added for another 30 minutes at 20°C (1 : 1000 in PBS containing 1% FCS and 100 μL/well). For the biotinylated rituximab and

biotinylated trastuzumab series, the plates were washed and 100 μL/well of 1 : 1000 dilution of streptavidin peroxidase (Fitzgerald Industries, Acton, MA) was added for 30 minutes at 20°C, followed by washing and addition of tetramethylbenzidine substrate (100 μL/well). Following the addition of antihuman IgGFc-biotin rituximab and Herceptin series, the plates were washed and incubated with 1:1000 streptavidin peroxidase for 30 minutes at 20°C prior to the final washing and the addition of tetramethylbenzidine substrate (100 μL/well). Following colour development, the reaction was stopped by the addition of 1 M HCl (100 μL/well), and the absorbance was read at 450 nm. The absorption reading gives an indication of the particle size.

2.4.3. Gold Labelling of Cells. SKBR3 (20–100 million) and Raji (20–100 million) cells were harvested, washed as described, and each cell type was divided into two portions. Each portion was incubated with either Herceptin or rituximab (1 : 100 of 2 mg/mL in PBS containing 1% FCS) for 30 minutes at 20°C in 1.5 mL Eppendorf tubes and continually mixed. The cells were then washed and antihuman IgGFc-biotin (1 : 100 in PBS containing 1% FCS) was added for 30 minutes at 20°C. Following three washes in PBS, streptavidin-Au was added (1 : 10 in PBS containing 1% FCS) for a further 30 minutes at 20°C. The cells were finally washed three times in PBS and transferred to 0.5 mL Eppendorf tubes and pelleted for MARS scanning.

3. Results

3.1. Gold Nanoparticle Characterisation. The streptavidin-modified AuNPs of size 40 nm showed the lambda max peak at 530 nm. Similar observations have been reported in literature, concluding the expected size as 40 nm [44]. The dynamic light scattering (DLS) confirmed the NPs hydrodynamic size to be 50 nm (expected 40 nm). The standard absorbance graph obtained has been included in supporting information along with a typical size distribution graph by dynamic light scattering (Figure S1).

The cell-based ELISA studies on the immobilised CD20-positive Raji cell line showed higher responses with rituximab dilutions and antihuman IgG-biotin and streptavidin peroxidase compared with the same dilutions of biotinylated-rituximab and streptavidin peroxidase (open and filled circles, respectively,, in Figure 1(a)). Similarly, cell-based ELISA studies on immobilised confluent HER2-positive human breast cancer cells (SKBR3) showed higher responses with the Herceptin, antihuman IgGFc-biotin, and streptavidin peroxidase combination compared with the biotinylated-Herceptin and streptavidin peroxidase combination (open and closed triangles, respectively, in Figure 1(b)). The trastuzumab and rituximab controls are also shown in Figures 1(a) and 1(b) and show that the two antibodies can clearly be distinguished in a crossover study.

Hence, for the present study, the former combination, with the addition of streptavidin-Au in the final step, was chosen with the rationale that this combination would provide a higher gold payload for scanning. Indeed, we confirmed this rationale by small-scale experiments and visualisation of cell-bound gold nanoparticles (data not shown).

3.2. Spectral Photon-Counting CT Imaging. The attenuation signal in Hounsfield units (HU) as a function of concentration data has been included in Figure 2(a). By fitting a line that best describes the data, the linearity of attenuation for each energy bin was established [45]. Linearity determines the ability of a system to detect the presence or absence of any materials. This information directly feeds into the material quantification. Furthermore, the spectral response of the detector was plotted in Figure 2(b). Considering the K-edge of gold to be 80.7 keV, and an energy threshold set at 75 keV, we observed, as expected, an enhancement of attenuation in energy bin 4 (75–118 keV) for each concentration of AuNPs.

Greater HU was observed for Raji cells with rituximab-functionalised AuNPs and SKBR3 with Herceptin-functionalised AuNPs, as shown in Figures 2(c) and 2(d), respectively. By only observing the spectral response of the detector, spectral CT imaging is capable of indicating the presence of an attenuating material: the gold attached to trastuzumab, thus showing trastuzumab uptake into the SKBR3 cells and rituximab uptake into Raji cells. Furthermore, Figures 3(a) and 3(b) visualised, using MARS material decomposition, the detection of AuNPs in SKBR3 cells and Raji cells, respectively. Quantification of the resulting MD images was performed and shown in Figures 4(a) and 4(b). A significantly lower amount of AuNPs was detected and quantified in the control cells. Eightfold lower in SKBR3 cells incubated with rituximab modified AuNPs, and sixfold lower in Raji cells incubated with Herceptin modified AuNPs.

4. Discussion

The key outcomes of this *in vitro* study are first that spectral photon-counting CT can measure gold-labelled specific antibodies targeted to specific cancer cells; and second, that NPs can be integrated with spectral CT to generate a combined diagnostic imaging and a therapeutic agent, which can be detected and monitored. The concepts of using AuNPs with biotin to deliver a drug are well known [46]. Rituximab has been delivered using AuNPs [47]. Herceptin delivered by indium radiolabelled AuNPs has been shown to be cytotoxic *in vitro* [48]. Methods of using biotin and streptavidin with antibodies to target HER2-positive tumours are an established way [49]. In this study, we utilised these established methodologies and demonstrated the proof of principle that spectral molecular CT imaging can identify and quantify specific monoclonal antibody-labelled gold nanoparticles taken up by Raji cells and HER2-positive SKBR3 breast cancer cells.

Medical imaging is key to the diagnosis or assessment of disease response in many areas of medicine. Nevertheless, measuring disease activity, host response, and the effectiveness of treatment is frequently indirect, slow, and qualitative unless invasive procedures are performed. SKBR3, a breast cancer cell line which overexpresses epidermal growth factor

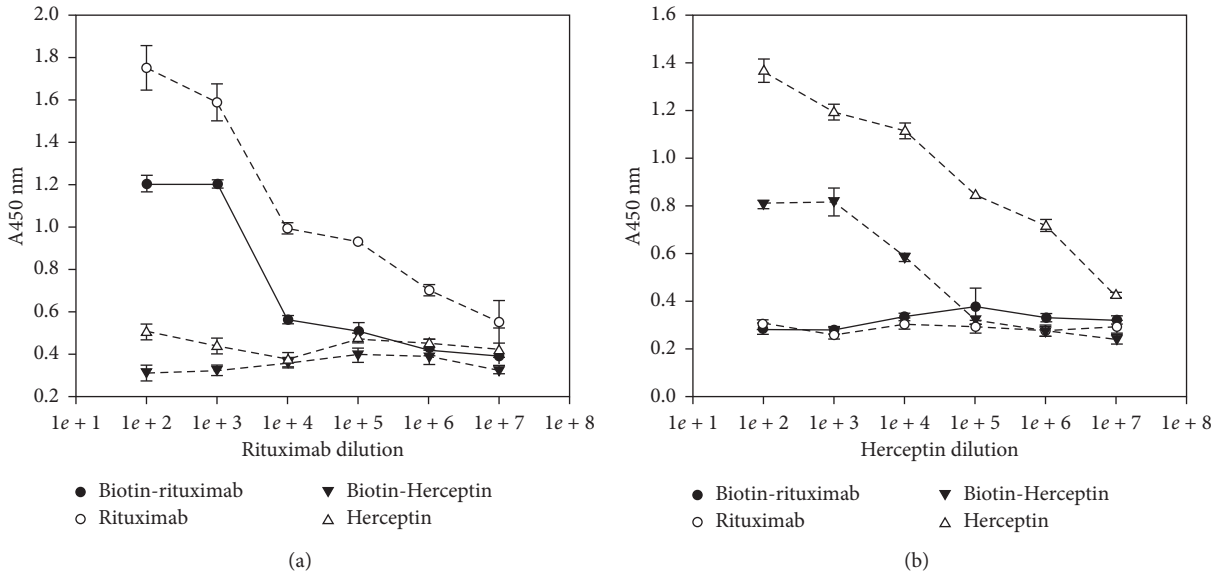

Figure 1: The quantitative data collected using the ELISA kit in the form of absorbance against drug dilution. The absorbance was read at 450 nm for (a) rituximab dilution in the case of Raji cells and (b) Herceptin dilution in the case of SKBR3.

receptor 2 (HER2), and Herceptin monoclonal antibody were used to test both the molecular specific binding of functionalised AuNPs and MARS spectral CT imaging. Herceptin works by attaching to HER2 on the cancer cells and inhibiting intracellular signalling. Crossover experiment was conducted to further support our findings. Rituximab, a monoclonal antibody which destroys both normal and malignant B cells that have CD20 receptors on their surface, is used to treat diseases that have overexpressed or dysfunctional B cells, for instance, Raji cells. Using multiple energy thresholds, the broad X-ray spectrum was divided into narrow energy bins to discriminate gold, water, and lipid. Establishing linearity of attenuation in each energy bin essentially creates multiple monochromatic CTs from a polychromatic CT X-ray source [45]. Accurate linearity of the system for any material (R^2 value ≈ 0.99 for all four energy bins was established) validates the quantification of that material. During the course of data analysis, we observed hidden K-edge phenomenon [50], which could be associated with low concentrations of AuNPs uptake by Raji and SKBR3; no enhancement of attenuation in energy bin 4 (Figures 2(c) and 2(d)) [50, 51]. However, our material decomposition algorithm [50] was able to recover this hidden information using the effective linear attenuation for each material (for each concentration and energy bin), which was estimated by taking the mean of respective regions in the reconstructed data, and demonstrates the uniqueness of spectral CT imaging [20].

Anticancer drugs are often hydrophobic, and attaching nanoparticles is a way of transporting the toxic drugs safely to the target site, where the drug will then be taken up by the cell and become active [52]. Molecules are too small to image directly; therefore, specific and sensitive contrast material is used to overcome this limitation and enhance targeted pathology. Nanoparticles provide unique and desirable physiochemical properties, ideal for CT imaging. A study by Kumar et al. suggested that size and cell type influenced the uptake of "as prepared" AuNPs by ovarian cancer cells [53]. Optimisation of the cellular uptake of AuNPs is required for different cell types to achieve enough payload. Functionalisation of AuNPs, or active uptake, improves specificity and payload. Examining molecular abnormalities of disease via noninvasive molecular imaging has allowed earlier detection, disease progression monitoring, and treatment assessment. This is achieved as molecular imaging plays a primary role in the optimisation of pathology, locating pathological lesions, guiding surgery and biopsy, and enabling more accurate diagnostic decision-making by the oncologist. The target-specific molecular probe is a crucial aspect for the development of diagnostic and therapeutic methods that address personalised treatment. Treatment focus becomes the individual patient rather than the disease [54]. Herceptin is often used with other chemotherapy medication for the treatment of breast cancer. Studies have shown slower tumour growth, which has a profound effect on the course of disease and survival of women with aggressive HER2-positive breast cancer [55–58]. Spectral imaging is a new frontier in molecular imaging which, if, used in conjunction with nanoparticle contrast material has the potential to accelerate the study of pharmacokinetics and the development of drugs for the treatment of cancer.

Distinguishing HER2-positive breast cancer cells from other cancer cell lines with photon-counting spectral CT will allow tumour heterogeneity to be imaged, spatially located, and measured noninvasively. ER expression in breast tumours could be targeted at the same time in future studies. It is hypothesized that the current nonspecific imaging approach where most cancers are staged with imaging, then reimaged to assess tumour size to see if treatment is working, or with PET to see if the metabolic activity has reduced, implying treatment is working, will be transformed. Moreover, current pathological methods to assess biopsy and whole breast specimens are unable to determine tumour heterogeneity mostly because

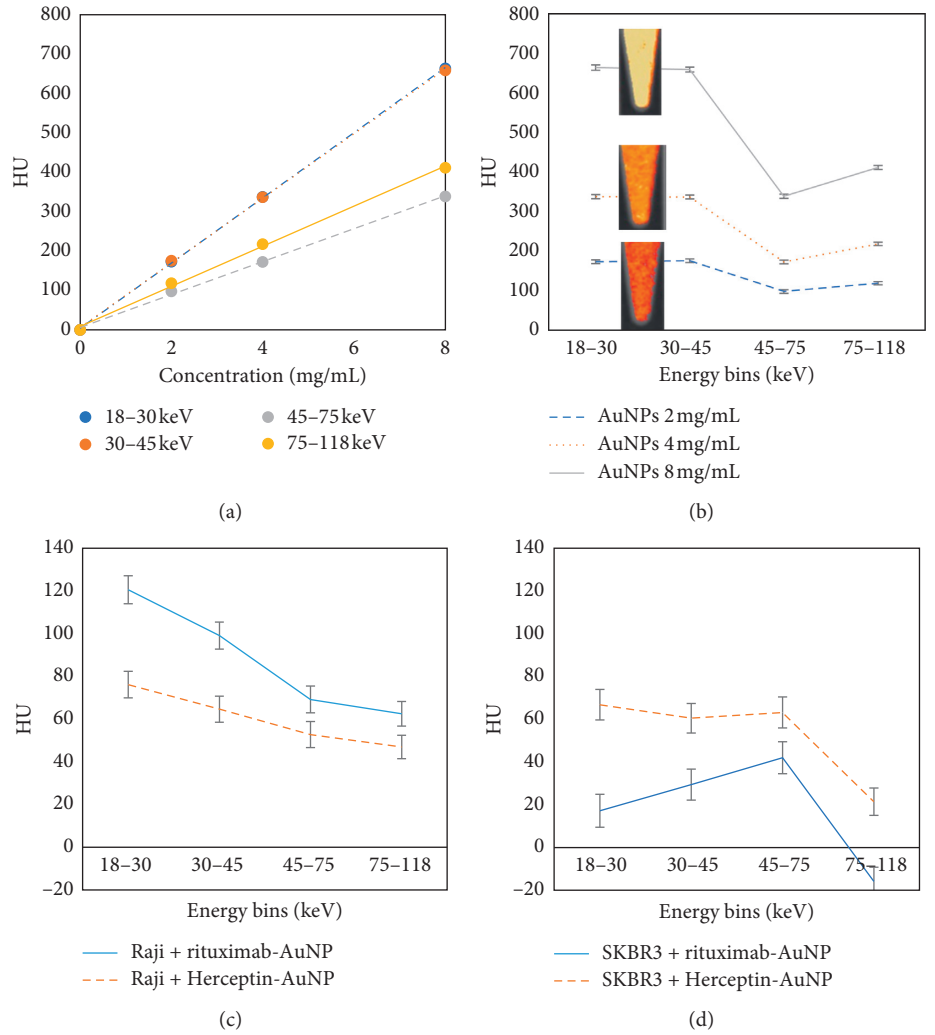

Figure 2: (a) Linearity of attenuation of calibration vials containing AuNP for each energy bin. $R^2 = 0.99$ for all linearity trends. (b) Spectral response of the detector for calibration vials. Enhancement of attenuation due to K-edge observed in energy bin 4 (75–118 keV). Insets show material decomposed images corresponding to each concentration. (c) and (d) Spectral response of Raji and SKBR3 cells, respectively. Standard errors are shown for spectral response data.

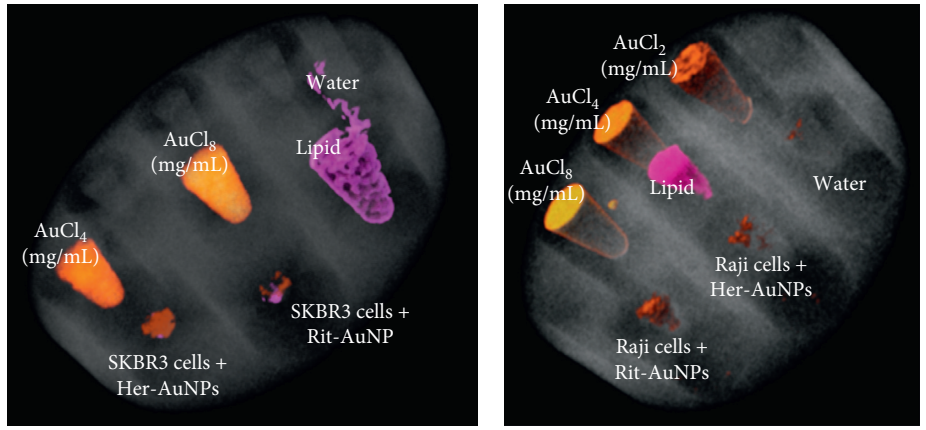

Figure 3: (a) SKBR3 cell line phantom. SKBR3 cells with Herceptin-AuNPs show more volume, indicating more gold is present. Material decomposition basis images show Au (yellow/orange, the hue represents the concentration), lipids (pink), and water-like material (grey). (b) Raji cell line phantom; Raji cells with rituximab-AuNPs show more volume and brighter hue, indicating a high concentration of gold present.

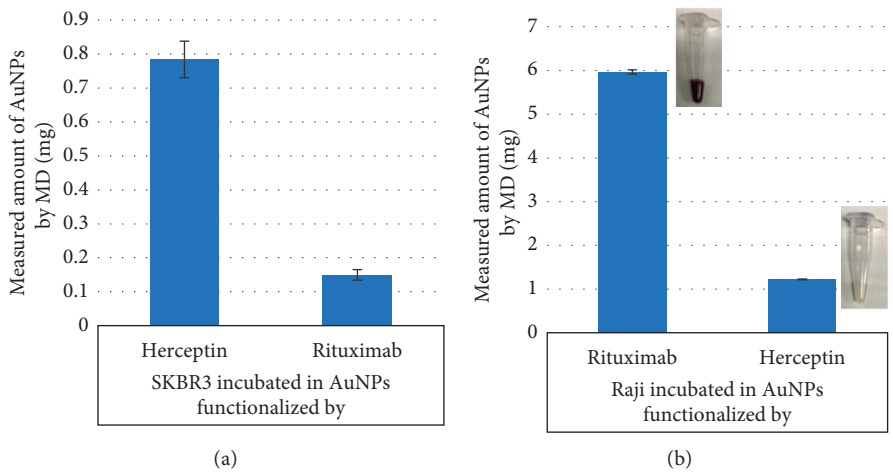

Figure 4: (a) Measured amount of targeted and nontargeted AuNPs (mg) within SKBR3 quantified from MD images displayed. (b) Measured amount of targeted and nontargeted AuNPs (mg) within Raji cells calculated from MD images. Insets show Raji cells plus Rit-AuNPs and Raji cells plus Her-AuNPs.

specimen has to be cut into sections and sampled. Heterogeneity can be underreported or missed due to sampling errors. These results may also pave the way towards providing a new approach to characterise breast cancer cell types within the specimens, where whole biopsy specimens can be used with multiple targeted markers in conjunction with spectral CT to map out and specifically identify the different populations of breast cancer cells (or different cancer cells in case of different tumour types) within the specimen, identifying and measuring breast cancer heterogeneity.

Our results illustrate the proof of concept that spectral molecular CT imaging in conjunction with functionalised gold nanoparticles can provide valuable information on tumour heterogeneity while providing important physiologic data at the cellular level. The proof of principle reported in the current study has the potential to have a major impact on the management of cancers that express specific biomarkers, such as the expression of HER2. With regard to other potential models, HER2 has also been suggested as a target for lung [59] and colorectal cancers [60]. This laboratory methodology is specifically designed to translate to human imaging so that in the future, women with breast cancer can have their treatment tuned to match changes in their tumour. The significance of this work is that once spectral CT scanners are available for clinical use, clinicians will in future be able to monitor HER2 receptor status of all sites of breast cancer in an individual, detect how and where this status changes, monitor drug delivery and disease response, and adjust treatment to keep pace with these biological changes in breast cancer, that is, be able to detect and respond to tumour heterogeneity. In this context, it is important to note that spectral CT has recently progressed to imaging the first ever human scan [61].

5. Conclusion

AuNPs are being studied and developed as a promising multifunctional platform for imaging and drug delivery applications. The present study successfully established *in vitro* methodology that aimed to measure gold-labelled specific monoclonal antibodies targeted to specific cancer cells; trastuzumab and rituximab to HER2-positive SKBR3 breast cancer and Raji B-cell lymphoma, respectively. Spectral photon-counting CT results show that Raji cells and HER2-positive SKBR3 breast cancer cells take up gold nanoparticles, if the nanoparticles are conjugated with a monoclonal antibody specific to them. A key issue that was observed and fulfilled during the study was to load the optimal amount of AuNPs for quantitative and qualitative analyses using spectral CT. The information provided is relevant for the development of more sensitive and specific targeted imaging tests for various malignancies using a range of off-the-shelf, stable functionalised nanoparticles. Spectral imaging has the potential to allow accurate diagnosis of tumour type, size, and location. The methodology in the present study was designed to translate to human imaging so that in the future, tumour heterogeneity can be detected, and treatment tuned accordingly, leading to more effective personalised cancer treatment.

Data Availability

The data used to support the findings of this study are available from the corresponding author upon request.

Conflicts of Interest

Anthony Butler is a director of MARS Bioimaging Ltd., and Nigel Anderson is a shareholder of the company. Others have no financial holding in the company.

Authors' Contributions

Mahdieh Moghiseh and Chiara Lowe contributed equally to this work.

Acknowledgments

The MARS spectral scanner was developed through a project funded by the Ministry of Business, Innovation and

Employment (MBIE), New Zealand, under the contract number UOCX0805. The authors would like to thank Raylene Fredericks at the School of Chemical Engineering, University of Canterbury, for access to Malvern Nano Zetasizer. The authors are very grateful to MARS Research team in Christchurch, New Zealand.

Supplementary Materials

Figure S1: gold nanoparticle characterisation using ultraviolet-visible spectra and a maximum absorption at 530 nm, observed in literature. Figure S2: extended methods for the quantification of material-decomposed (MD) results from MARS computed tomography molecular imaging, indicating the reliability and accuracy of MD results. (*Supplementary Materials*)

References

[1] J. V. Frangioni, "New technologies for human cancer imaging," *Journal of Clinical Oncology*, vol. 26, no. 24, pp. 4012–4021, 2008.

[2] A. N. Hisham and C.-H. Yip, "Overview of breast cancer in Malaysian women: a problem with late diagnosis," *Asian Journal of Surgery*, vol. 24, no. 2, pp. 130–133, 2004.

[3] C. A. Doubeni, S. Weinmann, K. Adams et al., "Screening colonoscopy and risk for incident late-stage colorectal cancer diagnosis in average-risk adults: a nested case–control study," *Annals of internal medicine*, vol. 158, no. 5_Part_1, pp. 312–320, 2013.

[4] G. Rubin, A. Berendsen, S. Michael Crawford et al., "The expanding role of primary care in cancer control," *The Lancet Oncology*, vol. 16, no. 12, pp. 1231–1272, 2015.

[5] K. Taguchi and J. S. Iwanczyk, "Vision 20/20: single photon counting x-ray detectors in medical imaging," *Medical Physics*, vol. 40, no. 10, article 100901, 2013.

[6] N. G. Anderson and A. P. Butler, "Clinical applications of spectral molecular imaging: potential and challenges," *Contrast Media and Molecular Imaging*, vol. 9, no. 1, pp. 3–12, 2014.

[7] P. Baturin, Y. Alivov, and S. Molloi, "Spectral CT imaging of vulnerable plaque with two independent biomarkers," *Physics in Medicine and Biology*, vol. 57, no. 13, pp. 4117–4138, 2012.

[8] D. P. Cormode, S. Si-Mohamed, D. Bar-Ness et al., "Multicolor spectral photon-counting computed tomography: in vivo dual contrast imaging with a high count rate scanner," *Scientific Reports*, vol. 7, no. 1, p. 4784, 2017.

[9] D. Muenzel, D. Bar-Ness, E. Roessl et al., "Spectral photon-counting CT: initial experience with dual-contrast agent K-edge colonography," *Radiology*, vol. 283, no. 3, pp. 723–728, 2017.

[10] D. Pan, A. H. Schmieder, A. SenPan et al., "Molecular imaging with spectral CT nanoprobes," in *Design and Applications of Nanoparticles in Biomedical Imaging*, J. W. M. Bulte and M. M. J. Modo, Eds., pp. 385–402, Springer International Publishing, Cham, Switzerland, 2017.

[11] R. B. Zainon, *Spectral Micro-CT Imaging of Ex Vivo Atherosclerotic Plaque in Physics and Astronomy Department*, University of Canterbury, Christchurch, New Zealand, 2012.

[12] H. Prebble, S. Cross, E. Marks et al., "Induced macrophage activation in live excised atherosclerotic plaque," *Immunobiology*, vol. 223, no. 8-9, 2018.

[13] R. Aamir, A. Chernoglazov, C. J. Bateman et al., "MARS spectral molecular imaging of lamb tissue: data collection and image analysis," *Journal of Instrumentation*, vol. 9, no. 2, article P02005, 2014.

[14] T. D. Maya Rajeswari Amma, A. Atharifard, A. Y. Raja, N. Anderson, B. Bamford, and A. Butler, "Optimisation of parameters for imaging bone-metal interface using spectral photon-counting computed tomography," *Journal of Medical Radiation Sciences*, vol. 65, no. S1, pp. 114–117, 2018.

[15] K. Rajendran, M. F. Walsh, N. J. A. de Ruiter et al., "Reducing beam hardening effects and metal artefacts in spectral CT using Medipix3RX," *Journal of Instrumentation*, vol. 9, no. 3, article P03015, 2014.

[16] T. E. Kirkbride, A. Y. Raja, K. Müller, C. J. Bateman, F. Becce, and N. G. Anderson, "Discrimination between calcium hydroxyapatite and calcium oxalate using multienergy spectral photon-counting CT," *American Journal of Roentgenology*, vol. 209, no. 5, pp. 1088–1092, 2017.

[17] A. Viry, A. Y. Raja, T. E. Kirkbride et al., "Multi-energy spectral photon-counting CT in crystal-related arthropathies: initial experience and diagnostic performance *in vitro*," in *Proceedings of Conference on Medical Imaging 2018: Physics of Medical Imaging, SPIE Medical Imaging*, Houston, TX, USA, March 2018.

[18] K. Rajendran, C. Löbker, B. S. Schon et al., "Quantitative imaging of excised osteoarthritic cartilage using spectral CT," *European Radiology*, vol. 27, no. 1, pp. 384–392, 2016.

[19] M. Moghiseh, R. Aamir, R. K. Panta et al., "Discrimination of multiple high-Z materials by multi-energy spectral CT–A phantom study," *JSM Biomedical Imaging Data Papers*, vol. 3, 2016.

[20] A. Raja, M. Moghiseh, C. Bateman et al., "Measuring identification and quantification errors in spectral CT material decomposition," *Applied Sciences*, vol. 8, no. 3, p. 467, 2018.

[21] S. Myung, A. Solanki, C. Kim, J. Park, K. S. Kim, and K.-B. Lee, "Graphene-encapsulated nanoparticle-based biosensor for the selective detection of cancer biomarkers," *Advanced Materials*, vol. 23, no. 19, pp. 2221–2225, 2011.

[22] X. Liu, Q. Dai, L. Austin et al., "A one-step homogeneous immunoassay for cancer biomarker detection using gold nanoparticle probes coupled with dynamic light scattering," *Journal of the American Chemical Society*, vol. 130, no. 9, pp. 2780–2782, 2008.

[23] W. Zhou, X. Gao, D. Liu, X. Chen et al., "Gold nanoparticles for *in vitro* diagnostics," *Chemical Reviews*, vol. 115, no. 19, pp. 10575–10636, 2015.

[24] P. C. Ray, S. A. Khan, A. K. Singh, D. Senapati, and Z. Fan, "Nanomaterials for targeted detection and photothermal killing of bacteria," *Chemical Society Reviews*, vol. 41, no. 8, pp. 3193–3209, 2012.

[25] G. Konvalina and H. Haick, "Sensors for breath testing: from nanomaterials to comprehensive disease detection," *Accounts of Chemical Research*, vol. 47, no. 1, pp. 66–76, 2013.

[26] A. C. Anselmo and S. Mitragotri, "Nanoparticles in the clinic," *Bioengineering and Translational Medicine*, vol. 1, no. 1, pp. 10–29, 2016.

[27] A. Khan et al., "Gold nanoparticles: synthesis and applications in drug delivery," *Tropical Journal of Pharmaceutical Research*, vol. 13, no. 7, pp. 1169–1177, 2014.

[28] E. Boisselier and D. Astruc, "Gold nanoparticles in nanomedicine: preparations, imaging, diagnostics, therapies and toxicity," *Chemical Society Reviews*, vol. 38, no. 6, pp. 1759–1782, 2009.

[29] P. D. Howes, R. Chandrawati, and M. M. Stevens, "Colloidal nanoparticles as advanced biological sensors," *Science*, vol. 346, no. 6205, article 1247390, 2014.

[30] K. E. Sapsford, W. Russ Algar, L. Berti et al., "Functionalizing nanoparticles with biological molecules: developing chemistries that facilitate nanotechnology," *Chemical Reviews*, vol. 113, no. 3, pp. 1904–2074, 2013.

[31] L. E. Cole, R. D. Ross, J. M. R. Tilley, T. Vargo-Gogola, and R. K. Roeder, "Gold nanoparticles as contrast agents in x-ray imaging and computed tomography," *Nanomedicine*, vol. 10, no. 2, pp. 321–341, 2015.

[32] A. Ambrosi, F. Airo, and A. Merkoçi, "Enhanced gold nanoparticle based ELISA for a breast cancer biomarker," *Analytical Chemistry*, vol. 82, no. 3, pp. 1151–1156, 2009.

[33] X. Zhang, "Gold nanoparticles: recent advances in the biomedical applications," *Cell Biochemistry and Biophysics*, vol. 72, no. 3, pp. 771–775, 2015.

[34] L. Dykman and N. Khlebtsov, "Biomedical applications of multifunctional gold-based nanocomposites," *Biochemistry (Moscow)*, vol. 81, no. 13, pp. 1771–1789, 2016.

[35] D. Pissuwan, T. Niidome, and M. B. Cortie, "The forthcoming applications of gold nanoparticles in drug and gene delivery systems," *Journal of Controlled Release*, vol. 149, no. 1, pp. 65–71, 2011.

[36] J. Fornaro, S. Leschka, D. Hibbeln et al., "Dual- and multi-energy CT: approach to functional imaging," *Insights into Imaging*, vol. 2, no. 2, pp. 149–159, 2011.

[37] X. Wang, D. Meier, K. Taguchi, D. J. Wagenaar, B. E. Patt, and E. C. Frey, "Material separation in x-ray CT with energy resolved photon-counting detectors," *Medical Physics*, vol. 38, no. 3, pp. 1534–1546, 2011.

[38] R. Ballabriga, J. Alozy, G. Blaj et al., "The Medipix3RX: a high resolution, zero dead-time pixel detector readout chip allowing spectroscopic imaging," *Journal of Instrumentation*, vol. 8, no. 2, article C02016, 2013.

[39] C. Bateman, D. Knight, B. Brandwacht et al., "MARS-MD: rejection based image domain material decomposition," *Journal of Instrumentation*, vol. 13, no. 5, article P05020, 2018.

[40] M. J. Marshall, R. J. Stopforth, and M. S. Cragg, "Therapeutic antibodies: what have we learnt from targeting CD20 and where are we going?," *Frontiers in immunology*, vol. 8, p. 1245, 2017.

[41] R. K. Panta, M. F. Walsh, S. T. Bell, N. G. Anderson, A. P. Butler, and P. H. Butler, "Energy calibration of the pixels of spectral x-ray detectors," *IEEE transactions on medical imaging*, vol. 34, no. 3, pp. 697–706, 2015.

[42] D. Kumar, B. J. Meenan, and D. Dixon, "Glutathione-mediated release of Bodipy® from PEG cofunctionalized gold nanoparticles," *International Journal of Nanomedicine*, vol. 7, p. 4007, 2012.

[43] J. Zhao and S.-S. Feng, "Effects of PEG tethering chain length of vitamin E TPGS with a Herceptin-functionalized nanoparticle formulation for targeted delivery of anticancer drugs," *Biomaterials*, vol. 35, no. 10, pp. 3340–3347, 2014.

[44] D. P. Clark, K. Ghaghada, E. J. Moding, D. G. Kirsch, and C. T. Badea, "In vivo characterization of tumor vasculature using iodine and gold nanoparticles and dual energy micro-CT," *Physics in Medicine and Biology*, vol. 58, no. 6, pp. 1683–1704, 2013.

[45] W. A. Weber, J. Czernin, M. E. Phelps, and H. R. Herschman, "Technology insight: novel imaging of molecular targets is an emerging area crucial to the development of targeted drugs," *Nature Reviews Clinical Oncology*, vol. 5, no. 1, pp. 44–54, 2008.

[46] D. N. Heo, D. H. Yang, H.-J. Moon et al., "Gold nanoparticles surface-functionalized with paclitaxel drug and biotin receptor as theranostic agents for cancer therapy," *Biomaterials*, vol. 33, no. 3, pp. 856–866, 2012.

[47] L. Fan, D. Lou, Y. Zhang, and N. Gu, "Rituximab-Au nanoprobes for simultaneous dark-field imaging and DAB staining of CD20 over-expressed on Raji cells," *The Analyst*, vol. 139, no. 22, pp. 5660–5663, 2014.

[48] Z. Cai, N. Chattopadhyay, K. Yang et al., "In-labeled trastuzumab-modified gold nanoparticles are cytotoxic *in vitro* to HER2-positive breast cancer cells and arrest tumor growth *in vivo* in athymic mice after intratumoral injection," *Nuclear Medicine and Biology*, vol. 43, no. 12, pp. 818–826, 2016.

[49] H. Wartlick, K. Michaelis, S. Balthasar, K. Strebhardt, J. Kreuter, and K. Langer, "Highly specific HER2-mediated cellular uptake of antibody-modified nanoparticles in tumour cells," *Journal of Drug Targeting*, vol. 12, no. 7, pp. 461–471, 2004.

[50] C. J. Bateman, "The hidden K-edge signal in K-edge imaging," 2015, http://arxiv.org/abs/1506.04223.

[51] M. Moghiseh, *Optimization of Spectral CT Data Acquisition for Novel Applications of Nanoparticles, in Department of Bioengineering*, University if Otago, Christchurch, New Zealand, 2018.

[52] V. Guarneri, M. V. Dieci, and P. Conte, "Enhancing intracellular taxane delivery: current role and perspectives of nanoparticle albumin-bound paclitaxel in the treatment of advanced breast cancer," *Expert Opinion on Pharmacotherapy*, vol. 13, no. 3, pp. 395–406, 2012.

[53] D. Kumar, I. Mutreja, K. Chitcholtan, and P. Sykes, "Cytotoxicity and cellular uptake of different sized gold nanoparticles in ovarian cancer cells," *Nanotechnology*, vol. 28, no. 47, p. 475101, 2017.

[54] L. Mansi, V. Cuccurullo, and R. Grassi, "Diagnostic imaging and pathology," in *Advanced Imaging Techniques in Clinical Pathology*, F. M. Sacerdoti, A. Giordano, and C. Cavaliere, Eds., pp. 107–111, Springer New York, New York, NY, USA, 2016.

[55] T. Tian, J. Ye, and S. Zhou, "Effect of pertuzumab, trastuzumab, and docetaxel in HER2-positive metastatic breast cancer: A meta-analysis," *International Journal of Clinical Pharmacology and Therapeutics*, vol. 55, 2017.

[56] G. Bianchini and L. Gianni, "The immune system and response to HER2-targeted treatment in breast cancer," *The Lancet Oncology*, vol. 15, no. 2, pp. e58–e68, 2014.

[57] S. M. Swain, S.-B. Kim, J. Cortés et al., "Pertuzumab, trastuzumab, and docetaxel for HER2-positive metastatic breast cancer (CLEOPATRA study): overall survival results from a randomised, double-blind, placebo-controlled, phase 3 study," *The Lancet Oncology*, vol. 14, no. 6, pp. 461–471, 2013.

[58] N. E. Buckley, C. Forde, D. G. McArt et al., "Quantification of HER2 heterogeneity in breast cancer–implications for identification of sub-dominant clones for personalised treatment," *Scientific Reports*, vol. 6, no. 1, p. 23383, 2016.

[59] G. Cox, M. Vyberg, B. Melgaard, J. Askaa, A. Oster, and K. J. O'Byrne, "Herceptest: Her2 expression and gene amplification in non-small cell lung cancer," *International Journal of Cancer*, vol. 92, no. 4, pp. 480–483, 2001.

[60] M. Greally, C. Kelly, and A. Cercek, "HER2: an emerging target in colorectal cancer," *Current Problems in Cancer*, 2018, In press.

[61] P. A. H. Butler, "First living human images from a MARS photon-counting 8-energy CT," in *IEEE NSS-MIC*, IEEE, Sydney, Australia, 2018.

Hindawi
Contrast Media & Molecular Imaging
Volume 2018, Article ID 9840962, 12 pages
https://doi.org/10.1155/2018/9840962

Research Article

Prostate Osteoblast-Like Cells: A Reliable Prognostic Marker of Bone Metastasis in Prostate Cancer Patients

Manuel Scimeca,[1,2] **Nicoletta Urbano**,[3] **Bonfiglio Rita**,[4] **Sarah Natalia Mapelli**,[5] **Carlo Vittorio Catapano**,[5] **Giuseppina Maria Carbone**,[5] **Sara Ciuffa**,[4] **Mario Tavolozza**,[3] **Orazio Schillaci**,[1,6] **Alessandro Mauriello**,[4] **and Elena Bonanno**[4,7]

[1]*Department of Biomedicine and Prevention, University of Rome "Tor Vergata", Via Montpellier 1, Rome 00133, Italy*
[2]*University San Raffaele, Via di Val Cannuta 247, 00166 Rome, Italy*
[3]*Nuclear Medicine, Policlinico "Tor Vergata", Rome, Italy*
[4]*Department of Experimental Medicine and Surgery, University "Tor Vergata", Via Montpellier 1, Rome 00133, Italy*
[5]*Università della Svizzera Italiana (USI), Institute of Oncology Research (IOR), Via Vela 6, Bellinzona, Switzerland*
[6]*IRCCS Neuromed, Pozzilli, IS, Italy*
[7]*IRCCS Neuromed Lab. "Diagnostica Medica" and "Villa dei Platani", Avellino, Italy*

Correspondence should be addressed to Elena Bonanno; elena.bonanno@uniroma2.it

Received 10 July 2018; Accepted 20 November 2018; Published 9 December 2018

Academic Editor: Ralf Schirrmacher

The main aim of this study was to investigate the putative association among the presence of prostate cancer cells, defined as prostate osteoblast-like cells (POLCs), and showing the expression of typical morphological and molecular characteristics of osteoblasts, the development of bone metastasis within 5 years of diagnosis, and the uptake of 18F-choline evaluated by PET/CT analysis. To this end, prostate biopsies ($n = 110$) were collected comprising 44 benign lesions and 66 malignant lesions. Malignant lesions were further subdivided into two groups: biopsies from patients that had clinical evidence of bone metastasis (BM+, $n = 23$) and biopsies from patients that did not have clinical evidence of bone metastasis within 5 years (BM−, $n = 43$). Paraffin serial sections were obtained from each specimen to perform histological classifications and immunohistochemical (IHC) analysis. Small fragments of tissue were used to perform ultrastructural and microanalytical investigations. IHC demonstrated the expression of markers of epithelial-to-mesenchymal transition (VIM), bone mineralization, and osteoblastic differentiation (BMP-2, PTX-3, RUNX2, RANKL, and VDR) in prostate lesions characterized by the presence of calcium-phosphate microcalcifications and high metastatic potential. Ultrastructural studies revealed the presence of prostate cancer cells with osteoblast phenotype close to microcalcifications. Noteworthy, PET/CT analysis showed higher uptake of 18F-choline in BM+ lesions with high positivity (≥300/500 cells) for RUNX2 and/or RANKL immunostaining. Although these data require further investigations about the molecular mechanisms of POLCs generation and role in bone metastasis, our study can open new and interesting prospective in the management of prostate cancer patients. The presence of POLCs along with prostate microcalcifications may become negative prognostic markers of the occurrence of bone metastases.

1. Introduction

Metastasis to bone is a common feature in advanced prostate cancer (PCa) patients. PCa is one of the most frequent cancer in men and represents a great public health problem, with a total of 265,000 new diagnosis every year in both Europe and United States of America [1]. Frequently, prostate cancer patients show bone osteoblastic metastatic lesions at diagnosis [1, 2]. The evidence that prostate cancer cells in patients enter the circulation in large numbers but still preferentially colonise to the bone has a number of implications. Prostate cancer cells have the ability to adhere at the main proteins of the extracellular matrix or at the bone marrow [2]. Also, the colonisation bone by prostate cancer

cells suggests that metastatic cells have morphological and/or molecular characteristics that make them capable to survive in the bone [2–4].

The type of bone metastases formed in prostate cancer is a reflection of the local interaction between tumour cells and the bone remodeling system—a complex mechanism which remains to be fully characterized. Bone metastases in prostate cancer are most often osteoblastic (involving the deposition of newly formed bone), but can also be osteolytic (characterized by destruction of normal bone) or mixed. The development of either osteolytic or osteoblastic lesions results from functional interactions between tumour cells and osteoclasts or osteoblasts, respectively [5]. However, the mechanisms responsible for the formation of prostate cancer metastasis to bone are complex and certainly involve both osteoclasts and osteoblasts activity [6]. In this context, the binary classification between osteoblastic and osteolytic lesions represents two extremes of a continuum which involves dysregulation of the normal bone remodeling process and which is yet to be fully understood. A detailed characterization of the osteoblastic-osteolytic spectrum and of premetastatic tumour cells could therefore pave the way for both the identification of early markers for bone metastasis and of novel drug targets to improve quality of life of patients with advanced prostate cancer.

As concerns the origin of metastatic cells, different hypotheses have been formulated. For a long time, the main theories of the formation of bone metastases contemplated the occurrence of specific genetics change in primary cancer cells that thus acquired the ability to spread to and thrive in distant organs [7, 8]. In this context, the epithelial-to-mesenchymal transition (EMT) could represent the key biological process adopted by epithelial cancer cells to promote tissue dissemination [9]. On note, in our recent study, we demonstrated a putative association between the occurrence of EMT and the development of breast cancer cells showing an osteoblast-like cells phenotype in lesions with microcalcifications [10, 11]. In addition, we observed that the presence of breast osteoblast-like cells (BOLCs) in breast infiltrating cancer was associated with the formation of bone metastatic lesions within 5 years from diagnosis [12, 13].

The main aim of this study was to investigate the putative association among the presence of prostate cancer cells, defined as prostate osteoblast-like cells (POLCs), and showing the expression of typical morphological and molecular characteristics of osteoblasts, the development of bone metastasis within 5years of diagnosis, and the uptake of ^{18}F-choline evaluated by PET/CT analysis.

2. Materials and Methods

2.1. Collection of Prostate Samples. In this study, we enrolled 110 patients undergoing prostate biopsies. From this selection, we collected prostate biopsies from each patient and, when available, data of PET/CT analysis. The study was approved by Institutional Ethical Committee of the "Policlinico Tor Vergata." Experimental procedures here reported were performed in agreement with the The Code of Ethics of the World Medical Association (Declaration of Helsinki). All patients have signed the informed consent prior to surgical procedures. From each sample, paraffin serial sections were used for both histological and immunohistochemical investigation. Also, 1 mm^3 of tissue were studied by transmission electron microscopy and microanalytical analysis. Exclusion criteria were history of previously or concomitant other neoplastic diseases, autoimmune diseases, viral chronic infections (HBV, HCV, and HIV), and any antitumoral treatment received before biopsy.

2.2. Histology. Fixation and haematoxylin and eosin staining were performed as previously described [14].

2.3. Immunohistochemistry. To study the immunophenotypical profile of prostate metastatic cells, we performed immunohistochemical reactions to investigate the expression of the following biomarkers: vimentin (EMT), BMP-2, PTX-3, RUNX2, RANKL, and VDR (mineralization process). For antigen retrieval, 3 μm thick paraffin sections were treated with citrate pH 6.0 or EDTA citrate pH 7.8 buffers (95°C for 30 min). Then, primary antibodies listed in Table 1 were incubated for 1 hour at room temperature. HRP-DAB Detection Kit (UCS Diagnostic, Rome, Italy) was used to reveal the reaction of primary antibodies with their specific target. Immunohistochemical signal was assessed independently by two investigators by counting the number of positive cancer cells (out of a total of 500 in randomly selected regions).

2.4. Transmission Electron Microscopy (TEM) and Energy Dispersive X-Ray (EDX) Microanalysis. Small fragment of prostate tissue (1 mm^3) was fixed in 4% paraformaldehyde and postfixed in 2% osmium tetroxide. Then, the sample was dehydrated in alcohol and infiltrated with propylene oxide before being embedded in Epon (Agar Scientific, Stansted CM24 8GF, Essex, United Kingdom) [15]. Eighty-micrometer ultrathin sections were cut by ultramicrotome and mounted on copper grids. All samples were examined with a transmission electron microscope (Model JEM-1400, JEOL) [16–18].

For EDX microanalysis, 80 μm ultrathin sections were mounted on copper grids. Hydroxyapatite crystals were identified by EDX detector (Thermo Scientific, Waltham, MA, USA) at an acceleration voltage of 75KeV and magnification of 12.000 [16–18]".

2.5. 18F-Choline PET/CT Analysis. Among patients enrolled in the study, 11 were subjected to ^{18}F-methylcholine (^{18}F-choline) PET/CT analysis. Results of 18F-choline PET/CT were collected to verify a possible correlation between ^{18}F-choline uptake in prostate tumours and the presence of POLCs. ^{18}F-choline PET/CT analysis was performed as previously described [19, 20]. From each patient, standardized uptake value (SUV) max and SUV average were recorded.

Table 1: List of primary antibodies.

Antibody	Characteristics	Dilution	Retrieval
Antivimentin	Mouse monoclonal clone V9; Ventana, Tucson, AZ, USA	Prediluted	EDTA citrate pH 7.8
Anti-BMP-2	Rabbit monoclonal clone N/A; Novus Biologicals, Littleton, CO, USA	1 : 250	Citrate pH 6.0
Anti-PTX-3	Rat monoclonal clone MNB1; AbCam, Cambridge, UK	1 : 100	Citrate pH 6.0
Anti-RUNX2	Mouse monoclonal clone EPR14334; AbCam, Cambridge, UK	1 : 100	Citrate pH 6.0
Anti-RANKL	Rabbit monoclonal clone 12A668; AbCam, Cambridge, UK	1 : 100	EDTA citrate pH 7.8
Anti-VDR	Rabbit polyclonal clone NBP1-19478; Novus Biologicals, Littleton, CO, USA	1 : 100	Citrate pH 6.0

2.6. Retrieval and Analysis of Gene Expression Datasets. Gene expression data from two studies in prostate cancer patients [21, 22] were retrieved from the cBioPortal platform. Expression of the selected genes was compared between primary tumours and metastatic CRPC and, for the second dataset, among primary and different metastatic sites. Heatmaps show the results of unsupervised hierarchical clustering based on the gene set expression.

2.7. Statistical Analysis. We performed groupwise comparisons of the expression of analysed biomarkers through nonparametric Kruskal–Wallis test (KW) ($p < 0.05$). Post hoc testing was performed by the Mann–Whitney test [12].

3. Results

3.1. Histological Classification. Prostate biopsies were classified in 44 benign lesions (BL) and 66 malignant lesions according to EAU-ESTRO-SIOG Guidelines 2017 [23]. We subdivided the malignant lesions in those (BM+, $n = 23$) taken from patients with clinical evidence of bone metastasis and those (BM−, $n = 43$) from patients without clinical evidence of bone metastasis after 5 years from diagnosis. From radiological point of view, all metastatic sites showed typical characteristics of osteoblastic lesions. Calcifications were present in 38 out of 110 prostate biopsies. In particular, we observed psammoma bodies in 32% of BL, 87% of BM+, and 79% of BM−. Patient baseline characteristics are reported in Table 2.

3.2. EMT Characterization. Immunohistochemical analysis of vimentin expression was performed in order to evaluate the number of prostate cells that acquire mesenchymal phenotype (Figure 1(a)–1(c)). As shown in a recent study [24], significant group effect was detected in the rate of vimentin-positive prostate cells ($p = 0.0025$), and post hoc testing showed a significantly higher rate of vimentin-positive prostate cells in BM+ (274.4 ± 30.76) compared to both BL (90.79 ± 14.82) and BM− (198.8 ± 22.8) (BL vs BM− $p = 0.0298$; BL vs BM+ $p < 0.0001$; BM− vs BM+ $p = 0.047$).

3.3. Expression of Bone Markers in Prostate Tissues. Our results showed a significant group effect on BMP-2 expression ($p = 0.0494$), and post hoc testing showed increased BMP-2 expression in BM− (349.8 ± 13.13) compared to BL (BL 209.2 ± 39.22) (BL vs BM− $p = 0.0083$) (Figures 1(d)–1(f)). No other significant differences were found (BM+ 335.1 ± 22.05). Our results show that prostate cells, especially cancer cells, express PTX-3, an innate-immune protein. We observed a significant group effect on PTX-3 ($p = 0.0076$). Post hoc testing showed very strong expression of PTX-3 in the cytoplasm of BM+ (321.77 ± 21.10) compared to both BL (154.1 ± 23.16) and to BM− (205.8 ± 28.51) (BL vs BM− $p = 0.2205$; BL vs BM+ $p < 0.0001$; BM− vs BM+ $p = 0.0158$) (Figures 1(g)–1(i)).

Table 2: Baseline characteristics of patients.

	n	Age ≤55	Age ≥55	Gleason ≤6	Gleason 7	Gleason ≥8	PSA ($ng\,ml^{-1}$)
BL	44	20	24	/	/	/	/
BM+	23	5	18	4	4	15	1122.11 ± 1348.02
BM−	43	13	30	13	6	25	1001.09 ± 147938

3.4. Immunophenotypic Characterization of POLCs. A significant group effect was observed on the number of RUNX2-positive cancer cells ($p = 0.0187$), after which post hoc testing showed significantly in BM− (375.4 ± 20.97) respect to BL (273.3 ± 27.14) ($p = 0.0006$). No other significant differences were found (BM+ 338.2 ± 31.84) (Figures 2(a)–2(c)). RANKL exhibited a significant group effect ($p < 0.0001$), and in post hoc testing, its expression was significantly higher in BM+ (386.7 ± 32.26) with respect to both BL (169.6 ± 25.74) and BM− (278.3 ± 15.24) (BM+ vs BL $p = 0.0011$; BM+ vs BM− $p = 0.0014$) (Figures 2(d)–2(f)). Also, significant differences were observed by comparing BL and BM− groups ($p < 0.0001$). VDR exhibited a similar group effect ($p < 0.0001$) (Figure 2(g)–2(i)). In addition, we detected significantly higher VDR expression when comparing BM+ (357 ± 25.59) to both BL (3.58 ± 2.03) and BM− (229.5 ± 15.55) (BL vs BM− $p < 0.0001$; BL vs BM+ $p < 0.0001$; BM− vs BM+ $p = 0.0002$) (Figure 2(g)). In particular, the signal in BM+ appeared very intense both in nucleus and in cytoplasm (Figure 2(h)), while it was less intense and mainly nuclear in BM− (Figure 2(i)).

3.5. Expression of POLC Biomarkers in Gene Expression Datasets. We examined expression of the EMT and bone markers studied by IHC in public datasets comprising gene expression profiling data from patients with primary tumours or metastatic castration-resistant prostate cancer (CRPC). Individual gene comparisons did not show a univocal behaviour (Figure 3(a)). Only VDR expression was

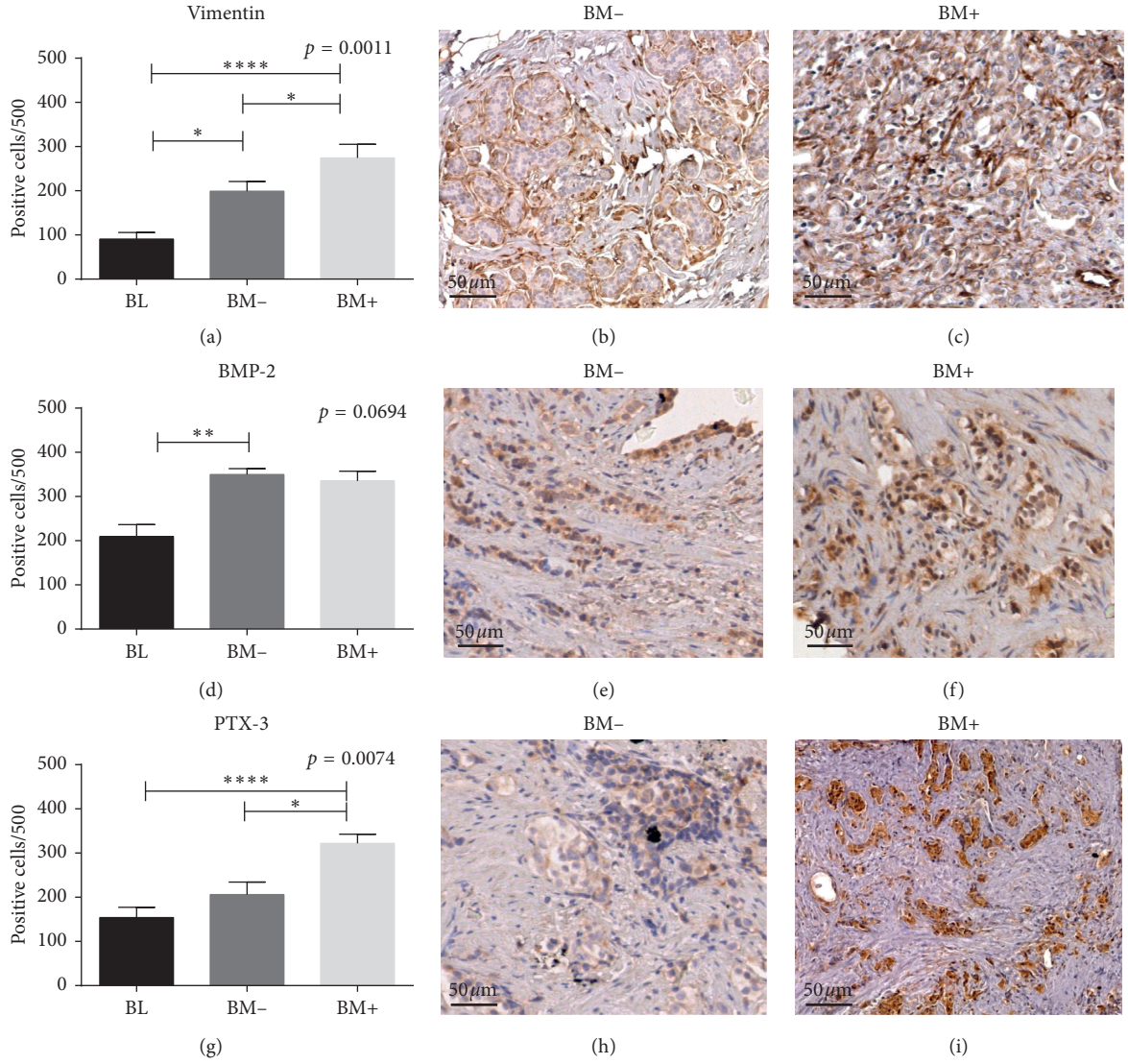

Figure 1: Immunohistochemical analysis of vimentin, BMP-2, and PTX-3. (a) Graph shows the number of vimentin-positive prostate cells in BL, BM+, and BM− lesions. (b) Vimentin-positive prostate cancer cells in BM− lesions (scale bar represents 50 μm). (c) Image shows numerous vimentin-positive prostate cancer cells in BM+ lesions (scale bar represents 50 μm). (d) Graph shows the number of BMP-2-positive prostate cells in BL, BM+, and BM− lesions. (e) BM+ lesion displaying numerous BMP-2-positive cancer cells (scale bar represents 50 μm). (f) BMP-2-positive prostate cancer cells in BM+ lesions (scale bar represents 50 μm). (g) Graph shows the number of PTX-3-positive prostate cells in BL, BM+, and BM− lesions. (h) Rare PTX-3-positive cells in BM− lesions (scale bar represents 50 μm). (i) Image shows several PTX-3-positive prostate cancer cells in BM+ (scale bar represents 50 μm).

significantly upregulated in CRPC compared to primary tumours. Interestingly, however, the small set of genes was able to discriminate most of the primary tumours from metastatic CRPCs in unsupervised clustering (Figure 3(b)). Furthermore, analysis of a second dataset with annotated metastatic sites showed that the gene set expression was remarkably higher in tumour specimens taken from bone metastases compared to primary tumours and other metastatic sites (Figure 3(c)).

3.6. Prostate Calcifications. In order to verify if the presence of prostate microcalcifications was linked to the expression of mineralization factors, we subdivided our samples in prostate lesions with (Micro+) or without (Micro−) calcifications, independently from the type of lesion. We observed significantly higher expression of BMP-2 in Micro+ respect to Micro− (Micro+ 431.60 ± 23.35 vs Micro− 288.30 ± 18.00; $p = 0.0017$) (Figure 4(a)). We found an increase of PTX-3-positive prostate cells in Micro+ as compared to Micro− (Micro+ 234.20 ± 18.40 vs Micro− 120.7 ± 25.82; $p = 0.0045$) (Figure 4(b)). Conversely, no significant difference was observed for the analysis of RUNX2-positive prostate cells (Micro+ 331.50±20.52 vs Micro− 281.50 ± 26.65; $p = 0.1980$) (Figure 4(c)). Analysis of RANKL showed a significant difference between the presence of RANKL-positive prostate cells between Micro+ and Micro− (Micro+ 283.70 ± 24.23 vs Micro− 216.60 ± 18.07; $p = 0.0252$)

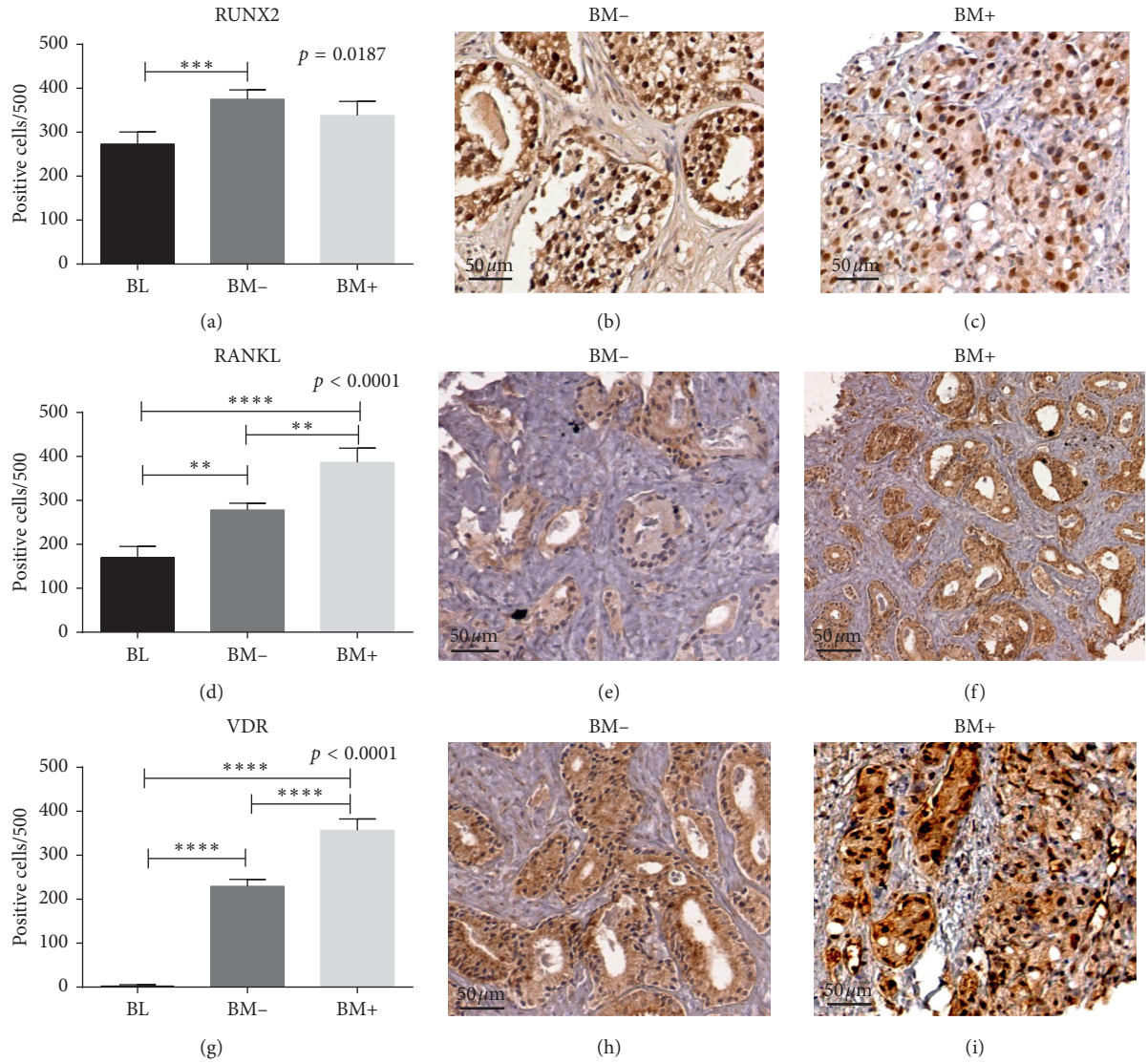

Figure 2: Expression of bone markers in prostate cells. (a) Graph shows the number of RUNX2-positive prostate cells in BL, BM+, and BM− lesions. (b) Numerous nuclear RUNX2-positive cancer cells in BM− lesions (scale bar represents 50 μm). (c) Nuclear RUNX″ expression in prostate cancer cells of a BM+ patient (scale bar represents 50 μm). (d) Graph displays the number of RANKL-positive prostate cells in BL, BM−, and BM+ lesions. (e) RANKL expression in a case of BM− patient (scale bar represents 50 μm). (f) Numerous prostate cancer cells expressing RANKL in BM+ (scale bar represents 50 μm). (g) Graph shows the number of nuclear VDR-positive prostate cells in BL, BM−, and BM+ lesions. (h) VDR-positive prostate cancer cells in a BM− lesion (scale bar represents 50 μm). (i) Several nuclear VDR-positive prostate cancer cells in a BM+ lesion (scale bar represents 50 μm).

(Figure 4(d)). Finally, significant differences in VDR expression were observed (Micro+ 192.00 ± 18.02 vs Micro− 109.30 ± 19.14; $p = 0.001$) (Figure 4(e)).

3.7. Ultrastructural Characterization of Prostate Cancer Cells. TEM analysis allowed us to characterize ultrastructure of prostate cells in malignant lesions. Specifically, we observed both cuboidal and large spindle-shaped cells with abundant clear cytoplasm in BM+ (Figure 5(a)). Moreover, in these lesions, we identified several calcifications and prostate cancer cells with morphological appearance of osteoblasts containing cytoplasmic electrondense granules made of HA (Figure 5(b)). In addition, EDX microanalysis demonstrated that all calcifications here detected were made of calcium-phosphate (hydroxyapatite) (Figure 5(b)).

3.8. 18F-Choline PET/CT Analysis. We collected PET/CT data of 11 patients: 5 BM+ and 6 BM− (Figure 5(c)). Despite the low number of patients, we found significant differences between both SUV max and SUV average between BM+ and BM− (Figure 5(d), 5(e)). Noteworthy, the cancer lesions with higher value of SUV max (BM+ patients) (Figure 5(f)) were characterized by the presence of calcium-phosphate calcifications and a higher number (>300) of RUNX2-positive (Figure 5(g)) and RANKL-positive (Figure 5(h)) prostate cancer cells.

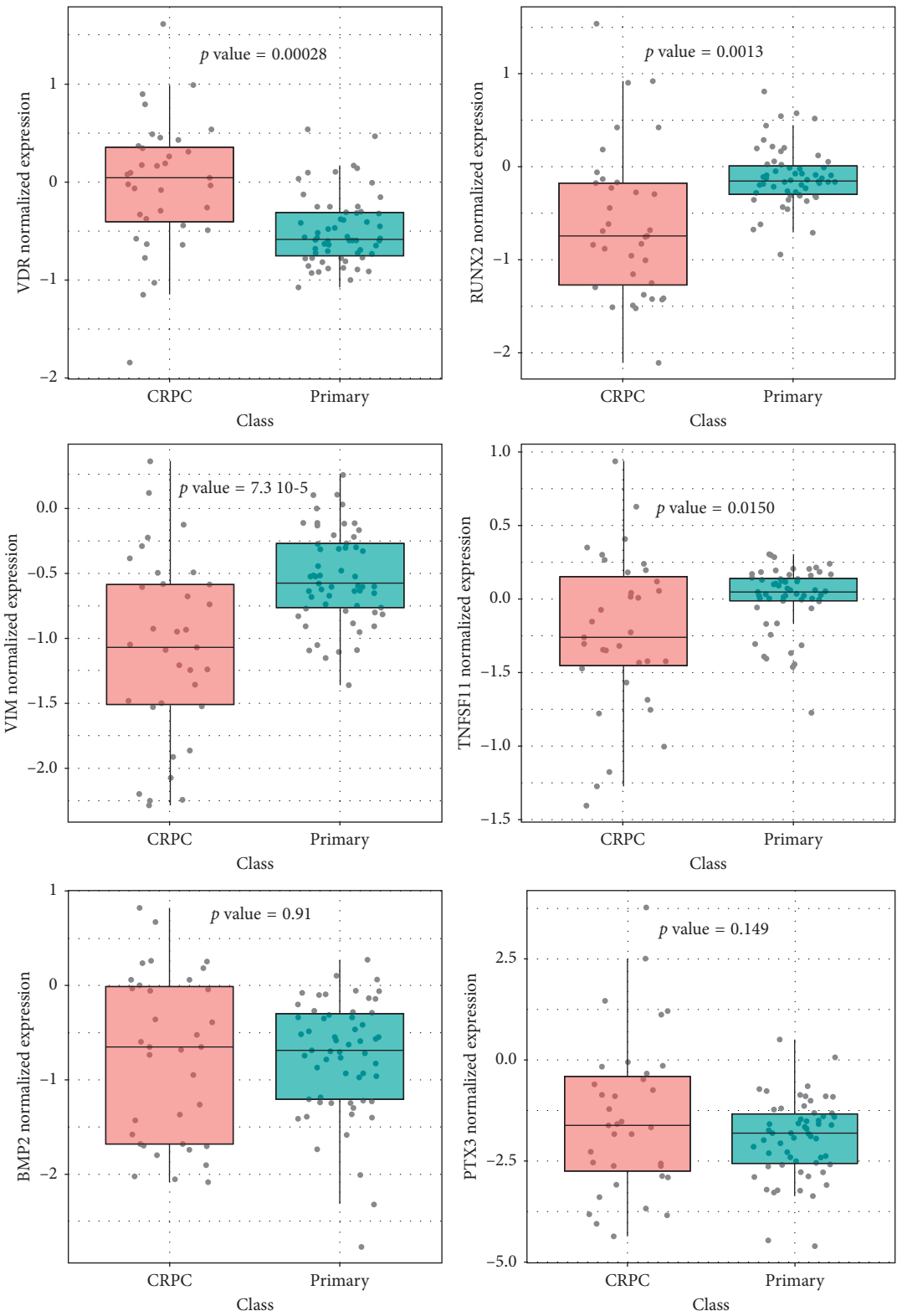

(a)

Figure 3: Continued.

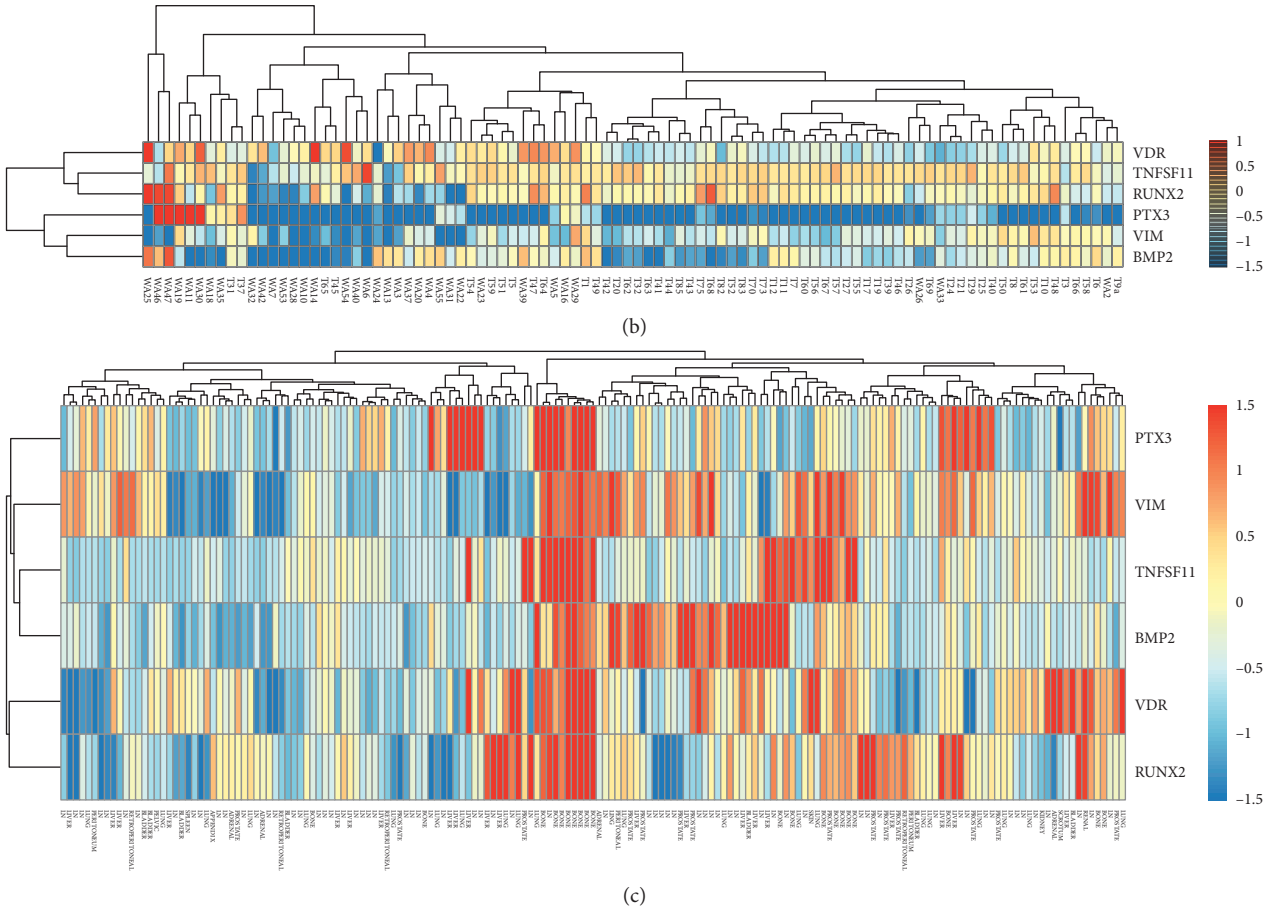

Figure 3: Expression of bone markers in prostate cancer patient datasets. (a) Graphs show the mRNA levels of the genes VDR, RUNX2, vimentin, TNFSF11, BMP-2, and PTX3 in metastatic castration resistant prostate cancer (CRPC) and primary prostate tumours (primary). (b) Unsupervised hierarchical clustering of metastatic (WA) and primary (T) prostate cancers based on expression of the indicated gene set. Metastatic samples are labelled in red; primary samples are labelled in black. (c) Unsupervised hierarchical clustering of primary (prostate) and metastatic prostate cancers at the indicated distinct metastatic sites. Primary/localized samples are indicated in black; distal metastases are indicated in red.

4. Discussion

Prostate metastasis to the bone more often results in osteoblastic lesions, though it is known that prostate bone metastases can display both blastic and lytic characteristics during the early phases of their formation [25]. In addition, there is evidence that during the early phases of osteoblastic metastases formation, it is possible to observe osteolytic lesions, suggesting an overall increase of bone remodeling at these sites. The pathophysiology of bone metastases is frequently explained by the theory of the vicious cycle proposed for the first time by Mundy and Guise [26]. According to this theory, cancer cells resident in bone cause bone destruction because they are capable to stimulate osteoclast activity. In return, cancer cells receive positive feedbacks from humoral factors released by the bone microenvironment during bone destruction and remodeling [27]. Indeed, it is widely accepted that the bone microenvironment is crucial to the success of cancer cells in bone.

In a recent study, we described for the first time the characteristics of prostate cells involved in the production of prostate calcifications demonstrating their similarity with osteoblasts [24]. In addition, our research group described the presence of osteoblast-like cells in breast cancer (BOLCs) showing a correlation between the appearance of BOLCs in primary lesions and development of bone metastases. Based on these studies, the main aim of this study was to investigate the possible correlation between the presence of prostate cancer cells showing expression of typical morphological and molecular markers of osteoblasts and the development of bone metastasis in prostate cancer patients within 5 years from diagnosis of primary lesion. To this end, we collected 110 prostate biopsies (44 benign and 66 malignant lesions). Malignant lesions were subdivided in biopsies from patients with clinical evidence of bone metastasis (BM+, $n = 23$) and those from patients without clinical evidence of bone metastasis (BM−, $n = 43$).

As already reported by Scimeca et al., we found a significant correlation between vimentin expression, one of the most important markers of mesenchymal cells [14], and the presence of prostate osteoblast-like cells (POLCs). Specifically, our data showed a significant increase of positive cells

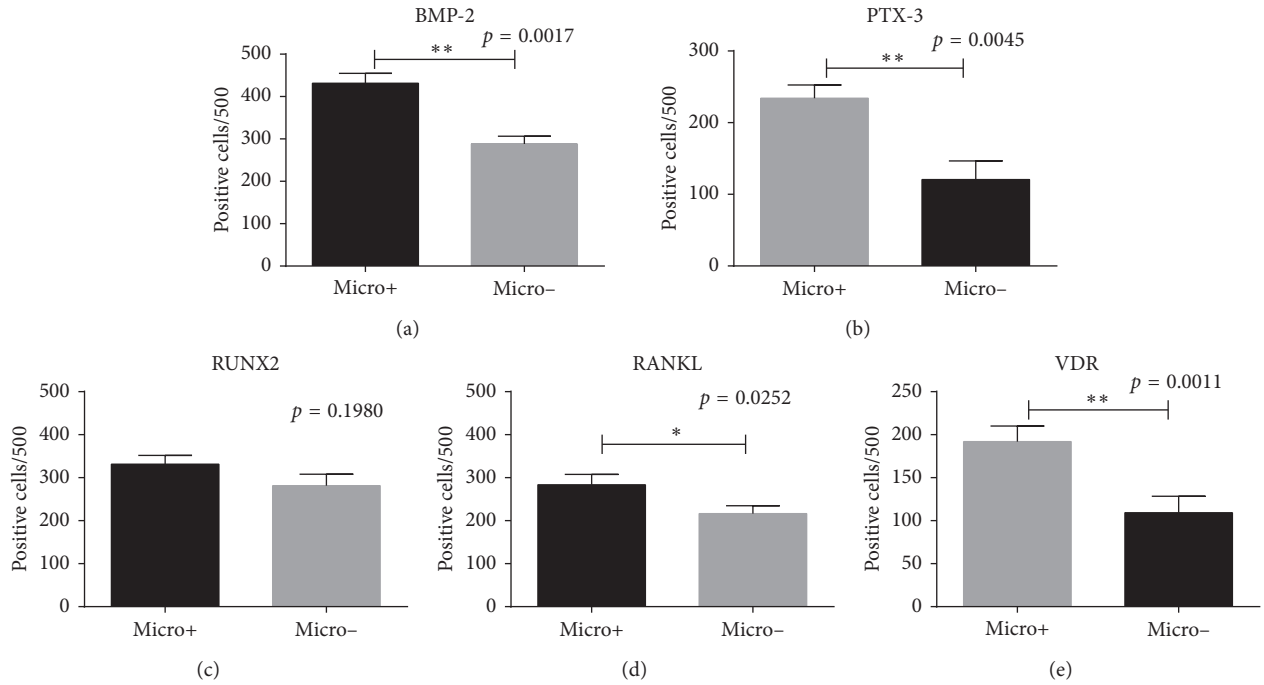

Figure 4: Expression of bone markers in prostate lesions with or without calcification. (a) Graph shows the number of BMP-2-positive prostate cells in Micro+ and Micro− lesions. (b) Graph displays the number of PTX-3-positive prostate cells in Micro− and Micro+ lesions. (c) Graph shows the number of RUNX2-positive prostate cells in Micro+ and Micro−lesions. (d) Graph displays the number of RANKL-positive prostate cells in Micro+ and Micro−lesions. (e) Graph shows the number of VDR-positive prostate cells in Micro+ and Micro− lesions.

in prostate cancer of BM+ group as compared with BM−. In addition, we proved that primary prostate cancer lesions of BM+ patients were characterized by the expression of osteogenic molecules able to induce osteoblast differentiation and to increase osteoblast function such as mineralization. Among them, BMP-2 is a potent inducer of bone formation through the stimulation of osteoblast differentiation. BMP-2 exerts this effect via two types of serine/threonine kinase receptors: BMP-2 binds the type II receptor, which subsequently activates the type I receptor by a direct association [28]. Our results showed an increase of BMP-2 expression in prostate malignant lesions. Conversely, the absence of significant differences of BMP-2 expression between BM+ and BM− suggests that it could be involved in the early phases of cancer transformation rather than during metastatic process. In support of this, several studies demonstrated the ability of BMP-2 to induce malignant transformation of epithelial tissues [29–31]. However, we also demonstrated the association between BMP-2 expression and the presence of prostate calcifications, regardless of the lesion type. Thus, BMP-2, in association to EMT phenomenon, can participate to induce mesenchymal-like cells to acquire osteoblast phenotype. As concerns PTX-3, PTX-3 is a multifunctional glycoprotein produced by a variety of cells [32, 33]; our results displayed a significant correlation between the presence of PTX-3-positive prostate cells and bone metastasis formation. Also, it is important to emphasize that BM− group showed the same number of PTX-3-positive cells of BL, suggesting that the presence of PTX-3-positive cells could represent a reliable predictive element for the development of bone metastasis from prostate cancer. These data are in line with recent studies that demonstrated the involvement of PTX-3 in osteoblast proliferation, differentiation and function [34–36], and bone metastasis from breast cancer formation.

To further characterize the phenotype of POLCs, we investigate the expression of the main markers of osteoblasts, RUNX2, RANKL, and VDR. RUNX2 is the first transcription factor required for the determination of the osteoblast lineage [37]. In particular, RUNX2 is detected first in preosteoblasts and its expression is upregulated during the early phases of osteoblast differentiation. In line with this, our results displayed an increase of RUNX2-positive prostate cells in malignant lesions respect to BL, but no difference was observed between BM+ and BM−. Therefore, the acquisition of RUNX2 expression by prostate cells seems to be linked to cancer transformation rather than to metastatic process.

In agreement with the physiological role of RUNX2 in osteoblast function [38], we did not observe an increase of RUNX2-positive cells in Micro+ with respect to Micro− lesions. Indeed, mature osteoblasts lose the expression of RUNX2 during the mineralization phase of bone formation. Conversely, analysis of RANKL and VDR showed a putative correlation among the presence of RANKL and/or VDR positive prostate cancer cells, bone metastasis formation, and microcalcifications. As regards the formation of bone metastasis, the presence of RANKL-positive prostate cancer cells can trigger osteoclast activity by binding to the osteoclast receptor RANK [39]. Indeed, RANKL is a type II membrane protein expressed by osteoblasts that is able to induce osteoclasts proliferation and function. In addition, at the primary lesion site, RANKL expression can reflect the presence of cells

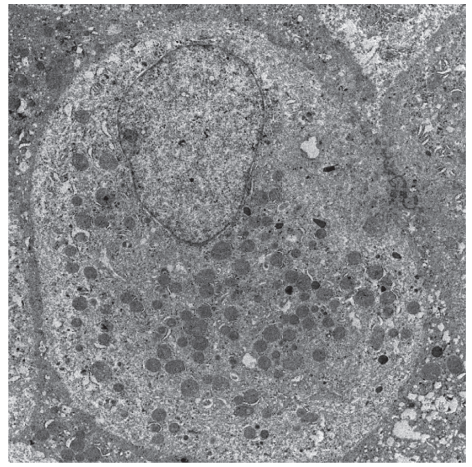

(a)

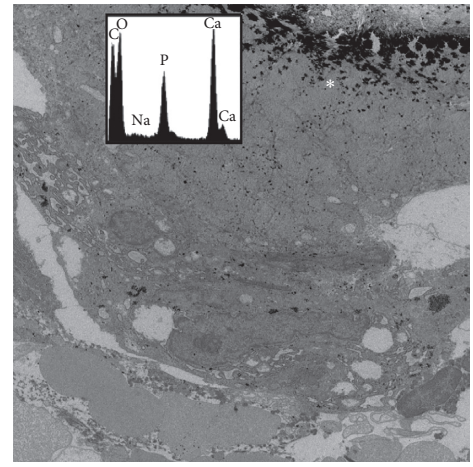

(b)

	SUV max	SUV average	p value
BM+	34.21 ± 3.3	22.83 ± 3.35	0.0303
BM−	13.00 ± 2.64	9.15 ± 0.95	0.0442

(c)

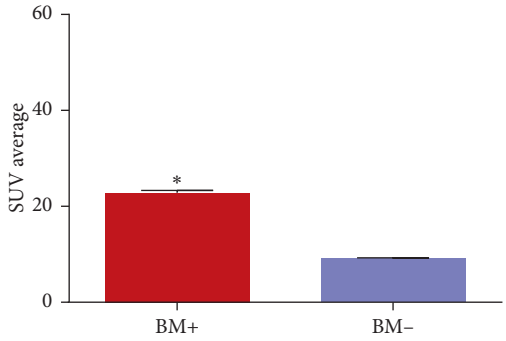

(d)

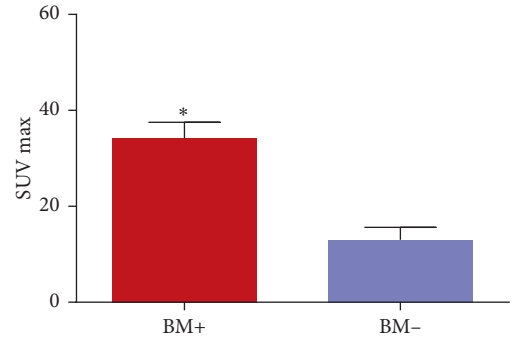

(e)

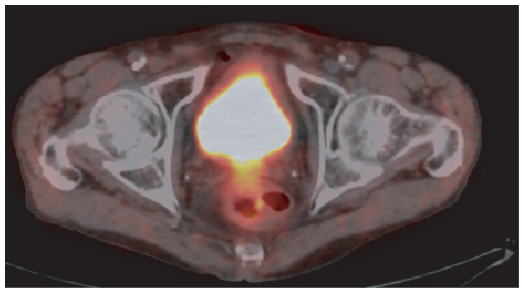

(f)

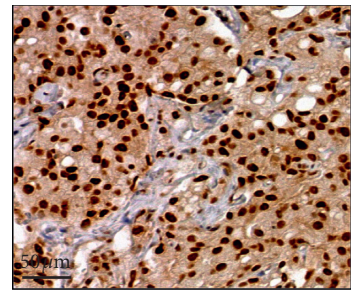

(g)

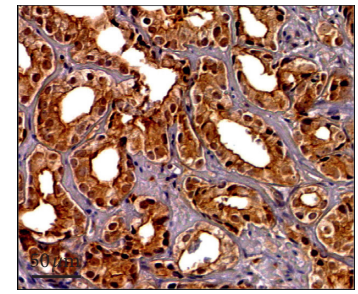

(h)

Figure 5: Ultrastructural and molecular imaging analysis. (a) Electron micrograph shows prostate cancer cells of a BM− biopsy. (b) Prostate cancer cells next to calcium-phosphate calcification in a BM+ lesion. SUV max and SUV average of BM+ and BM− lesions. (c) Graph shows significant difference between the SUV max value of BM+ and BM−patients. (d) Graph shows significant difference between the SUV average value of BM+ and BM− patients. (e) Graph shows significant difference between the SUV max value of BM+ and BM− patients. (f) Dual fusion 18F-choline PET/CT image of BM+ patients. (g) Image displays numerous RUNX2-positive prostate cancer cells in BM+ patient of (e) (scale bar represents 50 μm). (h) Image displays numerous RANKL-positive prostate cancer cells in BM+ patient of (e) (scale bar represents 50 μm).

responsible for microcalcification production. Similar to what occurs during bone mineralization, our data support the hypothesis that the nuclear translocation of VDR participates in production of microcalcifications in prostate lesions. Thus, nuclear translocation of VDR could be considered a marker of POLCs since it could be linked to bone metastasis formation. Notably, nuclear VDR is the only protein that we did not find expressed in BL, among all proteins studied here. This evidence candidates nuclear VDR as a reliable prognostic and/or predictive marker of prostate cancer occurrence. Combined

analysis of this set of genes in patients with primary and metastatic prostate cancer further showed that deregulated expression of these markers of EMT, bone mineralization, and osteoblastic differentiation occurred preferentially in the setting of metastatic disease and particularly at metastases in bone, further supporting their relevance as adverse prognostic markers.

It is important to highlight that in this study, POLCs were also characterized from the ultrastructural point of view. In particular, we observed the presence of cytoplasmic vesicles containing HA granules in prostate cancer cells showing osteoblast phenotype (POLCs) [24, 40–42].

Of note, although preliminary, our data showed a significant correlation between the uptake of 18F-choline PET/CT and the presence of POLCs in prostate cancer tissues. If confirmed in a larger patient cohort, this evidence could provide the scientific rationale for the development of algorithms able to predict the metastatic potential of primary prostate cancer lesions by 18F-choline PET/CT analysis [43].

This study proposes a new cell type generated by a process of cell transdifferentiation and related to formation of bone metastasis: the POLCs. Although our data require further investigations about the molecular mechanisms of both POLCs generation and metastasization to the bone, this study opens new and interesting prospective for the management of prostate cancer patients. The presence of POLCs could become prognostic markers for occurrence of bone metastatic disease.

5. Conclusion

The clinical course of metastatic bone disease in prostate cancers is often long, with patients experiencing sequential skeletal complications over a period of several years. These include bone pain, fractures, hypercalcemia, and spinal cord compression, all of which may profoundly impair patient's quality of life. In addition, once prostate tumour cells are engrafted in the skeleton, curative therapy is no longer possible and palliative treatment becomes the only option. Thus, the identification of early markers of bone metastasis and especially the characterization of the cells involved in the metastatic process can lay the foundation for the identification of new tools for monitoring, prevention, or cure of bone metastatic diseases and providing support to the physicians in the management of prostate patients. In this context, positron emission tomography (PET)/computed tomography (CT) has emerged as a significant and promising staging modality for primary, recurrent, and metastatic prostate cancer. Much more important, the identification of highly sensitive and specific radiotracers can implement the therapeutic/diagnostic perspectives for prostate cancer patients "opening the way" for the development of new theranostic approaches. PSMA PET/CT ligands labelled with ^{18}F and ^{68}Ga have certainly revolutionized the management of metastatic prostate cancer selecting patients who may benefit from targeted systemic radionuclide therapy. In a nuclear oncology theranostic design, ^{68}Ga-PSMA already constitutes the diagnostic positron-emitting of beta$^-$ emitter Lutetium-177 PSMA (^{177}Lu-PSMA) [44] and alpha-emitter Actinium-225 PSMA (^{225}Ac-PSMA) [45]. Finally, the results reported here about the phenotypic characterization of POLCs could provide a scientific rationale for the development of theranostic anti-POLC radiomolecules for the cure and prevention of prostate cancer bone metastasis.

Data Availability

The data used to support the findings of this study are included within the article. Gene expression data from two studies in prostate cancer patients (reference [21] and [22]) were retrieved from the cBioPortal platform. Expression of the selected genes was compared between primary tumours and metastatic CRPC and, for the second dataset, among primary and different metastatic sites.

Conflicts of Interest

The authors declare that there are no potential conflicts of interest relating to the manuscript.

Acknowledgments

The authors wish to thank Dr. Sara Fazi, Dr. Alessandro Polidori, and Dr. Serena Chiantini for technical support.

References

[1] C. L. Eaton and R. E. Coleman, "Pathophysiology of bone metastases from prostate cancer and the role of bisphosphonates in treatment," *Cancer Treatment Reviews*, vol. 29, no. 3, pp. 189–98, 2003.

[2] S. Sethi, J. Macoska, W. Chen, and F. H. Sarkar, "Molecular signature of epithelial-mesenchymal transition (EMT) in human prostate cancer bone metastasis," *American Journal of Translational Research*, vol. 3, no. 1, pp. 90–9, 2010.

[3] A. M. Demarzo, W. G. Nelson, W. B. Isaacs, and J. I. Epstein, "Pathological and molecular aspects of prostate cancer," *The Lancet*, vol. 361, no. 9361, pp. 955–964, 2003.

[4] S. De, J. Chen, N. V. Narizhneva et al., "Molecular pathway for cancer metastasis to bone," *Journal of Biological Chemistry*, vol. 278, no. 40, pp. 39044–39050, 2003.

[5] J. J. Yin, C. B. Pollock, and K. Kelly, "Mechanisms of cancer metastasis to the bone," *Cell Research*, vol. 15, no. 1, pp. 57–62, 2005.

[6] T. Martin, L. Ye, A. J. Sanders, J. Lane, and W. G. Jiang, *Cancer Invasion and Metastasis: Molecular and Cellular Perspective*, Landes Bioscience, Austin, TX, USA, 2000–2013.

[7] I. J. Fidler and M. L. Kripke, "Metastasis results from preexisting variant cells within a malignant tumor," *Science*, vol. 197, no. 4306, pp. 893–5, 1977.

[8] G. Poste and I. J. Fidler, "The pathogenesis of cancer metastasis," *Nature*, vol. 283, no. 5743, pp. 139–46, 1980.

[9] Y. Wu, M. Sarkissyan, and J. V. Vadgama, "Epithelial-mesenchymal transition and breast cancer," *Journal of Clinical Medicine*, vol. 5, no. 2, 2016.

[10] M. Scimeca, E. Giannini, C. Antonacci et al., "Microcalcifications in breast cancer: an active phenomenon mediated by epithelial cells with mesenchymal characteristics," *BMC Cancer*, vol. 14, no. 1, p. 286, 2014.

[11] M. Scimeca, C. Antonacci, and E. Bonanno, "Breast microcalcifications: a focus," *Journal of Cell Science and Therapy*, vol. S8, p. e101, 2015.

[12] M. Scimeca, C. Antonacci, N. Toschi et al., "Breast osteoblast-like cells: a reliable early marker for bone metastases from breast cancer," *Clinical Breast Cancer*, vol. 18, no. 4, pp. e659–e669, 2018.

[13] M. Scimeca, R. Bonfiglio, M. Montanaro, and E. Bonanno, "Osteoblast-like cells in human cancers: new cell type and reliable markers for bone metastasis," *Future Oncology*, vol. 14, no. 1, pp. 9–11, 2018.

[14] M. Scimeca, C. Antonacci, D. Colombo, R. Bonfiglio, O. C. Buonomo, and E. Bonanno, "Emerging prognostic markers related to mesenchymal characteristics of poorly differentiated breast cancers," *Tumor Biology*, vol. 37, no. 4, pp. 5427–35, 2016.

[15] R. Bonfiglio, M. Scimeca, N. Toschi et al., "Radiological, histological and chemical analysis of breast micro-calcifications: diagnostic value and biological significance," *Journal of Mammary Gland Biology and Neoplasia*, vol. 23, no. 1-2, pp. 89–99, 2018.

[16] M. Scimeca, S. Bischetti, H. K. Lamsira, R. Bonfiglio, and E. Bonanno, "Energy Dispersive X-ray (EDX) microanalysis: a powerful tool in biomedical research and diagnosis," *European Journal of Histochemistry*, vol. 62, no. 1, p. 2841, 2018.

[17] M. Scimeca, A. Pietroiusti, F. Milano et al., "Elemental analysis of histological specimens: a method to unmask nano asbestos fibers," *European Journal of Histochemistry*, vol. 60, no. 1, p. 2573, 2016.

[18] M. Scimeca, A. Orlandi, I. Terrenato, S. Bischetti, and E. Bonanno, "Assessment of metal contaminants in non-small cell lung cancer by EDX microanalysis," *European Journal of Histochemistry*, vol. 58, no. 3, p. 2403, 2014.

[19] F. Calabria, A. Chiaravalloti, C. Cicciò et al., "PET/CT with 18F-choline: physiological whole bio-distribution in male and female subjects and diagnostic pitfalls on 1000 prostate cancer patients: 18F-choline PET/CT bio-distribution and pitfalls. A southern Italian experience," *Nuclear Medicine and Biology*, vol. 51, pp. 40–54, 2017.

[20] F. Calabria, D. Rubello, and O. Schillaci, "The optimal timing to perform 18F/11C–choline PET/CT in patients with suspicion of relapse of prostate cancer: trigger PSA versus PSA velocity and PSA doubling time," *International Journal of Biological Markers*, vol. 29, no. 4, pp. e423–30, 2014.

[21] C. S. Grasso, Y. M. Wu, D. R. Robinson et al., "The mutational landscape of lethal castration-resistant prostate cancer," *Nature*, vol. 487, no. 7406, pp. 239–43, 2012.

[22] A. Kumar, I. Coleman, C. Morrissey et al., "Substantial interindividual and limited intraindividual genomic diversity among tumors from men with metastatic prostate cancer," *Nature Medicine*, vol. 22, no. 4, pp. 369–78, 2016.

[23] N. Mottet, J. Bellmunt, M. Bolla et al., "EAU-ESTRO-SIOG Guidelines on prostate cancer. Part 1: screening, diagnosis, and local treatment with curative intent," *European Urology*, vol. 71, no. 4, pp. 618–629, 2017.

[24] M. Scimeca, R. Bonfiglio, F. Varone, S. Ciuffa, A. Mauriello, and E. Bonanno, "Calcifications in prostate cancer: an active phenomenon mediated by epithelial cells with osteoblast-phenotype," *Microscopy Research and Technique*, vol. 81, no. 7, pp. 745–748, 2018.

[25] S. Ziaee, G. C. Chu, J. M. Huang, S. Sieh, and L. W. Chung, "Prostate cancer metastasis: roles of recruitment and reprogramming, cell signal network and three-dimensional growth characteristics," *Translational Andrology and Urology*, vol. 4, no. 4, pp. 438–54, 2015.

[26] T. A. Guise and G. R. Mundy, "Cancer and bone," *Endocrine Reviews*, vol. 19, no. 1, pp. 18–54, 1998.

[27] S. Casimiro, A. R. Ferreira, A. Mansinho, I. Alho, and L. Costa, "Molecular mechanisms of bone metastasis: which targets came from the bench to the bedside?," *International Journal of Molecular Sciences*, vol. 17, no. 9, 2016.

[28] T. Ogasawara, H. Kawaguchi, S. Jinno et al., "Bone morphogenetic protein 2-induced osteoblast differentiation requires Smad-mediated down-regulation of Cdk6," *Molecular and Cellular Biology*, vol. 24, no. 15, pp. 6560–8, 2004.

[29] P. Huang, A. Chen, W. He et al., "BMP-2 induces EMT and breast cancer stemness through Rb and CD44," *Cell Death Discovery*, vol. 3, p. 17039, 2017.

[30] J. Spanjol, G. Djordjević, D. Markić, M. Klarić, D. Fuckar, and D. Bobinac, "Role of bone morphogenetic proteins in human prostate cancer pathogenesis and development of bone metastases: immunohistochemical study," *Collegium Antropologicum*, vol. 34, no. 2, pp. 119–25, 2010.

[31] B. Herrera, S. Dooley, and K. Breitkopf-Heinlein, "Potential roles of bone morphogenetic protein (BMP)-9 in human liver diseases," *International Journal of Molecular Sciences*, vol. 15, no. 4, pp. 5199–220, 2014.

[32] F. Moalli, S. Jaillon, A. Inforzato et al., "Pathogen recognition by the long pentraxin PTX3," *Journal of Biomedicine and Biotechnology*, vol. 2011, Article ID 830421, 15 pages, 2011.

[33] C. Cappuzzello, A. Doni, E. Dander et al., "Mesenchymal stromal cell-derived PTX3 promotes wound healing via fibrin remodeling," *Journal of Investigative Dermatology*, vol. 136, no. 1, pp. 293–300, 2016.

[34] M. Scimeca, A. Salustri, E. Bonanno et al., "Impairment of PTX3 expression in osteoblasts: a key element for osteoporosis," *Cell Death and Disease*, vol. 8, no. 10, p. e3125, 2017.

[35] U. Tarantino, M. Feola, M. Celi, and M. Scimeca, "PTX3: a new mediator of bone metabolism and osteoporosis," *Muscle, Ligaments and Tendons Journal*, vol. 7, no. 1, pp. 200-201, 2017.

[36] D. Grčević, M. Sironi, S. Valentino et al., "The long pentraxin 3 plays a role in bone turnover and repair," *Frontiers in Immunology*, vol. 9, p. 417, 2018.

[37] T. Komori, "Regulation of osteoblast differentiation by Runx2," *Advances in Experimental Medicine and Biology*, vol. 658, pp. 43–9, 2010.

[38] T. Komori, "Roles of Runx2 in skeletal development," *Advances in Experimental Medicine and Biology*, vol. 962, pp. 83–93, 2017.

[39] J. H. Kim and N. Kim, "Signaling pathways in osteoclast differentiation," *Chonnam Medical Journal*, vol. 52, no. 1, pp. 12–7, 2016.

[40] B. Ecarot-Charrier, N. Shepard, G. Charette, M. Grynpas, and F. H. Glorieux, "Mineralization in osteoblast cultures: a light and electron microscopic study," *Bone*, vol. 9, no. 3, pp. 147–154, 1988.

[41] C. R. Howlett, "The fine structure of the proximal growth plate of the avian tibia," *Journal of Anatomy*, vol. 128, pp. 377–399, 1979.

[42] M. Rohde and H. Mayer, "Exocytotic process as a novel model for mineralization by osteoblasts in vitro and in vivo determined by electron microscopic analysis," *Calcified Tissue International*, vol. 80, no. 5, pp. 323–336, 2007.

[43] M. Scimeca, N. Urbano, R. Bonfiglio, O. Schillaci, and E. Bonanno, "Management of oncological patients in the digital era: anatomic pathology and nuclear medicine teamwork," *Future Oncology*, vol. 14, no. 11, pp. 1013–1015, 2018.

[44] J. Ferdinandus, J. Violet, S. Sandhu, and M. S. Hofman, "Prostate-specific membrane antigen theranostics: therapy

with lutetium-177," *Current Opinion in Urology*, vol. 28, no. 2, pp. 197–204, 2018.

[45] S. Kojima, J. M. Cuttler, N. Shimura, H. Koga, A. Murata, and A. Kawashima, "Present and future prospects of radiation therapy using α-emitting nuclides," *Dose Response*, vol. 16, no. 1, article 1559325817747387, 2018.

Hindawi
Contrast Media & Molecular Imaging
Volume 2018, Article ID 8494031, 11 pages
https://doi.org/10.1155/2018/8494031

Research Article

Nuclear Imaging Study of the Pharmacodynamic Effects of Debio 1143, an Antagonist of Multiple Inhibitor of Apoptosis Proteins (IAPs), in a Triple-Negative Breast Cancer Model

Pierre-Simon Bellaye,[1] Alexandra Oudot,[1] Jean-Marc Vrigneaud,[1] Olivier Raguin,[2] Francis Bichat,[2] Anne Vaslin,[3] Hélène Maby-El Hajjami,[3] Claudio Zanna,[3] Grégoire Vuagniaux,[3] Pierre Fumoleau,[1] Franck Denat,[4] François Brunotte,[1] and Bertrand Collin[1,4]

[1]*Centre Georges-François Leclerc, Dijon, France*
[2]*Oncodesign, Dijon, France*
[3]*Debiopharm International SA, Lausanne, Switzerland*
[4]*ICMUB, Dijon, France*

Correspondence should be addressed to Pierre-Simon Bellaye; psbellaye@cgfl.fr

Received 13 July 2018; Accepted 18 October 2018; Published 2 December 2018

Academic Editor: Orazio Schillaci

Background. Debio 1143, a potent orally available SMAC mimetic, targets inhibitors of apoptosis proteins (IAPs) members and is currently in clinical trials. In this study, nuclear imaging evaluated the effects of Debio 1143 on tumor cell death and metabolism in a triple-negative breast cancer (TNBC) cell line (MDA-MB-231)-based animal model. *Methods*. Apoptosis induced by Debio 1143 was assessed by FACS (caspase-3, annexin 5 (A5)), binding of ^{99m}Tc-HYNIC-Annexin V, and a cell proliferation assay. ^{99m}Tc-HYNIC-Annexin V SPECT and [^{18}F]-FDG PET were also performed in mice xenografted with MDA-MB-231 cells. *Results*. Debio 1143 induced early apoptosis both *in vitro* and *in vivo* 6 h after treatment. Debio 1143 inhibited tumor growth, which was associated with a decreased tumor [^{18}F]-FDG uptake when measured during treatment. *Conclusions*. This imaging study combining SPECT and PET showed the early proapoptotic effects of Debio 1143 resulting in a robust antitumor activity in a preclinical TNBC model. These imaging biomarkers represent valuable noninvasive tools for translational and clinical research in TNBC.

1. Background

The World Health Organization (WHO) reported that 1.7 million women were diagnosed with breast cancer in 2012 with a global number of 6.3 million women diagnosed with breast cancer between 2008 and 2012 [1]. Since the last WHO report in 2008, breast cancer incidence and mortality have increased by more than 20% and 14%, respectively. Breast cancer is also the leading cause of cancer-related death among women (522,000 deaths in 2012) and the most frequently diagnosed cancer in 140 of 184 countries worldwide [1]. The combination of surgery, radiation therapy, chemotherapy, and hormone therapy represents the common therapeutic strategies used nowadays in clinic to treat breast cancer. Clinical and pathologic features (based on conventional histology and immunohistochemistry) allow breast cancer classification as hormone-receptor positive (estrogen receptor (ER) and progesterone receptor (PR)), HER2 (human epidermal growth factor receptor 2) positive, and triple negative (ER, PR, and HER2 negative). This classification process is currently necessary for prognosis evaluation and individualized selection of therapy. Triple-negative breast cancer (TNBC) is a heterogeneous disease associated with a high risk of recurrence and poor prognosis.

Therapeutic options for TNBC are currently limited to cytotoxic therapy, whereas other types of breast cancer expressing receptors are eligible for targeted therapies such as antihormonal or anti-HER2 therapies. Therefore, TNBC is considered as a real challenging disease since no targeted therapies has been approved yet. In this context, numerous new targets are currently under investigations for pharmacological purposes such as Notch signaling, Wnt/β-catenin, and Hedgehog pathways; EGFR, PARP1, mTOR, TGF-β, and angiogenesis inhibitors [2]. The targeting of the inhibitors of apoptosis proteins (IAPs), which are key negative regulators of programmed cell death, represents another promising approach in managing TNBC. Indeed, IAPs have been reported to be upregulated in most cancer types contributing to tumor cell survival and resistance to cancer therapy [3]. Among IAPs, four of them, namely, XIAP, cIAP1, cIAP2, and ML-IAP, negatively regulate apoptosis by downregulating the activity of caspases [4]. In addition to apoptosis, IAPs also influence a multitude of other cellular processes, such as ubiquitin-dependent signaling events that regulate activation of the nuclear factor κB (NFκB), which in turn drive the expression of genes important for inflammation, immunity, cell migration, and cell survival. It has been reported that XIAP protein expression was significantly correlated with a more aggressive tumor phenotype and decreased overall and disease-free survival, suggesting a prognostic value of XIAP for invasive ductal breast cancer with triple-negative phenotype [5]. IAPs are antagonized by the endogenous Second Mitochondria-derived Activator of Caspases (SMAC), also called DIABLO (Direct IAP-Binding Protein with Low PI). SMAC is released from mitochondria into the cytosol when mitochondria are damaged by apoptotic *stimuli* such as UV radiation [4]. Such a mechanism has paved the way for the design of SMAC-mimetic agents to promote apoptosis in cancer cells by antagonizing the activity of IAPs and create conditions in which apoptosis can proceed. A number of SMAC mimetics have been advanced into early clinical development for cancer treatment as single agent or in combination. Interestingly, it has been proposed that TNBC may be more sensitive to SMAC-mimetic drugs than other malignancies, suggesting that SMAC-mimetic could represent a targeted therapy of TNBC which remains to be discovered [4]. Recently, Debio 1143, a new potent orally available monovalent SMAC mimetic targeting multiple IAPs member, has been developed and is currently in clinical trials for cancer treatment [6]. Molecular imaging certainly represents a reliable technique to improve such a drug development since it is recognized to expedite cancer drug discovery, predict responders versus nonresponders to specific treatments, and help determine the overall effectiveness of therapies longitudinally [7]. In oncology, molecular imaging of glucidic metabolism with [^{18}F]-FDG PET has already a crucial impact on several aspects from detection/staging to monitoring/predicting therapeutic effects in both preclinical and clinical settings, so that it remains a gold standard procedure in management of various malignancies. Nevertheless, even if [^{18}F]-FDG uptake reflects the viable tumor cell fraction, it also accumulates in noncancer tissues (e.g., inflammatory lesions, brain, and heart) what can induce pitfalls in images interpretation. The combination of [^{18}F]-FDG imaging with other modalities and/or probes able to image a specific biomarker related to the mechanism of action of the anticancer drugs to be tested is then a reliable way to circumvent these drawbacks. Most of anticancer drugs typically induce cell death through induction of apoptosis which can be noninvasively imaged with molecular imaging probe such as ^{99m}Tc-HYNIC-Annexin V. Such a noninvasive imaging measure of apoptosis would therefore be helpful for demonstrating the efficacy of apoptosis-inducing treatments (e.g., Debio 1143) without requiring tissue sampling. As [^{18}F]-FDG, ^{99m}Tc-HYNIC-Annexin V is a well-known radiotracer and has been extensively assessed in preclinical and clinical settings, making it a safe and reliable probe in spite of a certain lack of specificity since it also labels necrosis [8]. In the current study, we combined SPECT and PET imaging techniques as pharmacodynamic biomarkers to measure the early pro-apoptotic and antitumor effects of Debio 1143 in a preclinical TNBC model. Using MDA-MB-231 xenografted mice, we successfully demonstrated that Debio 1143 induces apoptosis (^{99m}Tc-HYNIC-Annexin V) at early time points and reduced glucidic metabolism ([^{18}F]-FDG PET) over time, which was accompanied by a robust antitumor activity. These imaging biomarkers represent valuable noninvasive tools for translational research and might be useful for SMAC mimetic clinical development in TNBC.

2. Materials and Methods

Materials and methods are available in detail in Supplemental Methods.

2.1. Cell Culture (MDA-MB-231). Breast adenocarcinoma MDA-MB-231 cells (European Collection of Authenticated Cell Cultures (ECACC), Salisbury, UK) have been cultured as a monolayer in RPMI 1640 containing 2 mM of L-glutamine (Lonza, Verviers, Belgium) supplemented with 10% fetal bovine serum (Lonza) at 37°C in a humidified atmosphere (5% CO_2).

2.2. MTS Assay. MDA-MB-231 cells were plated in 190 μL of medium per well in flat-bottom 96-well plates (Dutscher, Brumath, France). Plates were incubated in a drug-free culture medium at 37°C in a humidified atmosphere (5% CO_2) for 24 hours before experiments. Then, cells have been incubated for 72 h with 10 increasing concentrations of Debio 1143 (5 pM to 10 μM) and paclitaxel (0.5 pM to 1 μM). Paclitaxel and Debio 1143 have been diluted in 0.3% DMSO. See details in Supplemental Methods.

2.3. Flow Cytometry. MDA-MB-231 cells were plated in 6-well flat-bottom plates (Dutscher) in 3.8 ml of RPMI 1640 and incubated at 37°C in a humidified atmosphere (5% CO_2) for 24 hours before treatments. Debio 1143 (final concentration 0.3, 1, and 3 μM in 0.3% DMSO) or staurosporine

(final concentration 0.3, 1, and 3 μM in 0.3% DMSO) was added to the corresponding wells, and control (vehicle) cells received 0.3% DMSO alone and incubated for 6 hours at 37°C in a humidified atmosphere (5% CO_2). The effect of Debio 1143 and staurosporine on plasmatic membrane disruption was evaluated using an Annexin V-FITC/7-AAD KIT (Beckman Coulter, Roissy, France). Alternatively, the caspase-3 activity of MDA-MB-231 cells treated 24 h with Debio 1143 or staurosporine (both at a final concentration of 0.3, 1, and 3 μM in 0.3% DMSO) was evaluated by FACS. Cells were plated in 25 cm^2 flat-bottom flasks (Dutscher) in 9.5 ml of RPMI 1640 and incubated at 37°C under 5% CO_2 for 24 hours before treatment. After incubation, cells were detached from the culture flask using trypsin, transferred to FACS tubes, and stained with PE Active Xaspase-3 Apoptosis KIT (BD Pharmigen, France). See details in Supplemental Methods.

2.4. ^{99m}Tc-HYNIC-Annexin V. Annexin-V (A5) was functionalized with a bifunctional chelating agent (HYNIC) and was radiolabeled with technetium 99 m (99 mTc) according to an existing standardized protocol. Briefly, HYNIC-Annexin-V was provided by NIH and shipped frozen and stored at −80°C until use. Gamma-counting results are represented as the percentage of radioactivity bound to the apoptotic cells and will be determined according to %Bound = (A/A + B) × 100 (A: activity of the cell pellet; B: activity of the supernatant). See details in Supplemental Methods.

2.5. Animal Experiments. All animal experiments were performed according to the guidelines of the Ministère de la Recherche (Paris, France). All experiments were approved by the ethical committee of the "centre George François Leclerc" (Dijon, France). Tumors were induced subcutaneously by injecting 5.106 of MDA-MB-231 cells in 200 μL of RPMI 1640 containing matrigel (50 : 50, v : v, BD Biosciences, France) into the right shoulder of female SCID mice.

In vivo evaluation of apoptosis was performed with SPECT-CT imaging (^{99m}Tc-HYNIC-Annexin V). When tumors reached a mean volume of 340 mm^3, ^{99m}Tc-HYNIC-Annexin V SPECT-CT imaging was performed 6 and 24 hours after a single administration of vehicle (*p.o.*, $n = 8$), Debio 1143 (*p.o.*, 100 mg/kg, $n = 8$), or paclitaxel (IV, 7.5 mg/kg, $n = 8$, Taxol®, 6 mg/mL, Bristol-Myers Squibb SpA, France). Mice were anesthetized through isoflurane inhalation for intravenous injection (tail vein) of 10–20 MBq of ^{99m}Tc-HYNIC-Annexin V one hour prior the imaging study. At the end of the last image acquisition, the animals were sacrificed, and tumors were harvested and used for gamma counting in order to confirm image analyses.

In vivo evaluation of antitumor activity was performed with [^{18}F]-FDG PET-CT. Treatments started when the tumors reached a mean volume of 100–200 mm^3. The animals from group 1 ($n = 4$) received daily *p.o.* administrations of vehicle for 14 consecutive days (D11 to D25), the animals from group 2 ($n = 4$) received daily *p.o.* administrations of Debio 1143 at 100 mg/kg for 14 consecutive days (D11 to D25), and the animals from group 3 ($n = 4$) received one IV injection of paclitaxel at 7.5 mg/kg every 7 days for a total of 2 injections (D18 and D25). [^{18}F]-FDG-PET-CT imaging was performed in overnight fasted mice at one week of treatment (D18), two weeks of treatment (D25), and one week after last treatment (D32). Mice were anesthetized through isoflurane inhalation for intravenous injection (tail vein) of 15–20 MBq of [^{18}F]-FDG 30 minutes prior the imaging study. Alternatively, mice receiving vehicle, Debio 1143, or paclitaxel received an intravenous injection (tail vein) of 15–20 MBq of [^{18}F]-FDG and were immediately imaged by dynamic PET-CT for 240 seconds to evaluate tracer circulation and tumor perfusion.

At the end of the last imaging, the mice were intraperitoneally injected with an overdose of pentobarbital for euthanasia and tumors harvested for gamma counting (Perkin Elmer, France). See details in Supplemental Methods.

2.6. Statistical Analysis. All results are presented as mean ± SEM. Statistical analysis was determined using one-way (^{99m}Tc-HYNIC-Annexin V experiments) or two-way ANOVA ([^{18}F]-FDG PET-CT). Analysis was performed with GraphPad Prism 6.0 (GraphPad Software Inc.), and in all cases, a p value less than 0.05 was considered significant.

3. Results

3.1. The Cytotoxic Activity of Debio 1143 on Human Breast Adenocarcinoma Cells Is Comparable to Paclitaxel. The incubation of MDA-MB-231 cells with increasing concentration of Debio 1143 and paclitaxel demonstrated a dose-dependent cytotoxic activity of both drugs on human breast adenocarcinoma cells. The mean IC50 of D1143 was 137 nM, while the mean IC50 of paclitaxel was 7.44 nM (Figure 1(a)). Our results confirm the findings of previous studies which report an IC50 of 144 nM for Debio 1143 [9].

3.2. Debio 1143 Induces Apoptosis of Human Breast Adenocarcinoma Cells. After 6 hours of incubation of MDA-MB-231 cells with Debio 1143, a significant dose-dependent increase of cells in early apoptosis (Annexin-V+/7-AAD-) was observed compared to vehicle-treated cells (Figure 1(b)). This increase in early apoptosis was observed starting at 0.3 μM with a maximal effect at 3 μM of Debio 1143. Staurosporine, used as positive control in this experiment, also induced a significant increase in early apoptosis in MDA-MB-231 cells (Figure 1(b)). Interestingly, Debio 1143 also induced a significant increase in late apoptosis/necrosis (Annexin-V+/7-AAD+) of MDA-MB-231 cells starting at 1 μM and increased with dose (Figure 1(b)). These results were confirmed by a dose-dependent increase in proportion of cells harboring active caspase-3, the major effector of apoptosis, after Debio 1143 treatment (Figure 1(c)). Furthermore, gamma counting of MDA-MB-231 cells after staining with ^{99m}Tc-HYNIC-Annexin V, which specifically stains Annexin-V positive cells, demonstrated that Debio 1143 (3 μM) induced an increase in cells presenting Annexin-V (Figure 1(d)). All together, these results highlight the proapoptotic effects of Debio 1143 on human breast adenocarcinoma cells.

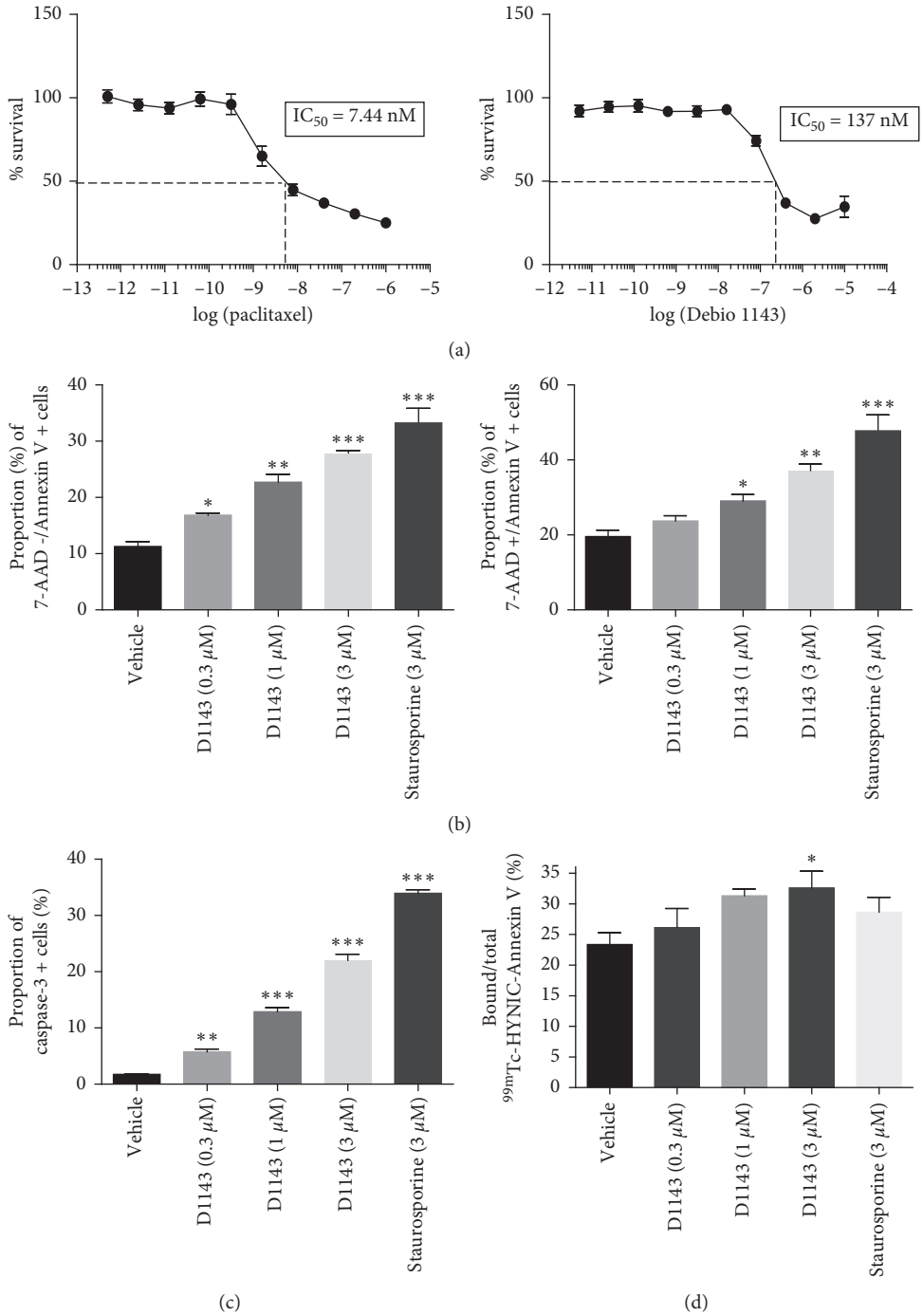

Figure 1: D1143 induces apoptosis of human breast adenocarcinoma cells. (a) Viable *MDA-MB-231* cells (%) after treatment with increasing concentration of paclitaxel (left panel) or D1143 (right panel) for 72 h. Paclitaxel and D1143 are expressed as log[concentration] for IC50 determination. Results are presented as mean ± SEM; $n = 8$. (b) Annexin-V+/7-AAD- (left panel) and Annexin-V +/7-AAD+ (right panel) *MDA-MB-231* cells (%) after treatment with D1143 (0.3 μM, 1 μM, and 3 μM) or staurosporine (3 μM) for 6 h. Results are presented as mean ± SEM; $n = 4$; $^{*}p < 0.05$, $^{**}p < 0.01$, $^{***}p < 0.001$. (c) Active caspase-3 positive *MDA-MB-231* cells (%) after treatment with D1143 (0.3 μM, 1 μM, and 3 μM) or staurosporine (3 μM) for 6 h. Results are presented as mean ± SEM; $n = 4$; $^{**}p < 0.01$, $^{***}p < 0.001$. (d) Bound/Total ^{99m}Tc-HYNIC-Annexin V *MDA-MB-231* cells (%) after treatment with D1143 (0.3 μM, 1 μM, and 3 μM) or staurosporine (3 μM) for 6h. Results are presented as mean ± SEM; $n = 4$; $^{*}p < 0.05$.

3.3. Debio 1143 Induces Tumor-Apoptosis In Vivo in a Human Breast Adenocarcinoma Murine Model. ^{99m}Tc-HYNIC-Annexin V SPECT-CT imaging experiments were carried out when tumors reached a mean volume of 340 mm^3. Imaging was performed at 6 h after treatment for vehicle-treated mice and at 6 and 24 h after treatment for paclitaxel- and Debio 1143-treated mice. One hour after ^{99m}Tc-HYNIC-Annexin V administration, mice from all

group showed an apparent similar whole body distribution of radioactivity localized mainly in kidneys, bladder, and liver concentrating more than 80% of overall radioactive signal as previously described in the literature ([8]; Figures 2(a) and 2(b)). A weak ^{99m}Tc-HYNIC-Annexin V signal was observed in tumors from vehicle-treated mice, comparable with signal observed in paclitaxel-treated mice. Interestingly, a significant increase in tumor ^{99m}Tc-HYNIC-Annexin V signal was observed at 6h following Debio 1143 treatment (Figures 2(c) and 2(d)). An increase in ^{99m}Tc-HYNIC-Annexin V signal was also observed after 24 h of paclitaxel although not significant (Figure 2(d)). These results were consistent with *ex vivo* gamma counting of tumors with an increase of ^{99m}Tc-HYNIC-Annexin V tumor uptake 6 h after Debio 1143 compared to vehicle-treated mice (Figure 2 (e)). All together, these results demonstrate that Debio 1143 specifically induces tumor apoptosis *in vivo* in a human breast adenocarcinoma murine model.

3.4. In Vivo Evaluation of the Antitumor Activity of Debio 1143 by [^{18}F]-FDG PET-CT. After tumor induction, mice received vehicle, Debio 1143, or paclitaxel for 2 weeks. Treatment started when mean tumor volume reached approximately 120–170 mm^3 (D11). Mice received corresponding treatment from D11 to D25 (2 weeks) and were left untreated for another week up to D32. While mice receiving vehicle continued to gain weight throughout the experiment, paclitaxel and Debio 1143 induced a slight and transient decrease of body weight recovered once treatments ended (Figure 3 (a)). Tumor volume increased regularly and similarly in vehicle-treated mice from D11 (treatment initiation) to D32 (end of experiment; Figure 3(b)). Paclitaxel did not induce any decrease in tumor growth throughout the experiment, while Debio 1143 displayed a significant antitumor activity after 2 weeks of treatment (D25) that was sustained up to D32 (Figure 3(b)). [^{18}F]-FDG PET-CT was performed on D18 (1 week of treatment), D25 (2 weeks of treatment), and D32 (1 week after treatment end). [^{18}F]-FDG uptake measured by SUV (standardized uptake values) max and mean SUV was significantly lower in Debio 1143-treated mice compared to vehicle at D18 (Figures 3(c)–3(e)). [^{18}F]-FDG uptake remained lower in Debio 1143-treated mice compared to vehicle throughout the experiment but not significantly at D25 and D32 (Figures 3(c)–3(e)). Paclitaxel also reduced not significantly [^{18}F]-FDG uptake as compared to vehicle-treated mice (Figures 3(c)–3(e)). Interestingly, gamma counting performed on tumors at D32 (1 week after treatment end) confirmed our imaging results with a significant lower tumor [^{18}F]-FDG uptake in Debio 1143 and paclitaxel-treated mice compared to vehicle (Figure 3(f)). We also performed dynamic [^{18}F]-FDG PET-CT imaging for 4 minutes after injection on all groups at D18, D25, and D32 to evaluate tumor perfusion. Interestingly, dynamic monitoring of mean tumor SUV (every 5 seconds for 240 seconds) showed a significant decrease in tumor perfusion in mice treated with Debio 1143 and paclitaxel at D18 and D32 and only in mice treated with D1143 at D25 (Figures 4(a)–4(c)). No changes were observed in mean aorta SUV (control [^{18}F]-FDG SUV). All together, these results demonstrate the antitumor activity of Debio 1143 and highlight [^{18}F]-FDG PET-CT imaging as a reliable method to follow the activity of Debio 1143 in human breast adenocarcinoma tumors in a noninvasive manner.

4. Discussion

In order to improve the management of malignancies, it is now well established that an early and reliable assessment of therapy response is a crucial issue. It allows guidance of the oncologist to the best options for the patients: modulations of the doses, treatment switching, or treatment combinations. In the current study, using two different molecular imaging modalities (SPECT-CT and PET-CT), we assessed the effect of Debio 1143, a new potent oral SMAC mimetic, as a single agent in a preclinical model of TNBC, in immunodeficient mice xenografted with MDA-MB-231 cells. The xenografted models still constitute a major preclinical screen for the development of novel cancer therapeutics, included human-targeted therapies. Despite limitations, these models have identified clinically efficacious agents, suggesting that they are still a "workhorse" of the pharmaceutical industry [10]. TNBC represents 15–20% of breast cancers and remains a challenging disease regarding its aggressive nature, its poor prognosis, and the lack of targeted therapies. As no well-defined molecular targets have been described so far, cytotoxic chemotherapy is currently the only treatment option for TNBC whose major drawback is an unacceptable deterioration in the quality of life. Currently, paclitaxel is commonly used in clinical practice to treat TNBC. However, the clinical efficacy of paclitaxel has been weakened by the development of drug resistance and the emergence of side-effects, including neutropenia and neurotoxicity [11]. Paclitaxel induces apoptosis by targeting microtubules and resulting in cell cycle arrest [12]. Although paclitaxel has been shown to eliminate most tumor cells including TNBC, paclitaxel resistance has been estimated to cause treatment failure in more than 90% of patients [13]. Therefore, the development of alternative therapeutic strategies is essential. Inhibitor of apoptosis proteins (IAPs) play key roles in resistance to cell death induced by a variety of anticancer drugs in various indications including in TNBC, and thus are promising drug targets [4]. Debio 1143 (a.k.a. AT-406 or SM-406) is a monovalent, orally available, small molecule antagonist of IAPs in clinical development that has demonstrated potent single-agent antitumor activity in multiple models of human cancer such as lung adenocarcinoma [14, 15], head and neck squamous cell carcinoma [16], and TNBC [9, 17]. Debio 1143 has also been shown to work synergistically with conventional chemotherapeutic agents (such as taxanes) or radiotherapy RT in nonclinical cancer models [14, 16]. SMAC mimetics have been shown to promote apoptosis by inhibiting IAP-mediated caspase repression [18]. *In vitro* SMAC-mimetics treatment has been shown to increase Annexin-V positive cells and activate caspases-3 and -8 in various cancer cell lines [16, 19, 20]. Our results are in line with previous studies and confirm the increase in Annexin-V and

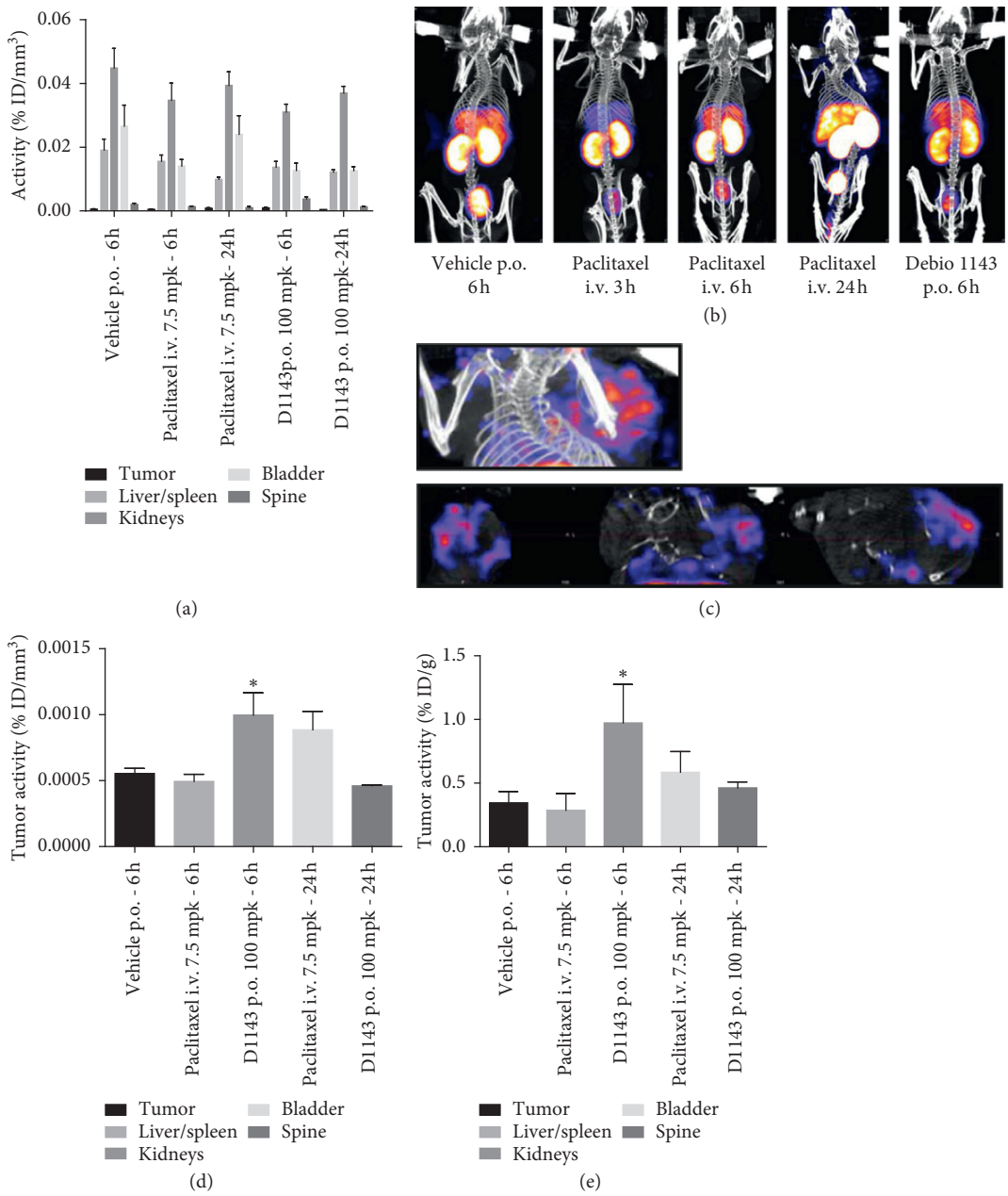

Figure 2: D1143 induces tumor apoptosis *in vivo* in a human breast adenocarcinoma murine model. (a) *In vivo* biodistribution of ^{99m}Tc-HYNIC-Annexin V in tumor (*MDA-MB-231* cells) bearing SCID mice (tumor in the right shoulder) 6 h and 24 h after receiving paclitaxel (iv), D1143 (po), or vehicle as control. Liver/spleen, kidneys, bladder, spine, and tumor activity are expressed as % ID/mm^3. Results are presented as mean ± SEM; $n = 8$. (b) Representative SPECT pictures of ^{99m}Tc-HYNIC-Annexin V in tumor (*MDA-MB-231* cells) bearing SCID mice 6 h and 24 h after receiving paclitaxel (iv), D1143 (po), or vehicle as control. (c) Representative tumor-centered SPECT pictures of tumor (*MDA-MB-231* cells) bearing SCID mice 6 h after receiving D1143 (po). (d) Specific ^{99m}Tc-HYNIC-Annexin V tumor activity (% ID/mm^3) of tumor- (*MDA-MB-231* cells-) bearing SCID mice (tumor in the right shoulder) 6 h and 24 h after receiving paclitaxel (iv), D1143 (po), or vehicle as control. Results are presented as mean ± SEM; $n = 8$; $^*p < 0.05$. (e) Gamma counting of ^{99m}Tc-HYNIC-Annexin V in tumors in SCID mice 6h and 24h after receiving paclitaxel (iv), D1143 (po), or vehicle as control (%ID/g). Results are presented as mean ± SEM; $n = 8$ and $n = 2$ for the paclitaxel group 6 h, $^*p < 0.05$.

activation of caspase-3 after Debio 1143 treatment in MDA-MB-231 cells. Our results also demonstrate that, this increase in Annexin-V can be measured in tumor *in vivo* in a preclinical model of breast adenocarcinoma with radiolabelled ^{99m}Tc-HYNIC-Annexin V. This tool could represent a reliable way to monitor early apoptosis induced by anticancer agents in order to evaluate early treatment efficacy and allow improvement of therapeutic strategies.

Interestingly, Debio 1143 presented a higher antitumor activity *in vivo* in comparison with paclitaxel despite an apparent higher intrinsic cytotoxic activity of paclitaxel *in vitro* suggesting that targeting IAPs may offer the potential

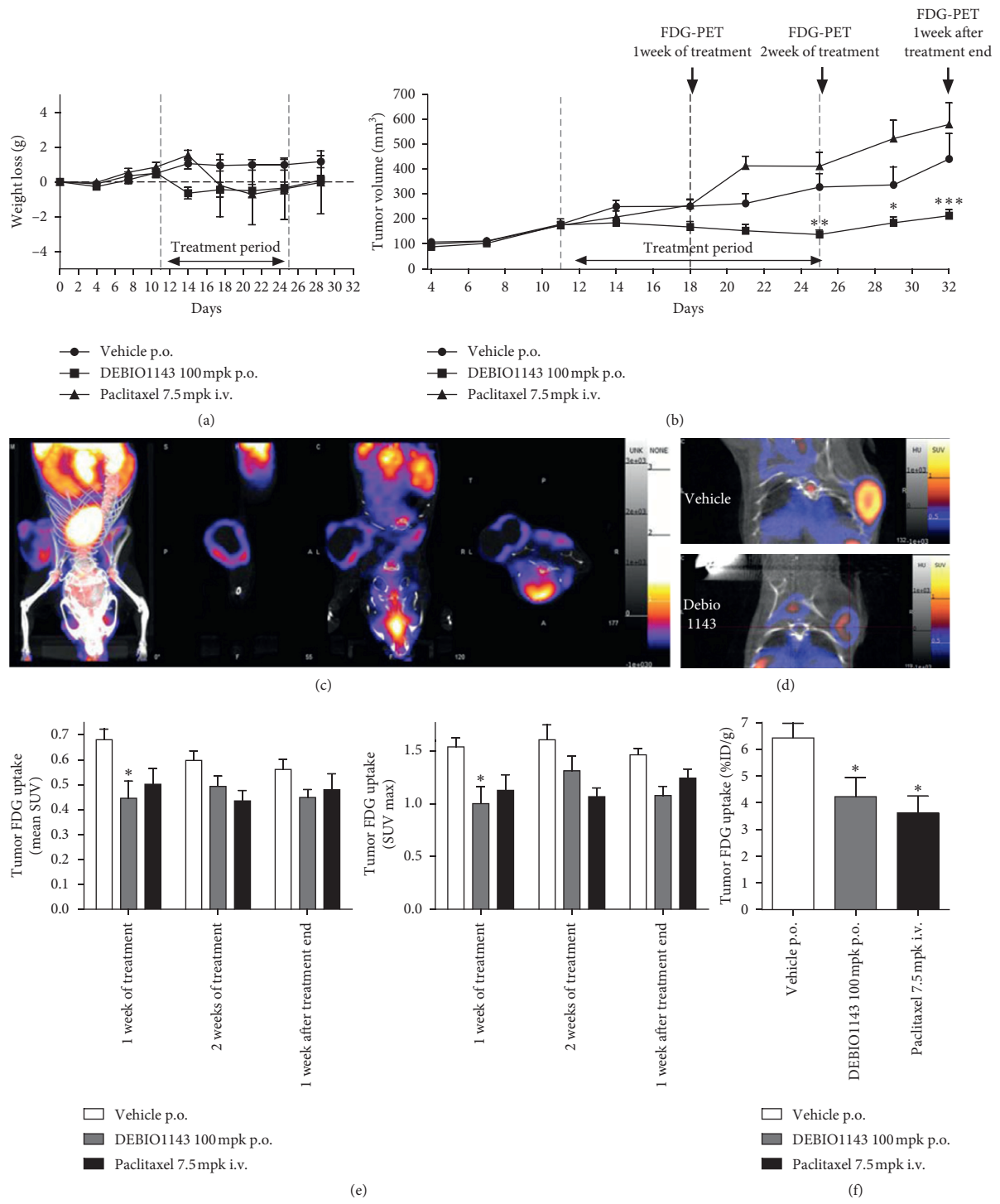

Figure 3: *In vivo* evaluation of the antitumor activity of D1143 by [18F]-FDG PET-CT. (a) Weight loss (g) monitoring of tumor-bearing SCID mice receiving D1143, paclitaxel, or vehicle as control. Treatment started at D11 and ended at D25. Mice were sacrificed at D32. Results are presented as mean ± SEM; $n = 8$. (b) Tumor volume (mm^3) of tumor-bearing SCID mice receiving D1143, paclitaxel, or vehicle as control. Treatment started at D11 and ended at D25. Results are presented as mean ± SEM; $n = 8$; $^{**}p < 0.01$, $^{***}p < 0.01$. (c) Representative [^{18}F]-FDG PET-CT picture of tumor-bearing SCID mice (tumor in the right shoulder) receiving vehicle at D32. (d) Representative [^{18}F]-FDG PET-CT picture of tumor-bearing SCID mice (tumor in the right shoulder) receiving vehicle or D1143 at D32. (e) Tumor [^{18}F]-FDG uptake in SCID mice receiving vehicle, D1143, or paclitaxel. Measures have been performed at D18 (1 week of treatment), D25 (2 weeks of treatment), and D32 (1 week after treatment). Results are expressed as mean SUV (left panel) and SUV max (right panel). Results are presented as mean ± SEM; $n = 8$, $^{*}p < 0.05$. (f) Gamma counting of [^{18}F]-FDG in tumors of SCID mice receiving paclitaxel (iv), D1143 (po), or vehicle as control (%ID/g). Results are presented as mean ± SEM; $n = 8$; $^{*}p < 0.05$.

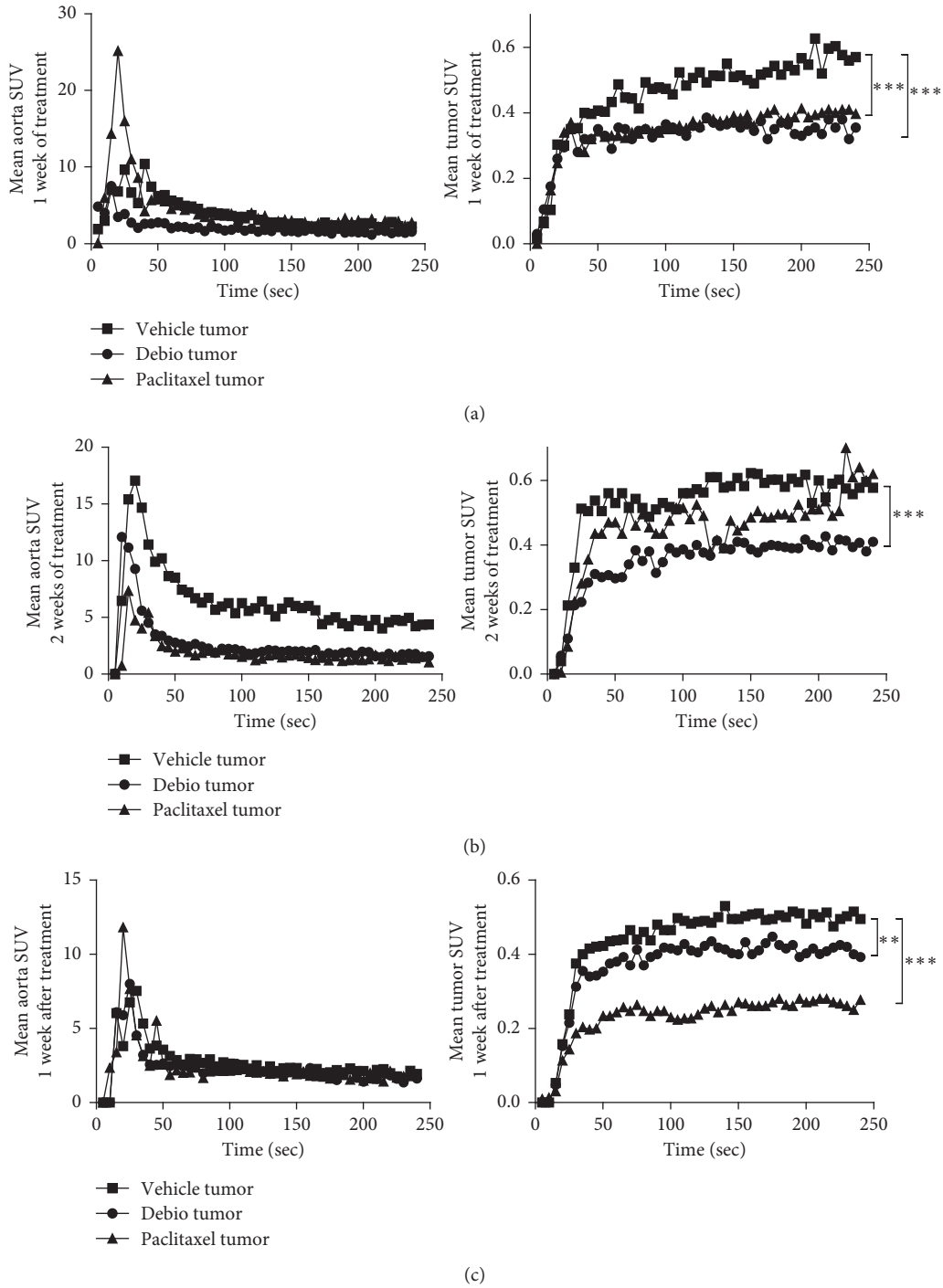

Figure 4: *In vivo* dynamic [18F]-FDG PET-CT. (a) Dynamic [18F]-FDG PET-CT performed on tumor-bearing SCID mice receiving paclitaxel, D1143, or vehicle at D18 (1 week of treatment). Mean aorta SUV (left panel) and mean tumor SUV (right panel) have been measured every 5 seconds for 240 seconds. (b) Dynamic [18F]-FDG PET-CT performed on tumor-bearing SCID mice receiving paclitaxel, D1143, or vehicle at D25 (week of treatment). Mean aorta SUV (left panel) and mean tumor SUV (right panel) have been measured every 5 seconds for 240 seconds. (c) Dynamic [18F]-FDG PET-CT performed on tumor-bearing SCID mice receiving paclitaxel, D1143, or vehicle at D32 (1 week after treatment). Mean aorta SUV (left panel) and mean tumor SUV (right panel) have been measured every 5 seconds for 240 seconds.

for a greater therapeutic window than conventional chemotherapy *in vivo*. In addition, our results show that Debio 1143 and placlitaxel presented differentiated proapoptotic effects over time *in vivo*. Debio 1143 induced an earlier and stronger cancer cell apoptosis as early as 6 h after treatment, whereas paclitaxel induced-apoptosis was only detectable (although not significant) 24 h after treatment. Apoptosis is an early event expected to occur after successful chemotherapy and is highly predictive of treatment success. Thus, apoptosis quantification represents a major way to

assess therapy response. Annexin V (A5) has been widely used in basic and clinical research as an apoptosis marker in conjunction with propidium iodide to distinguish between apoptotic and necrotic cells. Therefore, it has been labeled with radionuclides for measuring apoptosis *in vitro* and *in vivo* in animal models and patients [8, 21, 22]. ^{99m}Tc-HYNIC-Annexin V, used in the current study, is the most widely applied probe in preclinical and clinical settings for A5 imaging [23]. Kemerink et al. demonstrated that highest uptake of ^{99m}Tc-HYNIC-Annexin V in humans was observed in the kidneys followed by the liver and spleen [24]. These results are in accordance with our findings in mice where the highest uptake was found in the kidney at 6h and 24h.

Moreover, ^{99m}Tc-HYNIC-Annexin V showed a fast blood clearance with more than 90% of the tracer cleared with a half-life of 24 min [24], allowing imaging at 6 h after injection. Therefore, ^{99m}Tc-HYNIC-Annexin V has been used successfully to assess therapy response in patients after radiation therapy or chemotherapy [25–27]. ^{99m}Tc-HYNIC-Annexin V uptake has also been demonstrated to predict prognostic value and efficacy of anticancer therapies. In our study, Debio 1143 induced a significantly higher tumor (MDA-MB-231) uptake of ^{99m}Tc-HYNIC-Annexin V compared to vehicle and paclitaxel. In parallel, Debio 1143 showed an improved efficacy in preventing tumor growth compared to vehicle and paclitaxel after 1 and 2 weeks of treatment and remained 1 week after treatment arrest confirming the predictive value of ^{99m}Tc-HYNIC-Annexin V tumor uptake on therapy efficacy. Unexpectedly, paclitaxel did not induce a strong *in vivo* apoptosis in our study and, in parallel, did not prevent tumor growth. Despite some controversy, MDA-MB-231 has been demonstrated to be rather insensitive to paclitaxel compared to other TNBC cells [28–30]. Interestingly, Panayotopoulou et al. identified, by high throughput screening, that SMAC mimetics were able to eliminate MDA-MB-231 short-term paclitaxel resistance suggesting a benefit of such drugs for TNBC patients [31]. Similar results have also been found in other cancer types including ovarian cancer [32], non-small cell lung cancer [14], and breast cancer [33], in which SMAC mimetics were able to potentiate the effect of standard chemotherapy, including paclitaxel [14, 34, 35]. However, this study did not evaluate the efficacy of the combination of SMAC mimetics and paclitaxel with [^{18}F]-FDG PET imaging. Moreover, Panayotopoulou et al. identified that long-term paclitaxel was associated with desensitization to SMAC mimetics. Therefore, combination therapy of SMAC mimetics and short-term paclitaxel could be an effective therapeutic strategy for TNBC.

Most interestingly, the effect of the SMAC mimetic birinapant on caspase-3 activation has recently been investigated by *in vivo* imaging [36]. In this study, Yang et al. used a specific caspase-3 PET radiotracer, [^{18}F]ICMT-11, and demonstrated that birinapant induced *in vitro* a rapid and transient activation of caspase-3 on MDA-MB-231 cells 6 h after treatment. Moreover, a similar activation of caspase-3 was also shown *in vivo* in a preclinical model of colon cancer. These results are in accordance with Debio 1143 presented in the current study using ^{99m}Tc-HYNIC-Annexin V. In addition, Yang et al. also observed a decrease [^{18}F]-FDG uptake and a delay in tumor growth *in vivo* after birinapant treatment similarly to what was observed with Debio 1143 in our study. Interestingly, the *in vivo* activation of caspase-3 and decrease in [^{18}F]-FDG uptake induced by birinapant was only transient and returned to baseline 24 h and 48 h after treatment highlighting the need of multiple dosing of SMAC mimetics to elicit antitumor activity as monotherapy.

5. Conclusions

[^{18}F]-FDG PET is nowadays the main tool for detection, staging, and monitoring of tumor clinically. However, [^{18}F]-FDG uptake accumulates in noncancer tissues and can be influenced by physiologic uptake of FDG (for example, infection and inflammation) [37].

Moreover, some adenocarcinoma are characterized by low-grade or absence of FDG uptake [38, 39]. In our study, we demonstrate that both ^{99m}Tc-HYNIC-Annexin V and [^{18}F]-FDG PET data can be associated to predict therapy efficacy and outcome. Therefore, the combination of [^{18}F]-FDG PET and ^{99m}Tc-HYNIC-Annexin V appears as a reliable and noninvasive way to monitor early therapy efficacy and subsequent tumor activity in TNBC patients.

Abbreviations

7-AAD: 7-Aminoactinomycin D
A5: Annexin-5
DIABLO: Direct IAP-Binding Protein with Low PI
DMSO: Dimethylsulfoxide
EGFR: Epidermal growth factor receptor
ER: Estrogen receptor
FDG: Fluorodeoxyglucose
HER2: Human epidermal growth factor receptor 2
IAP: Inhibitor of apoptosis proteins
IV: Intravenous
NIH: National Institute
PET: Positron emission tomography
PR: Progesterone receptor
SMAC: Second Mitochondria-derived Activator of Caspases
SPECT: Single-photon emission tomography
SUV: Standardized uptake values
TGF-β: Transforming growth factor-β
TNBC: Triple-negative breast cancer
WHO: World Health Organization.

Data Availability

The datasets used and/or analyzed during the current study are available from the corresponding author on reasonable request.

Ethical Approval

All applicable international, national, and/or institutional guidelines for the care and use of animals were followed.

All animal studies were sanctioned by the accredited ethical committees (Oncomet n°91 and C2ea Grand Campus n°105) and were carried out in accordance with the legislation on the use of laboratory animals (directive 2010/63/EU). Experiments were conducted following the European Union's animal care directive (86/609/EEC).

Conflicts of Interest

This work was performed as a part of a collaborative research project with Debiopharm International SA. Anne Vaslin, Hélène Maby-El Hajjami, Claudio Zanna, and Grégoire Vuagniaux are employees of Debiopharm International SA. The other authors declare that they have no conflicts of interest.

Authors' Contributions

PSB, AO, AV, HM, CZ, GV, and BC designed the study and wrote the protocol. JMV, OR, and FB performed radiolabeling of compounds. PSB, AO, OR, and JMV conducted the SPECT/PET experiments. PSB, BC, FD, PF, and FB analyzed the data. PSB and AO wrote the first draft of the manuscript. FD, FB, PF, AV, HM, CZ, GV, and BC mainly revised the manuscript. All authors read and approved the final manuscript.

Acknowledgments

This work was supported by Debiopharm International SA. It was performed within Pharm'image, a regional center of excellence in pharmacoimaging. This work was also supported by a French Government Grant managed by the French National Research Agency (ANR) under the program "Investissements d'Avenir" (reference ANR-10-EQPX-05- 01/IMAPPI Equipex).

Supplementary Materials

Materials and methods are provided in detail in the Supplementary Materials file. (*Supplementary Materials*)

References

[1] J. Ferlay, I. Soerjomataram, M. Ervik et al., *GLOBOCAN 2012 v1.0, Cancer Incidence and Mortality Worldwide*, IARC CancerBase No. 11. International Agency for Research on Cancer, Lyon, France, 2013, http://globocan.iarc.fr.

[2] V. S. Jamdade, N. Sethi, N. A. Mundhe, P. Kumar, M. Lahkar, and N. Sinha, "Therapeutic targets of triple-negative breast cancer: a review," *British Journal of Pharmacology*, vol. 172, no. 17, pp. 4228–4237, 2015.

[3] L. Dubrez, J. Berthelet, and V. Glorian, "IAP proteins as targets for drug development in oncology," *OncoTargets and Therapy*, vol. 9, pp. 1285–1304, 2013.

[4] S. Wang, L. Bai, J. Lu, L. Liu, C. Y. Yang, and H. Sun, "Targeting inhibitors of apoptosis proteins (IAPs) for new breast cancer therapeutics," *Journal of Mammary Gland Biology and Neoplasia*, vol. 17, no. 3-4, pp. 217–228, 2012.

[5] J. Wang, Y. Liu, R. Ji et al., "Prognostic value of the X-linked inhibitor of apoptosis protein for invasive ductal breast cancer with triple-negative phenotype," *Human Pathology*, vol. 41, no. 8, pp. 1186–1195, 2010.

[6] H. I. Hurwitz, D. C. Smith, H. C. Pitot et al., "Safety, pharmacokinetics, and pharmacodynamic properties of oral DEBIO1143 (AT-406) in patients with advanced cancer: results of a first-in-man study," *Cancer Chemotherapy and Pharmacology*, vol. 75, no. 4, pp. 851–859, 2015.

[7] M. L. James and S. S. Gambhir, "A molecular imaging primer: modalities, imaging agents, and applications," *Physiological Reviews*, vol. 92, no. 2, pp. 897–965, 2012.

[8] T. Z. Belhocine, F. G. Blankenberg, M. S. Kartachova et al., "99mTc-Annexin A5 quantification of apoptotic tumor response: a systematic review and meta-analysis of clinical imaging trials," *European Journal of Nuclear Medicine and Molecular Imaging*, vol. 42, no. 13, pp. 2083–2097, 2015.

[9] Q. Cai, H. Sun, Y. Peng et al., "A potent and orally active antagonist (SM-406/AT-406) of multiple inhibitor of apoptosis proteins (IAPs) in clinical development for cancer treatment," *Journal of Medicinal Chemistry*, vol. 54, no. 8, pp. 2714–2726, 2011.

[10] T. F. Vandamme, "Rodent models for human diseases," *European Journal of Pharmacology*, vol. 759, pp. 84–89, 2015.

[11] T. Fojo and M. Menefee, "Mechanisms of multidrug resistance: the potential role of microtubule-stabilizing agents," *Annals of Oncology*, vol. 18, no. 5, pp. v3–v8, 2007.

[12] R. Z. Yusuf, Z. Duan, D. E. Lamendola, R. T. Penson, and M. V. Seiden, "Paclitaxel resistance: molecular mechanisms and pharmacologic manipulation," *Current Cancer Drug Targets*, vol. 3, no. 1, pp. 1–19, 2003.

[13] D. B. Longley and P. G. Johnston, "Molecular mechanisms of drug resistance," *Journal of Pathology*, vol. 205, no. 2, pp. 275–292, 2005.

[14] C. G. Langdon, N. Wiedemann, M. A. Held et al., "SMAC mimetic Debio 1143 synergizes with taxanes, topoisomerase inhibitors and bromodomain inhibitors to impede growth of lung adenocarcinoma cells," *Oncotarget*, vol. 6, no. 35, pp. 37410–37425, 2015.

[15] N. Liu, Z. Tao, J. M. Blanc et al., "Debio 1143, an antagonist of multiple inhibitor-of-apoptosis proteins, activates apoptosis and enhances radiosensitization of non-small cell lung cancer cells in vitro," *American Journal of Cancer Research*, vol. 4, no. 6, pp. 943–951, 2014.

[16] O. Matzinger, D. Viertl, P. Tsoutsou et al., "The radiosensitizing activity of the SMAC-mimetic, Debio 1143, is TNFα-mediated in head and neck squamous cell carcinoma," *Radiotherapy and Oncology*, vol. 116, no. 3, pp. 495–503, 2015.

[17] T. Zhang, Y. Li, P. Zou et al., "Physiologically based pharmacokinetic and pharmacodynamic modeling of an antagonist (SM-406/AT-406) of multiple inhibitor of apoptosis proteins (IAPs) in a mouse xenograft model of human breast cancer," *Biopharmaceutics & Drug Disposition*, vol. 34, no. 6, pp. 348–359, 2013.

[18] S. Fulda and D. Vucic, "Targeting IAP proteins for therapeutic intervention in cancer," *Nature Reviews Drug Discovery*, vol. 11, no. 2, pp. 109–124, 2012.

[19] D. Yang, Y. Zhao, A. Y. Li, S. Wang, G. Wang, and Y. Sun, "Smac-mimetic compound SM-164 induces radiosensitization in breast cancer cells through activation of caspases and induction of apoptosis," *Breast Cancer Research and Treatment*, vol. 133, no. 1, pp. 189–199, 2012.

[20] J. Yang, D. McEachern, W. Li et al., "Radiosensitization of head and neck squamous cell carcinoma by a SMAC-mimetic compound, SM-164, requires activation of caspases," *Molecular Cancer Therapeutics*, vol. 10, no. 4, pp. 658–669, 2011.

[21] H. H. Boersma, B. L. Kietselaer, L. M. Stolk et al., "Past, present, and future of annexin A5: from protein discovery to clinical applications," *Journal of Nuclear Medicine*, vol. 46, no. 12, pp. 2035–2050, 2005.

[22] X. Wang, H. Feng, S. Zhao et al., "SPECT and PET radiopharmaceuticals for molecular imaging of apoptosis: from bench to clinic," *Oncotarget*, vol. 8, no. 12, pp. 20476–20495, 2017.

[23] F. L. Schaper and C. P. Reutelingsperger, "99mTc-HYNIC-Annexin A5 in oncology: evaluating efficacy of anti-cancer therapies," *Cancers*, vol. 5, no. 4, pp. 550–568, 2013.

[24] G. J. Kemerink, X. Liu, D. Kieffer et al., "Safety, biodistribution, and dosimetry of 99mTc-HYNIC-annexin V, a novel human recombinant annexin V for human application," *Journal of Nuclear Medicine*, vol. 44, no. 6, pp. 947–952, 2003.

[25] M. Kartachova, R. L. Haas, R. A. Olmos, F. J. Hoebers, N. van Zandwijk, and M. Verheij, "In vivo imaging of apoptosis by 99mTc-Annexin V scintigraphy: visual analysis in relation to treatment response," *Radiotherapy and Oncology*, vol. 72, no. 3, pp. 333–339, 2004.

[26] M. Kartachova, N. van Zandwijk, S. Burgers, H. van Tinteren, M. Verheij, and R. A. Valdes Olmos, "Prognostic significance of 99mTc Hynic-rh-annexin V scintigraphy during platinum-based chemotherapy in advanced lung cancer," *Journal of Clinical Oncology*, vol. 25, no. 18, pp. 2534–2539, 2007.

[27] S. Rottey, G. Slegers, S. Van Belle, I. Goethals, and C. Van de Wiele, "Sequential 99mTc-hydrazinonicotinamide-annexin V imaging for predicting response to chemotherapy," *Journal of Nuclear Medicine*, vol. 47, no. 11, pp. 1813–1818, 2006.

[28] M. L. Flores, C. Castilla, R. Avila, M. Ruiz-Borrego, C. Saez, and M. A. Japon, "Paclitaxel sensitivity of breast cancer cells requires efficient mitotic arrest and disruption of Bcl-xL/Bak interaction," *Breast Cancer Research and Treatment*, vol. 133, no. 3, pp. 917–928, 2012.

[29] E. D. Arisan, O. Kutuk, T. Tezil, C. Bodur, D. Telci, and H. Basaga, "Small inhibitor of Bcl-2, HA14-1, selectively enhanced the apoptotic effect of cisplatin by modulating Bcl-2 family members in MDA-MB-231 breast cancer cells," *Breast Cancer Research and Treatment*, vol. 119, no. 2, pp. 271–281, 2010.

[30] Y. Tabuchi, J. Matsuoka, M. Gunduz et al., "Resistance to paclitaxel therapy is related with Bcl-2 expression through an estrogen receptor mediated pathway in breast cancer," *International Journal of Oncology*, vol. 34, no. 2, pp. 313–319, 2009.

[31] E. G. Panayotopoulou, A. K. Muller, M. Borries, H. Busch, G. Hu, and S. Lev, "Targeting of apoptotic pathways by SMAC or BH3 mimetics distinctly sensitizes paclitaxel-resistant triple negative breast cancer cells," *Oncotarget*, vol. 8, no. 28, pp. 45088–45104, 2017.

[32] H. L. Mao, Y. Pang, X. Zhang et al., "Smac peptide potentiates TRAIL- or paclitaxel-mediated ovarian cancer cell death in vitro and in vivo," *Oncology Reports*, vol. 29, no. 2, pp. 515–522, 2013.

[33] C. A. Benetatos, Y. Mitsuuchi, J. M. Burns et al., "Birinapant (TL32711), a bivalent SMAC mimetic, targets TRAF2-associated cIAPs, abrogates TNF-induced NF-kappaB activation, and is active in patient-derived xenograft models," *Molecular Cancer Therapeutics*, vol. 13, no. 4, pp. 867–879, 2014.

[34] R. M. Greer, M. Peyton, J. E. Larsen et al., "SMAC mimetic (JP1201) sensitizes non-small cell lung cancers to multiple chemotherapy agents in an IAP-dependent but TNF-alpha-independent manner," *Cancer Research*, vol. 71, no. 24, pp. 7640–7648, 2011.

[35] C. Yang, H. Wang, B. Zhang et al., "LCL161 increases paclitaxel-induced apoptosis by degrading cIAP1 and cIAP2 in NSCLC," *Journal of Experimental & Clinical Cancer Research*, vol. 35, no. 1, p. 158, 2016.

[36] Q. D. Nguyen, I. Lavdas, J. Gubbins et al., "Temporal and spatial evolution of therapy-induced tumor apoptosis detected by caspase-3-selective molecular imaging," *Clinical Cancer Research*, vol. 19, no. 14, pp. 3914–3924, 2013.

[37] G. S. Shroff, B. W. Carter, C. Viswanathan et al., "Challenges in interpretation of staging PET/CT in thoracic malignancies," *Current Problems in Diagnostic Radiology*, vol. 46, no. 4, pp. 330–341, 2016.

[38] B. T. Kim, Y. Kim, K. S. Lee et al., "Localized form of bronchioloalveolar carcinoma: FDG PET findings," *American Journal of Roentgenology*, vol. 170, no. 4, pp. 935–939, 1998.

[39] K. Higashi, Y. Ueda, M. Yagishita et al., "FDG PET measurement of the proliferative potential of non-small cell lung cancer," *Journal of Nuclear Medicine*, vol. 41, no. 1, pp. 85–92, 2000.

Hindawi
Contrast Media & Molecular Imaging
Volume 2018, Article ID 5247153, 10 pages
https://doi.org/10.1155/2018/5247153

Research Article

^{177}Lu-DOTA-HYNIC-Lys(Nal)-Urea-Glu: Biokinetics, Dosimetry, and Evaluation in Patients with Advanced Prostate Cancer

Clara Santos-Cuevas,[1] Guillermina Ferro-Flores,[1] Francisco O. García-Pérez,[2] Nallely Jiménez-Mancilla,[3] Gerardo Ramírez-Nava,[1,4] Blanca Ocampo-García,[1] Myrna Luna-Gutiérrez,[1] Erika Azorín-Vega,[1] Jenny Davanzo,[2] and Irma Soldevilla-Gallardo[2,5]

[1]*Departamento de Materiales Radiactivos, Instituto Nacional de Investigaciones Nucleares (ININ), Ocoyoacac 52750, Estado de México, Mexico*
[2]*Departamento de Medicina Nuclear, Instituto Nacional de Cancerología, Ciudad de México 14000, Mexico*
[3]*CONACyT, Instituto Nacional de Investigaciones Nucleares (ININ), Ocoyoacac 52750, Estado de México, Mexico*
[4]*Departamento de Posgrado, Instituto Politécnico Nacional, Ciudad de México 07340, Mexico*
[5]*Unidad de de Medicina Nuclear, Centro Médico ABC Campus Observatorio, Ciudad de México 01120, Mexico*

Correspondence should be addressed to Guillermina Ferro-Flores; ferro_flores@yahoo.com.mx

Received 20 July 2018; Accepted 8 October 2018; Published 11 November 2018

Guest Editor: Elena Bonanno

SPECT/CT images in patients have demonstrated the ability of [^{99m}Tc]Tc-EDDA/HYNIC-Lys(Nal)-Urea-Glu ([^{99m}Tc]Tc-iPSMA) to detect tumors and metastases of prostate cancer. Considering that theranostics combines the potential of therapeutic and diagnostic radionuclides in the same molecular probe, the aim of this research was to estimate the biokinetics and dosimetry of ^{177}Lu-DOTA-HYNIC-Lys(Nal)-Urea-Glu (^{177}Lu-iPSMA) in healthy subjects and analyze the response in patients receiving ^{177}Lu-iPSMA therapeutic doses. ^{177}Lu-iPSMA was obtained from lyophilized formulations with radiochemical purities >98%. Whole-body images from five healthy subjects were acquired at 20 min, 6, 24, 48, and 120 h after ^{177}Lu-iPSMA administration (185 MBq). The image sequence was used to extrapolate the ^{177}Lu-iPSMA time-activity curves of each organ to adjust the biokinetic model and calculate the total number of disintegrations (N) that occurred in the source regions. N data were the input for the OLINDA/EXM code to calculate internal radiation doses. Ten patients (median age: 68 y; range 58–86 y) received from 1 to 4 cycles of ^{177}Lu-iPSMA (3.7 or 7.4 GBq) every 8–10 weeks. Response was evaluated using the ^{68}Ga-PSMA-ligand-PET/CT or ^{99m}Tc-iPSMA-SPECT/CT diagnostic images and serum PSA levels before and after ^{177}Lu-iPSMA treatment. The blood activity showed a half-life value of 1.1 h for the fast component ($T_{1/2}\alpha$ = ln2/0.614), 9.2 h for the first slow component ($T_{1/2}\beta$ = ln2/0.075), and 79.6 h for the second slow component ($T_{1/2}\gamma$ = ln2/0.008). The average absorbed doses were 0.23, 0.28, 0.88, and 1.17 Gy/GBq for the spleen, liver, kidney, and salivary glands. A total of 18 cycles were performed in 10 patients. A PSA decrease and some reduction of the radiotracer uptake (SUV) in tumor lesions occurred in 60% and 70% of the patients, respectively. ^{177}Lu-iPSMA obtained from kit formulations showed high tumor uptake with good response rates in patients. The results obtained in this study warrant further clinical studies to establish the optimal number of treatment cycles and for evaluating the effect of this therapeutic agent on survival of patients.

1. Introduction

Prostate-specific membrane antigen (PSMA) is a metallopeptidase overexpressed predominantly in prostate cancer (PCa) cells [1]. The therapeutic application of two different lutetium-177-labeled PSMA inhibitors ([^{177}Lu]Lu-PSMA-617 and [^{177}Lu]Lu-PSMA-I&T) has shown a decrease of >50% in the prostate antigen (PSA) levels and a significant

survival increase in 70% of patients with metastatic PCa [2–4]. However, before any radiotherapeutic treatment, the radiopharmaceutical uptake in tumors must be evaluated by nuclear imaging to confirm whether the treatment will be useful for the patient.

Because of their high sensitivity and specificity, several ^{68}Ga-PSMA inhibitors for PET/CT imaging of prostate cancer are currently used in clinical trials [5–7]. However, technetium-99m is still the most widely used radionuclide for diagnostic imaging. Recently, our group reported the preparation and biokinetics and dosimetry of [^{99m}Tc]Tc-EDDA/HYNIC-iPSMA ([^{99m}Tc]Tc-ethylenediamine-*N*,*N*′-diacetic acid (EDDA)/hydrazinonicotinyl(HYNIC)-Lys (Nal)-Urea-Glu) as a radiopharmaceutical with the ability to specifically detect PSMA expression in tumors of prostate cancer by SPECT/CT imaging [8–10].

Considering that theranostics combines the potential of therapeutic and diagnostic radionuclides in the same molecular probe, we have also reported the synthesis, preparation, and preclinical studies of the therapeutic radiopharmaceutical ^{177}Lu-DOTA-HYNIC-iPSMA [^{177}Lu-(1,4,7,10-tetraazacyclododecane-*N*,*N*′,*N*″,*N*‴-tetraacetic acid)-HYNIC-Lys(Nal)-Urea-Glu] in order to develop a new theranostic ^{99m}Tc/^{177}Lu pair, useful in prostate cancer (Figure 1) [11, 12].

The aim of this study was to estimate the biokinetics and dosimetry of ^{177}Lu-DOTA-HYNIC-iPSMA (^{177}Lu-iPSMA) in five healthy subjects and analyze the response in ten patients with histologically confirmed prostate cancer that received therapeutic doses of ^{177}Lu-iPSMA.

2. Materials and Methods

2.1. Reagents. The DOTA-HYNIC-iPSMA peptide conjugate (1,4,7,10-tetraazacyclododecane-*N*,*N*′,*N*″,*N*‴-tetraacetic acid-hydrazinonicotinyl-Lys(Nal)-Urea-Glu derivative, MW 1038 g/mol) was designed at ININ, and the synthesis was requested from Ontores Biotechnology Co., Ltd (Zhejiang, China), with a purity > 98% as analyzed by reversed-phase HPLC (RP-HPLC) and mass spectroscopy. Lutetium (^{177}Lu) chloride was obtained from ITG, Germany (EndolucinBeta 40 GBq/mL, in sterile 0.04 M HCl solution, noncarrier-added). All the other reagents were purchased from Sigma-Aldrich Chemical Co. and were used as received.

2.2. Preparation of ^{177}Lu-iPSMA. Lutetium-177-labeled iPSMA (^{177}Lu-iPSMA) was prepared from a multidose lyophilized formulation under aseptic conditions in a GMP-certified facility according to the method described by Luna-Gutierrez et al. [11]. For the radiochemical synthesis, the $^{177}LuCl_3$ vial (40 GBq/mL) was vented with a needle and 1.0–1.5 mL of the 1 M acetate buffer (pH 5.0) was added. The total volume was withdrawn using a sterile syringe and was afterwards employed for the reconstitution of the DOTA-HYNIC-iPSMA lyophilized kit. The reconstituted vial was heated in a dry bath at 95°C for 30 min. After cooling to room temperature, the vial was vented with a needle and the volume was taken up to 10 mL with 0.9% saline solution (Pisa, Mexico), using a sterile syringe. The dosing step was carried out directly in delivery syringes using a dosing GMP module (Musa, Comecer, Italy). In this way, ^{177}Lu-iPSMA was obtained from lyophilized formulations after reconstitution with sterile solutions of $^{177}LuCl_3$ without the need to perform further purification or sterilization processes and without the need of using commercially available radiochemical synthesizers. For the quality control, parameters such as color, appearance, pH, sterility, bacterial endotoxins, and radiochemical purity (reversed-phase HPLC) were evaluated in accordance with the Mexican Pharmacopoeia [11].

^{68}Ga was obtained from a ^{68}Ge/^{68}Ga generator (Isotope Technologies, Garching) and Glu-CO-Lys(Ahx)-HBED-CC (PSMA-11, GMP) from ABX advanced biomedical compounds. The synthesis of ^{68}Ga-PSMA-11 or ^{68}Ga-iPSMA (^{68}Ga-DOTA-HYNIC-iPSMA) was carried out on an iQS Ga-68 Fluidic Labeling Module (Isotope Technologies, Garching). The [^{99m}Tc]Tc-pertechnetate was obtained from a GETEC ^{99}Mo/^{99m}Tc generator (ININ-Mexico). [^{99m}Tc]Tc-EDDA/HYNIC-iPSMA ([^{99m}Tc]Tc-ethylenediamine-*N*,*N*′-diacetic acid (EDDA)/hydrazinonicotinyl(HYNIC)-Lys (Nal)-Urea-Glu) was prepared from a lyophilized formulation (ININ-Mexico) as previously reported [8].

2.3. Evaluation of Radiochemical Purity. Radiochemical purity analyses were performed by reversed-phase high-performance liquid chromatography (HPLC) with a Waters instrument running Empower software with both radioactivity and UV-photodiode array in-line detectors and a μBondapak C_{18} column (5 μm, 3.9 × 300 mm). A gradient using 0.1% TFA/water as solvent A and 0.1% TFA/acetonitrile as solvent B was used at a flow rate of 1 mL/min. The gradient began at 100% solvent A for 3 min, changed to 50% solvent A over 10 min and was maintained for 10 min, changed to 30% solvent A over 3 min and finally returned to 100% solvent A over 4 min. In this system, retention times for free $^{177}LuCl_3$ and ^{177}Lu-iPSMA were 3–4 min and 14–15 min, respectively. The same system was used for [^{99m}Tc]Tc-iPSMA (t_R = 13–14 min; t_R = 3–4 min for [^{99m}Tc]TcO_4Na) and ^{68}Ga-PSMA-11/^{68}Ga-iPSMA (t_R = 10–12 min; t_R = 3-4 min for $^{68}GaCl_3$) radiochemical purities (RPs) assessment in order to verify RP over 95%.

2.4. Healthy Subjects and Patients. Five healthy subjects (mean age ±SD, 47 ± 7 y; age range, 36–53 y; 5 men) were included. Prescreening consisted of a detailed review of medical history and a physical examination. Subjects with evidence of clinical disease or a history of organ-removal surgery were excluded. The mean (±SD) subject weight was 74 ± 8 kg (range, 64–82 kg). All subjects signed a consent form after receiving detailed information regarding the aims of the study and agreed to the collection of data that is necessary for a complete biokinetic study. The activity administered to healthy subjects was 185 MBq (from 3 to 5 μg of DOTA-HYNIC-iPSMA peptide).

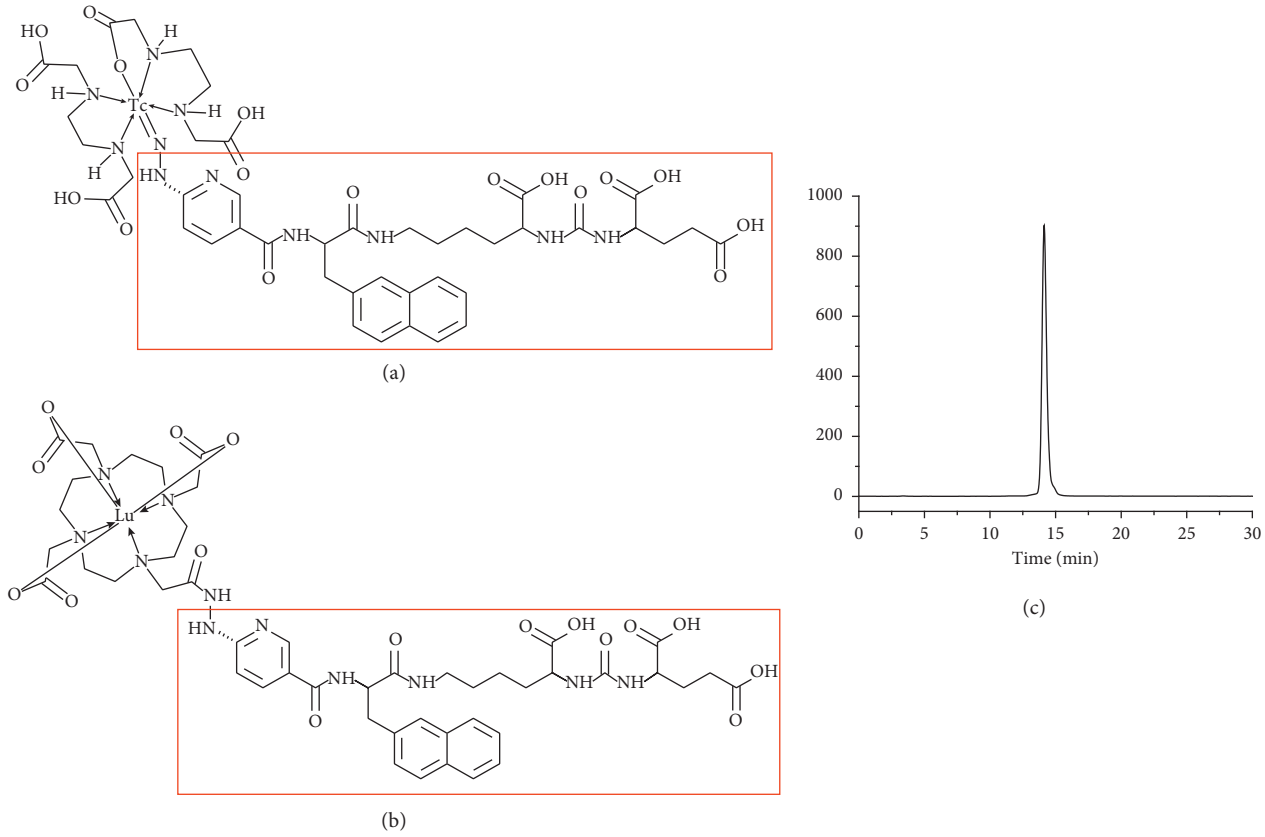

Figure 1: Schematic structure of the theranostic pair: (a) [^{99m}Tc]Tc-EDDA/HYNIC-iPSMA ([^{99m}Tc]Tc-iPSMA) and (b) ^{177}Lu-DOTA-HYNIC iPSMA (^{177}Lu-iPSMA). (c) Radio-HPLC analysis of ^{177}Lu-iPSMA obtained from a multidose lyophilized kit before injection to patients with high radiochemical purity (>99%).

Ten patients (median age: 68 y; range 58–86 y) with histologically confirmed prostate cancer were enrolled in this study and received from 1 to 4 cycles of ^{177}Lu-iPSMA (3.7 or 7.4 GBq, from 60 to 120 μg of DOTA-HYNIC-iPSMA peptide) every 8–10 weeks. The activity to be administered in each treatment was established according to the tumor volume estimated by the SPECT/CT or PET/CT diagnostic study. For example, patients with greater bone tumor load were initially treated with 3.7 GBq due to the higher probability of myelotoxicity, with gradual scaling. The criterion to determine the number of cycles to be administered was the biochemical and imaging progression. In Tables 1 and 2, the patient characteristics before ^{177}Lu-iPSMA treatments and the radiotracer used in each patient for evaluation of the therapy effect are shown. Response was evaluated using the ^{68}Ga-PSMA-11 PET/CT or ^{68}Ga-iPSMA PET/CT or [^{99m}Tc]Tc-iPSMA-SPECT/CT diagnostic images and serum PSA levels before and after ^{177}Lu-iPSMA treatment. Renal scintigraphy using [^{99m}Tc]Tc-MAG3 was performed in all patients. Additional renal laboratory parameters and blood counts were performed to rule out clinically relevant impairment of renal or hepatic function and bone marrow depression. Written informed consent was obtained from each patient. Immediately after radiopharmaceutical administration, healthy subjects and patients were hydrated with 500 mL of pure water and they voided the bladder before the image acquisition. The study was approved by the hospital's Medical Ethics Committee, taking into account the following aspects: (a) the ethical standards of the responsible committee on human experimentation (institutional and national) and with the Helsinki Declaration of 1975, as revised in 2008, (b) the GMP certificate issued by COFEPRIS (Federal Commission for Protection against Health Risks, the regulatory authority in Mexico) to ININ, (c) the clinical background of PSMA

Table 1: Patient characteristics before ^{177}Lu-iPSMA treatments.

Site of metastases	Patients (18 treatments)	
	N	%
Bone	6	60
Lymph nodes	10	100
Liver	4	40
Lung	1	10
Prior therapies		
Radical prostectomy	8	80
Radiation therapy (prostate region)	8	80
Docetaxel	7	70
Cabazitaxel, abiraterone, and/or enzalutamide	7	70
Radium-223	1	10
Radiation therapy to bone	2	20

Table 2: Description of the reported disease of patients and the radiotracer used in each case for evaluation of the response to ^{177}Lu-iPSMA therapy.

Patient no.	Age	Reported disease	Radiotracer
1	86	Prostate cancer, resistant to castration, with retroperitoneal, external, and common iliac bilateral chains lymph node metastases	^{68}Ga-iPSMA
2	72	Prostate cancer, resistant to castration, with bone, lungs, liver, and lymph node metastases; right nephrectomy and adrenalectomy with resection of the diaphragm by tumor infiltration	[^{99m}Tc]Tc-iPSMA
3	71	Prostate cancer, resistant to castration, with bone and lymph node metastases	[^{99m}Tc]Tc-iPSMA
4	61	Prostate cancer with lymph node metastasis	[^{99m}Tc]Tc-iPSMA
5	60	Prostate cancer, resistant to castration, diabetes mellitus type 2, chronic kidney disease, kidney transplant, with liver, retroperitoneal, and left iliac chain lymph nodes and vertebral T6 metastases	[^{99m}Tc]Tc-iPSMA
6	72	Prostate cancer, resistant to castration, with inguinal lymph nodes and bone metastases; kidney cancer with left nephrectomy; gastric cancer	^{68}Ga-PSMA-11
7	58	Prostate cancer, resistant to castration, with right sacrum bone metastasis; retroperitoneal, iliac bilateral chains, inguinal, and gluteus lymph node metastases, bladder and liver metastases (Ra-223 treatment)	^{68}Ga-PSMA-11
8	65	Prostate cancer with liver and lymph node metastases	^{68}Ga-PSMA-11
9	66	Prostate cancer, resistant to castration, with multiple bone metastases (radiotherapy treatment)	^{68}Ga-PSMA-11
10	74	Prostate cancer, resistant to castration, with multiple lymph node metastases (brachytherapy treatment)	^{68}Ga-iPSMA

inhibitors for imaging and therapy, (d) the techno-surveillance report of the [^{99m}Tc]Tc-EDDA/HYNIC-iPSMA and ^{177}Lu-DOTA-peptides that ININ distributes with the approval of COFEPRIS for clinical use, (e) the complete preclinical studies of ^{177}Lu-iPSMA and (f) the basis of microdosing studies.

2.5. Acquisition of Images. ^{177}Lu-iPSMA images were obtained to calculate the biokinetic and dosimetry parameters with a dual head gamma camera (Symbia TruePoint SPECT/CT, Siemens), equipped with medium energy general purpose collimators. The scan velocity was 12 cm/min. For all acquisitions, a matrix size of 256 × 1024 pixels was used and a symmetric 15% window was set at 208 keV. For scatter corrections, the dual-energy window method was used by simultaneous acquisition in a lower scatter window centered on 176 keV with 15% width [13]. Transmission factors for the chest and abdomen were calculated using the ratio of the count rates I/I_0 obtained with a 37 MBq ^{177}Lu-filled flood source with (I) and without (I_0) the patient in position, from which the regional attenuation of the body was calculated. In healthy subjects, whole-body anterior and posterior scintigraphy was performed at 20 min, 6, 24, 48, and 120 h after radiopharmaceutical administration.

In patients, whole-body planar scintigraphy ^{177}Lu-iPSMA images (anterior and posterior) were obtained at 24 h after radiopharmaceutical administration. ^{68}Ga-PSMA-11-PET/CT or ^{68}Ga-iPSMA-PET/CT images before (basal) and after ^{177}Lu-iPSMA therapy (40–50 d after therapy) were acquired in four patients and two patients, respectively. Studies were performed on an mCT Excel 20 PET/CT scanner (Siemens Medical Solutions). The acquisition parameters of the helical CT scan were 120 kVp, 180 mAs, and 5 mm slice thickness. After intravenous injection of ^{68}Ga-PSMA-11 or ^{68}Ga-iPSMA, whole-body emission scans were acquired at 60 min. The whole-body PET scans were obtained from the vertex to mid thighs, at 2–3 min per bed position in the 3-dimensional mode. PET images were reconstructed using a 2-dimensional ordered-subset expectation maximization algorithm. ROIs were drawn, and the maximum standardized uptake values (SUV_{max}) were calculated. [^{99m}Tc]Tc-EDDA/HYNIC-iPSMA SPECT/CT images before and after ^{177}Lu-iPSMA treatment (40–50 d after therapy) were obtained from four patients at 3 h posttracer injection. A 360-degree rotation with a non-circular orbit continuous technique, 128 × 128 matrix, window of 15% centered on 140 keV with scattering correction, 120 images of 10 seconds in all acquisitions, were used. CT images were acquired from the skull to the middle third of thighs, obtaining an attenuation correction map using low-dose CT parameters. Reconstruction of raw data was carried out using the iterative method by the order of sets and subsets (8 iterations/4 subsets) and a Butterworth filter (0.5 cut, order 5). ROIs were drawn, and the SUV_{max} were calculated.

2.6. ^{177}Lu-iPSMA Biokinetics. For scattering correction, the images obtained by the dual-energy window method were archived in DICOM (Digital imaging and Communication in Medicine) format and processed with the ImageJ Software (Image Processing and Analysis in Java, Version 1.51i). ROIs were drawn around source organs (heart, breast, lungs, kidneys, liver, spleen, intestine, bladder, salivary glands, lacrimal glands, and whole body) in each time frame. The same set of ROIs was used for all scans, and the counts in each ROI were corrected by attenuation using the transmission factors (I/I_0) experimentally calculated as described above, in agreement with the conjugate-view counting method for additional scattering correction as follows [9, 13]:

$$A = \frac{I}{I_0}\sqrt{I_A I_P}, \quad (1)$$

where A represents the compartment activity in counts and I_A/I_P are the anterior/posterior view counting rates, respectively. Counts were also corrected by physical decay and by the background correction factor, in accordance with the Buijs method [14].

Each organ activity was divided by the whole-body (WB) activity obtained from the first image acquired (100% of injected activity), in order to determine the fraction of the injected activity (IA) in each source organ as follows:

$$\%\mathrm{IA}_{\text{source organ}} = \frac{A_{\text{source organ}}}{A_{\text{WB at the first image acquisition}}} \times 100. \quad (2)$$

The image sequence was used to derive ^{177}Lu time-activity curves in each organ. As the heart does not overexpress PSMA, its activity was considered as having blood activity kinetics. The blood activity curve was derived from the heart activity by fitting the heart data to a function with three exponential terms. The OLINDA/EXM code allows the user to enter kinetic data for each source organ (% IA at different times) and fit it to one or more exponential terms [15]. The activity was integrated over time to calculate the total number of disintegrations (N) expressed per unit of initial activity in the source region (MBq·h/MBq). The ICRP 30 GI tract model included in the OLINDA/EXM code was used for the excretion model, assuming an activity fraction of 0.034–0.080 entering the small intestine, as images revealed that 5.9 ± 2.9% of the total activity was excreted into the intestine at 20 min after injection. The estimated bladder activity (% IA in urine) was input data for the OLINDA/EXM code. Total urine excretion at 24 h was estimated from the acquired images as follows:

$$\text{urine excretion} = \left(\frac{A_{\text{WB at 24 h, corrected by decay}}}{A_{\text{WB at the first image acquisition}}} \times 100\right) - (\%\text{hepatobiliary excretion}). \quad (3)$$

2.7. ^{177}Lu-iPSMA-Absorbed Dose Calculations. The absorbed dose to organs was evaluated according to the following equation as previously reported [9]:

$$\mathrm{D}_{\text{target}\leftarrow\text{source}} = \sum_{\text{sources}} \mathrm{N}_{\text{source}} \times \mathrm{DF}_{\text{target}\leftarrow\text{source}}, \quad (4)$$

where $\mathrm{D}_{\text{target}\leftarrow\text{source}}$ is the mean absorbed dose to a target organ from a source region, $\mathrm{N}_{\text{source}}$ represents the total number of nuclear transitions that occurred in the source region, and $\mathrm{DF}_{\text{target}\leftarrow\text{source}}$ is a dose factor that is specific for the isotope, source, and target configuration. In this study, the equivalent absorbed dose estimates were obtained by entering the experimental N values for all source organs into the OLINDA/EXM code [15], but the effective doses were calculated according to the ICRP 103, in which salivary and lacrimal glands are included. The mass and DF-values of the salivary and lacrimal glands were obtained according to Liu et al. [16].

3. Results and Discussion

The radiochemical purity of ^{177}Lu-iPSMA (Figure 1) obtained from multidose lyophilized kits was 99 ± 1%, as obtained by HPLC analyses without postlabeling purification. The average molar activity was 70 GBq/μmol before injection to patients.

None of the five healthy subjects reported adverse reactions such as nausea, vomiting, dyspnea, bronchospasm, decreased blood pressure, itching, flushing, hives, chills, coughing, bradycardia, muscle cramps, or dizziness after the radiopharmaceutical was administered. No significant change in hemoglobin and the blood cell count was observed after therapy in patients, and there was no evidence of nephrotoxicity (Figure 2). Patients 2, 5, and 6 had abnormal creatinine values before the treatment which did not change after therapy. The same behavior was observed with the GFR values, which were in the normal range (72–89 mL/min) before and after treatments except in patients with renal complications (patient 2, 5, and 6, GFR range of 58–62 mL/min). Three patients (30%) showed mild reversible xerostomia following treatment. Fatigue was a side effect in two patients (20%), and nausea was observed in one man treated with a ^{177}Lu-iPSMA therapeutic dose (10%) at 24 h. One patient reported complete pain relief (patient 6).

The ^{177}Lu-iPSMA blood activity was fitted to a triexponential function as follows as follows (Figure 3):

$$A(t) = 2.11e^{0.614t} + 0.88e^{0.075t} + 0.13e^{0.0081t}. \quad (5)$$

The half-life value was 1.1 h for the fast component ($T_{1/2}\alpha$ = ln2/0.614), 9.2 h for the first slow component ($T_{1/2}\beta$ = ln2/0.075), and 79.6 h for the second slow component ($T_{1/2}\gamma$ = ln2/0.008) (Figure 2). The activity was mainly accumulated in the kidneys, liver, and parathyroid, salivary, and lacrimal glands (Figure 4). Twenty minutes after radiopharmaceutical administration, the mean percentage of the injected activity in the kidneys was 17.58 ± 7.13% and after 24 h, it decreased to 7.01 ± 3.36%. Twenty-four hours after the administration of ^{177}Lu-iPSMA, the total activity excreted in urine was 63.99 ± 10.58%.

The radiation-absorbed doses for the main source organs are shown in Table 3. ^{177}Lu-iPSMA showed to have similar

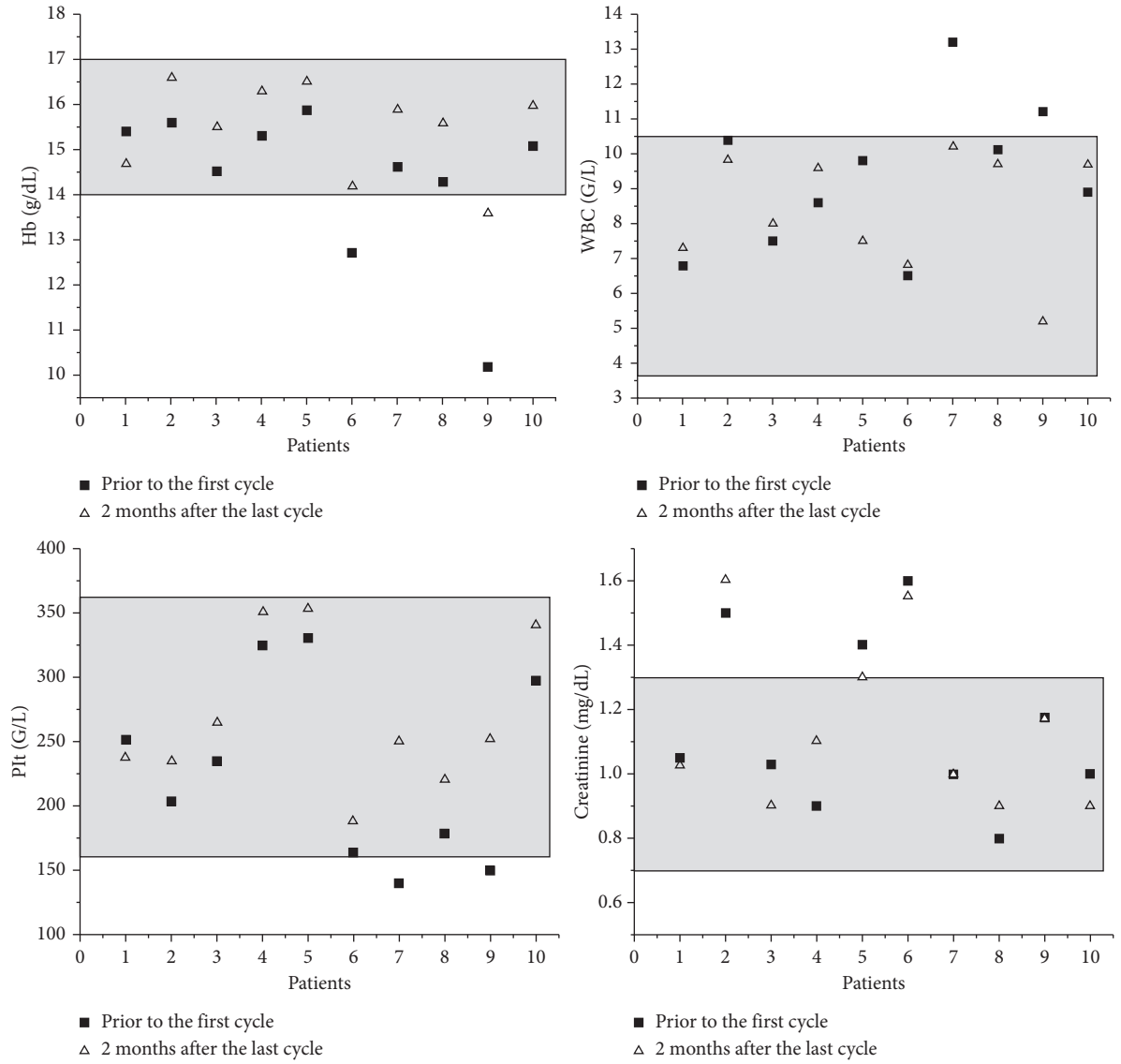

Figure 2: Hemoglobin levels, blood cell count, and creatinine values of patients before and after ^{177}Lu-iPSMA therapy.

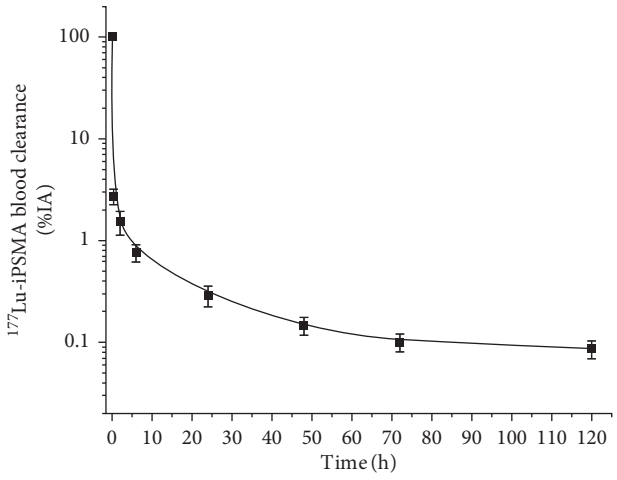

Figure 3: ^{177}Lu-iPSMA clearance from blood of healthy volunteers. The curve shows three different slopes with $T_{1/2}\alpha$ = 1.1 h, $T_{1/2}\beta$ = 9.2 h, and $T_{1/2}\gamma$ = 79.6 h.

pharmacokinetics, dosimetry, and therapeutic response compared to other ^{177}Lu-PSMA inhibitors previously informed [17, 18]. The mean radiation-absorbed doses of ^{177}Lu-iPSMA in the kidney (0.88 Gy/GBq) and liver (0.28 Gy/GBq) were slightly different from that reported for [^{177}Lu]Lu-PSMA-I&T (kidney = 0.75 Gy/GBq, liver = 0.12 Gy/GBq) and quite comparable with those of [^{177}Lu]Lu-PSMA-617 (kidney = 0.82 Gy/GBq, liver = 0.13 Gy/GBq) [17, 18]. Patient no. 1, who received 4 cycles of ^{177}Lu-iPSMA with a total activity of 18.5 GBq (Table 4), had the highest mean radiation dose of 16.28 Gy to the kidney, which is safe considering that the maximum tolerated dose or dose limit is 28 Gy (50% probability of developing severe late kidney damage within 5 y) [19]. Absorbed doses for lacrimal and salivary glands in patient 1 were 21.6 and 24.4 Gy, respectively, which have been stated as well tolerated by patients. For example, using external-beam radiation therapy, doses to glands below 26 Gy were reported safe [20].

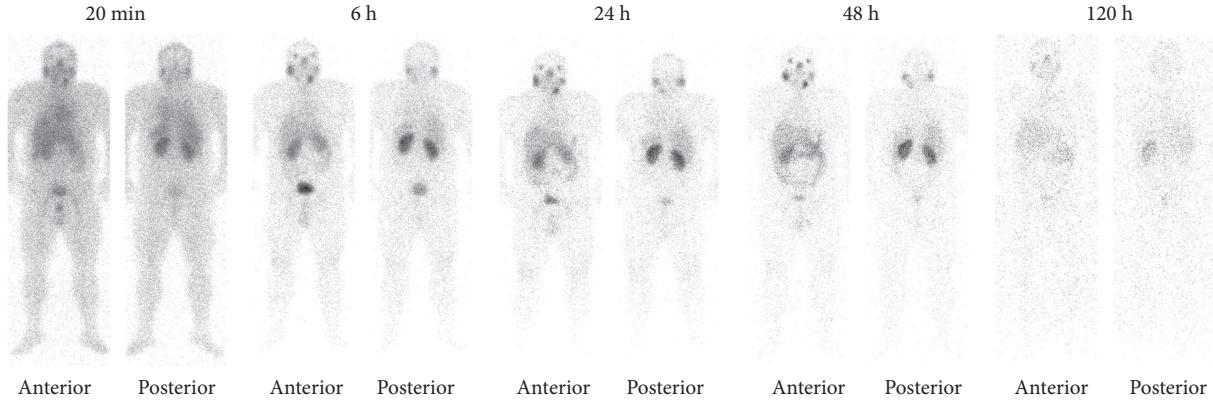

Figure 4: Anterior and posterior whole-body images of a healthy volunteer (man) at 20 min, 6, 24, 48, and 120 h after ^{177}Lu-iPSMA administration (185 MBq).

Table 3: Average total number of disintegrations (N) in source organs, organ-absorbed doses, and effective dose of ^{177}Lu-iPSMA, calculated from five healthy subjects (men).

Target organ	N (mean ± SD)	Organ doses (Gy/GBq)	
	(MBq·h/MBq)	Average	SD
Adrenals	—	0.030	0.007
Brain	—	0.024	0.005
Breasts	—	0.024	0.004
Gallbladder wall	—	0.032	0.006
LLI wall	—	0.041	0.011
Small intestine	0.300 ± 0.018	0.027	0.006
Stomach wall	—	0.027	0.006
ULI wall	—	0.044	0.010
Heart wall	—	0.049	0.005
Kidneys	2.953 ± 0.475	0.880	0.040
Liver	6.322 ± 0.352	0.280	0.090
Lungs	0.400 ± 0.098	0.030	0.010
Muscle	—	0.025	0.006
Ovaries	—	0.040	0.010
Pancreas	—	0.030	0.007
Red marrow	—	0.030	0.010
Osteogenic cells	—	0.077	0.017
Skin	—	0.024	0.004
Spleen	0.450 ± 0.036	0.232	0.070
Testes	—	0.025	0.006
Thymus	—	0.025	0.004
Thyroid	—	0.024	0.007
Salivary glands	0.225 ± 0.005	1.170	0.310
Lacrimal glands	0.041 ± 0.013	1.321	0.091
Urinary bladder wall	—	0.249	0.103
Urinary bladder	1.369 ± 0.441	—	—
Uterus	—	0.028	0.007
Remainder of the body	19.380 ± 1.550	—	—
Total body	—	0.040	0.021

All patients showed high ^{177}Lu-iPSMA uptake in the prostate cancer metastases (Figures 5 and 6) with an average tumor/background ratio of 6.3 ± 1.7 at 24 h. ^{177}Lu-iPSMA was able to target both soft tissue tumors and bone metastatic lesions of the prostate cancer (Figure 6). A total of 18 cycles were performed in 10 patients. A PSA decrease and some reduction of the radiotracer uptake in tumor lesions (SUV_{max}) occurred in 60% and 70% of the patients, respectively (4/10 patients with a PSA decrease ≥50% and 2/10 with a PSA decrease ≤42%) (Table 4). Baum et al. [4] found that 80% of all men (n = 56) treated with [^{177}Lu]Lu-PSMA-I&T had a PSA decrease. Therefore, differences with our preliminary study could be related with the total number of enrolled patients and the total cycles of ^{177}Lu-iPSMA therapies. Furthermore, Rahbar et al. [21] reported that a relevant number of patients treated with [^{177}Lu]Lu-PSMA-617 showed a delayed response, even if they did not respond to the first cycle of the therapy.

Three patients (30%) that showed a decrease in SUVs of soft tissue tumor lesions (visceral or lymph nodes) had a progressive disease mainly with an increase in bone metastases (Table 4, Figure 7). Bone metastases appeared to respond to treatment with ^{177}Lu-iPSMA less well than visceral or lymph nodal disease in agreement with previous clinical studies [22]. This fact could be related with the inability of ^{177}Lu-PSMA inhibitors to specifically target the homing process in the bone (bone microenvironment which promotes homing of a cancer cell to the bone) [23].

Decrease in PSA levels or SUV values were not related with previous therapeutic treatments. One patient (10%) had complete response (Figure 5).

Progressive disease despite ^{177}Lu-iPSMA treatment occurred in 30% of patients (Table 4). As others have reported, this can be related to the different density expression of the PSMA receptor in all cells. Heterogeneity of PSMA receptor activity within the tumor population may mean that some sites will not respond to treatment with ^{177}Lu-iPSMA, which will manifest as disease progression and a rising serum PSA level [22].

It is important to mention that, although the evaluation of ^{68}Ga-iPSMA for diagnostic images was not the aim of this research, results also evidenced the feasibility of using the ^{68}Ga-iPSMA/^{177}Lu-iPSMA pair in theranostic applications and that ^{68}Ga-PSMA-11 and ^{68}Ga-iPSMA tracers have comparable ability to target the PSMA protein. Nevertheless, a complete clinical comparative study between ^{68}Ga-PSMA-11 and ^{68}Ga-iPSMA is needed before generating any conclusion.

Several ^{68}Ga-PSMA inhibitors for PET/CT imaging in prostate carcinoma are being used in the clinical practice

Table 4: PSA levels in patients before and after treatment.

Patient no. (no. of cycles, total activity administered (GBq))	PSA levels (ng/mL) (SUV_{max} in soft tissue tumor lesions)	
	Before treatment	After treatment
1 (4, 18.5)	58 (73)	4 (1)
2 (2, 7.4)	53 (32)	55 (14)
3 (2, 7.4)	20 (33)	30 (17)
4 (1, 5.5)	31 (46)	18 (4)
5 (1, 7.4)	101 (38)	45 (16)
6 (2, 7.4)	46 (33)	25 (19)**
7 (2, 7.4)	217 (56)	322 (21)**
8 (2, 7.4)	34 (47)	11 (26)
9 (1, 7.4)	37 (101)	40 (33)**
10 (1, 3.7)	182 (79)	76 (28)

**Progressive disease: bone metastases.

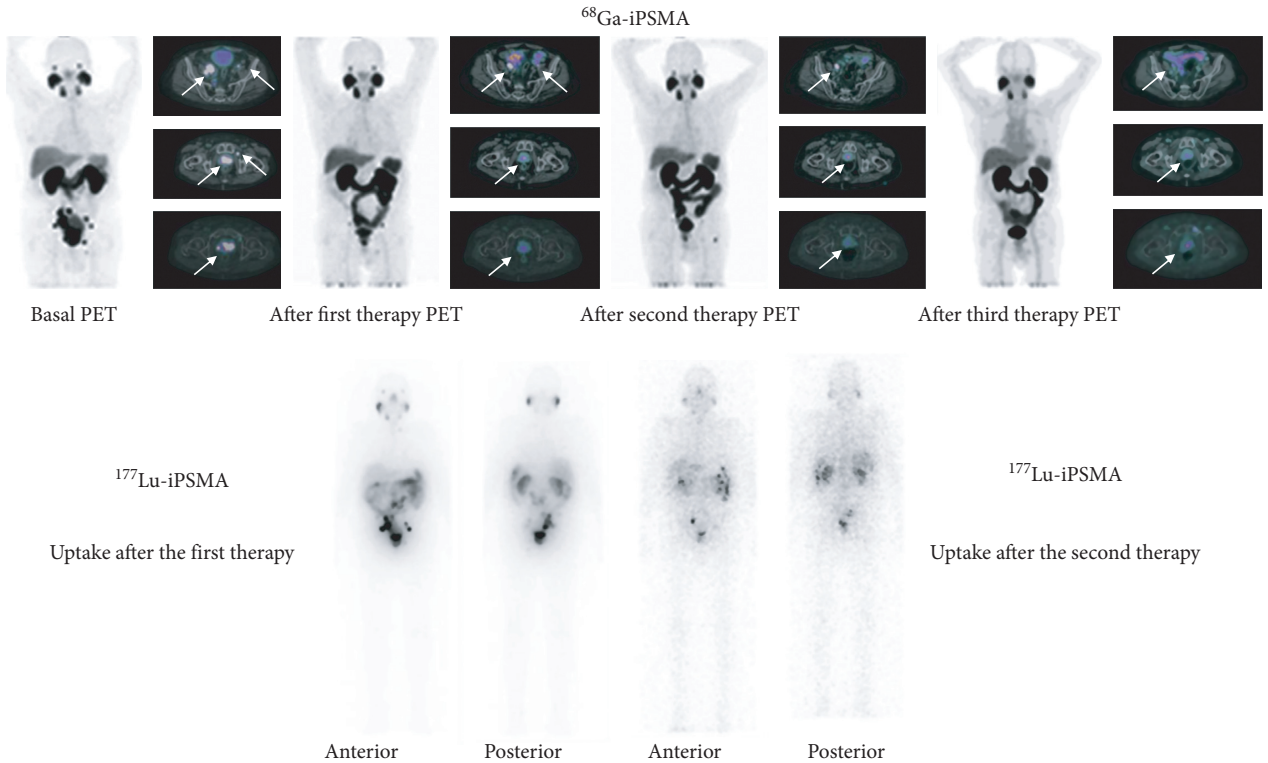

Figure 5: Treatment response evaluated using the ^{68}Ga-iPSMA-PET/CT diagnostic images (upper images) after three cycles with ^{177}Lu-iPSMA (bottom: images at 24 h after the first cycle and 6 d after the second cycle with ^{177}Lu-iPSMA) (patient 1, complete response).

[5–7]. However, a single elution from a ^{68}Ge/^{68}Ga generator is only sufficient to prepare ^{68}Ga-PSMA ligand for a few patients. This limits the number of studies that can be carried out in a single day. Technetium-99m can be produced with large activities from ^{99}Mo/^{99m}Tc generators to be used in the preparation of [^{99m}Tc]Tc-PSMA inhibitors (SPECT/CT images) for a multitude of patients every day [24]. Furthermore, there are fewer PET cameras installed worldwide than SPECT systems. That is the reason why we developed a lyophilized formulation for the preparation of [^{99m}Tc]Tc-EDDA/HYNIC-iPSMA, in which hydrazinonicotinamide (HYNIC) was proposed to act as a critical chemical group in the increase of the lipophilicity of the molecule for the coupling to hydrophobic sites of PSMA [10]. The new ^{177}Lu-DOTA-HYNIC-iPSMA (^{177}Lu-iPSMA) therapeutic radiopharmaceutical can potentially work as the theranostic pair of the [^{99m}Tc]Tc-EDDA/HYNIC-iPSMA ([^{99m}Tc]Tc-iPSMA) diagnostic agent previously reported [8, 9].

PSMA activity in tumor cells is measured by assessing the SUV values with ^{68}Ga-PSMA-11, ^{68}Ga-PSMA-617, or ^{68}Ga-PSMA-I&T PET/CT before ^{177}Lu-PSMA inhibitor therapies. The use of [^{99m}Tc]Tc-iPSMA/^{177}Lu-iPSMA theranostic pair (similar active molecular sequence) could be useful to establish cutoffs of SUVs with [^{99m}Tc]Tc-iPSMA below which ^{177}Lu-iPSMA therapy may not be effective.

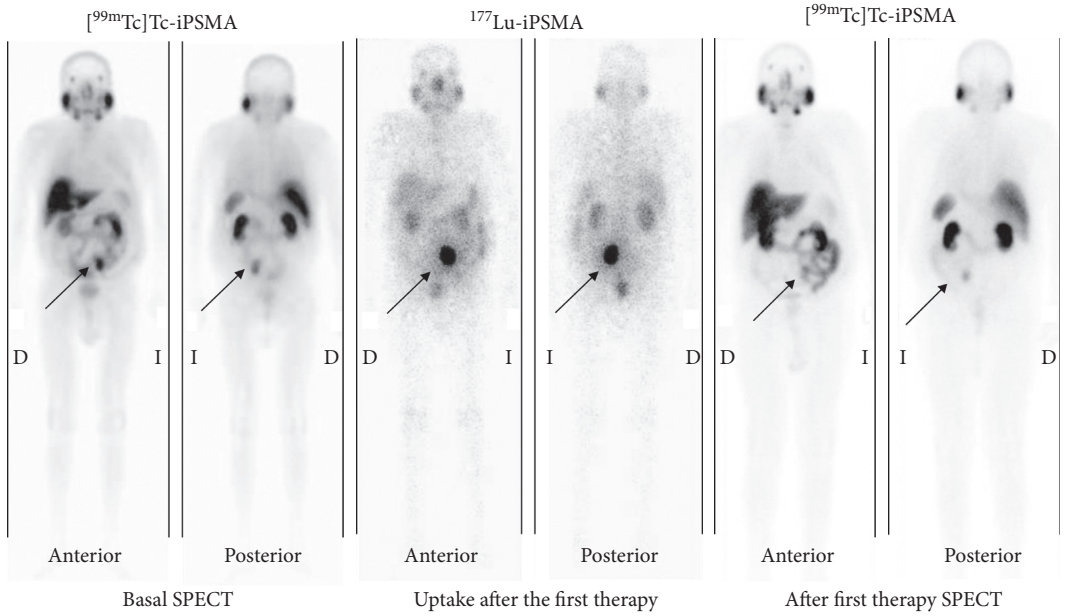

Figure 6: Treatment response evaluated using the [^{99m}Tc]Tc-iPSMA-SPECT diagnostic images (right and left, anterior and posterior images) after the therapy with ^{177}Lu-iPSMA (middle: anterior and posterior images at 24 h after the first cycle with ^{177}Lu-iPSMA) (patient 4, partial response).

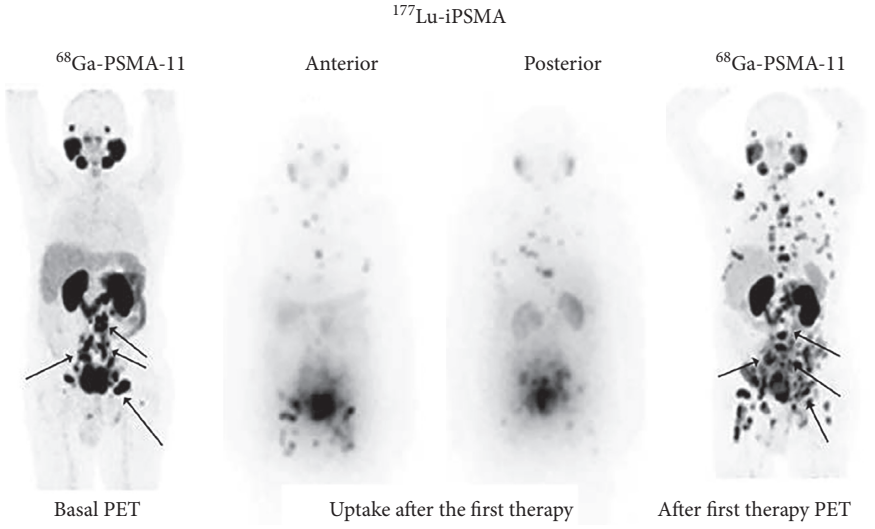

Figure 7: Treatment response evaluated using the ^{68}Ga-PSMA-11-PET/CT diagnostic images (right and left anterior images) after the therapy with ^{177}Lu-iPSMA (middle: anterior and posterior images at 24 h after the first cycle with ^{177}Lu-iPSMA) (patient 7, partial response in soft tissue lesions but progressive disease in bone).

Although ^{177}Lu-iPSMA obtained from kit formulations showed high tumor uptake with good response rates in patients, further clinical studies in randomized trials are necessary for evaluating the effect of this therapeutic agent on the survival of patients.

4. Conclusions

This preliminary study suggests that radioligand therapy with ^{177}Lu-iPSMA is safe, well-tolerated, and has a considerable effect on PSA levels in patients with advanced prostate cancer. Further studies are needed to evaluate response and toxicity after several therapy cycles and to determine the optimal number of cycles, as well as to assess the effect of this therapeutic agent on the survival of patients.

Data Availability

The data used to support the findings of this study are included within the article.

Conflicts of Interest

The authors declare that there are no conflicts of interest regarding the publication of this paper.

Acknowledgments

This study was carried as part of the activities of the "Laboratorio Nacional de Investigación y Desarrollo de Radiofármacos, CONACyT, Mexico." This study was supported by the Mexican National Council of Science and Technology, CONACyT (Grant no. 242443).

References

[1] A. K. Rajasekaran, G. Anilkumar, and J. J. Christiansen, "Is prostate-specific membrane antigen a multifunctional protein?," *American Journal of Physiology-Cell Physiology*, vol. 288, no. 5, pp. C975–C981, 2005.

[2] K. Rahbar, M. Schmidt, A. Heinzel et al., "Response and tolerability of a single dose of ^{177}Lu-PSMA-617 in patients with metastatic castration-resistant prostate cancer: a multicenter retrospective analysis," *Journal of Nuclear Medicine*, vol. 57, no. 9, pp. 1334–1338, 2016.

[3] K. Rahbar, H. Ahmadzadehfar, C. Kratochwil et al., "German multicenter study investigating ^{177}Lu-PSMA-617 radioligand therapy in advanced prostate cancer patients," *Journal of Nuclear Medicine*, vol. 58, no. 1, pp. 85–90, 2017.

[4] R. P. Baum, H. R. Kulkarni, C. Schuchardt et al., "177Lu-labeled prostate-specific membrane antigen radioligand therapy of metastatic castration-resistant prostate cancer: safety and efficacy," *Journal of Nuclear Medicine*, vol. 57, no. 7, pp. 1006–1013, 2016.

[5] M. Eder, O. Neels, M. Müller et al., "Novel preclinical and radiopharmaceutical aspects of [68Ga] Ga-PSMA-HBED-CC: a new PET tracer for imaging of prostate cancer," *Pharmaceuticals*, vol. 7, no. 7, pp. 779–96, 2014.

[6] M. Weineisen, M. Schottelius, J. Simecek et al., "68Ga-and 177Lu-labeled PSMA I and T: optimization of a PSMA-targeted theranostic concept and first proof-of-concept human studies," *Journal of Nuclear Medicine*, vol. 56, no. 8, pp. 1169–76, 2015.

[7] A. Afshar-Oromieh, U. Haberkorn, H. Schlemmer et al., "Comparison of PET/CT and PET/MRI hybrid systems using a 68Ga-labelled PSMA ligand for the diagnosis of recurrent prostate cancer: initial experience," *European Journal of Nuclear Medicine and Molecular Imaging*, vol. 41, no. 5, pp. 887–97, 2014.

[8] G. Ferro-Flores, M. Luna-Gutiérrez, B. Ocampo-Garcia et al., "Clinical translation of a PSMA inhibitor for ^{99m}Tc-based SPECT," *Nuclear Medicine and Biology*, vol. 48, pp. 36–44, 2017.

[9] C. Santos-Cuevas, J. Davanzo, G. Ferro-Flores et al., "^{99m}Tc-labeled PSMA inhibitor: biokinetics and radiation dosimetry in healthy subjects and imaging of prostate cancer tumors in patients," *Nuclear Medicine and Biology*, vol. 52, pp. 1–6, 2017.

[10] G. Ferro-Flores, B. Ocampo-Garcia, C. Santos-Cuevas et al., "^{99m}Tc-EDDA/HYNIC-iPSMA as a radiopharmaceutical for detecting the overexpression of prostate-specific membrane antigen," Patent Cooperation Treaty Application. Patent No. WO2017222362, 2017.

[11] M. Luna-Gutierrez, T. Jimenez-Hernandez, L. Serrano-Espinoza et al., "Freeze-dried multi-dose kits for the fast preparation of ^{177}Lu-Tyr^3-octreotide and ^{177}Lu-PSMA (inhibitor) under GMP conditions," *Journal of Radioanalytical and Nuclear Chemistry*, vol. 314, no. 3, pp. 2181–2188, 2017.

[12] T. Jimenez-Hernandez, G. Ferro-Flores, B. Ocampo-Garcia et al., "^{177}Lu-DOTA-HYNIC-Lys(Nal)-Urea-Glu: synthesis and in vitro and in vivo assessment to target the prostate-specific membrane antigen," *Journal of Radioanalytical and Nuclear Chemistry*, 2018.

[13] J. A. Siegel, S. R. Thomas, J. B. Stubbs et al., "MIRD pamphlet no. 16: techniques for quantitative radiopharmaceutical biodistribution data acquisition and analysis for use in human radiation dose estimates," *Journal of Nuclear Medicine*, vol. 40, no. 2, pp. 37S–61S, 1999.

[14] W. C. Buijs, J. A. Siegel, O. C. Boerman et al., "Absolute organ activity estimated by five different methods of background correction," *Journal of Nuclear Medicine*, vol. 39, no. 12, pp. 2167–2172, 1998.

[15] M. G. Stabin, R. B. Sparks, and E. Crowe, "OLINDA/EXM: the second-generation personal computer software for internal dose assessment in nuclear medicine," *Journal of Nuclear Medicine*, vol. 46, no. 6, pp. 1023–1027, 2005.

[16] B. Liu, R. Huang, A. Kuang et al., "Iodine kinetics and dosimetry in the salivary glands during repeated courses of radioiodine therapy for thyroid cancer," *Medical Physics*, vol. 38, no. 10, pp. 5412–5419, 2011.

[17] A. Afshar-Oromieh, H. Hetzheim, C. Kratochwil et al., "The theranostic PSMA ligand PSMA-617 in the diagnosis of prostate cancer by PET/CT: biodistribution in humans, radiation dosimetry, and first evaluation of tumor lesions," *Journal of Nuclear Medicine*, vol. 56, no. 11, pp. 1697–1705, 2015.

[18] S. Okamoto, A. Thieme, J. Allmann et al., "Radiation dosimetry for 177Lu-PSMA-I and T in metastatic castration-resistant prostate cancer: absorbed dose in normal organs and tumor lesions," *Journal of Nuclear Medicine*, vol. 58, no. 3, pp. 445–450, 2017.

[19] B. Emami, J. Lyman, A. Brown et al., "Three-dimensional photon treatment planning report of the collaborative working group on the evaluation of treatment planning for external photon beam radiotherapy tolerance of normal tissue to therapeutic irradiation," *International Journal of Radiation Oncology∗Biology∗Physics*, vol. 21, no. 1, pp. 109–122, 1991.

[20] J. Hey, J. Setz, R. Gerlach et al., "Parotid gland-recovery after radiotherapy in the head and neck region: 36 months follow-up of a prospective clinical study," *Radiation Oncology*, vol. 6, no. 1, p. 125, 2011.

[21] K. Rahbar, M. Bogeman, A. Yordanova et al., "Delayed response after repeated 177Lu-PSMA-617 radioligand therapy in patients with metastatic castration resistant prostate cancer," *European Journal of Nuclear Medicine and Molecular Imaging*, vol. 45, no. 2, pp. 243–246, 2018.

[22] L. Emmett, K. Willowson, J. Violet et al., "Lutetium177 PSMA radionuclide therapy for men with prostate cancer: a review of the current literature and discussion of practical aspects of therapy," *Journal of Medical Radiation Sciences*, vol. 64, no. 1, pp. 52–60, 2017.

[23] A. Mishra, Y. Shiozawa, K. J. Pienta et al., "Homing of cancer cells to the bone," *Cancer Microenvironment*, vol. 4, no. 3, pp. 221–235, 2011.

[24] I. O. Lawa, A. O. Ankrah, N. P. Mokgoro et al., "Diagnostic sensitivity of Tc-99m HYNIC-PSMA SPECT/CT in prostate carcinoma: a comparative analysis with Ga-68 PSMA PET/CT," *Prostate*, vol. 77, no. 11, pp. 1205–1212, 2017.

Hindawi
Contrast Media & Molecular Imaging
Volume 2018, Article ID 5693058, 10 pages
https://doi.org/10.1155/2018/5693058

Research Article

Towards More Structure: Comparing TNM Staging Completeness and Processing Time of Text-Based Reports versus Fully Segmented and Annotated PET/CT Data of Non-Small-Cell Lung Cancer

Raphael Sexauer,[1] Thomas Weikert,[1] Kevin Mader,[1,2] Andreas Wicki,[3] Sabine Schädelin,[4] Bram Stieltjes,[1] Jens Bremerich,[1] Gregor Sommer,[1] and Alexander W. Sauter[1]

[1]*University Hospital Basel, University of Basel, Department of Radiology, Petersgraben 4, 4031 Basel, Switzerland*
[2]*4Quant, Technoparkstrasse 1, 8005 Zurich, Switzerland*
[3]*University Hospital Basel, University of Basel, Department of Oncology, Spitalstrasse 21, 4031 Basel, Switzerland*
[4]*University Hospital Basel, University of Basel, Clinical Trial Unit, Department of Clinical Research, Spitalstrasse 12, 4056 Basel, Switzerland*

Correspondence should be addressed to Alexander W. Sauter; alexander.sauter@usb.ch

Received 30 May 2018; Revised 10 September 2018; Accepted 26 September 2018; Published 1 November 2018

Guest Editor: Nicola Toschi

Results of PET/CT examinations are communicated as text-based reports which are frequently not fully structured. Incomplete or missing staging information can be a significant source of staging and treatment errors. We compared standard text-based reports to a manual full 3D-segmentation-based approach with respect to TNM completeness and processing time. TNM information was extracted retrospectively from 395 reports. Moreover, the RIS time stamps of these reports were analyzed. 2995 lesions using a set of 41 classification labels (TNM features + location) were manually segmented on the corresponding image data. Information content and processing time of reports and segmentations were compared using descriptive statistics and modelling. The TNM/UICC stage was mentioned explicitly in only 6% ($n = 22$) of the text-based reports. In 22% ($n = 86$), information was incomplete, most frequently affecting T stage (19%, $n = 74$), followed by N stage (6%, $n = 22$) and M stage (2%, $n = 9$). Full NSCLC-lesion segmentation required a median time of 13.3 min, while the median of the shortest estimator of the text-based reporting time ($R1$) was 18.1 min ($p = 0.01$). Tumor stage (UICC I/II: 5.2 min, UICC III/IV: 20.3 min, $p < 0.001$), lesion size ($p < 0.001$), and lesion count ($n = 1$: 4.4 min, $n = 12$: 37.2 min, $p < 0.001$) correlated significantly with the segmentation time, but not with the estimators of text-based reporting time. Numerous text-based reports are lacking staging information. A segmentation-based reporting approach tailored to the staging task improves report quality with manageable processing time and helps to avoid erroneous therapy decisions based on incomplete reports. Furthermore, segmented data may be used for multimedia enhancement and automatization.

1. Introduction

Non-small-cell lung cancer (NSCLC) is a common malignant tumor and the leading cause of cancer-related death worldwide [1]. NSCLC is staged according to the American Joint Committee on Cancer (AJCC) and the Union for International Cancer Control (UICC) manuals that implement current medical knowledge to optimize patient survival [2]. 18F-fluorodeoxyglucose (FDG) PET/CT is currently considered the standard imaging procedure for noninvasive staging of NSCLC [3].

Accurate image-based staging is key for further diagnostic workup and therapy management. However, the discordance between preoperative staging using PET/CT

and surgical pathology is considerable: according to Cerfolio and Bryant, approximately 32% of patients are preoperatively understaged [4]. Furthermore, patients with predicted stage IA have a pathological confirmation of this stage in only 65% [5]. Sources of misclassification may be biological and technical limitations [6], but the process chain from image acquisition, interpretation, and reporting may be error-prone as well [7]. This has not yet been quantified in the context of NSCLC staging. Such misclassification might be reduced by introduction of more structured text reports [8].

Next to the discordance as shortcoming of the current reading process, it can be argued that this process does not extract all potentially relevant information from imaging data. Despite being only partially reflected in the current staging system, factors like tumor burden are of great prognostic relevance for patients with NSCLC. Oh et al. have shown that, in patients with brain metastases, the overall survival is inversely correlated with the volume of all metastases [9]. Moreover, the number of positive lymph nodes has been identified as an independent prognostic factor of survival in patients with stage N1 disease. Furthermore, a recent study by He et al. pointed out that advanced NSCLC can be further divided into 3 prognostic subgroups: according to the genotype, number of metastatic organ sites, and metastasis lesions [10]. Such detailed information is neither included in regular text-based reports nor covered by structured reporting tools. Contrarily, new applications such as multimedia enhancement and image segmentation can capture this information [11]. However, in the light of health-care cost savings, personnel shortages, and subsequently decreasing available reporting time [12], investment into such new approaches requires careful consideration.

The aim of this study was to quantify the amount of TNM information missing in conventional text-based PET/CT reports for staging of NSCLC, to outline an implementation for structured, multimedia-enhanced segmentation-based reporting of imaging findings in NSCLC, and to compare this approach to conventional, text-based reporting in terms of staging accuracy and processing time.

2. Materials and Methods

2.1. Patient Population. The local ethics committee approved this retrospective, observational study. All work was conducted in accordance with the Declaration of Helsinki (1964).

From 1327 FDG-PET/CTs examinations that were performed with the ICD-10 diagnosis code C34 between 01/2008 and 12/2016, 395 were selected according to the inclusion criteria "histologically proven NSCLC" and "primary staging situation." Exclusion criteria are listed in Figure 1.

2.2. Imaging Protocol and Reporting. PET/CT examinations were performed on an integrated PET/CT system with 16-slice CT (Discovery STE, GE Healthcare, Chalfont St Giles, UK) from 01/2008 to 11/2015 and on a PET/CT with 128-slice CT (Biograph mCT-X RT Pro Edition, Siemens Healthineers, Erlangen, Germany) from 12/2015 to 12/2016. Before tracer injection, patients were fasting for at least 6 h. Scans were obtained 1 h after intravenous injection of 5 MBq FDG/kg body weight at glycaemic levels below 10 mmol/L. All text-based reports were created by a resident in nuclear medicine in daily clinical practice using electronic reports with findings structured by anatomic regions [13] and were reviewed and signed by a board-certified radiologist and a board nuclear medicine physician in consensus.

2.3. Report-Based TNM Extraction. A dual-board-certified radiologist and nuclear medicine physician (G.S.) interpreted and extracted the TNM stage by analyzing the text-based reports for T (1–4), N (0–3), and M (0-1) descriptors or other text information that are stage defining without access to other clinical information or PET/CT images. It was also recorded whether the TNM or UICC stage was mentioned in the report explicitly. The descriptor was reported as missing when neither the TNM descriptor nor equivalent stage-defining information such as tumor size was found. From the extracted TNM, we derived the UICC (7th edition) stage.

2.4. TNM Annotation and Image Segmentation. For each patient, the PET/CT image dataset was loaded to a 3D Slicer-based segmentation software (version 4.6.2, BSD-style open source license, Slicer Python Interactor 2.7.11, http://www.slicer.org, Boston, USA) [14]. This software was modified in order to support direct-structured annotation using a set of labels that represent predefined features of lesions according to the TNM classification (7th edition) (Table 1). More detailed information about the subcategories can be found in the supplementary material (Tables S1–S3). Annotation and volumetric image segmentation with reference to the report was performed manually in random order by a dual-board-certified radiologist and nuclear medicine physician (A.S., reader 1, $n = 168$) with 9 years' experience in PET/CT reading as well as a supervised radiology resident with 2 years of professional experience (T.W., reader 2, $n = 227$). Each lesion was segmented as a 3D volume defined by multiple 2D regions of interest (ROIs) that were drawn on contiguous transversal slices of the CT component of the dataset. Fused PET information was used in addition whenever the boundaries of a lesion were not clearly definable on CT.

Output files were saved as JavaScript Object Notation (JSON) files, including time measurement registries and annotations (3007 lesions in total). From these, TNM and UICC were automatically derived.

2.5. Data Analysis. For comparison, we focused on TNM/UICC stage as qualitative and on time as quantitative measures.

2.6. TNM/UICC. The TNM information extracted from the text-based reports was analyzed for the frequency of missing information using Excel 2010 (14.0, Microsoft Corporation, Redmond, USA).

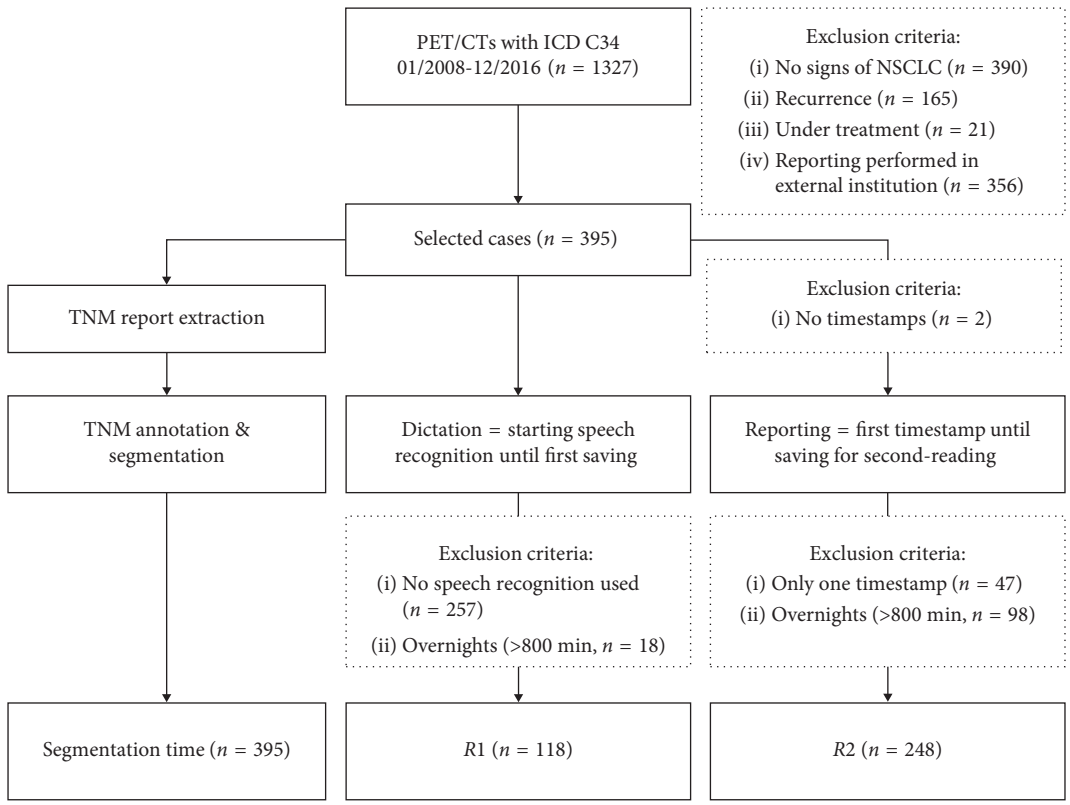

Figure 1: Study flowchart. 395 (30%) NSCLC patients that underwent PET/CT for primary staging were selected. These cases were included for both TNM extraction and segmentation.

Table 1: Description of label sets. The specific T-label stage is followed by a morphological descriptor that is stage defining. The N-label is defined by stage (first) and region (second) according to the IASLC lymph node map [35]. The M-label is defined by M stage and metastasis location. Additional findings that are non-NSCLC-related: T_benign referred to a benign lesion, T_other is another primary tumor, N_inflammation is an inflammatory/reactive lymph node, N_other is a nodal metastasis from another primary tumor.

T descriptor	N descriptor	M descriptor	Additional findings
T1	N1_10-11i	M1a_contralat	T_benign
T2	N1_12-15i	M1a_pleura	T_other
T2_main_bronchus	N2_2i	M1b_adrenal	N_inflammation
T2_visc_pleura	N2_3	M1b_brain	N_other
T2_obstr_lobe	N2_4i	M1b_liver	
T3_Inv_chest_wall	N2_5i	M1b_bone	
T3_main_bronchus	N2_6	M1b_node	
T3_obstr_lung	N2_7	M1b_other	
T3_nodule_same_lobe	N2_8i		
	N2_9		
T4_inv_mediastinum	N3_1		
	N3_2c		
	N3_4c		
	N3_5c		
T4_nodule_diff_lobe	N3_8c		
	N3_9c		
	N3_10-11c		
	N3_12-15c		

2.7. Estimators of Text-Based Reporting Time. The RIS timestamps were recorded since 05/2010 and registered in 393 of 395 cases. Since reporting time cannot be derived directly from RIS time entries, we used three timestamps for estimation: starting speech recognition, first saving, and saving for second reading. The consistency between RIS time entries and real-time was confirmed by testing 5 sample reports.

As a lower estimator of the text-based reporting time, we defined the time between starting speech recognition and

first saving as $R1$. Cases in which no speech recognition was used ($n = 257$) and registries >800 min (= overnight, $n = 18$) were excluded.

As an upper estimator of the text-based reporting time, we defined the time between the start of speech recognition or first saving until the saving for second reading as $R2$. Cases without speech recognition which were only saved once ($n = 47$) and registries >800 min (= overnight, $n = 98$) were excluded.

To evaluate if these estimators are representative, we used all oncological PET/CTs from 05/2010 to 01/2018 ($n = 14239$) (Table S4). A model based on expectation-maximization (EM) algorithm [15] was applied for outlier detection and simulation of lower ($R1$) and upper ($R2$) boundaries for verification. Using a Gaussian mixture model, we identified registries >800 min as outliers. Then, we developed a mathematical simulation using *R* (3.4.3, R Core Team, GNU GPL//RStudio, 1.1.414, RStudio Inc., Boston, USA) to differentiate interruptions from real reporting time ($R1$ and $R2$). This model was used to test the upper ($R2$) and lower estimators ($R1$). Further information including the *R* code can be found in Supplementary Materials modelling for reporting time estimation.

2.8. Segmentation Time. Segmentation time per lesion was extracted from the JSON file. 99.6% (2995/3007) lesions were segmented in <175 min. 12 lesions segmented in >800 min were excluded as outliers. Registries were analyzed regarding reader, lesion count, TNM, and UICC. Statistically significant impact factors of segmentation time were tested on RIS time registries for comparison.

2.9. Statistical Analysis. For descriptive statistics, median, arithmetic mean, and median test were used. For statistical analysis of segmentation, we pooled the data from readers 1 and 2. For outlier detection, we utilized mixture modelling with maximum likelihood estimation for RIS time registries. Spearman's rank correlation (r_s) coefficient was used for ordinal (e.g., UICC with time) and Pearson's correlation coefficient (r) for interval-scaled data (e.g., lesion count) to evaluate correlation. For linear models, we used ANOVA (analysis of variance; R^2, F) to show significance. To evaluate multifactorial impact, we used automatic linear modelling in SPSS (IBM Statistics 22.0.0.0, IBM Corporation, New York, USA). To include impact factors, we used a 95% confidence level and Akaike information criterion (AIC). We used the Wilcoxon signed-rank test to compare two related samples such as dictation and segmentation time of the same patient. For differences in distribution, we used Mann–Whitney U test (U) for independent samples like reader dependency or incomplete versus complete reports and Kruskal–Wallis if there were more than two variables. To test normal distribution, Kolmogorov–Smirnov was used. The t-test was used to determine significant differences in normal distributed samples. $P < 0.05$ was set as the level for statistical significance.

3. Results

Our NSCLC study population ($n = 395$) comprised 28% female and 72% male patients with ages between 38 and 97 years (71.7 ± 10.5 years). An example of the annotation and segmentation process of NSCLC lesions is shown in Figure 2 for a 71-year-old male patient case suffering from T4 N3 M1 squamous cell carcinoma. The distribution of the T/N/M stages according to the text-based reports and segmentations is presented in Figure 3. Table 2 gives an overview of descriptive time statistics for both segmentation and text-based reporting.

3.1. Completeness of TNM Information in Text-Based Reports. Due to lack of information, TNM extraction was not possible for 86 out of 395 text-based reports (22%). Of these, the T stage was most frequently affected ($n = 74$, 19%) as shown in Figure 3. Stage identification information was missing in 6% for the N ($n = 22$) and in 2% ($n = 9$) for the M descriptor. In four cases (1%), TNM information was missing completely. An explicit mention of the absence of metastasis was present in 20% for nodal ($n = 80$) and in 32% ($n = 126$) for distant metastasis. A statement on the specific TNM or UICC stage was made in only 6% ($n = 22$) of the text-based reports.

3.2. Analysis of Text-Based Reporting Time. The reporting time of the extracted RIS reports was estimated from $R1$ as the lower benchmark and $R2$ as the upper benchmark. The median total time was 18.1 min for $R1$ ($n = 118$) and 151.6 min for $R2$ ($n = 248$) (Table 2). To assess the general applicability of this approach, a simulation was done based on a larger number of non-disease-specific PET/CT examinations performed between 05/2010 and 01/2018 (Table S4). Here, a median of 26.6 min ($n = 3700$) for $R1$ as the lower benchmark and 146.1 min for $R2$ ($n = 7190$) as the upper benchmark were found (Table 2). There was no significant difference between the sampled and modeled $R1$s ($F = 10.34$, $p = 0.603$) but between the sampled and modeled $R2$s ($F = 25.918$, $p = 0.010$). UICC stage and lesion count were neither correlated with $R1$ (UICC: $r_s = 0.002$, $p = 0.986$; lesion count: $r = -0.042$, $p = 0.652$) nor with $R2$ (UICC: $r_s = 0.031$, $p = 0.649$; lesion count: $r = 0.119$, $p = 0.061$) (Figure 4). Those text-based reports where report-based TNM extraction was possible due to sufficient information (78%) took longer ($R1$: 19.5 min) than text-based reports with no or incomplete TNM information ($R1$: 14.8 min).

3.3. Analysis of Segmentation Time. In contrast to the text-based reports, TNM and UICC could be defined readily in all cases by annotation and segmentation. Reader 1 (experienced reader, 168 cases, 1172 lesions) required a median of 13.8 min, and reader 2 (resident, 227 cases, 1835 lesions) needed a median of 17.2 min per case. The median test ($p = 0.184$) showed no significant difference, even if the differences in distribution show a slightly faster segmentation by reader 1 ($U = 22113$ $p = 0.002$). The central

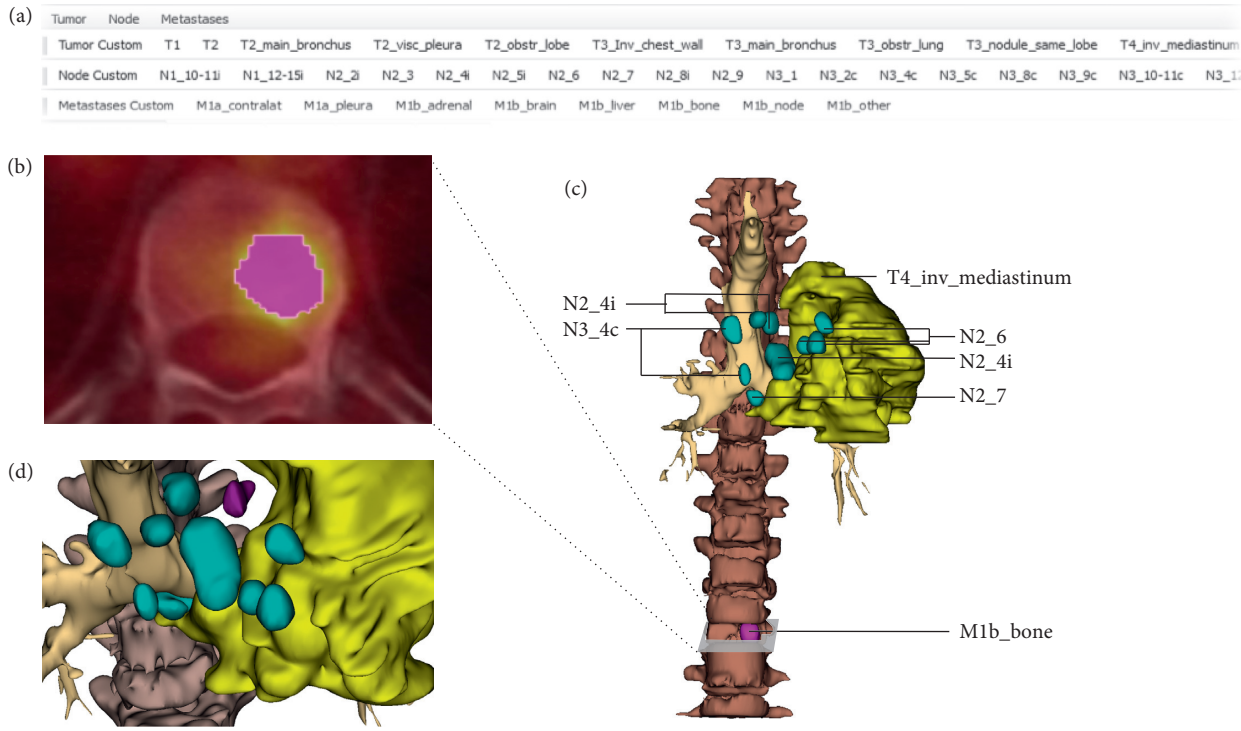

FIGURE 2: Example of a three-dimensional annotation and segmentation of NSCLC lesions from FDG-PET/CT data of a 71-year-old male patient with squamous cell carcinoma. (a) After selecting the label from the toolbar, (b) the lesions were manually segmented. (c) Tumor lesions as a visual report of primary staging including stage information and location. (d) Detailed view of the infiltrating primary tumor (yellow), lymph node metastasis (green), and pleural metastasis (purple).

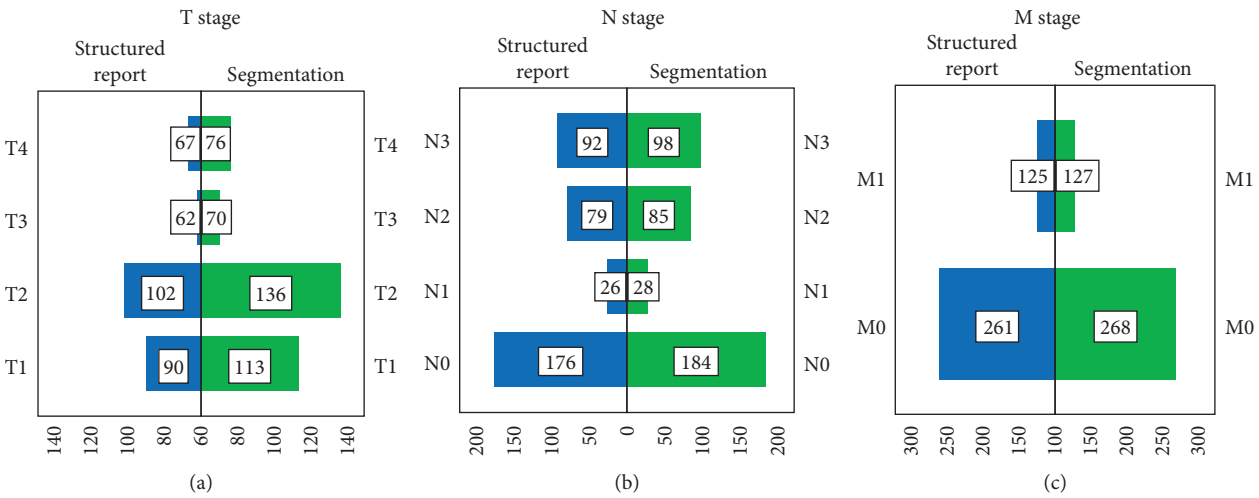

FIGURE 3: Completeness of TNM information and stage distribution. The T (a), N (b), and M (c) stages of the different TNM descriptors (7th edition), as well as their frequency in segmentation and the text-based reports, are shown.

tendencies regarding T ($U = 0.091$ $p = 0.927$), N ($U = -0.881$, $p = 0.378$), and UICC ($U = -1.161$, $p = 0.246$) stages and age ($t = 1.01$, $p = 0.312$) do not differ significantly between both readers. M stage shows that reader 2 (36.6%) segmented more cases with distant metastases than reader 1 ($U = -2.1$, $p = 0.035$), which in part explains longer segmentation time periods. Results from both readers were used for further analysis.

The segmentation required a median of 13.3 min for the staging of NSCLC and 3.8 min extra, if there were additional findings (Figure 5). For segmentation of one lesion, a median of 1.5 min was needed.

The time registries showed that segmentation-based staging was dependent on the lesion count and tumor stage. As the lesion count increased, the total segmentation time increased linearly ($R^2 = 0.361$, $F = 221.536$, $p < 0.001$),

Table 2: Segmentation time versus structured reporting time.

	Segmentation time* (min)	Study population (NSCLC)		Simulation (miscellaneous oncological indications)	
		*R*1 (min)	*R*2 (min)	*R*1 (min)	*R*2 (min)
Mean	25.0	31.0	181.8	29.0	154.2
Standard deviation	30.9	38.2	137.2	18.7	96.5
CI	21.9–28.0	24.0–38.0	164.6–198.9	25.6–32.4	142.1–166.3
Min	0.9	1.0	3.0	0.4	0.3
Median	16.3	18.1	151.6	26.6	146.1
Max	326.0	226.0	792.9	92.9	464.4

The descriptive statistics for the collected and simulated data in minutes are shown. *Including additional lesions. CI = confidence interval; *R*1 = lower estimator of the text-based reporting time; *R*2 = upper estimator of the text-based reporting time.

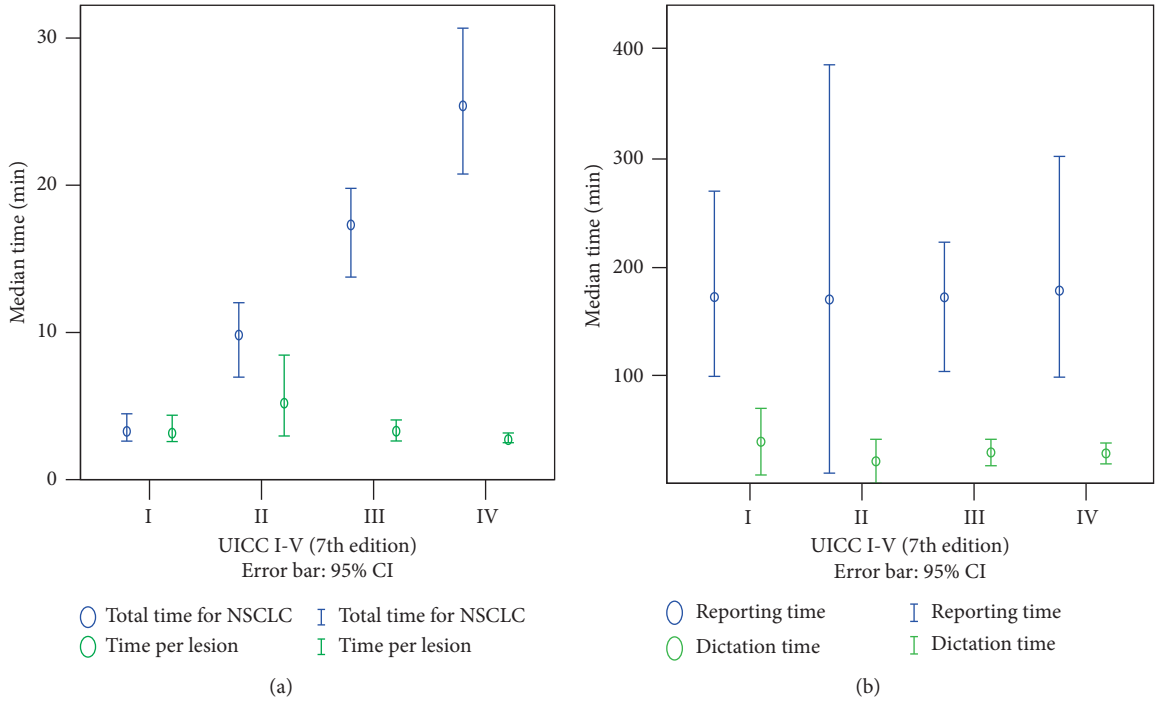

Figure 4: Comparison of time needed for staging depending on UICC stage. The median is indicated by a circle, accompanied by its 95% confidence interval. (a) Segmentation time is correlated with UICC stage, whereas the medians of total time and time per lesion show an inverse correlation. (b) Neither *R*2 nor *R*1 is related to the UICC stage. *R*1 = lower estimator of the text-based reporting time. *R*2 = upper estimator of the text-based reporting time.

whereas time per lesion slightly decreased ($R^2 = 0.01$, $F = 32.4$, $p < 0.001$) (Figure 5). According to linear regression, an average of 2.1 min was needed for each additional lesion. In addition, lesion size (independent from the lesion type) showed a positive correlation with segmentation time ($R^2 = 0.284$, $F = 1106.466$, $p < 0.001$).

Table 3 gives an overview of the relationship between diameter and segmentation time per lesion. The average T lesion diameter was 18.1 mm. The median time required per T lesion was 2.9 min and, according to linear regression, each additional T lesion led to an increase by 0.84 min ($F = 13.0$, $p < 0.001$) on average. In contrast to the T stage (average count: 1.7), average N (average count: 2.9) and M (average count: 5.6) lesion counts were higher. On the other hand, average diameters of N (12.2 ± 4.8 mm) and M (13.0 ± 4.6 mm) lesions were smaller. Subsequently, segmentation times per metastatic and nodal lesion were approximately half of T lesions (Table 3) (T vs. N lesions: $p < 0.001$, T vs. M lesions: $p < 0.001$).

The total time for the segmentation correlated with the T ($r_S = 0.426$, $p < 0.001$), N ($r_S = 0.694$, $p < 0.001$), and M ($r_S = 0.512$, $p < 0.001$) stages and thus also with the UICC stage ($r_S = 0.564$, $p < 0.001$). N ($F = 40.9$, $p < 0.001$) and M ($F = 42.5$, $p < 0.001$) stages have a greater impact on total staging time as the T stage ($F = 17.0$, $p < 0.001$), estimating 67.3% for N stage, 23.4% for M stage, and only 9.3% for T stage. A median of 5.1 min segmentation time was needed for UICC I/II versus 6.8 min for UICC III/IV per T stage ($U = 32355$, $p < 0.001$).

In contrast to the reporting times, the median segmentation time for those cases with sufficient information for TNM extraction in the text-based reports (78%) was not

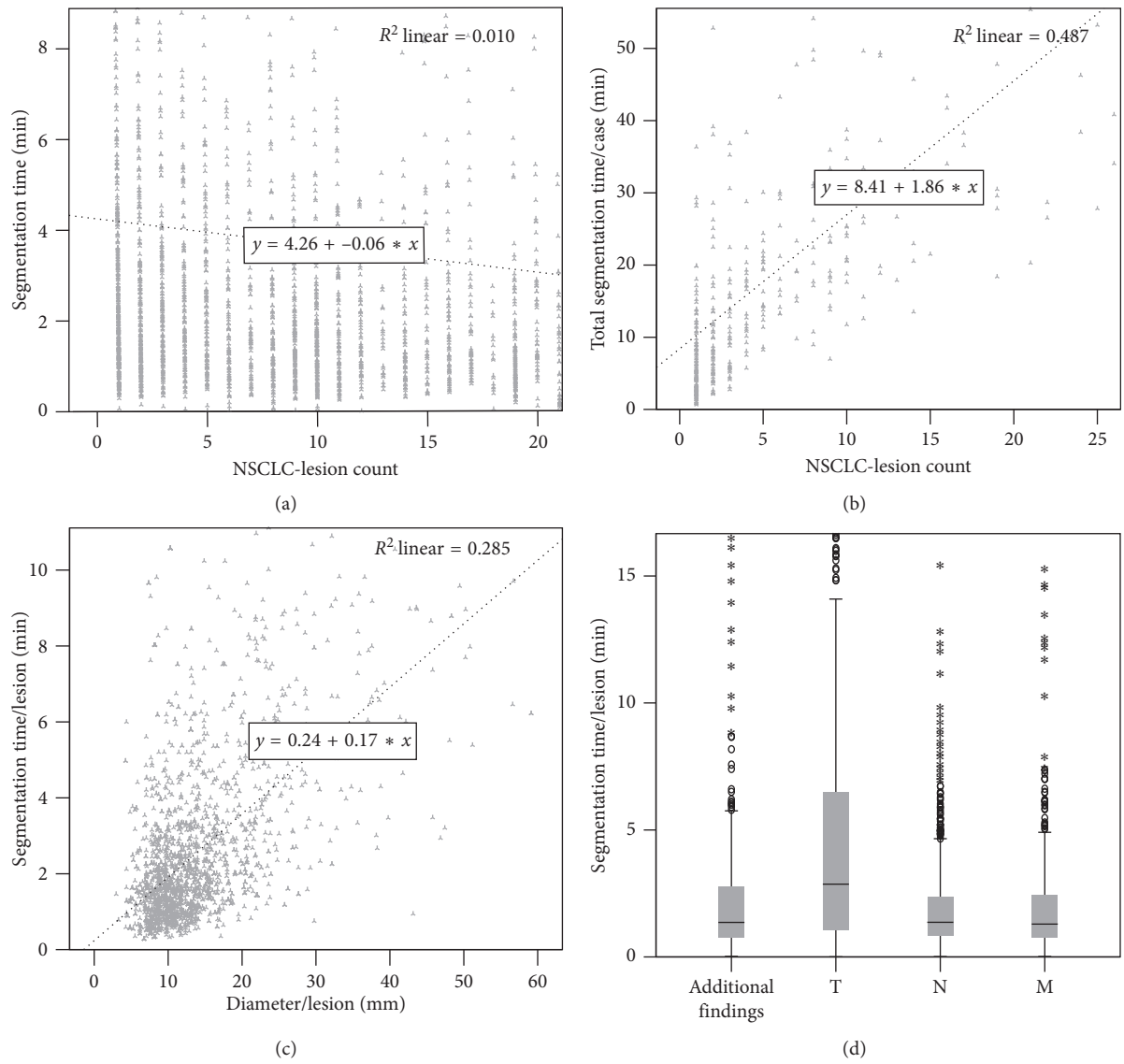

Figure 5: Factors influencing the segmentation time. (a) Scatter plot of NSCLC-lesion count versus segmentation time per lesion (grey): segmentation time per lesion slightly decreases with lesion count as shown by a linear regression line (black dotted). (b) Scatter plot of NSCLC-lesion count versus total segmentation time: the linear regression (black dotted) shows that total segmentation time increases with lesion count. (c) Scatter plot of lesion diameter versus segmentation time per lesion showing an increase in segmentation time with lesion diameter. (d) Box plots displaying the required segmentation time per individual lesion depending on its main category.

Table 3: Descriptive statistics of diameter and segmentation time per lesion.

	Diameter (mm)			Time per lesion (min)		
	T	N	M	T	N	M
Mean	18.2	12.2	13.0	5.7	2.3	2.1
Standard deviation	13.7	4.8	4.6	9.7	4.9	4.8
CI	17.1–19.3	12.0–12.5	12.7–13.3	4.9–6.4	2.0–2.6	1.7–2.5
Min	4.3	4.9	4.9	0.0	0.0	0.0
Median	12.8	11.0	12.3	2.8	1.4	1.3
Max	81.0	56.6	30.6	126.0	111.0	119.2

An overview of the time required for segmentation per lesion and the lesion diameter relative to the respective T/N/M descriptors are shown. Compared to N and M lesions, T lesions have the largest diameter and highest segmentation time. CI = confidence interval.

longer than for those with no or incomplete TNM information in the text-based reports (13.3 min for each group).

4. Discussion

Our objective was to analyze the amount of TNM information missing in text-based PET/CT reports for staging of NSCLC and to compare this conventional reporting with a new segmentation and annotation approach of the total tumor burden. The most important findings can be summarized as follows: TNM stage was frequently missing in structured text-based PET/CT reports (22%). Annotated image segmentation always includes tumor stage and thus enhances the quality of the diagnosis. Segmentation time (median = 16.3 min) increases with the TNM and UICC stage as well as the lesion count, whilst text-based reporting times (lower boundary estimator $R1$ = 18.1 min) are neither correlated with the tumor stage nor lesion count.

Definitions and implementations of free text versus structured text reporting are currently under debate. According to Weiss et al., structured reporting can be divided into the following three steps [16]:

(i) Level 1: use of common headings

(ii) Level 2: use of subheadings specifying organs or organ systems ("itemized")

(iii) Level 3: use of standardized language ("clickable")

Most guidelines for PET/CT suggest 3 principal style formats of reporting: order of importance, anatomic site, and hybrid [13]. In our institution, the preferred style is driven by the anatomic site. In our sample, we found that in 22% of text-based level 2 structured reports the TNM stage is missing. Since further treatment depends in particular on the tumor stage, the absence of TNM in 22% of the examined cases is alarmingly high. In such cases with undocumented TNM, miscommunication and uncontrolled interpretation might entail misstaging and wrong treatment decisions. Furthermore, missing TNM will decrease efficiency of multidisciplinary tumor boards. It is noteworthy that the tumor stage is an important part of the report for the oncologist and missing findings, in general, are the most common cause of malpractice suits [17].

A first approach that might come to mind as a potential remedy is the introduction of level 3 structured reporting approaches. However, as direct links between the text and the image are missing, this approach offers limited options in terms of reporting tumor burden and communicating measurements. Therefore, according to Folio et al., the use of image-based annotated measurements in a standardized format would significantly improve the report quality even beyond the results of text-based structuring alone [18].

However, as the time available per image becomes increasingly shorter [19] and increasing workload can be a source of error on its own [20], an evaluation of the required time for segmentation is of pivotal importance. In our study, a median time of 13.3 min was needed for segmentation of the total NSCLC tumor burden with explicit annotation of T, N, and M lesions. Velazquez et al. have compared manual and semiautomatic computed tomography- (CT-) based segmentation of primary lung tumors [21]. The authors measured a mean segmentation time of 10.6 min (range: 4.85–18.25 min) for the manual slice-by-slice delineations. Furthermore, in the Multimodal Brain Tumor Image Segmentation Benchmark (BRATS), MRI scans were segmented by a trained team of radiologists using 3D slicer software, taking about 60 min per subject [22]. Thus, in this context, our segmentation times seem to be quite low in comparison.

To estimate the time required for normal text-based reporting as a reference value, we used a time stamp-based approach on the sample. Since time stamps only give a rough estimate of the true reporting time, we tried to fortify our estimate with a modeled timing based on an extensive sample of PET/CTs. While the median of $R1$ between the two groups are comparable, $R2$ of the samples differed significantly from the simulation. This suggests the lower benchmark ($R1$) to be more reliable because of the small difference between the sample and modelling. According to a web-based survey performed by Karantanis et al. [23], most PET/CT readers estimate the mean reading time between 15 and 20 min, which is comparable in particular to our lower benchmark. The duration of comparable whole-body CT reports has been calculated based on RIS entries at approximately 30 minutes [24]. This is within the range of $R1$–$R2$. Overall, based on our data, the reference values published in literature, and from our own personal experience, it seems justified to estimate the reading time for a PET/CT exam in NSCLC in between 20 and 30 minutes. Interestingly, the time requirements for conventional text-based reporting in our analysis were independent of factors such as lesion number or TNM stage.

We have analyzed factors that influence the time needed for segmentation. Here, the time required can be estimated by case complexity and is dependent on lesion number, tumor size, infiltration, and metastasis. The relevance of total tumor burden, expressed as total tumor volume or lesion count, for patient prognosis has been shown by several studies [10, 25, 26]. This is also recognized by the International Association for the Study of Lung Cancer (IASLC), who in the framework of the current 8th edition of the TNM staging system for lung cancer, gives a strong recommendation for physicians to record the number of metastatic lymph nodes (or stations) in their staging reports [25]. It follows that the process of segmentation, with the search for all lesions and definition of each single lesion extension, is the only possibility to capture the tumor burden thoroughly and relate it to prognostic factors. Next, text-based reporting is frequently only a description of the major tumor burden and will never reflect every single lesion in full extent. This emphasizes the importance to develop methods for reporting towards more dedicated tumor stage information. Furthermore, while a segmentation of raw image data is largely independent of individual interpretations or these are objectively traceable, level 1 and 2 reports are commonly misinterpreted [27]. Therefore, segmentation-based reports with supplementary interpretations would

be desirable, because they could enhance objectivity in the communication of radiological findings.

Beyond that, segmentation enables a multitude of new applications. It goes without saying that these are neither limited to NSCLC as a disease entity nor to tumor staging as a diagnostic task. Full tumor segmentations may be used for staging, restaging, and follow-up assessment of various kinds of malignancies, e.g., lymphoma, breast cancer, and prostate cancer [28–30], and other fields such as pathology reporting. It can be used as enriched image-guidance to plan procedures, such as biopsies, surgical procedures [31], or radiotherapy [32]. Segmentations might also serve as training data sets for machine learning by creating a machine-readable format [33]. Additional time required for segmentation may result in time-saving in the future. Therefore, IT solutions might enhance quality of TNM staging whilst reducing the workload for radiologists.

There are some limitations in our study. Evaluation of text-based RIS reports, collection of their reporting duration, and segmentation were retrospectively performed. Therefore, there was an unavoidable selection bias. In contrast to a prospective survey of real-time reporting, it was not possible to evaluate external factors and interruptions influencing the duration of a report. Since segmentation of each case was not performed by more than one reader, inter-reader agreement cannot be evaluated. However, given the fact that text-based reports were previously performed in clinical routine and served as basis for tumor segmentation, the variability is certainly lower compared to segmentation without clinical or radiological information. Although the median segmentation time of both readers was comparable, differences in distribution were found linked to slightly different patient groups and readers' experience. In addition, segmentations were performed with a manual approach and not using semi- or automatic PET or CT segmentation that can improve the objectivity of tumor volume measurements, e.g., in head and neck cancer [34]. Furthermore, the differences in the reading environments with different sources of interruption for the reading and segmentation task complicate direct, one-to-one comparisons. Finally, the retrospective study design did also affect the validity of our data regarding the accuracy of the TNM staging information, as it was not possible to obtain clinical or even pathological confirmation for each particular lesion of interest in our rather large patient sample. In our opinion, this does not represent a major limitation in terms of the purpose of this article, as tumor stage did not serve as an endpoint of our analysis, but was investigated only with regard to its secondary effects on reporting and segmentation times.

5. Conclusions

In current text-based PET/CT reports, TNM staging information is frequently incomplete. Structured reporting with annotated image segmentation provides enhanced report quality with complete TNM information with manageable additional workload. Moreover, annotated image segmentation opens the door towards training artificial intelligence algorithms and better integration of imaging data in clinical workflows.

Data Availability

RIS time entries of all patients are provided as anonymized list in the supplementary materials (Table S4). PET/CT and corresponding annotation data are patient-related and thus confidential. Upon request, a minimal anonymized subset will be available to interested researchers. 3D Slicer and associated plugins are available in their entirety at https://github.com/Slicer/slicer.

Conflicts of Interest

Kevin Mader is an employee and shareholder of 4Quant Ltd. He was mainly involved in technical developments (questionnaire for report-based TNM extraction, PET/CT data transfer, and 3D-Slicer-based segmentation software). Neither the funding agency nor any outside organization has participated in the study design or have any conflicts of interest. All other authors declare that there are no conflicts of interest.

Acknowledgments

We appreciate the support by Achim Escher concerning RIS time stamp queries. This work was funded by CTI (Commission for Technology and Innovation) "LungStage - ComputerAided Staging of Non-Small Cell Lung Cancer (NSCLC)" (Project no. 25280.1).

Supplementary Materials

Table S1: detailed description of the T-label sets. Table S2: detailed description of the N-label sets. Table S3: detailed description of the M-label sets. Table S4: list with anonymized RIS time entries. Modelling for reporting time estimation (text and R code). (*Supplementary Materials*)

References

[1] R. L. Siegel, K. D. Miller, and A. Jemal, "Cancer statistics," *CA: A Cancer Journal for Clinicians*, vol. 68, no. 1, pp. 7–30, 2018.

[2] R. Rami-Porta, V. Bolejack, D. J. Giroux et al., "The IASLC lung cancer staging project: the new database to inform the eighth edition of the TNM classification of lung cancer," *Journal of Thoracic Oncology*, vol. 9, no. 11, pp. 1618–1624, 2014.

[3] G. A. Silvestri, A. V. Gonzalez, M. A. Jantz et al., "Methods for staging non-small cell lung cancer," *Chest*, vol. 143, no. 5, pp. e211S–e250S, 2013.

[4] R. J. Cerfolio and A. S. Bryant, "Survival of patients with true pathologic stage I non-small cell lung cancer," *Annals of Thoracic Surgery*, vol. 88, no. 3, pp. 917–923, 2009.

[5] B. M. Stiles, E. L. Servais, P. C. Lee, J. L. Port, S. Paul, and N. K. Altorki, "POINT: clinical stage IA non–small cell lung cancer determined by computed tomography and positron emission tomography is frequently not pathologic IA non–small cell lung cancer: the problem of understaging," *Journal of Thoracic and Cardiovascular Surgery*, vol. 137, no. 1, pp. 13–19, 2009.

[6] N. Navani and S. G. Spiro, "PET scanning is important in lung cancer; but it has its limitations: editorial," *Respirology*, vol. 15, no. 8, pp. 1149–1151, 2010.

[7] A. P. Brady, "Error and discrepancy in radiology: inevitable or avoidable?," *Insights into Imaging*, vol. 8, no. 1, pp. 171–182, 2017.

[8] D. K. Powell and J. E. Silberzweig, "State of structured reporting in radiology, a survey," *Academic Radiology*, vol. 22, no. 2, pp. 226–233, 2015.

[9] Y. Oh, S. Taylor, B. N. Bekele et al., "Number of metastatic sites is a strong predictor of survival in patients with nonsmall cell lung cancer with or without brain metastases," *Cancer*, vol. 115, no. 13, pp. 2930–2938, 2009.

[10] Y. He, X. Zhang, J. Yang et al., "Prognostic significance of genotype and number of metastatic sites in advanced non–small-cell lung cancer," *Clinical Lung Cancer*, vol. 15, no. 6, pp. 441–447, 2014.

[11] L. R. Folio, L. B. Machado, and A. J. Dwyer, "Multimedia-enhanced radiology reports: concept, components, and challenges," *RadioGraphics*, vol. 38, no. 2, pp. 462–482, 2018.

[12] M. Bhargavan, A. H. Kaye, H. P. Forman, and J. H. Sunshine, "Workload of radiologists in United States in 2006–2007 and trends since 1991–1992," *Radiology*, vol. 252, no. 2, pp. 458–467, 2009.

[13] R. D. Niederkohr, B. S. Greenspan, J. O. Prior et al., "Reporting guidance for oncologic 18F-FDG PET/CT imaging," *Journal of Nuclear Medicine*, vol. 54, no. 5, pp. 756–761, 2013.

[14] A. Fedorov, R. Beichel, J. Kalpathy-Cramer et al., "3D slicer as an image computing platform for the quantitative imaging network," *Magnetic Resonance Imaging*, vol. 30, no. 9, pp. 1323–1341, 2012.

[15] R. A. Redner and H. F. Walker, "Mixture densities, maximum likelihood and the EM algorithm," *SIAM Review*, vol. 26, no. 2, pp. 195–239, 1984.

[16] D. L. Weiss and C. P. Langlotz, "Structured reporting: patient care enhancement or productivity nightmare?," *Radiology*, vol. 249, no. 3, pp. 739–747, 2008.

[17] S. R. Baker, R. H. Patel, L. Yang, V. M. Lelkes, and A. Castro, "Malpractice suits in chest radiology: an evaluation of the histories of 8265 radiologists," *Journal of Thoracic Imaging*, vol. 28, no. 6, pp. 388–391, 2013.

[18] L. R. Folio, C. J. Nelson, M. Benjamin, A. Ran, G. Engelhard, and D. A. Bluemke, "Quantitative radiology reporting in oncology: survey of oncologists and radiologists," *American Journal of Roentgenology*, vol. 205, no. 3, pp. W233–W243, 2015.

[19] R. J. McDonald, K. M. Schwartz, L. J. Eckel et al., "The effects of changes in utilization and technological advancements of cross-sectional imaging on radiologist workload," *Academic Radiology*, vol. 22, no. 9, pp. 1191–1198, 2015.

[20] T. N. Hanna, C. Lamoureux, E. A. Krupinski, S. Weber, and J.-O. Johnson, "Effect of shift, schedule, and volume on interpretive accuracy: a retrospective analysis of 2.9 million radiologic examinations," *Radiology*, vol. 287, no. 1, pp. 205–212, 2018.

[21] E. R. Velazquez, C. Parmar, M. Jermoumi et al., "Volumetric CT-based segmentation of NSCLC using 3D-slicer," *Scientific Reports*, vol. 3, no. 1, 2013.

[22] B. H. Menze, A. Jakab, S. Bauer et al., "The multimodal brain tumor image segmentation benchmark (BRATS)," *IEEE Transactions on Medical Imaging*, vol. 34, no. 10, pp. 1993–2024, 2015.

[23] D. Karantanis, D. Kalkanis, M. S. Allen-Auerbach et al., "Oncologic PET/CT interpretation and reporting approaches: survey in clinical practice," *Nuklearmedizin*, vol. 53, no. 2, pp. 19–25, 2014.

[24] I. A. Cowan, S. L. MacDonald, and R. A. Floyd, "Measuring and managing radiologist workload: measuring radiologist reporting times using data from a radiology information system," *Journal of Medical Imaging and Radiation Oncology*, vol. 57, no. 5, pp. 558–566, 2013.

[25] H. Asamura, K. Chansky, J. Crowley et al., "The international association for the study of lung cancer lung cancer staging project," *Journal of Thoracic Oncology*, vol. 10, no. 12, pp. 1675–1684, 2015.

[26] S. Jonnalagadda, C. Smith, G. Mhango, and J. P. Wisnivesky, "The number of lymph node metastases as a prognostic factor in patients with N1 non-small cell lung cancer," *Chest*, vol. 140, no. 2, pp. 433–440, 2011.

[27] F. Pool and S. Goergen, "Quality of the written radiology report: a review of the literature," *Journal of the American College of Radiology*, vol. 7, no. 8, pp. 634–643, 2010.

[28] M. Puesken, B. Buerke, J. Gerss et al., "Prediction of lymph node manifestations in malignant lymphoma: significant role of volumetric compared with established metric lymph node analysis in multislice computed tomography," *Journal of Computer Assisted Tomography*, vol. 34, no. 4, pp. 564–569, 2010.

[29] M. D. Blackledge, D. J. Collins, N. Tunariu et al., "Assessment of treatment response by total tumor volume and global apparent diffusion coefficient using diffusion-weighted MRI in patients with metastatic bone disease: a feasibility study," *PLoS One*, vol. 9, no. 4, Article ID e91779, 2014.

[30] S. Schmuck, C. A. von Klot, C. Henkenberens et al., "Initial experience with volumetric ^{68} Ga-PSMA I and T PET/CT for assessment of whole-body tumor burden as a quantitative imaging biomarker in patients with prostate cancer," *Journal of Nuclear Medicine*, vol. 58, no. 12, pp. 1962–1968, 2017.

[31] X. Chen, L. Xu, H. Wang, F. Wang, Q. Wang, and R. Kikinis, "Development of a surgical navigation system based on 3D slicer for intraoperative implant placement surgery," *Medical Engineering and Physics*, vol. 41, pp. 81–89, 2017.

[32] J.-J. Sonke and J. Belderbos, "Adaptive radiotherapy for lung cancer," *Seminars in Radiation Oncology*, vol. 20, no. 2, pp. 94–106, 2010.

[33] S. L. Zimmerman, W. Kim, and W. W. Boonn, "Informatics in radiology: automated structured reporting of imaging findings using the AIM standard and XML," *RadioGraphics*, vol. 31, no. 3, pp. 881–887, 2011.

[34] E. Simon, T. H. Fox, D. Lee, A. F. Waller, P. Pantalone, and A. B. Jani, "PET lesion segmentation using automated iso-intensity contouring in head and neck cancer," *Technology in Cancer Research and Treatment*, vol. 8, no. 4, pp. 249–255, 2009.

[35] A. H. El-Sherief, C. T. Lau, C. C. Wu, R. L. Drake, G. F. Abbott, and T. W. Rice, "International association for the study of lung cancer (IASLC) lymph node map: radiologic review with CT illustration," *RadioGraphics*, vol. 34, no. 6, pp. 1680–1691, 2014.

Hindawi
Contrast Media & Molecular Imaging
Volume 2018, Article ID 3417190, 9 pages
https://doi.org/10.1155/2018/3417190

Research Article

Is SUVmax Helpful in the Differential Diagnosis of Enlarged Mediastinal Lymph Nodes? A Pilot Study

Congcong Yu,[1,2] Xiaotian Xia,[1,2] Chunxia Qin,[1,2] Xun Sun,[1,2] Yongxue Zhang,[1,2] and Xiaoli Lan[1,2]

[1]*Department of Nuclear Medicine, Union Hospital, Tongji Medical College, Huazhong University of Science and Technology, Wuhan 430022, China*
[2]*Hubei Province Key Laboratory of Molecular Imaging, Wuhan 430022, China*

Correspondence should be addressed to Xiaoli Lan; lxl730724@hotmail.com

Received 29 May 2018; Revised 2 September 2018; Accepted 20 September 2018; Published 28 October 2018

Guest Editor: Nicola Toschi

Objective. To explore the diagnostic value of maximum standard uptake value (SUVmax) from ^{18}F-FDG PET/CT images in enlarged mediastinal lymph nodes of unknown etiology. *Methods*. We performed a retrospective study of patients with enlarged mediastinal lymph nodes on ^{18}F-FDG PET/CT scans. SUVmax and the short axis and long axis of lymph nodes were recorded. These parameters were compared among the five commonest causes of mediastinal lymphadenopathy: lymphoma, metastatic disease, sarcoidosis, tuberculosis, and lymphadenitis. Histopathologic diagnosis was recorded as the final golden standard. *Results*. A total of 94 patients (62 men and 32 women; age range 7–85 y) were included with final diagnoses of 42 patients with benign pathology and 52 patients with malignancies. The sensitivity, specificity, and the accuracy of PET/CT in diagnosis of the benign and malignant mediastinal lymph nodes were 94.2%, 73.8%, and 85.1%, respectively. The SUVmax of benign and malignant groups were 13.10 ± 5.21 and 12.59 ± 5.50, respectively, which had no statistical difference ($P > 0.05$). However, the long axis and the short axis of lymph nodes in the benign and malignant groups were 2.86 ± 1.02 cm, 1.77 ± 0.60 cm and 6.04 ± 3.83 cm, 3.95 ± 2.08 cm, respectively ($P < 0.05$). The diagnostic values of PET/CT were higher than those of the long or short axis. However, the specificity of PET/CT was lower (73.8%) than that from the long or short axis (90.5% and 92.9%, respectively), although no statistical difference existed. Among the five common causes of mediastinal lymphadenopathy, significant differences could be seen in SUVmax and in the long axis and the short axis of lymph nodes ($P < 0.05$). *Conclusions*. SUVmax, a commonly used semiquantitative measurement, was not helpful for differentiation between benign and malignant lesions in patients with enlarged mediastinal lymph nodes in this study. Many benign lesions, such as sarcoidosis and tuberculosis, had high FDG uptake, possibly a trend that the size of the lymph nodes seems to have some diagnostic value.

1. Introduction

Unexplained mediastinal lymphadenopathy is not uncommon in clinical. Some patients visit a doctor due to dysphagia, hoarseness, or enlarged lymph nodes occasionally found in the physical examination. The symptoms may be caused by enlarged lymph nodes that compress the esophagus and recurrent laryngeal nerves. Lymph nodes may be enlarged due to benign or malignant etiologies. Early and accurate diagnosis and characterization of the etiology of mediastinal lymphadenopathy are essential to formulating a treatment plan.

The mediastinum is not an organ, but an anatomical area. In this area, there are several important tissues and organs, such as heart, large blood vessels, esophagus, trachea, thymus, nerves, and lymphatic tissue. Therefore, the mediastinal anatomy is complicated, and the tissue biopsy is difficult. There are invasive methods for evaluation of abnormal mediastinal lymph nodes, including mediastinoscopy (Med) [1], thoracoscopy [1], transbronchial needle

aspiration (TBNA) [2], endobronchial ultrasound-guided transbronchial needle aspiration (EBUS-TBNA) [3], and endoscopic ultrasound-guided fine needle aspiration (EUS-FNA) [4]. The advantages of these methods are visual and intuitive and can be obtained with accurate pathological diagnosis. Some studies reported the sensitivity for Med, TBNA, EBUS-TBNA, and EUS-FNA in detecting malignancy were 80%, 78%, 89%, and 91%, respectively, and the specificity were 100%, 100%, 100%, and 100%, respectively [1–4]. The reason for the difference of the sensitivity may be related to the biopsy methods which could not access all the lymph nodes in mediastinum. For example, Med and EBUS-TBNA could not reach prevascular, subaortic, paraaortic, paraesophageal, and pulmonary ligament nodes [5]. Although these methods can obtain pathological results and have high specificity, they are invasive and may lead to complications. For example, TBNA can lead to mediastinal gas, bleeding, infection, and so on, while these incidence rates are low in EBUS-TBNA.

The traditional noninvasive examinations, chest computed tomography (CT) and magnetic resonance imaging (MRI), are the standard imaging modalities for assessment of mediastinal lymph nodes. However, MRI spatial resolution is relatively poor due to the presence of the air in the lungs, and the calcification of lymph nodes is often ignored by MRI [6]. CT could detect lesions, but it is also difficult to obtain the differential diagnosis of benign and malignant lymph nodes [6].

Positron emission tomography/computed tomography (PET/CT), integrating morphological imaging with functional imaging, is a noninvasive imaging method based on molecular functional imaging, which improves the diagnostic sensitivity and accuracy [7–9]. To some degree, PET/CT complements the deficiencies of traditional imaging and plays an important role in the workup of mediastinal lymphadenopathy. According to Nguyen's retrospective study, the sensitivity and specificity of PET/CT in the diagnosis of the benign and malignant mediastinal lymph nodes were 87% and 89%, respectively [10]. Also, the sensitivity, specificity, and the accuracy of PET/CT (87%, 91%, and 82%) in detecting mediastinal lymph nodes metastases were higher than CT (68%, 61%, and 63%) based on a recent report [11].

In the PET imaging analysis, standard uptake value (SUV), as a semiquantitative data, points off the degree of metabolic activity (aerobic glycolysis) in selected tissues [10]. The maximum standardized uptake value (SUVmax) is the maximum number of counts within the pixels in a region of interest (ROI). SUVmean is the mean number of counts in an ROI. SUVmax is preferred over SUVmean as there is a variability of about 35% between observers when SUVmean is used, and this reduces to 3% when SUVmax is used [12]. The SUVmax cutoff value of 2.5 is used commonly to differentiate between benign and malignant lesions [13]. Kumar et al.'s study of 35 cases of mediastinal lymphadenopathy showed that appropriately increasing the cutoff values can improve the specificity while maintaining an acceptable sensitivity [6]. When 2.5 or 6.2 was used as the cutoff value, the sensitivity, specificity, positive predictive value (PPV), negative predictive value (NPV), and accuracy were 93%, 40%, 54%, 89%, and 63% and 87%, 70%, 68%, 87%, and 77%, respectively [6]. There are a significant number of false positives (due to inflammatory diseases) and false negatives (due to low-grade malignancies) [14].

Research on unexplained enlarged mediastinal lymph nodes is relatively rare. This is mainly due to the complicated mediastinal anatomy, fewer pathology results, and number of cases, which makes the research impossible. Furthermore, since there are different views on the clinical value of PET/CT in evaluating enlarged mediastinal lymph nodes, it is difficult to draw consistent conclusions. In particular, the significance of SUVmax in diagnosing mediastinal lymph nodes has not yet been reported in detail. Hence, we planned to explore the clinical value of PET/CT images in enlarged mediastinal lymph nodes of unknown etiology, especially the diagnostic value of some quantitative and semiquantitative measures in the differentiation of malignant from benign lesions, such as SUVmax and lymph node size.

2. Subjects and Methods

2.1. Patient Population. This study was approved by the Institutional Review Board of Union Hospital, Tongji Medical College, Huazhong University of Science and Technology. Patients with enlarged mediastinal lymph nodes of unknown etiology and ^{18}F-FDG PET/CT scans were included in this retrospective study. The following inclusion criteria were used to select patients: (1) the enlarged mediastinal lymph nodes were defined as the long axis >1 cm or generalized pulmonary hilar enlargement on CT images; (2) the enlarged mediastinal lymph nodes had higher FDG uptake than that of the adjacent blood pool; (3) the patients had not undergone treatment; (4) clinical data were complete, and formal follow-up was recorded; (5) histopathologic diagnosis was recorded as the final golden standard. Patients with diabetes were excluded.

2.2. Image Acquisition. All patients fasted for at least 6 hours before PET/CT examination. The images were obtained on a dedicated PET/CT scanner (Discovery VCT®, GE Medical Systems, Milwaukee WI, USA) 45–60 minutes after intravenous injection of 3.7–5.55 MBq/kg of ^{18}F-FDG. A low-dose CT scan was obtained for attenuation correction, using the following parameters: tube voltage 120 kV, 80 mAs, and 3.75 mm slice collimation. PET images were acquired from the level of the head to the upper part of the legs (usually 6–8 bed positions) at 3 minutes per bed position. PET data were reconstructed with the ordered-subset expectation maximization algorithm. Both CT and PET data were sent to a workstation (Xeleris®, GE Medical Systems) for evaluation.

2.3. Image Analysis. Two experienced nuclear medicine physicians, who were familiar with the patient's clinical history, laboratory examinations, and traditional images (CT or MRI), independently reviewed all the PET/CT images and gave diagnosis separately. If the diagnosis disagreement

happened, another two physicians participated in the discussion and finally reached an agreement about the final diagnosis from PET/CT images. An ROI was carefully drawn on the lymph nodes, and then the SUVmax was calculated according to the following formula:

$$\text{SUV} = \frac{\text{Tissue activity (MBq/mL tissue)}}{\text{Injected dose (MBq)/body weight (g)}}. \quad (1)$$

According to the new lung cancer lymph node distribution made by the International Association for the Study of Lung Cancer (IASLC), we located each lymph node and measured the long axis and short axis of the largest lymph node. If some lymph nodes were fused together, we measured it as one node [15].

2.4. Statistical Analysis. The data were collected and analyzed using commercial software (SPSS 19.0®, SPSS Inc., Chicago Il, USA). The SUVmax, the long axis, and the short axis of benign and malignant lymph nodes were compared using a two-sample *t*-test. A receiver operating characteristics (ROC) curve was drawn to find the best differential diagnostic point. The chi-squared test was used for multiple sample rates, and partitions of the χ^2 method were used for multiple comparisons. The SUVmax, the long axis, and the short axis of lymph nodes among common mediastinal lymphadenopathy diseases were compared using the analysis of variance. These diseases included lymphoma, metastatic lymph nodes, sarcoidosis, tuberculosis, and lymphadenitis. Multiple comparisons between multiple samples were made using LSD (least significant difference), *t*-test (homogeneity of variance), and the Tamhane test (heterogeneity of variance). P values <0.05 were considered statistically significant. P values <0.0125 were considered statistically significant when using partitions of the χ^2 method.

3. Results

There were 94 cases finally included in this study. Forty-two cases were found to have benign, and 52 had malignant etiologies on histopathology. Among the 42 benign pathologies, 16 were sarcoidosis, 17 were tuberculosis, eight were lymphadenitis, and one was Castleman disease. Among the 52 malignant pathologies, 25 were lymphoma, 26 were metastatic lymph nodes, and one was acute leukemic infiltration. The relevant features of all cases are summarized in Table 1.

3.1. Diagnostic Value of PET/CT, SUVmax, Long Axis, and Short Axis of Lymph Nodes in Benign and Malignant Lesions. The sensitivity, specificity, PPV, NPV, and the accuracy of FDG PET/CT in diagnosis of the benign and malignant mediastinal lymph nodes were 94.2% (49/52), 73.8% (31/42), 81.7% (49/60), 91.2% (31/34), and 85.1% (80/94), respectively. Eleven false-positive PET/CT cases and three false-negative cases were found (Table 2). Lesions of tuberculosis were easily misdiagnosed as malignant lesions among these false-positive cases. In this study, eight of 17 patients with tuberculosis were misdiagnosed as malignant lesions, for a misdiagnosis rate of 47%. A typical case is shown in Figure 1 (case no. 69 in Table 2).

Table 1: Patient characteristic of 94 patients.

Variable	No.		
Age			
Range	7–85 y		
Median	50 y		
Sex			
Male	62		
Female	32		
Follow-up time (d)			
Range	43–1100		
Median	462		
Pathologic diagnosis	No. patients	Age (y) (range/median)	Male/female
Benign pathology	42	18–85/52	21/21
Sarcoidosis	16	28–57/50	6/10
Tuberculosis	17	19–75/50	10/7
Lymphadenitis	8	18–85/65	4/4
CD	1	53	1/0
Malignant pathology	52	7–78/47	41/11
Lymphoma	25	7–78/34	21/4
Metastatic lymph nodes	26	23–71/58	20/6
AL	1	64	0/1

CD: Castleman disease; AL: acute leukemic.

The SUVmax, long axis, and short axis of lymph nodes in the two groups are listed in Table 3. No statistical difference was seen in SUVmax between the malignant (12.59 ± 5.50, $n = 52$) and benign cases (13.10 ± 5.21, $n = 42$). The long axis and the short axis of lymph nodes in the benign and malignant groups were 2.86 ± 1.02 cm, 1.77 ± 0.60 cm and 6.04 ± 3.83 cm, 3.95 ± 2.08 cm, respectively ($P < 0.05$). These results indicated that SUVmax is not useful in determining whether the lymph nodes are benign or malignant; however, the size of the nodes measured on CT may provide more accurate information.

An ROC curve was drawn to find the best diagnostic differential point of the long axis and the short axis of lymph nodes in the distinction between benign and malignant diseases. The optimal threshold of the long axis of lymph nodes was calculated at 4.05 cm with 59.6% sensitivity, 90.5% specificity, 73.4% accuracy, and an area under the curve of 0.811 (95% confidence interval (CI) 0.726–0.896) (Figure 2(a)). The optimal threshold of the short axis of the lymph nodes was calculated at 2.55 cm with sensitivity 73.1%, specificity 92.9%, accuracy 81.9%, and an area under the curve 0.891 (95% CI 0.825–0.957) (Figure 2(b)).

The sensitivities of PET/CT, the long axis, or the short axis used separately to detect the benign and malignant mediastinal lymph nodes were statistically different in the chi-squared test, as well as the specificity ($P < 0.05$) (Table 4). When the sensitivities of the above three methods were compared separately by partitions of the χ^2 method, the results were statistically significant for PET/CT and the long axis and PET/CT and the short axis (both $P < 0.00125$). These results indicated that the sensitivity of PET/CT was

Table 2: False positive and negative cases diagnosed by ^{18}F-FDG PET/CT.

Case no.	Sex	Age	SUVmax	Long axis (cm)	Short axis (cm)	PET/CT diagnosis	Pathological diagnosis
False-negative cases							
31	F	44	9.1	2.9	2.3	TB	Adenocarcinoma (high grade)
36	M	53	7.7	1.9	1.5	Lymphadenitis	Adenocarcinoma
93	F	64	10.6	3.1	1.9	Lymphadenitis	Leukemia infiltration
False-positive cases							
69	F	42	24.5	2.7	2.5	Malignant disease	TB
70	M	71	3.9	2.3	1.4	Malignant disease	TB
71	M	19	14.8	2.6	1.6	Lymphoma	TB
73	F	52	9.9	1.5	1.3	Malignant disease	TB
81	M	61	6.9	4.0	2.3	Malignant disease	TB
82	M	50	9.2	5.0	1.3	Malignant disease	TB
83	F	32	15.5	2.6	1.6	Lymphoma	TB
84	M	25	12.9	3.8	3.3	Malignant disease	TB
86	F	66	16.7	2.9	1.8	Malignant disease	Lymphadenitis
92	M	53	16.7	4.4	3.0	Malignant disease	CD
94	F	57	11.6	1.9	1.3	Malignant disease	Lymphadenitis

F: female; M: male; TB: tuberculosis; CD: Castleman disease.

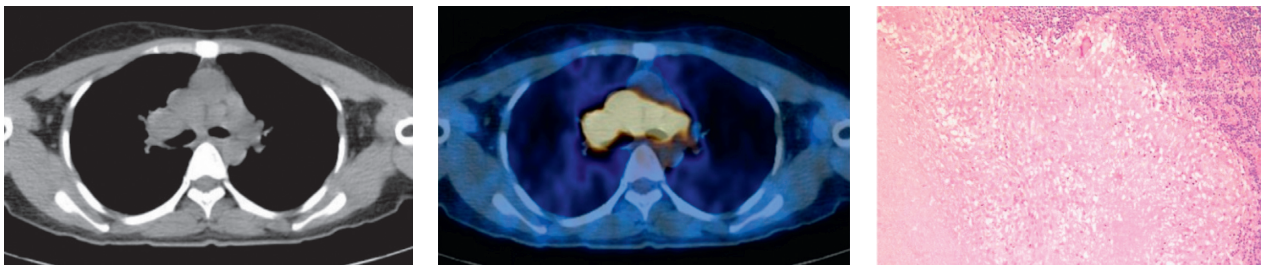

(a) (b) (c)

Figure 1: A 42-year-old female patient developed dry cough without fever. (a) Chest CT axial imaging showed enlarged lymph nodes in the mediastinum and right hilar areas. (b) PET/CT scan showed extensive hypermetabolic activity in the mediastinal and hilar lymph nodes (SUVmax 24.5). PET/CT indicated malignant lesions (lymphoma). The final pathological diagnosis was tuberculosis (c).

Table 3: Comparison of the SUVmax and size of the lymph nodes in the benign and malignant lesions.

	Benign ($n = 42$)	Malignant ($n = 52$)	t	P
SUVmax	13.10 ± 5.21	12.59 ± 5.50	0.458	0.648
Long axis (cm)	2.86 ± 1.02	6.04 ± 3.83	−5.238	<0.001
Short axis (cm)	1.77 ± 0.60	3.95 ± 2.08	−6.573	<0.001

significantly higher than that of the long axis or the short axis used separately to detect the benign and malignant mediastinal lymph nodes. Although the specificity of PET/CT (73.8%) seems lower than that of the long axis (90.5%) or short axis (92.9%), the similar pairwise comparison of specificities showed no statistical significance ($P > 0.0125$). Taken together, the diagnostic efficacy of PET/CT was higher than that of the long axis or the short axis. Comparing the diagnostic efficiency of long and short axis, the short axis measurement was superior to the long axis measurement.

3.2. Diagnostic Value of PET/CT in Different Common Diseases of Mediastinal Lymphadenopathy. SUVmax, the long axis, and the short axis of five common causes of mediastinal lymphadenopathy are listed in Table 5. The three measures of five diseases were statistically different by the analysis of variance.

Using the LSD-t-test, the pairwise comparison of SUVmax of five groups showed there are statistical differences. SUVmax of sarcoidosis is statistically higher than that of tuberculosis and lymphadenitis; however, it had no significant difference with that of lymphoma (Figure 3(a)).

Using the Tamhane test, the pairwise comparison of the long axis of five groups showed significant differences between lymphoma and all other diseases including metastatic lymph nodes, which indicated that the size of lymphomatous nodes was larger than that of the other lesions. The size of lymphadenitis nodes was smaller compared with the other diseases except tuberculosis (Figure 3(b)).

Using the Tamhane test, the pairwise comparison result of the short axis of five groups is shown in Figure 3(c). Obviously, the size of lymphoma and metastatic lymph nodes was significantly larger than that of benign lesions.

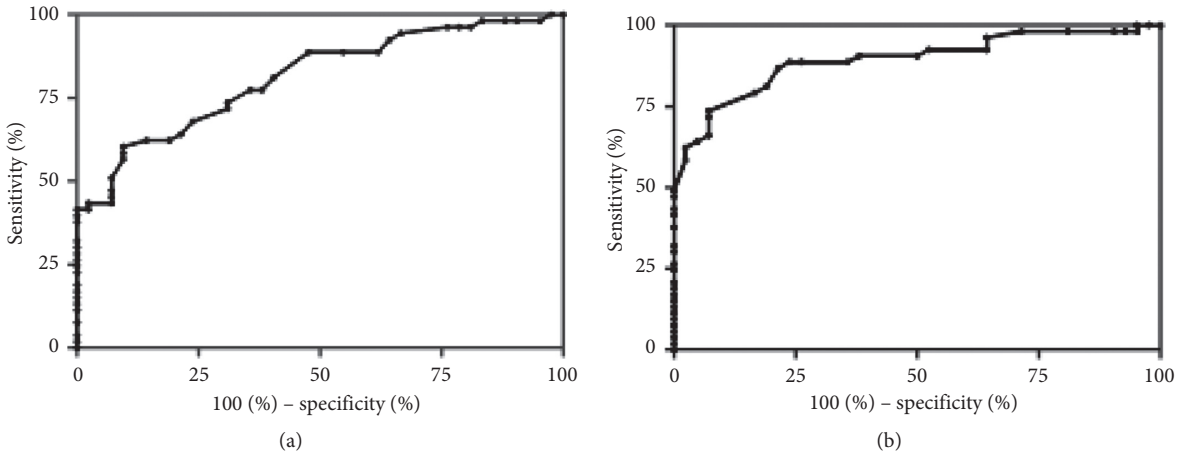

Figure 2: ROC curves of the long axis (a) and short axis (b) of lymph nodes in the differentiation between the benign and malignant diseases.

Table 4: Comparison of PET/CT, long axis, and short axis diagnostic efficacy.

Methods	Sensitivity (%)	Specificity (%)	Accuracy (%)
PET/CT	94.2	73.8	85.1
Long axis	59.6	90.5	73.4
Short axis	73.1	92.9	81.9
χ^2	17.186	7.389	4.323
P	<0.001	0.025	0.115

These results indicate that the short axis of lymph nodes is important in the distinction between benign and malignant lesions.

4. Discussion

Enlarged mediastinal lymph nodes incidentally found on chest X-ray or CT need evaluation to determine their benign or malignant etiology. Because of the complicated anatomy of the mediastinum and the possible risk of tissue biopsy, noninvasive methods play an important role in the diagnosis of the benign and malignant mediastinal lymph nodes. In this study, a total of 94 patients with pathological diagnosis were included with 42 benign and 52 malignant etiologies on histopathology. The sensitivity, specificity, PPV, NPV, and accuracy of PET/CT in the diagnosis of the benign and malignant mediastinal lymph nodes were 94.2% (49/52), 73.8% (31/42), 81.7% (49/60), 91.2% (31/34), and 85.1% (80/94), respectively. This indicated PET/CT seemed to have some diagnostic value in mediastinal lymphadenopathy. However, SUVmax had no significant relationship with the benignity or malignancy of lesions in this set of cases. The long axis and the short axis of lymph nodes had a certain diagnostic value in benign and malignant lesions, with the risk of malignancy increasing with size.

PET/CT has been widely used for tumor diagnosis, differential diagnosis, staging, follow-up, therapy planning, and prognosis [16, 17]. In our cases, the accuracy of PET/CT in the diagnosis of the benign and malignant mediastinal lymph nodes was 85.1% combined with whole body PET/CT imaging and clinical information. Our results are consistent with prior research [6, 10].

There are a significant number of false-positive and false-negative PET/CT findings in the evaluation of primary tumors [14]. The major causes of false-positive lymph nodes are lymph node involvement by underlying inflammatory processes such as reaction to the presence of lung tumor, obstructive pneumonia, anthracosis, or granulomatous inflammation [18–21]. The major cause of false positivity may vary from region to region. In a study from Alabama, histoplasmosis infection was the most common cause of false positives [19]. Silicosis has been found to be a cause of false positives in a study from Germany [22]. In our study, patients with tuberculosis were easily misdiagnosed as malignant lesions among these false-positive cases, which accounted for 72.7% (8/11) of all misdiagnosed cases.

Mediastinal tuberculous lymphadenitis (MTL) is mostly seen in primary tuberculosis in children; it is uncommon in adults [23]. Absence of typical tuberculosis clinical features during the nonsuppurative lymphadenitis phase and age distribution characteristics makes the distinction between MTL and lymphoma and metastatic lymph nodes difficult, especially MTL during the active phase which has higher FDG uptake [23]. Patients with lymphoma usually have hyperpyrexia, hepatosplenomegaly, superficial chain lymphadenopathy, and obvious anemia. Homogeneous enhancement is more commonly seen in lymphoma than tuberculosis according to contrast-enhanced CT [24]. Metastases usually have a primary malignant disease. The commonest nodal metastases were from lung cancer, followed by gastroenteric tumor and prostatic cancer. For most metastases, diagnosis is not difficult after the primary disease has emerged [25]. Patients with sarcoidosis usually have chest, skin, and eye involvement. The CT scan of sarcoidosis usually shows symmetrical enlargement of bilateral hilar and peritracheal lymph nodes, which can be used to differentiate it from tuberculosis [24]. The enlarged lymph nodes mainly locate in the upper and middle zone of the mediastinum and more in the right side than the left side [24, 26]. In our study, the enlarged and fused lymph nodes of eight misdiagnosed

Table 5: The comparison of SUVmax, long axis, and short axis of lymph nodes in the common causes of mediastinal lymphadenopathy.

Diseases	n	SUVmax	Long axis (cm)	Short axis (cm)
Lymphoma	25	14.36 ± 6.35	8.51 ± 4.13	5.03 ± 2.40
Metastatic lymph nodes	26	10.97 ± 4.11	3.77 ± 1.29	3.00 ± 1.00
Sarcoidosis	16	15.90 ± 5.07	3.34 ± 0.91	1.98 ± 0.47
Tuberculosis	17	11.29 ± 5.16	2.60 ± 1.04	1.74 ± 0.63
Lymphadenitis	8	10.90 ± 3.16	2.25 ± 0.59	1.28 ± 0.32
F	—	3.529	23.594	21.386
P	—	0.010	<0.001	<0.001

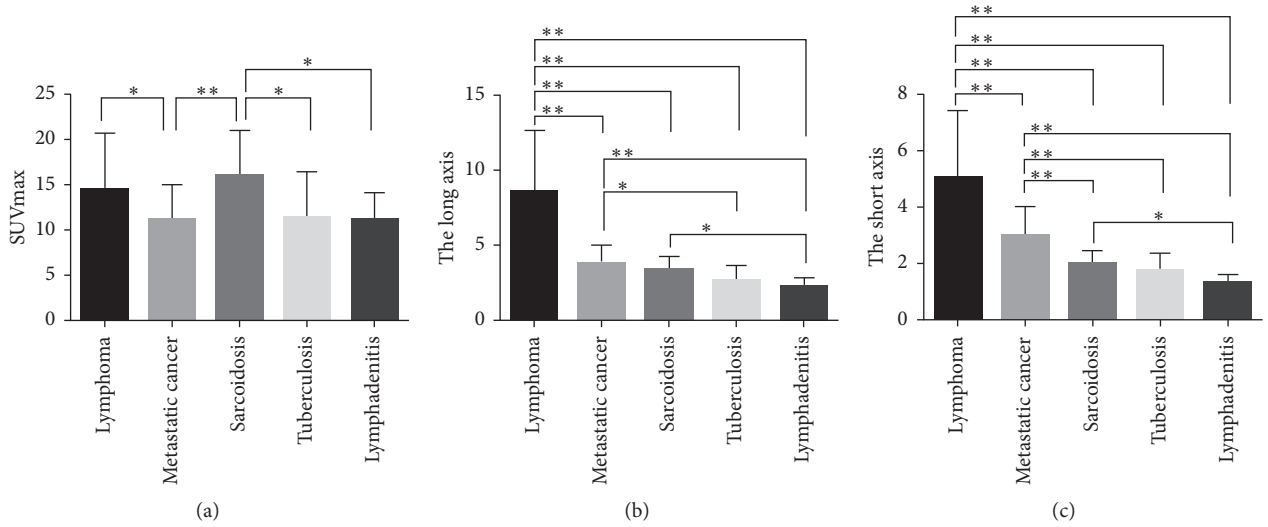

Figure 3: The comparison of SUVmax (a), long axis (b), and short axis (c) in five common mediastinal lymphadenopathy diseases ($^{**}P < 0.01$, $^{*}P < 0.05$).

cases had higher FDG uptake and a lack of typical tuberculosis clinical features with no caseous necrosis, which did not support tuberculosis. Hence, these findings need to be analyzed along with the clinical symptoms and laboratory test results.

The common causes of false negatives in the diagnosis of benign and malignant lesions are as follows. First, some low-grade tumors with lower FDG uptake may give rise to false negative results. Some researchers confirmed that the malignant tumor pathological type and degree of malignancy are closely related to FDG uptake [27]. There is a direct correlation between FDG uptake and extent of tumor invasion and growth rate. High-grade malignant tumors, bronchioloalveolar carcinoma, clear cell carcinoma, mucinous cell carcinoma, cystadenocarcinoma, and carcinoid often have low SUVmax measurements [28]. Second, smaller lymph nodes may give rise to false-negative results as well. The limited resolution of FDG-PET and the partial volume effect may prevent visualization of such small tumor deposits despite their potential accumulation of FDG [21, 29]. Several studies have shown a positive correlation between FDG uptake and the size of a lesion [30]. The threshold size of missed lesions is considered to be <8 mm [30]. A study from Takamochi showed that it was difficult for PET to detect metastatic lymph nodes measuring <5 mm [31]. In our study, three false-negative cases were misdiagnosed as benign lesions because the lymph nodes were all calcified and not fused, with pulmonary infection, and no evidence of a primary lesion or findings suggestive of malignancy on laboratory tests.

Our study found SUVmax was not of significant value in differentiating between benign and malignant mediastinal lymph nodes. The mean SUVmax in the benign group (13.10 ± 5.21) was greater than that in the malignant group (12.59 ± 5.50), which was different from the research of Kumar et al. With SUVmax of 6.2 as the cutoff as reported, the sensitivity, specificity, PPV, NPV, and accuracy were 87%, 70%, 68%, 87%, and 77%, respectively [6]. In our cases, the lymph nodes of the benign lesions had high FDG uptake, such as sarcoidosis (SUVmax 15.90 ± 5.07, $n = 16$) and tuberculosis (SUVmax 11.29 ± 5.16, $n = 17$). The further analysis of five common causes of mediastinal lymphadenopathy revealed that there was no significant difference between malignant lesions and sarcoidosis or tuberculosis.

SUVmax measured on PET/CT is a semiquantitative value that indicates the degree of aerobic glycolysis in a lesion [32]. In clinical diagnosis, the use of SUV in FDG-PET to diagnose cancer is an issue of ongoing controversy [10]. Interpretation of FDG PET is usually based on visual evaluation and not on SUV measurements because data have shown that the use of SUV failed to be more accurate than the visual evaluation in predicting the presence of malignancy [33, 34]. It is often assumed that FDG uptake is primarily within the malignant tumor cells and SUVmax is

a well-known measure indicating the aggressiveness of the tumor [35, 36]. But other cellular components such as normal parenchymal cells, atypical cells, inflammatory cells, fibroblasts, or hematopoietic progenitor cells may also take up FDG [32]. The SUVmax cutoff value of 2.5 was used commonly to differentiate between benign and malignant lesions based on an early literature report [13]. Kumar et al.'s study of mediastinal lymphadenopathy showed that appropriately increasing the cutoff values can improve the specificity while maintaining an acceptable sensitivity [6]. When 5.3 or 6.2 was used as the cutoff value, the accuracy would be improved (74% or 77%) [6].

In this study, the long axis and the short axis of lymph nodes were helpful in distinguishing between benign and malignant mediastinal lymph nodes, especially the short axis. The bigger the lymph nodes were, the higher the possibility of malignancy was. The result was consistent with some other researchers' view of the short axis as the most accurate indicator in the diagnosis of malignant lesions [37, 38]. Among five common causes of mediastinal lymphadenopathy, the short axis of lymphoma and metastatic lymph nodes was larger than that of other benign lesions.

There is no accurate cutoff for the short axis of lymph nodes to differentiate benign from malignant lymph nodes. Using ROC curve analysis in our study, the optimal threshold of the short axis of lymph nodes was 2.55 cm with sensitivity 73.1%, specificity 92.9%, and accuracy 81.9%. The mean of the short axis in malignant groups (3.95 ± 2.08 cm) was greater than that in benign groups (1.77 ± 0.60 cm). The malignant lymph nodes are high-grade, fast-growing, and fuse, which leads to the increased size of malignant lymph nodes. But there is still a certain misdiagnosis rate for the following reasons: First, the response to the same disease varies from person to person, such as sluggish response in elderly, immature immune system in children, a strong response in young adults, different response between the strong person and the infirm person [39]. Second, early stages of the disease are easily misdiagnosed as benign lesions. Hence, the short axis of lymph nodes is still not very accurate in distinguishing benign from malignant.

In addition, digital pathology has the potential to transform the histopathological data more and more "real," quantifiable and comparable to that of other disciplines such as nuclear medicine [40]. The examination of bioptic samples of patients subjected to PET/CT investigation can provide information about quantification of PET/CT targets or even the exact localization of the radiolabeled molecules in the tissues [40]. Taking advantage of this, a structured collaboration model between anatomic pathology and nuclear medicine can play a valuable role in the management of patients with unexplained mediastinal lymphadenopathy.

Our study showed that there was a certain value of PET/CT imaging combined with the size and metabolism of lymph nodes in the comprehensive evaluation of mediastinal lymphadenopathy. Although numerous studies have confirmed SUVmax has some value in the diagnosis of neoplastic diseases, SUVmax could not be the main index to distinguish between benign and malignant lesions, especially in locations where tuberculosis and other granulomatous disease are endemic. The integrated analysis of the PET/CT images and case history, clinical manifestation, laboratory tests, and a variety of imaging techniques is necessary. However, the size of the lymph nodes seems to have some diagnostic value, especially the short axis of lymph nodes.

Our study has some limitations. Firstly, since it is a retrospective study and has a limited number of cases, a study incorporating a large number of patients is needed. Secondly, because the enhanced CT was not performed, we were unable to accurately calculate the number of lymph nodes. The analysis based on lymph nodes would be much helpful. Thirdly, partial volume effect is not considered in this study, which is important to accurately correct the PET/CT signal in the lymph nodes. Moreover, metabolic tumor volume (MTV) and total lesion glycolysis (TLG) obtained from PET/CT images show more and more diagnosis and prognosis information. In the next work, we may continue to conduct the research about the role of MTV and TLG in the differential diagnosis of enlarged mediastinal lymph nodes.

5. Conclusions

SUVmax, a commonly used semiquantitative value for the lesion aerobic glycolytic rate, was not of significant value in patients with enlarged mediastinal lymph nodes in this study. Some benign lesions, such as sarcoidosis and tuberculosis, had high FDG uptake. Utilizing both the PET FDG uptake and CT characteristics including size and attenuation in an overall integrated report along with high quality clinical and laboratory data in a multidisciplinary meeting-like environment enables one more likely to reach the overall correct diagnosis for the patient.

Data Availability

The data used to support the findings of this study are available from the corresponding author upon request.

Ethical Approval

This retrospective study of existing patient data and images was approved by the institutional review board of Union Hospital, Tongji Medical College, Huazhong University of Science and Technology. The requirement for informed consent was waived.

Disclosure

An earlier version of the article has been presented as an abstract in the Annual Congress of the European Association of nuclear Medicine (EANM'14) 2014, according to the following link: https://link.springer.com/article/10.1007%2Fs00259-014-2901-9.

Conflicts of Interest

The authors declare that there are no conflicts of interest.

Authors' Contributions

Congcong Yu and Xiaotian Xia contributed equally to the article.

Acknowledgments

This work was supported by the National Natural Science Foundation of China (No. 81630049), the Clinical Research Physician Program of Tongji Medical College, and the Huazhong University of Science and Technology (No. 5001530008).

References

[1] F. C. Detterbeck, M. A. Jantz, M. Wallace, J. Vansteenkiste, G. A. Silvestri, and American College of Chest Physicians, "Invasive mediastinal staging of lung cancer: ACCP evidence-based clinical practice guidelines (2nd edition)," *Chest*, vol. 132, no. 3, pp. 202S–220S, 2007.

[2] E. M. Toloza, L. Harpole, F. Detterbeck, and D. C. McCrory, "Invasive staging of non-small cell lung cancer: a review of the current evidence," *Chest*, vol. 123, no. 1, pp. 157S–166S, 2003.

[3] F. J. Herth, R. Eberhardt, M. Krasnik, and A. Ernst, "Endobronchial ultrasound-guided transbronchial needle aspiration of lymph nodes in the radiologically and positron emission tomography-normal mediastinum in patients with lung cancer," *Chest*, vol. 133, no. 4, pp. 887–191, 2008.

[4] J. T. Annema, M. I. Versteegh, M. Veseliç, P. Voigt, and K. F. Rabe, "Endoscopic ultrasound-guided fine-needle aspiration in the diagnosis and staging of lung cancer and its impact on surgical staging," *Journal of Clinical Oncology*, vol. 23, no. 33, pp. 8357–8361, 2005.

[5] K. Czarnecka-Kujawa and K. Yasufuku, "The role of endobronchial ultrasound versus mediastinoscopy for non-small cell lung cancer," *Journal of Thoracic Disease*, vol. 9, no. 2, pp. S83–S97, 2017.

[6] A. Kumar, R. Dutta, U. Kannan, R. Kumar, G. C. Khilnani, and S. D. Gupta, "Evaluation of mediastinal lymph nodes using F-FDG PET-CT scan and its histopathologic correlation," *Annals of Thoracic Medicine*, vol. 6, no. 1, pp. 11–16, 2011.

[7] X. L. Lan, Y. X. Zhang, Z. J. Wu, Q. Jia, H. Wei, and Z. R. Gao, "The value of dual time point (18)F-FDG PET imaging for the differentiation between malignant and benign lesions," *Clinical Radiology*, vol. 63, no. 7, pp. 756–764, 2008.

[8] S. Rankin, "[(18)F]2-fluoro-2-deoxy-D-glucose PET/CT in mediastinal masses," *Cancer Imaging*, vol. 10, no. 1A, pp. S156–S160, 2010.

[9] K. Kubota, K. Murakami, T. Inoue et al., "Additional value of FDG-PET to contrast enhanced-computed tomography (CT) for the diagnosis of mediastinal lymph node metastasis in non-small cell lung cancer: a Japanese multicenter clinical study," *Annals of Nuclear Medicine*, vol. 25, no. 10, pp. 777–786, 2011.

[10] N. C. Nguyen, A. Kaushik, M. K. Wolverson, and M. M. Osman, "Is there a common SUV threshold in oncological FDG PET/CT, at least for some common indications? a retrospective study," *Acta Oncologica*, vol. 50, no. 5, pp. 670–677, 2011.

[11] X. Li, H. Zhang, L. Xing et al., "Mediastinal lymph nodes staging by 18F-FDG PET/CT for early stage non-small cell lung cancer: a multicenter study," *Radiotherapy and Oncology*, vol. 102, no. 2, pp. 246–250, 2012.

[12] R. J. Cerfolio and A. S. Bryant, "Ratio of the maximum standardized uptake value on FDG-PET of the mediastinal (N2) lymph nodes to the primary tumor may be a universal predictor of nodal malignancy in patients with nonsmall-cell lung cancer," *Annals of Thoracic Surgery*, vol. 83, no. 5, pp. 1826–1829, 2007.

[13] G. Antoch, F. M. Vogt, L. S. Freudenberg et al., "Whole-body dual-modality PET/CT and whole-body MRI for tumor staging in oncology," *JAMA*, vol. 290, no. 24, pp. 3199–3206, 2003.

[14] S. Rankin, "PET/CT for staging and monitoring non-small cell lung cancer," *Cancer Imaging*, vol. 8, pp. S27–S31, 2008.

[15] X. Zhu, W. G. Xu, W. C. Ma, X. Y. Song, D. Dai, and L. Zhu, "A comparative study of 18F-FDG PET/CT and CT imaging in detection of axillary lymph node status of breast cancer," *Chinese Journal of Oncology*, vol. 37, pp. 388–391, 2010.

[16] E. M. Rohren, T. G. Turkington, and R. E. Coleman, "Clinical applications of PET in oncology," *Radiology*, vol. 231, no. 2, pp. 305–332, 2004.

[17] P. H. Jarritt, K. J. Carson, A. R. Hounsell, and D. Visvikis, "The role of PET/CT scanning in radiotherapy planning," *British Journal of Radiology*, vol. 79, no. 1, pp. S27–35, 2006.

[18] J. Konishi, K. Yamazaki, E. Tsukamoto et al., "Mediastinal lymph node staging by FDG-PET in patients with non-small cell lung cancer: analysis of false-positive FDG-PET findings," *Respiration*, vol. 70, no. 5, pp. 500–506, 2003.

[19] A. S. Bryant, R. J. Cerfolio, K. M. Klemm, and B. Ojha, "Maximum standard uptake value of mediastinal lymph nodes on integrated FDG-PET-CT predicts pathology in patients with non-small cell lung cancer," *Annals of Thoracic Surgery*, vol. 82, no. 2, pp. 417–422, 2006.

[20] A. Nambu, S. Kato, Y. Sato et al., "Relationship between maximum standardized uptake value (SUVmax) of lung cancer and lymph node metastasis on FDG-PET," *Annals of Nuclear Medicine*, vol. 23, no. 3, pp. 269–275, 2009.

[21] G. Rizzo, I. Castiglioni, G. Russo et al., "Using deconvolution to improve PET spatial resolution in OSEM iterative reconstruction," *Methods of Information in Medicine*, vol. 46, no. 2, pp. 231–235, 2007.

[22] T. P. Graeter, D. Hellwig, K. Hoffmann, D. Ukena, C. M. Kirsch, and H. J. Schäfers, "Mediastinal lymph node staging in suspected lung cancer: comparison of positron emission tomography with F-18-fluorodeoxyglucose and mediastinoscopy," *Annals of Thoracic Surgery*, vol. 75, no. 1, pp. 231–235, 2003.

[23] R. V. Venkateswaran, D. J. Barron, W. J. Brawn et al., "A forgotten old disease: mediastinal tuberculous lymphadenitis in children," *European Journal of Cardio-Thoracic Surgery*, vol. 27, no. 3, pp. 401–404, 2005.

[24] S. S. Tang, Z. G. Yang, W. Deng, H. Shao, J. Chen, and L. Y. Wen, "Differentiation between tuberculosis and lymphoma in mediastinal lymph nodes: evaluation with contrast-enhanced MDCT," *Clinical Radiology*, vol. 67, no. 9, pp. 877–883, 2012.

[25] L. Xiong, X. Mao, C. Li, Z. Liu, and Z. Zhang, "Posterior mediastinal tuberculous lymphadenitis with dysphagia as the main symptom: a case report and literature review," *Journal of Thoracic Disease*, vol. 5, no. 5, pp. E189–E194, 2013.

[26] M. Y. Luo, L. Liu, L. S. Lai, Y. X. Dong, W. W. Liang, and J. Qin, "Deepgoing study on intrathoracic tuberculous lymphadenitis in adults using multidetector CT," *Chinese Medical Journal*, vol. 123, no. 10, pp. 1283–1288, 2010.

[27] S. Fenchel, D. Grab, K. Nuessle et al., "Asymptomatic adnexal masses: correlation of FDG PET and histopathologic findings," *Radiology*, vol. 223, no. 3, pp. 780–788, 2002.

[28] S. Koukouraki, L. G. Strauss, V. Georgoulias, M. Eisenhut, U. Haberkorn, and A. Dimitrakopoulou-Strauss, "Comparison of the pharmacokinetics of 68Ga-DOTATOC and 18FFDG in patients with metastatic neuroendocrine tumours scheduled for 90Y-DOTATOC therapy," *European Journal of Nuclear Medicine and Molecular Imaging*, vol. 33, no. 10, pp. 1115–1122, 2006.

[29] J. W. Lee, B. S. Kim, D. S. Lee et al., "18F-FDG PET/CT in mediastinal lymph node staging of non-small-cell lung cancer in a tuberculosis-endemic country: consideration of lymph node calcification and distribution pattern to improve specificity," *European Journal of Nuclear Medicine and Molecular Imaging*, vol. 36, no. 11, pp. 1794–1802, 2009.

[30] C. S. Yap, C. Schiepers, M. C. Fishbein, M. E. Phelps, and J. Czernin, "FDG-PET imaging in lung cancer: how sensitive is it for bronchioloalveolar carcinoma?," *European Journal of Nuclear Medicine and Molecular Imaging*, vol. 29, no. 9, pp. 1166–1173, 2002.

[31] K. Takamochi, J. Yoshida, K. Murakami et al., "Pitfalls in lymph node staging with positron emission tomography in non-small-cell lung cancer patients," *Lung Cancer*, vol. 47, no. 2, pp. 235–242, 2005.

[32] D. Koksal, F. Demirag, H. Bayiz et al., "The correlation of SUVmax with pathological characteristics of primary tumor and the value of Tumor/Lymph node SUVmax ratio for predicting metastasis to lymph nodes in resected NSCLC patients," *Journal of Cardiothoracic Surgery*, vol. 8, no. 1, p. 63, 2013.

[33] D. Hellwig, T. P. Graeter, D. Ukena et al., "18F-FDG PET for mediastinal staging of lung cancer: which SUV threshold makes sense?," *Journal of Nuclear Medicine*, vol. 48, no. 11, pp. 1761–1766, 2007.

[34] S. K. Kim, M. Allen-Auerbach, J. Goldin et al., "Accuracy of PET/CT in characterization of solitary pulmonary lesions," *Journal of Nuclear Medicine*, vol. 48, no. 2, pp. 214–220, 2007.

[35] T. Berghmans, M. Dusart, M. Paesmans et al., "Primary tumor standardized uptake value (SUVmax) measured on fluorodeoxyglucose positron emission tomography (FDG-PET) is of prognostic value for survival in non-small cell lung cancer (NSCLC): a systematic review and meta-analysis (MA) by the European lung cancer working party for the IASLC lung cancer staging project," *Journal of Thoracic Oncology*, vol. 3, no. 1, pp. 6–12, 2008.

[36] Y. Tsutani, Y. Miyata, H. Nakayama et al., "Prognostic significance of using solid versus whole tumor size on high-resolution computed tomography for predicting pathologic malignant grade of tumors in clinical stage IA lung adenocarcinoma: a multicenter study," *Journal of Thoracic and Cardiovascular Surgery*, vol. 143, no. 3, pp. 607–612, 2012.

[37] K. Yonetsu, M. Sumi, M. Izumi, M. Ohki, S. Eida, and T. Nakamura, "Contribution of Doppler sonography blood flow information to the diagnosis of metastatic cervical nodes in patients with head and neck cancer: assessment in relation to anatomic levels of the neck," *AJNR American Journal of Neuroradiology*, vol. 22, no. 1, pp. 163–169, 2001.

[38] M. Sumi, M. Ohki, and T. Nakamura, "Comparison of sonography and CT for differentiating benign from malignant cervical lymph nodes in patients with squamous cell carcinoma of the head and neck," *American Journal of Roentgenology*, vol. 176, no. 4, pp. 1019–1024, 2001.

[39] A. Al-Ibraheem, A. Buck, B. J. Krause, K. Scheidhauer, and M. Schwaiger, "Clinical applications of FDG PET and PET/CT in head and neck cancer," *Journal of Oncology*, vol. 2009, Article ID 208725, 13 pages, 2009.

[40] M. Scimeca, N. Urbano, R. Bonfiglio, O. Schillaci, and E. Bonanno, "Management of oncological patients in the digital era: anatomic pathology and nuclear medicine teamwork," *Future Oncology*, vol. 14, no. 11, pp. 1013–1015, 2018.

Hindawi
Contrast Media & Molecular Imaging
Volume 2018, Article ID 5308517, 11 pages
https://doi.org/10.1155/2018/5308517

Research Article

Automated Detection and Segmentation of Nonmass-Enhancing Breast Tumors with Dynamic Contrast-Enhanced Magnetic Resonance Imaging

Ignacio Alvarez Illan,[1] **Javier Ramirez**,[1] **J. M. Gorriz**,[1] **Maria Adele Marino**,[2] **Daly Avendano**,[2] **Thomas Helbich**,[3] **Pascal Baltzer**,[3] **Katja Pinker**,[2,3] **and Anke Meyer-Baese**[4]

[1]*Signal Theory and Communications Department, Universidad de Granada, Granada, Spain*
[2]*Department of Radiology, Memorial Sloan-Kettering Cancer Center, NewYork, USA*
[3]*Department of Biomedical Imaging and Image-Guided Therapy, Division of Molecular and Gender Imaging, Medical University Vienna/AKH Wien, Wien, Austria*
[4]*Scientific Computer Department, Florida State University, Tallahassee, FL 32306, USA*

Correspondence should be addressed to Ignacio Alvarez Illan; illan@ugr.es

Katja Pinker and Anke Meyer-Baese contributed equally to this work

Received 31 July 2018; Accepted 16 September 2018; Published 24 October 2018

Academic Editor: Orazio Schillaci

Nonmass-enhancing (NME) lesions constitute a diagnostic challenge in dynamic contrast-enhanced magnetic resonance imaging (DCE-MRI) of the breast. Computer-aided diagnosis (CAD) systems provide physicians with advanced tools for analysis, assessment, and evaluation that have a significant impact on the diagnostic performance. Here, we propose a new approach to address the challenge of NME lesion detection and segmentation, taking advantage of independent component analysis (ICA) to extract data-driven dynamic lesion characterizations. A set of independent sources was obtained from the DCE-MRI dataset of breast cancer patients, and the dynamic behavior of the different tissues was described by multiple dynamic curves, together with a set of eigenimages describing the scores for each voxel. A new test image is projected onto the independent source space using the unmixing matrix, and each voxel is classified by a support vector machine (SVM) that has already been trained with manually delineated data. A solution to the high false-positive rate problem is proposed by controlling the SVM hyperplane location, outperforming previously published approaches.

1. Introduction

Accurate methods for early diagnosis of breast cancer are pivotal and contribute to an improved prognosis and survival outcomes in breast cancer patients. There is a consensus that dynamic contrast-enhanced magnetic resonance imaging (DCE-MRI) is the most sensitive test for breast cancer detection and the backbone of any MRI protocol, enabling simultaneous assessment of tumor morphology and enhancement kinetics that evaluate neoangiogenesis as a tumor-specific feature. DCE-MRI has an excellent sensitivity and good specificity for lesions presenting as mass enhancement [1]. However, nonmass-enhancing (NME) lesions exhibit a heterogeneous appearance with high variations in kinetic characteristics and morphological patterns on DCE-MRI [2]. Consequently, DCE-MRI has reported lower specificity and sensitivity of 35% and 73% for NME lesions, much lower than those for mass-enhancing lesions. A set of computer-aided diagnosis (CAD) systems for breast cancer diagnosis on DCE-MRI has been developed with satisfactory performance results. However, in breast tumors presenting as NME lesions, the performance with low specificity is still suboptimal.

For a CAD system to be used in breast DCE-MRI, two features are important to evaluate (i) the ability of the CAD to correctly differentiate between malignant and benign lesions and (ii) the ability of the CAD system to correctly locate malignant lesions within the 3D spatial volume. To evaluate the first feature, the diagnostic accuracy, specificity, and sensitivity are usually reported. To evaluate the second feature, commonly, the Dice similarity coefficient (DCS) is calculated between the CAD segmentation and some other ground truth segmentation. In most cases, a manual segmentation of the lesions is performed by experienced radiologists as ground truth. However, it has to be noted that even with expert's interpretation, visual readings are prone to subjective errors [3], and specificity of DCE-MRI is limited particularly in small and nonmass-enhancing lesions, resulting in unnecessary breast biopsies [4]. In addition, CAD systems for breast cancer diagnosis have a reported high false-positive rate and, consequently, low specificity. However, this does not necessarily mean that CAD systems misclassify benign lesions as malignant. Therefore, it is not clear whether CAD systems can be optimized to improve lesion segmentation independently from lesion classification, or if irregardless, they will inherently suffer from the same limitations such as the low specificity reported in visual readings of DCE-MRI.

In this work, we examined the relationship between the false-positive rate of CAD systems for breast cancer diagnosis and lesion segmentation on DCE-MRI. To achieve our aim, we obtained rich characterization of data through advanced processing techniques, combined with machine-learning paradigms intended for big data analysis, and used the resulting information to build a CAD system. We did not introduce any a priori knowledge about the disease in the workflow in order that all information may be completely data driven, which thereby also enabled us to identify new features not currently in the Breast Imaging-Reporting and Data System (BI-RADS) classification criteria that could potentially improve segmentation of visual readings. Both morphological and kinetic descriptors are considered in BI-RADS lexicons. However, in NME lesions, morphological descriptors are hard to define, and therefore, kinetic behavior can be an important source of information. Therefore, using only dynamic information of the tissue, we performed a supervised method to detect and segment nonmass-enhanced lesions on the breast.

Lesion segmentation has been successfully achieved using unsupervised clustering methods [5], fuzzy c-means (FCM) [6], or improvements over FCM [7]. In unsupervised clustering, sophisticated preprocessing must be implemented to control the false-positive rate, with fine tuning of parameters and/or heuristic steps. On the contrary, it has been demonstrated that processing of dynamic signals provides relevant information for classification of tissues, such as principal component analysis- (PCA-) based decompositions closely related to the 3TP method [8].

Thus, we undertook a combination of supervised segmentation and signal processing to successfully segment NME lesions with control of the false-positive rate. Independent component analysis (ICA) was used to extract a set of independent curves that described the possible dynamic behavior of different breast tissues. ICA has been shown to provide richer descriptions of underlying patterns than PCA [9, 10], and therefore, it was used for supervised classification in our work. We also incorporated machine learning, whereby we trained a classifier using the information encoded in a whole dataset of subjects, including the dynamic behavior of benign and malignant tissues. Considering features at the voxel level, the system "learned" to characterize malignant tissues with a support vector machine (SVM). A procedure was implemented to fix the SVM hyperplane location, reducing and controlling the false-positive rate. Projecting new unseen data using the unmixing matrix allowed us to obtain the features for estimating the generalization capabilities in a cross-validation scheme and compare them with visual readings of the images reported in the literature and other CAD system approaches.

The methods proposed within this work demonstrate that NME lesions can be detected with kinetic information by using multiple enhancement curves, providing a promising approach for improving breast cancer diagnosis. Accurate diagnostic methods as the one we hereby present may have an impact not only on accurate diagnosis but also in reducing unnecessary breast biopsies.

1.1. Related Work. The use of CAD systems to improve visual readings of DCE-MRI in breast cancer ranges from purely visual methods to automatic classification. The present work combines visual comparison aspects with automatic classification techniques, thus adding a value to purely visual comparison techniques based on PCA or self-organizing map (SOM), such as in [8, 11], and complementing pure classification approaches, such as in [12, 13]. Specifically, the PCA approach in [8] extends the three-point technique (3PT) by adding an eigenvector decomposition of the time signals. However, that decomposition does not provide an independent set of sources, but only a set of uncorrelated ones. The time-intensity curve estimation in [14] also seeks for hidden kinetics, but applies them to mass lesions. Concerning the automatic classification CADs, most approaches are concentrated on the detection and classification of mass-enhancing lesions, by combining kinetic and morphological features [12, 13, 15, 16], like shape, margins, and internal enhancement distribution [17], textural kinetics [18], or more recently using deep neural networks [19, 20], among others. The detection and segmentation of lesions are usually performed as a manual or semimanual task, in which regions of interest (ROIs) are manually defined or obtained from seeds with manual inputs.

For automatic lesion segmentation, keeping an acceptable false-positive rate is a common issue in DCE-MRI CAD systems of the breast [21]. In many of these cases, unsupervised methods for lesion segmentation, such as FCM algorithms in [6, 22], are used, and then the features extracted from the lesions are used for classification. Complex workflows that include vessel detection, whole-breast segmentation, and several preprocessing steps have been proposed to control false-positive detection [5, 7, 23, 24].

2. Methods

Each voxel of the DCE-MRI image has a time signal representing the enhancement kinetics of the different contributing breast tissues. A set of DCE-MRI time signals can be analyzed in terms of the blind source separation problem, which proposes that the different dynamic behaviors can be expressed as a linear combination of a reduced set of sources, making very little assumptions on the nature of that combination. Those sources and their scores can be used as features for classification, as depicted in Figure 1.

2.1. ICA-Based Enhancement Curve Analysis. ICA offers a solution to the blind source separation problem estimating a set of sources that maximize the statistical independence between them, measured in terms of a cost function. In the literature, several functions have been used to measure statistical independence between signals [25]. Here, we used the FastICA algorithm [26] with mutual information as a measure function. Contrary to other eigenimage decompositions based on spatial ICA, like in face recognition [27] and brain imaging [9, 28], the independent sources are obtained here in the temporal domain; in other words, we work on a voxel level.

Thus, each voxel defines a temporal curve $\mathbf{x}(t_j)$ with $t_1, \ldots, t_N$ temporal points. A set of voxels $\{\mathbf{x}_i\}, i = 1, \ldots, M$ forms an image and defines the $N \times M$ matrix $\mathbf{X}$ of observed signals. The ICA task is to find the mixing matrix $\mathbf{A}$ and the set of sources $\mathbf{S}$:

$$\mathbf{X} = \mathbf{AS}. \tag{1}$$

The mixing matrix $\mathbf{A}$ is an $N \times N$ matrix that linearly combines the independent "images." Contrary to other related methods, such as PCA, ICA does not provide a natural way to sort the N independent components. However, it is a relevant question whether or not a reduced set $p < N$ of components contains noisy and discardable information. The mean squared error (MSE) between the enhancement time signals and the reconstructed signals using the k source $\mathbf{s}_k$ is calculated as follows:

$$\mathrm{MSE}(k) = \frac{1}{N_\mathrm{t} \cdot N_\mathrm{r}} \sum_{i,j} \left(\mathbf{x}_i\left(t_j\right) - a_{jk} \cdot s_{ki}\right)^2, \tag{2}$$

and used as a parameter to measure the noise content of each $\mathbf{s}_k$ source, with $k = 1, \ldots, N$.

When working at the voxel level, Equation (1) can also be understood as a linear decomposition of each vector $\mathbf{x}(t_j)$ into a set of temporal sources whose coefficients belong to the independent sources. Therefore, each voxel location $\{\mathbf{x}_i\}$ has N coefficients s_{ji} to $j = 1, \ldots, N$, whose values are maximally independent and measure the importance of each temporal source to recover that voxel dynamics, by linearly combining them (Figure 1). In the rest of the paper, we will refer to these coefficients as the scores.

It is important to stress that working on a voxel level will allow data from different patients to be included in the matrix set $\mathbf{X}$. Therefore, the obtained set of sources $\mathbf{S}$ does not have to be restricted to represent the particular dynamic enhancement present in a single subject but can be used to model all the possible curves that independently characterize each BI-RADS category.

For new unseen data $\tilde{x}$ at the voxel level, the scores are extracted from $\tilde{x}$ by projecting it onto the subspace E spanned by the signals from the matrix $\mathbf{A}$. Specifically, let $\{\mathbf{a}_1, \ldots, \mathbf{a}_p\}$ be the basis set of temporal curves spanning the subspace E and then $\mathbf{A}$ denote the N-by-p matrix of which columns are $\mathbf{a}_1, \ldots, \mathbf{a}_p$. Let $p \leq N$, as some of the signals may have been removed due to their noisy nature. Since this basis need not be orthogonal, a well-known result of linear algebra stated that the projection is given by

$$\mathbf{P}_\mathrm{A} = \mathbf{A}\left(\mathbf{A}^T\mathbf{A}\right)^{-1}\mathbf{A}^T, \tag{3}$$

so that the application of that operator on a voxel signal $\tilde{x}(t)$:

$$\mathbf{s} = \mathbf{P}_\mathrm{A}\tilde{x}, \tag{4}$$

projects it to the subspace E, obtaining its p scores $\mathbf{s}$ on that subspace.

The independent component scores $\mathbf{s}_k$ of the dataset are used as feature vector inputs of a SVM to learn the different enhancement patterns associated with malignant and benign tissues.

2.2. False-Positive Rate Control by SVM Hyperplane Translation. SVM is a machine-learning algorithm that separates a given set of binary labeled training data with a hyperplane that is maximally distant from the two classes (known as the maximal margin hyperplane). The objective is to build a function $f : \mathrm{IR}^p \longrightarrow \{1, 0\}$ using training data, consisting of p dimensional patterns x_i and class labels y_i:

$$(\mathbf{x}_1, y_1), (\mathbf{x}_2, y_2), \ldots, (\mathbf{x}_\mathrm{M}, y_\mathrm{M}) \in (\mathrm{IR}^p \times \{1, 0\}), \tag{5}$$

so that f will correctly classify new examples $(\tilde{x}, y)$. The problem of finding the maximal margin hyperplane is usually solved by quadratic programming algorithms that try to minimize a margin cost function J:

$$J(\mathbf{w}, w_0, \xi) = \frac{1}{2}\|\mathbf{w}\|^2 + C\sum_{i=1}^{l}\xi_i, \tag{6}$$

subject to the inequality constraints:

$$y_i\left[\mathbf{w}^T x_i + w_0\right] \geq 1 - \xi_i, \quad \xi_i \geq 0\, i = 1, 2, \ldots, l, \tag{7}$$

where the slack variables ξ_i incorporate to the optimization of those feature vectors that are not separable (details can be found in [29]). The solution to that problem can be expressed by a linear combination of a subset of vectors, called support vectors:

$$d(\mathbf{x}) = \sum_{i=1}^{N_\mathrm{S}} \alpha_i y_i K(\mathbf{s}_i, \mathbf{x}) + w_0, \tag{8}$$

where $K(.,.)$ is the kernel function, α_i is a weight constant derived from the SVM process, and $\mathbf{s}_i$ are the N_S support vectors [29]. Taking the sign of the function leads to the binary classification solution.

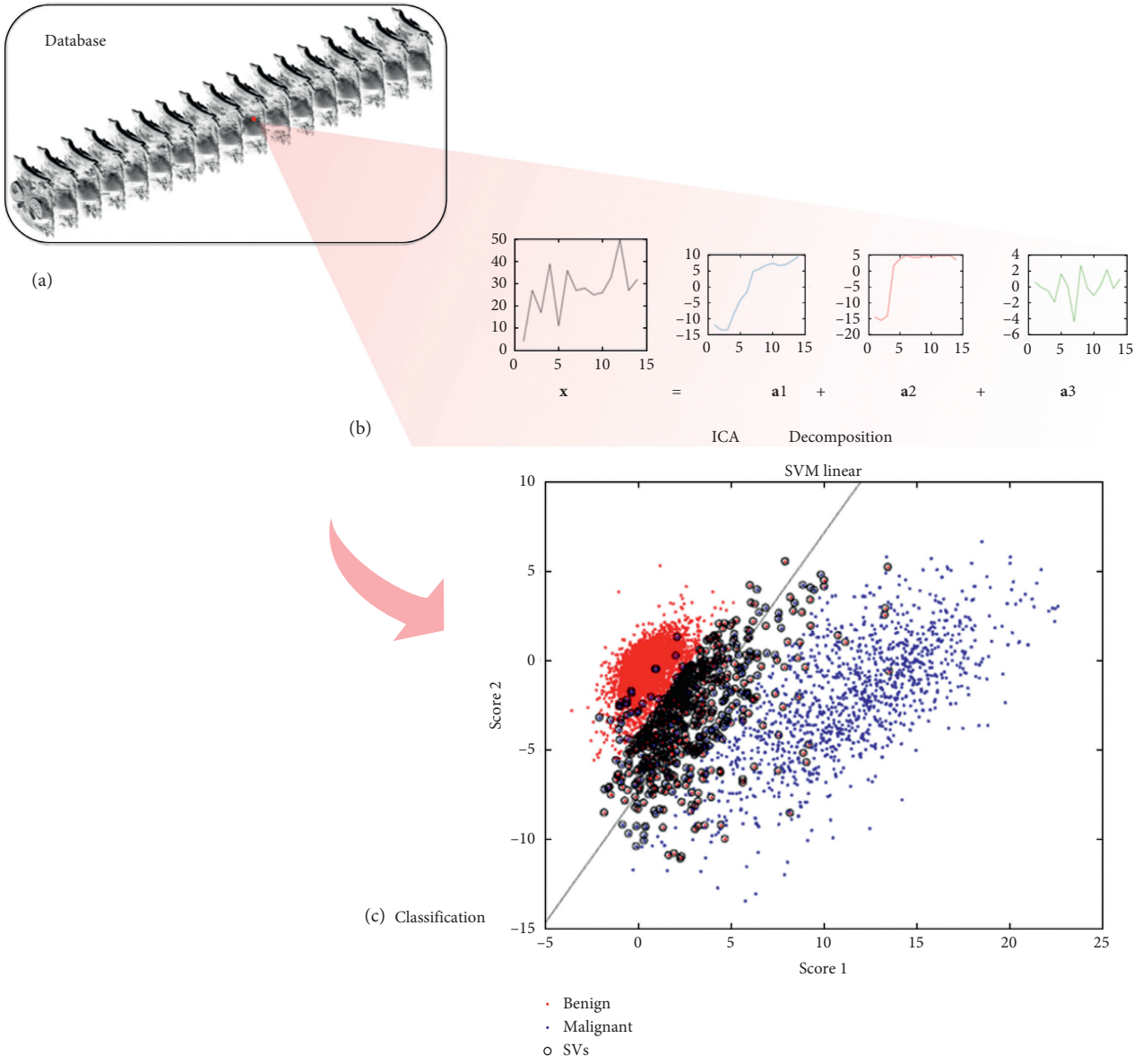

FIGURE 1: (a) Time sequence of database images. (b) Decomposition of a sample time signal $\mathbf{x}$ into a linear combination of independent sources by ICA and its corresponding scores $\mathbf{a}_1, \mathbf{a}_2, \ldots, \mathbf{a}_s$. (c) Scatter plot of the first scores and the SVM hyperplane classifier.

Here, we propose an SVM hyperplane translation in terms of the slack variables ξ_i to control the number of false positives. We add a new term $g(\mathbf{s}_i, \xi_i)$ to the hyperplane-defining function $d(\mathbf{x})$ so that the classification solution is now defined by

$$f(\mathbf{x}) = \text{sign}\{d(\mathbf{x}) + g(\mathbf{s}_i, \xi_i)\}, \tag{9}$$

where the function g takes the two-class average distance to the hyperplane of those support vectors with $\xi_i > 1$, measured by the kernel metric K. Common kernels that are used by SVM practitioners for the nonlinear feature mapping are as follows:

(i) Polynomial function:

$$K(\mathbf{x}, \mathbf{y}) = [\gamma(\mathbf{x} \cdot \mathbf{y}) + c]^{\text{d}}. \tag{10}$$

(ii) Radial basis function (RBF):

$$K(\mathbf{x}, \mathbf{y}) = \exp\left(-\gamma \|\mathbf{x} - \mathbf{y}\|^2\right), \tag{11}$$

as well as the linear kernel, in which $K(.,.)$ is simplified as a scalar product, and therefore, g in Equation (9) would average the Euclidean distance in that particular case.

2.3. Dataset. The dataset used for analysis consisted of sixteen patients that presented with NME breast tumors at DCE-MRI. This patient cohort is a subset from a larger cohort undergoing multiparametric MRI using inclusion criteria described in detail in [30]. All patients underwent MRI of the breast using a 3T MRI scanner (Tim Trio; Siemens, Erlangen, Germany) with a dedicated, bilateral, 4-

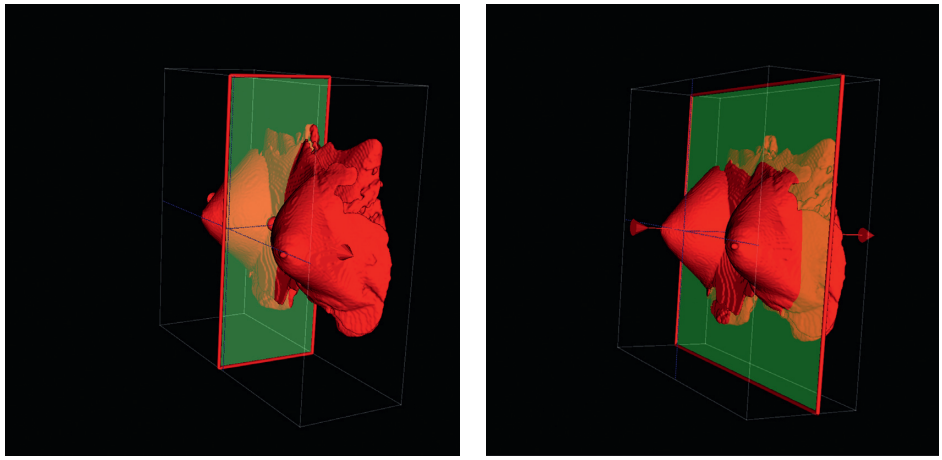

(a) (b)

Figure 2: Exclusion of internal organs by detection of the middle chest plane. (a) Middle sagittal plane. (b) Middle chest plane.

channel breast coil in vivo (Orlando, FL), and the imaging protocol comprised both high-spatial and -temporal resolution. Three high-spatial resolution images were taken, precontrast, peak, and postcontrast as a coronal T1-weighted (3D) FLASH sequence, with water excitation and fat suppression, with the following sequence parameters: TR/TE 877/3.82 milliseconds, FOVr 320 mm, SI 1 mm isotropic, 96 slices, flip angle 9°, matrix 320/134, 1 average, and acquisition time 2 minutes. A high-temporal resolution, contrast-enhanced, coronal T1-weighted (VIBE) sequence was obtained with the following sequence parameters: TR/TE 3.61/1.4 milliseconds, FOVr 320 mm, SI 1.7 mm isotropic, 72 slices, flip angle 6°, matrix 192/192, 1 average, and 13.2 seconds of acquisition time per volume leading to 3.45 minutes for 17 measurements. A second set of high-spatial resolution T1-weighted imaging (repeated 3D-FLASH) was acquired after these 17 low-spatial VIBE resolution images, as the peak enhancement of the lesion could be expected at the end of this time span ([30] and references therein). Finally, high-temporal resolution (repeated VIBE with 25 measurements, leading to an acquisition time of 5 minutes 35 seconds, and repeated 3D-FLASH for dynamic assessment of lesion wash-out) was performed, and then high-spatial resolution T1-weighted images were recorded. The contrast agent used was Gd-DOTA (generic name: gadoterate meglumine; Dotarem, Guerbet, France), injected intravenously as a bolus (0.1 mmol per kilogram body weight) and administered with a power injector (Spectris Solaris EP; Medrad, Pittsburgh, PA) at 4 mL/s followed by a 20 mL saline flush. The contrast agent was injected 75 seconds after starting the first coronal T1-weighted VIBE.

NME breast tumors were visually assessed by three expert radiologists following the American College of Radiology BI-RADS Atlas [31] and delineated using the OsiriX software on the 3T high-spatial resolution volumes. All NME lesions were classified as BI-RADS 4: suspicious, or BI-RADS 5: highly suspicious of malignancy. Histopathology was used as the standard of reference. There were eleven invasive ductal carcinomas (IDCs), three ductal carcinomas in situ (DCISs), and two invasive lobular carcinomas (ILCs).

2.4. Preprocessing. All dynamic sequences were registered to the precontrast volume. This preprocessing step was required to remove any spatial misalignments on the sequence caused by involuntary movements of the patient. The algorithm employed to perform this task was the SPM12 [32] registration algorithm, which performs affine and nonaffine transformations on the data by minimizing a similarity measure cost function, selected to be the mutual information metric. Afterwards, a 3D Gaussian filter of size 2FWHM was used to smoothen the images.

In spite of the existence of automatic and accurate methods for performing whole-breast segmentation [33, 34, 35, 36], we performed this task straightforwardly finding the middle chest point as in [12], and discarding the content of the image after this point, reducing the original number of $192 \times 192 \times 72 \approx 2.6 \cdot 10^6$ voxels contained in each image to $\approx 1.6 \cdot 10^5$, and guaranteeing the exclusion of heart and other organs' noisy signals. Concretely, the middle chest point was obtained by performing the following steps (Figure 2):

(1) Compute the cross-correlation of the convolution of the image with itself in the sagittal direction. The middle sagittal plane will lie in the symmetry plane of the body, and due to its symmetry, it will reach the maximum convoluted cross-correlation.

(2) Compute the intensity gradient of the middle chest slice in the coronal direction and find its maximum m_y. Remove the internal part of the image that lies in the coronal direction after the middle chest plane $y = m_y$.

The described procedure ensured the removal of voxels that lie inside the thoracic cavity and the chest wall as well as background voxels.

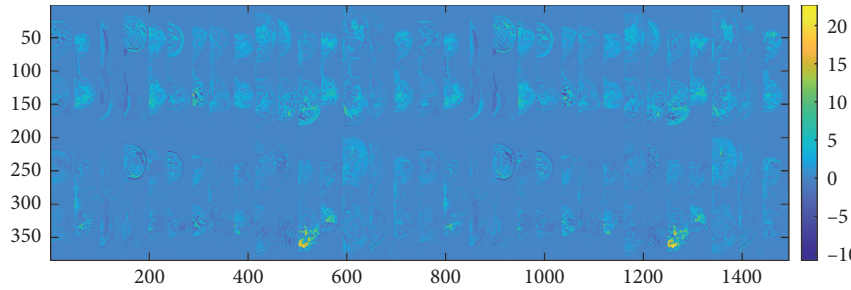

Figure 3: One middle axial slice for the 16 patients from the projected independent component space of the dataset. Intensity represents voxelwise scores of the first and second independent components in the 3D MRI space. The scores of the first IC, on the top, correspond with the IC1 in blue in Figure 5. The scores of the second IC, on the bottom, correspond with the IC2 in red in Figure 5. High values on the IC2 (in yellow) can be related to malignancy.

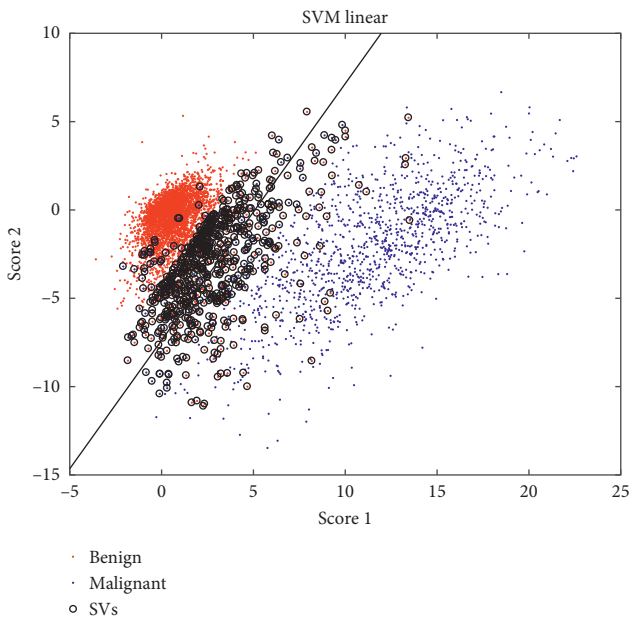

Figure 4: Scatter plot of the scores corresponding to the first two independent components of the training data, together with the linear decision SVM function (in black) and the support vectors (SVs).

The manual delineations of the lesions were performed by three expert radiologists on 3T high-spatial resolution images using the OsiriX software, recorded as a set of axial point coordinates in mm. The Bresenham algorithm [37] was used to transform the coordinate points into 3D binary masks, and a decimation was employed to downsample the masks to the size of the low-spatial high-temporal resolution images. Thus, the downsampled masks were used to define the class labels of each voxel: 1 if the voxel was in the mask, and 0 otherwise.

3. Experiments

The dataset was divided into three subsets: training data, validation data, and testing. Training and validation data comprised half of the dataset, while the test set consisted of the other half. The data were considered at the voxel level. Therefore, after discarding nonrelevant parts of the image, a random selection of $N_a \approx 5 \cdot 10^3$ benign voxel samples from the pool of all nonlesion voxels of the images was performed to balance the training set, resulting in a $2 * N_a \times p$ training and validating data matrix.

The voxel data were used as input to the FastICA algorithm, obtaining a set of scores for each voxel that served as feature vectors for training and validating an SVM in a cross-validation scheme. The validation step is performed in two stages:

(i) Firstly, different parameters were optimized within a 10-fold cross-validation scheme: (i) the optimal dimensionality of the data h and (ii) the optimal kernel (linear, polynomial, or RFB). The optimal value for h was obtained by sorting the independent components by their MSE defined in Equation (2), and the feature space dimension was changed by sequentially increasing the number of components included on the scores. The optimal kernel was selected by comparing the classification performance, based on the classification error.

(ii) Secondly, once the number of components and the kernel function were fixed, the decision boundary location of the SVM was analyzed in an enlarged test dataset of size $\approx 4 \cdot 10^5$, that contained all the discarded voxels in the validation step.

4. Results

The scores defined in Equation (1) are depicted in two different spaces: the 3DDCE-MRI space coregistered with the original data (Figure 3) and the E subspace spanned by the first two temporal sources $\mathbf{a}_1$ and $\mathbf{a}_2$ (Figure 4), sorted according to the MSE-defined criteria. The representation in the 3DDCE-MRI space shows that similar score values are grouped together around tissues that have a similar enhancement. On the bottom, voxels belonging to the lesions present a high score value, revealing that the associated independent component encodes the malignant dynamic information. On the top, the distribution of score values does not concentrate on specific regions but spreads over the breast tissues revealing a relation with normal tissue enhancement dynamics. That information complements the

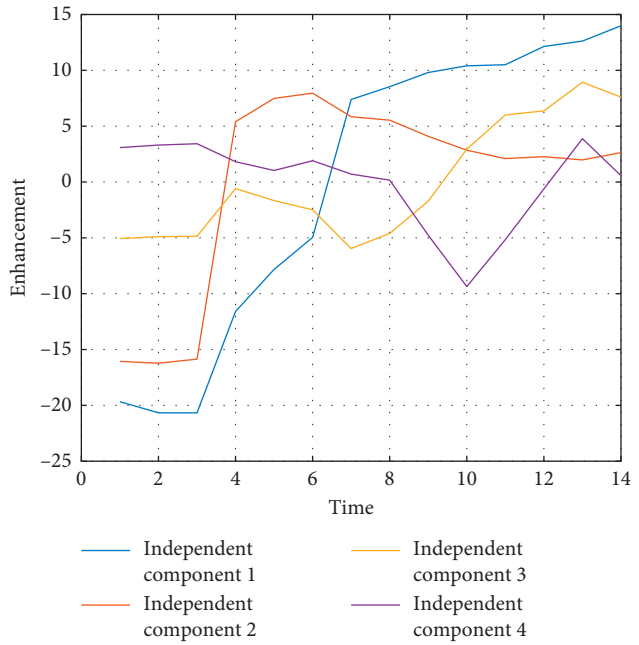

Figure 5: First four independent components sorted by MSE. In red, the IC2 shows typical "malignant" dynamics, while in blue, IC1 shows a persistent enhancement curve, characteristic of benign tissues.

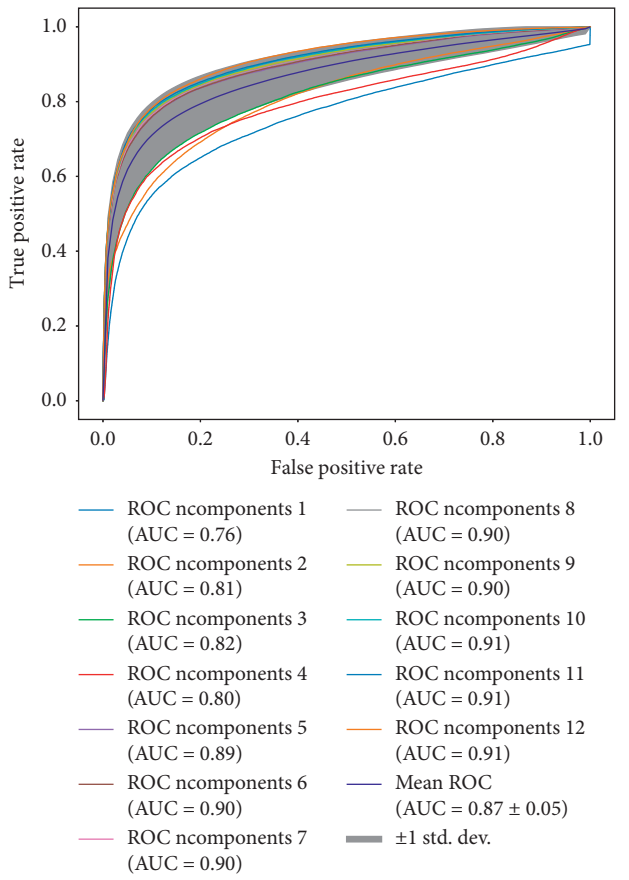

Figure 6: ROC and area under the curve (AUC) values on the cross-validation scheme for the RBF kernel by varying the number of components on ICA. ICA components are sorted according to MSE.

representation on the E subspace, where a clear separation between tumor tissues represented in blue and normal tissues in red can be inferred, although some regions of overlapping are present. Also, the independent components $\mathbf{s}_1$ and $\mathbf{s}_2$ are shown in Figure 5, together with other extracted sources. It is interesting to note that being automatically data-driven extracted, these independent components take the form of enhancement curves: curve IC1 is a normal enhancement, while curve IC2 has a "typical" malignant behavior, according to model-based descriptions [1]. The remaining set of independent components cannot be assigned to any particular dynamic nor tends to form clusters of similar enhancement when depicted in 3D, therefore not possessing an obvious interpretation. However, the common classification into wash-out, plateau, and permanent enhancement of dynamic curves is reduced by ICA to only two clearly identifiable curves. Therefore, the ICA-based signal processing analysis reveals that dynamic enhancement curves reaching a plateau do not behave independently in the ICA sense from wash-out curves, while permanent enhancement curves do.

The results of the cross-validation are shown in Figures 4 and 6 and also in the left part of Table 1. In Figure 4, the $2 * N_a \times p$ training data are shown after the SVM is trained, and the obtained support vectors are marked with circles. From Figure 6, the optimal number of components used to reconstruct the signal is above 5, revealing that a simple decomposition of signals into benign and malignant behaviors can be enriched with other significant components reaching ROC values over 0.90.

Figure 7 shows the NME lesion delineated by the expert radiologist (in red), together with a distance-to-hyperplane map (distance $d = 0$ is represented by a black contour). The value of each voxel in the map is defined in Equation (8). It can be seen that hyperplane location (value $d = 0$) produces big regions of false positives. Those regions are mostly concentrated around the delimited lesion, but extended regions can also be found in nonconnected regions where benign dynamics are expected. The false-positive rate can be controlled by modifying the defining value of the hyperplane location, set to 0 by definition in SVM. Translating the hyperplane towards the positive values produces a more conservative definition of feature vectors belonging to the +1 class. Therefore, only score values high above the hyperplane would be considered as malignant, while intermediate values not clearly projecting malignant-related score values will not be classified as lesion, decreasing the false-positive rate and increasing specificity. However, there must be a compromise between specificity and sensitivity, since increasing the defining value of the decision function also has an impact on the false-negative rate.This trade-off requires to be very finely tuned, as the number of benign samples is several orders of magnitude bigger than the number of malignant samples, producing an imbalanced classification problem. In Figure 8, the influence of the imbalanced classes can be perceived if compared with the scatter plot of the scores considering only the reduced training data of Figure 4. Although other solutions exist to the problem of imbalanced

Table 1: Performance parameters on training and validation data.

	Training				Validation DSC		
	Hinge loss	Accuracy	Specificity	Sensitivity	$d = 0$	Max.	DSC(μ_d) [DSC($\mu_d \pm \sigma_d$)]
PCA + linear SVM	0.9764	0.7263	0.6581	0.7944	0.31 ± 0.01	0.3382 ± 0.0005	0.3310 [0.3039 – 0.2169]
PCA + RBFSVM	0.9529	0.7263	0.6581	0.7944	0.31 ± 0.01	0.3382 ± 0.0005	0.3310 [0.3039 – 0.2169]
ICA + linear SVM	0.1254	0.9501	0.9410	0.9593	0.31 ± 0.01	**0.53 ± 0.01**	**0.5295 [0.475 − 0.484]**
ICA + RBFSVM	0.1083	0.9515	0.9573	0.9457	0.29 ± 0.01	0.44 ± 0.04	0.1085 [0.3711 – 0.0559]
Raw + linear SVM	2.4429	0.8026	0.8446	0.7605	0.15 ± 0.07	0.30 ± 0.05	0.2325 [0.1373 – 0.3058]

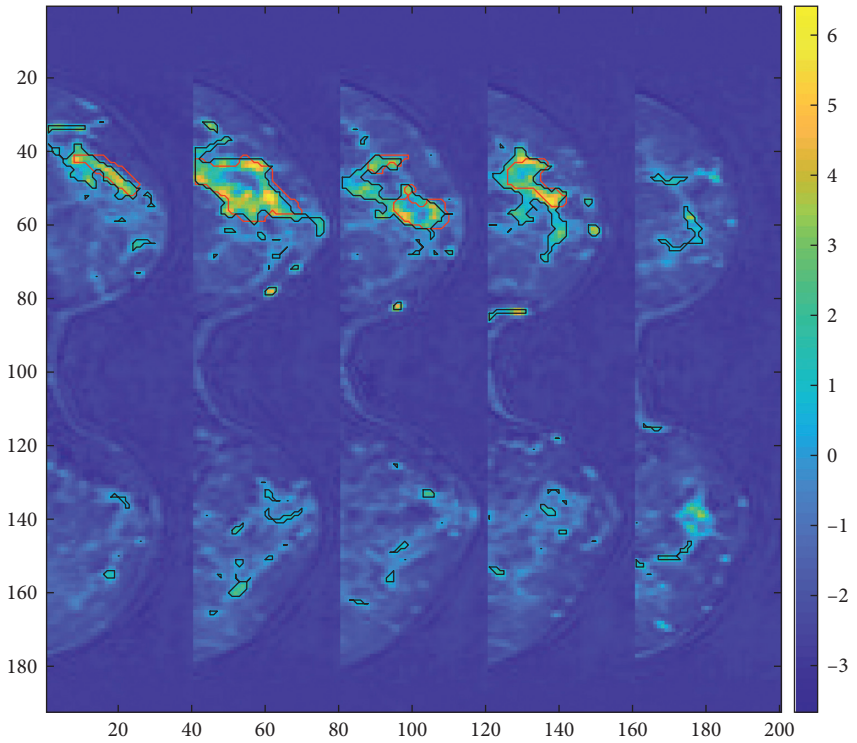

Figure 7: Five representative axial slices of an NME. The values on voxels represent the distance to the hyperplane after classification on a trained SVM. The black contour represents the location of the hyperplane at $d = 0$, and the red contour is the manual delineation of the lesion.

dataset in SVM classification, we propose here a very conservative approach, in which the hyperplane-defining value is translated into the +1 class region, guaranteeing that only very distant scores from the hyperplane are considered as malignant.The hyperplane-defining value g is given in Equation (9). Other values could be used to make this transformation but are prone to be affected by outlier support vectors that uncontrollably increase the false-negative rate. By averaging the support vector's distance to the hyperplane with the condition $\xi_i > 1$, we are smoothing the effect of possible outlier support vectors, while translating the hyperplane to actual relevant values. Alternatively, we calculate the decision-defining value experimentally, in the second validation on the training data, and test both on the test set: the theoretically derived value and the experimentally adjusted one. In the special case in which all ξ_i are less than 1, we average the support vector's distance to the hyperplane with the condition $1 > \xi_i > 0$.

To evaluate the lesion detection performance, the DSC is calculated as follows:

$$\mathrm{DSC} = 2 * \frac{A \cap M}{A \cup M}, \tag{12}$$

and the amount of overlap between segmentation algorithms (A) and manually generated (M) segmentations is measured with respect to the size of the segmented region.

Table 1 shows the validation values obtained by default SVM at $d = 0$, at empirical maximum, and at the proposed value, for 2-component PCA, ICA, and raw data using 2 kernels. Raw data are displayed for reference and correspond to the use of dynamic curves as feature vectors for SVM, without multicurve extraction. The PCA method [8] shows higher DSC at $d = 0$ than the proposed ICA approach. Hyperplane translation has a lower effect in the PCA case since all support vectors lie in the condition $\xi_i < 1$. In the ICA with a linear kernel case, the false positives are reduced significantly reaching the maximum DSC values, in agreement with the interval of maximum empirical values.

Figure 9 reports a free-response receiver-operating characteristic (FROC) curve analysis [38] at the voxel

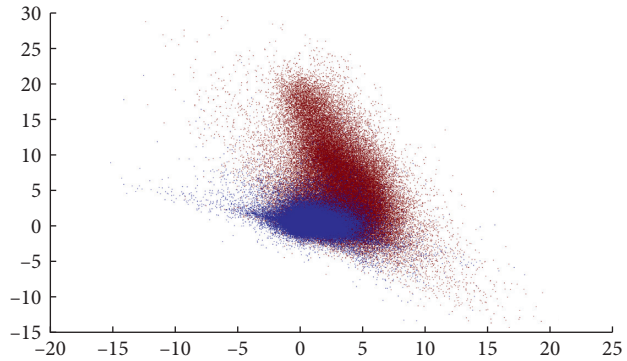

Figure 8: Scatter plot of the scores corresponding to the first two independent components of the validation data.

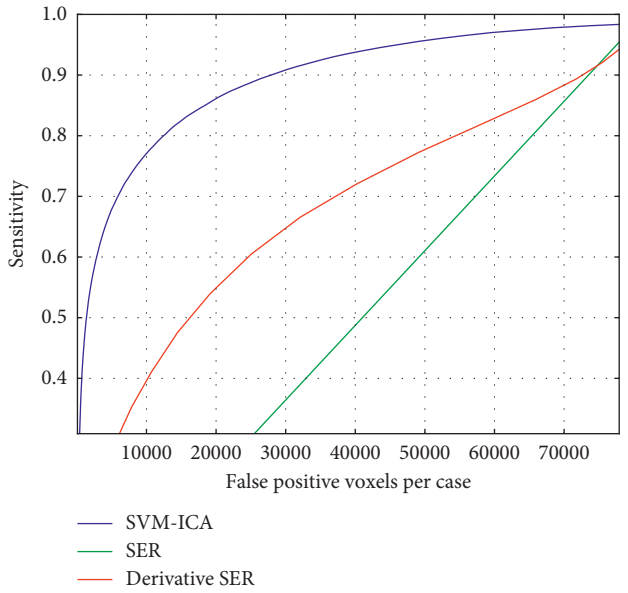

Figure 9: FROC curves for the proposed algorithm (SVM-ICA) in comparison with the references (SER and SER derivative [21]).

level. Although in mass lesions FROC analysis is usually reported at the lesion level, in NME lesions FROC analysis at the lesion level can be misleading, as can be seen from Figure 7: increasing the confidence threshold increases the number of false-positive lesions due to lesion fragmentation, although false positives at the voxel level decrease. Two reference methods are shown for comparison: the signal enhancement ratio (SER) method, based on the following SER=(SI(t=1st postcontrast time point)−SI(t=precontrast time point))/(SI(t=final postcontrast time point)−SI (t=precontrast time point)), with a varying threshold; and the derivative SER, a modified version of the method that uses the Laplacian of the image to obtain the SER, as defined in the work of Levman et al. [21]. The FROC curve for the ICA-SVM method proposed in this paper is obtained on the test set by adding a varying threshold k to the SVM output in Equation (8) and computing the sign $\text{sign}\{\mathbf{d}(x) + k\}$.

5. Discussion

The contributions of this work are twofold: first, visual interpretations of the DCE-MRI image can be enriched by using the proposed ICA-based processing of time signals, which produces a data-driven decomposition of dynamic enhancement signals into multicurve description signals, that are statistically independent and disease specific. The idea of producing multiple curves to characterize lesions has also been explored by Liu et al. [14], but from the total variation perspective, it is not data-driven but based on assumptions on the data. Other visual methods based on CAD techniques, such as PCA in Eyal et al. [8]or PCA-SOM-LDD in Varini et al. [11], have been proposed in the literature to enrich the well-known 3TP method. Thus, visual support is an important characteristic to evaluate in aiding diagnosis of breast cancer by computer systems. It is also important to stress that the ICA extraction must be done only in the training phase of the algorithm. The CAD system will then benefit from an online response, once the CAD is conveniently trained. The presented approach outperforms PCA-based methods as shown in Table 1 in terms of automatic segmentation performance and provides a meaningful visual support for experienced and unexperienced readers.

The low incidence of NME lesions reduces the available testing data, therefore limiting the validation of the presented method. Moreover, the heterogeneous nature of NME lesions also limits the accuracy in lesion annotation performed by experts when compared to CAD segmentations. Therefore, the reported DSC values when comparing ground truth and CAD results must be understood as a lower bound estimation of the segmentation capabilities of the presented CAD, since a semiautomatic annotation can potentially boost the DSC values.

The second contribution is the supervised nature of the detection and segmentation method, which allows control of the false-positive rate. Most CAD systems for lesion classification start from a manual or semimanual ROI delineation [8, 12, 16], that limits control of the false positives. The baseline approach to lesion segmentation is the FCM unsupervised method, which in Liang et al. [39]is reported to have a 6% ± 9% of overlap with manually defined ROIs, and is commonly used in many CAD systems for breast cancer diagnosis in DCE-MRI. In Jayender et al. [7], an enhancing preprocessing step is added to the usual FCM algorithm using linear dynamic system modeling. The overlap of the algorithm output with the radiologists' segmentation and CAD stream output, computed in terms of DSC, was 0.77 and 0.72, respectively. In the unsupervised approach of Cui et al. [23], a combination of Gaussian mixture modeling and marker-controlled watershed transform was used to segment the lesions. The overall overlap ratio between the two radiologists' manual segmentations and the proposed algorithm was 64.3% ± 10.4%. The supervised method of Liang et al. [39]shows overlap rates with the ground truth of 51% ± 26% and 48% ± 25%. This method required a robust intensity normalization method to make intrapatient comparisons, while the ICA method presented here characterizes the form of

the curve, thus not requiring intensity normalization. Moreover, we report higher or comparable DSC values than those in the literature, even in the more challenging case of NME breast lesions. We also report better control of false-positive rate than the method proposed by Levman et al. [21], with sensitivity greater than 75% at 10^5 false-positive voxels. Derivative SER reaches sensitivity 40% at that level, outperforming SER as already proved.

6. Conclusions

This paper presents promising results for challenging NME breast lesion detection in DCE-MRI. We propose an approach that develops a linear expansion of features for every voxel in the image based on ICA, allowing for a multicurve characterization of the enhancement behavior, in contrast with usual single-curve voxel characterization. The data-driven obtained features are used to train and test an SVM with satisfactory performance. In addition, previously, the imbalanced nature of the interest class features limited automatic detection by supervised methods such as SVM. In this work, we propose parameter optimization on the SVM hyperplane location, such that the false-positive rate is controlled, thus providing a solution to the low specificity problem in CAD of breast cancer. With that optimization, the DSC value is increased approximately a 50% from the default $d = 0$ margin value, reaching a peak value of 0.5295.

Data Availability

The DCE-MRI data used to support the findings of this study were supplied by Katja Pinker under license and so cannot be made freely available. Requests for access to these data should be made to Katja Pinker (pinkerdk@mskcc.org).

Conflicts of Interest

The authors declare that there are no conflicts of interest regarding the publication of this paper.

Acknowledgments

This work has received funding from the European Unions Horizon 2020 Research and Innovation Programme under the Marie Skodowska-Curie grant agreement No. 656886, the Austrian National Bank "Jubilaeumsfond" Project No. 16219, the 2020-Research and Innovation Framework Programme PHC-11-2015 No. 667211-2, and seed grants from Siemens Austria, Novomed, and Guerbet, France. Katja Pinker also received support from the NIH/NCI Cancer Center Support Grant P30CA008748. The authors also want to thank Elena G. Avidad for her contribution in study design.

References

[1] S. A. Jansen, A. Shimauchi, L. Zak, X. Fan, G. S. Karczmar, and G. M. Newstead, "The diverse pathology and kinetics of mass, nonmass and focus enhancement on MR imaging of the breast," *Journal of Magnetic Resonance Imaging*, vol. 33, no. 6, pp. 1382–1389, 2011.

[2] N. Sakamoto, M. Tozaki, K. Higa et al., "Categorization of non-mass-like breast lesions detected by MRI," *Breast Cancer*, vol. 15, no. 3, pp. 241–246, 2008.

[3] E. B. Pages, I. Millet, D. Hoa, F. C. Doyon, and P. Taourel, "Undiagnosed breast cancer at MR imaging: analysis of causes," *Radiology*, vol. 264, no. 1, pp. 40–50, 2012.

[4] S. H. Heywang-Kbrunner, P. Viehweg, A. Heinig, and C. Kchler, "Contrast-enhanced MRI of the breast: accuracy, value, controversies, solutions," *European Journal of Radiology*, vol. 24, no. 2, pp. 94–108, 1997.

[5] D. McClymont, A. Mehnert, A. Trakic, D. Kennedy, and S. Crozier, "Fully automatic lesion segmentation in breast MRI using mean-shift and graph-cuts on a region adjacency graph," *Journal of Magnetic Resonance Imaging*, vol. 39, no. 4, pp. 795–804, 2014.

[6] W. Chen, M. L. Giger, and U. Bick, "A fuzzy c-means (FCM)-based approach for computerized segmentation of breast lesions in dynamic contrast-enhanced MR images," *Academic Radiology*, vol. 13, no. 1, pp. 63–72, 2006.

[7] J. Jayender, S. Chikarmane, F. A. Jolesz, and E. Gombos, "Automatic segmentation of invasive breast carcinomas from DCE-MRI using time series analysis," *Journal of Magnetic Resonance Imaging*, vol. 40, no. 2, pp. 467–475, 2014.

[8] E. Eyal, D. Badikhi, E. Furman-Haran, F. Kelcz, K. J. Kirshenbaum, and H. Degani, "Principal component analysis of breast DCE-MRI adjusted with a model-based method," *Journal of magnetic resonance imaging*, vol. 30, no. 5, pp. 989–998, 2009.

[9] I. A. Illan, J. M. Gorriz, J. Ramirez et al., "18F-FDG PET imaging analysis for computer aided alzheimersdiagnosis," *Information Sciences*, vol. 181, no. 4, pp. 903–916, 2011.

[10] J. Illan, I. A. Gorriz, J. Ramirez et al., "Projecting independent components of SPECT images for computer aided diagnosis of alzheimer's disease," *Pattern Recognition Letters*, vol. 31, no. 11, pp. 1342–1347, 2010.

[11] C. Varini, A. Degenhard, and T. W. Nattkemper, "Visual exploratory analysis of DCE-MRI data in breast cancer by dimensional data reduction: a comparative study," *Biomedical Signal Processing and Control*, vol. 1, no. 1, pp. 56–63, 2006.

[12] Y.-C. Chang, Y.-H. Huang, C.-S. Huang, J.-H. Chen, and R.-F. Chang, "Computerized breast lesions detection using kinetic and morphologic analysis for dynamic contrast-enhanced MRI," *Magnetic Resonance Imaging*, vol. 32, no. 5, pp. 514–522, 2014.

[13] A. Gubern-Merida, R. Marti, J. Melendez et al., "Automated localization of breast cancer in DCE-MRI," *Medical Image Analysis*, vol. 20, no. 1, pp. 265–274, 2015.

[14] H. Liu, Y. Zheng, D. Liang et al., "Total variation based DCE-MRI decomposition by separating lesion from background for time-intensity curve estimation," *Medical Physics*, vol. 44, no. 6, pp. 2321–2331, 2017.

[15] S. Hoffmann, J. D. Shutler, M. Lobbes, B. Burgeth, and A. Meyer-Bse, "Automated analysis of non-mass-enhancing lesions in breast MRI based on morphological, kinetic, and spatio-temporal moments and joint segmentation-motion compensation technique," *EURASIP Journal on Advances in Signal Processing*, vol. 2013, no. 1, p. 172, 2013.

[16] T.-C. Wang, Y.-H. Huang, C.-S. Huang et al., "Computer-aided diagnosis of breast DCE-MRI using pharmacokinetic model and 3-D morphology analysis," *Magnetic Resonance Imaging*, vol. 32, no. 3, pp. 197–205, 2014.

[17] S. Agliozzo, M. De Luca, C. Bracco et al., "Computer-aided diagnosis for dynamic contrast-enhanced breast MRI of mass-like lesions using a multiparametric model combining a selection of morphological, kinetic, and spatiotemporal features," *Medical Physics*, vol. 39, no. 4, pp. 1704–1715, 2012.

[18] S. C. Agner, S. Soman, E. Libfeld et al., "Textural kinetics: a novel dynamic contrast-enhanced (DCE)-MRI feature for breast lesion classification," *Journal of Digital Imaging*, vol. 24, no. 3, pp. 446–463, 2011.

[19] N. Antropova, B. Huynh, and M. Giger, "SU-D-207b-06: predicting breast cancer malignancy on DCE-MRI data using pre-trained convolutional neural networks," *Medical Physics*, vol. 43, no. 6, pp. 3349-3350, 2016.

[20] R. Rasti, M. Teshnehlab, and S. L. Phung, "Breast cancer diagnosis in DCE-MRI using mixture ensemble of convolutional neural networks," *Pattern Recognition*, vol. 72, pp. 381–390, 2017.

[21] J. E. D. Levman, C. Gallego-Ortiz, E. Warner, P. Causer, and A. L. Martel, "A metric for reducing false positives in the computer-aided detection of breast cancer from dynamic contrast-enhanced magnetic resonance imaging based screening examinations of high-risk women," *Journal of Digital Imaging*, vol. 29, no. 1, pp. 126–133, 2016.

[22] Y.-C. Chang, Y.-H. Huang, C.-S. Huang, P.-K. Chang, J.-H. Chen, and R.-F. Chang, "Classification of breast mass lesions using model-based analysis of the characteristic kinetic curve derived from fuzzy c-means clustering," *Magnetic Resonance Imaging*, vol. 30, no. 3, pp. 312–322, 2012.

[23] Y. Cui, Y. Tan, B. Zhao et al., "Malignant lesion segmentation in contrast-enhanced breast MR images based on the marker-controlled watershed," *Medical Physics*, vol. 36, no. 10, pp. 4359–4369, 2009.

[24] L. Hu, Z. Cheng, M. Wang, and Z. Song, "Image manifold revealing for breast lesion segmentation in DCE-MRI," *Bio-Medical Materials and Engineering*, vol. 26, no. 1, pp. S1353–S1360, 2015.

[25] P. Comon, "Independent component analysis, a new concept?," *Signal Processing*, vol. 36, no. 3, pp. 287–314, 1994.

[26] A. Hyvarinen and E. Oja, "A fast fixed-point algorithm for independent component analysis," *Neural Computation*, vol. 9, no. 7, pp. 1483–1492, 1997.

[27] M. Bartlett, J. Movellan, and T. Sejnowski, "Face recognition by independent component analysis," *IEEE Transactions on Neural Networks*, vol. 13, no. 6, pp. 1450–1464, 2002.

[28] L. Khedher, I. A. Illn, J. M. Grriz, J. Ramrez, A. Brahim, and A. Meyer-Baese, "Independent component analysis-support vector machine-based computer-aided diagnosis system for alzheimers with visual support," *International Journal of Neural Systems*, vol. 27, no. 3, article 1650050, 2016.

[29] V. N. Vapnik, *Statistical Learning Theory*, John Wiley & Sons, New York, NY,USA, 1998.

[30] K. Pinker, G. Grabner, W. Bogner et al., "A combined high temporal and high spatial resolution 3 Tesla MR imaging protocol for the assessment of breast lesions: initial results," *Investigative Radiology*, vol. 44, no. 9, pp. 553–558, 2009.

[31] V. A. C. O. R. Reston, *Breast Imaging Reporting and Data System Atlas BI-RADS-MRI*, American College of Radiology, Reston, VA, USA, 2003.

[32] K. Friston, J. Ashburner, S. Kiebel, T. Nichols, and W. Penny, *Statistical Parametric Mapping: The Analysis of Functional Brain Images*, Academic Press, Cambridge, MA, USA, 2007.

[33] M. U. Dalm, G. Litjens, K. Holland et al., "Using deep learning to segment breast and fibroglandular tissue in MRI volumes," *Medical Physics*, vol. 44, no. 2, pp. 533–546, 2017.

[34] A. Gubern-Mrida, L. Wang, M. Kallenberg, R. Mart, H. K. Hahn, and N. Karssemeijer, "Breast segmentation in MRI: quantitative evaluation of three methods," in *Proceedings of Medical Imaging 2013: Image Processing*, vol. 8669, International Society for Optics and Photonics, Lake Buena Vista, FL, USA, February 2013.

[35] L. Jiang, X. Hu, Q. Xiao, Y. Gu, and Q. Li, "Fully automated segmentation of whole breast using dynamic programming in dynamic contrast enhanced MR images," *Medical Physics*, vol. 44, no. 6, pp. 2400–2414, 2017.

[36] S. Wu, S. P. Weinstein, E. F. Conant, M. D. Schnall, and D. Kontos, "Automated chest wall line detection for whole-breast segmentation in sagittal breast MR images," *Medical Physics*, vol. 40, no. 4, article 042301, 2013.

[37] J. E. Bresenham, "Algorithm for computer control of a digital plotter," *IBM Systems Journal*, vol. 4, no. 1, pp. 25–30, 1965.

[38] D. P. Chakraborty and L. H. Winter, "Free-response methodology: alternate analysis and a new observer-performance experiment," *Radiology*, vol. 174, no. 3, pp. 873–881, 1990.

[39] X. Liang, K. Ramamohanara, H. Frazer, and Q. Yang, "Lesion segmentation in dynamic contrast enhanced MRI of breast," in *Proceedings of 2012 International Conference on Digital Image Computing Techniques and Applications (DICTA)*, pp. 1–8, Fremantle, Australia, December 2012.

Hindawi
Contrast Media & Molecular Imaging
Volume 2018, Article ID 8659826, 7 pages
https://doi.org/10.1155/2018/8659826

Research Article

Functional Parameters of ^{18}F-FDG PET/CT in Patients with Primary Testicular Diffuse Large B-Cell Lymphoma

Jing Yang,[1,2] Sha Zhu,[2] Fuwen Pang,[2] Miao Xu,[3] Yiting Dong,[2] Jianqi Hao,[2] and Xuelei Ma[1,2]

[1]*State Key Laboratory of Biotherapy and Cancer Center, West China Hospital, Sichuan University and Collaborative Innovation Center for Biotherapy, Chengdu, China*
[2]*West China School of Medicine, West China Hospital, Sichuan University, Chengdu 610041, China*
[3]*Department of Pathology, West China Hospital, Sichuan University, Chengdu, China*

Correspondence should be addressed to Xuelei Ma; drmaxuelei@gmail.com

Received 11 April 2018; Revised 21 July 2018; Accepted 3 September 2018; Published 27 September 2018

Guest Editor: Elena Bonanno

Fluorine-18 fluorodeoxyglucose (^{18}F-FDG) positron-emission tomography/computed tomography (PET/CT), a hybrid imaging technique that simultaneously provides functional and anatomical information, has been reported to be useful in lymphoma. The present study was to evaluate the functional parameters of ^{18}F-FDG PET/CT in patients with testicular diffuse large B-cell lymphoma (DLBCL). We retrospectively reviewed medical records of 5095 patients with lymphoma who treated at West China Hospital between March 2003 and January 2017, and selected patients with ^{18}F-FDG PET/CT findings and subsequently biopsy confirmed the invasion of testis with DLBCL. Maximum standardized uptake values (SUV_{max}), peak standardized uptake values (SUV_{peak}), metabolic tumor volume (MTV), and total lesion glycolysis (TLG) of the patients were measured. We evaluated the characteristics of ^{18}F-FDG PET/CT in this population. Six patients ranged in age from 37 to 73 years (median age, 58 years) were included in the analysis. The mean SUV_{max} was 11.09 and varied between 7.20 and 19.75; mean SUV_{peak} was 9.56 and ranged between 6.79 and 14.39. In addition, mean MTV 42% was 18.4 and varied between 1.3 and 61.6; mean MTV 2.5 was 34.7 and varied significantly between 1.6 and 141.9. With regard to TLG, mean TLG 42% was 168.906 and ranged from 7.514 to 687.004, while mean TLG 2.5 was 253.972 and ranged from 8.400 to 1127.802. In conclusion, ^{18}F-FDG PET/CT scan is a useful tool in patients with testicular DLBCL. SUV, MTV, and TLG may vary a lot in different patients. SUV_{max} of testicular DLBCL lesion is relatively higher than that of normal testis. Also, we provided a set of MTV and TLG data and firstly showed their significant correlation with overall survival, which indicated a potential prognostic value of MTV and TLG. However, studies with larger population are needed to confirm these findings.

1. Introduction

Testicular lymphoma is a rare but aggressive form of extranodal lymphoma, accounting for 3–9% of testicular cancers and 1-2% of non-Hodgkin's lymphomas [1, 2]. In spite of the low overall incidence, testicular lymphoma is the most common testicular malignancy in men over 60 [2]. Testicular diffuse large B-cell lymphoma (DLBCL) is the most common histological subtype, accounting for about 80% to 98% of all cases [3]. Although radical inguinal orchiectomy is recommended in view of histological evaluation, invasiveness often hinders its wider adoption [4]. Other diagnostic methods include testicular ultrasound, computed tomography (CT), routine blood test, lactate dehydrogenase, bone marrow biopsy, and lumbar puncture [5].

Fluorine-18 fluorodeoxyglucose (^{18}F-FDG) positron-emission tomography/computed tomography (PET/CT) is a hybrid imaging technique that simultaneously provides functional and anatomical information. ^{18}F-FDG PET/CT is important in biomedical research and clinical diagnostics, and its application in lymphoma has already been reported [6, 7]. There are several parameters being repeatedly

discussed in recent studies, including maximum standardized uptake values (SUV_{max}), peak standardized uptake values (SUV_{peak}), metabolic tumor volume (MTV), and total lesion glycolysis (TLG), since they are believed to play important roles in the diagnosis and prognosis of patients with lymphoma [8–10]. Therefore, the National Comprehensive Cancer Network (NCCN) guidelines recommend the use of ^{18}F-FDG PET/CT for staging, response evaluation, and prognosis of lymphoma.

However, the role of ^{18}F-FDG PET/CT among patients with testicular DLBCL has still not been well established. In this study, we reported 6 patients with testicular DLBCL who had performed ^{18}F-FDG PET/CT scan and discussed the role of ^{18}F-FDG PET/CT in this population at the same time.

2. Materials and Methods

2.1. Patients. We retrospectively reviewed medical records of 5095 patients with lymphoma. All patients were treated at West China Hospital between March 2003 and January 2015. Inclusion criteria were as follows: (1) ^{18}F-FDG PET/CT findings before receiving orchiectomy were present and (2) subsequent biopsy confirmed the invasion of testis with DLBCL. Patients' characteristics including the histological type, Ann Arbor stage, International Prognostic Index (IPI) score, NCCN IPI score, ECOG performance status, B symptom, metastatic sites, and treatment were extracted. This study was approved by the Ethics Administration Office of West China Hospital, Sichuan University.

2.2. ^{18}F-FDG PET/CT Imaging. Standard whole-body ^{18}F-FDG PET/CT was performed using a Gemini GXL PET/CT scanner (Philips, Amsterdam, The Netherlands). Fasting for at least 6 hours was required before the examination, and the blood glucose level was measured immediately before the administration of ^{18}F-FDG. The PET/CT scan would be rescheduled if the blood glucose level was >150 mg/dL. Approximately 5 MBq of ^{18}F-FDG per kilogram of body weight was administered intravenously, and the patients rested in a quiet, dark environment for approximately 60 minutes before scanning. After initial low-dose CT (40 mA, 120 kVp), emission images were obtained from the top of the skull to the middle of the thigh, with acquisition times of 2 minutes per bed position in the three-dimensional mode. The PET images were reconstructed iteratively with CT-based attenuation correction (Figures 1 and 2).

2.3. Image Analysis. The image analysis was performed using Compass Viewer software. Circular regions of interest (ROIs) were manually drawn on axial, coronal, or sagittal coregistered PET/CT slices. Within the selected ROI, SUV_{max}, mean standardized uptake values (SUV_{mean}), SUV_{peak}, MTV, and TLG were measured. SUV_{max} were calculated using the following formula: mean ROI activity (MBq/g)/(injected dose (MBq)/body weight (g)). SUV_{peak} was defined as the mean of SUV_{max} and its 10 neighbors (roughly corresponding to a 0.5 cm ROI). MTV and TLG could be measured by a fixed background SUV cut-off or a fixed percentage of the SUV_{max}. In this study, we calculated SUV_{mean} and MTV based on a fixed threshold of 42% of SUV_{max} (SUV_{mean} 42%, MTV 42%) or based on a fixed background SUV cut-off of 2.5 (SUV_{mean} 2.5, MTV 2.5). TLG was defined as the MTV multiplied with the SUV_{mean} (TLG 42%, TLG 2.5).

2.4. Statistical Analysis. Correlation analysis between the functional parameters of ^{18}F-FDG PET/CT and overall survival (OS) was conducted, and Spearman's rank coefficients were used to assess the relationship between the functional parameters and outcomes of the patients. Statistical analyses were performed using the SPSS version 22.0 (IBM Corporation, Armonk, NY, USA) at a significance level of $p < 0.05$.

3. Results

A total of 34 patients with testicular lymphoma were selected from this population. Eighteen of them had ^{18}F-FDG PET/CT findings while only 6 had preoperative images. As a result, 6 patients ranging from 37 to 73 years old (median age, 58) were included in the analysis. Patients' characteristics including the histological type, Ann Arbor stage, IPI score, NCCN IPI score, ECOG performance status, B symptom, metastatic sites, and treatment are described in Table 1. All patients had histopathological confirmation of DLBCL. Five (83.3%) out of 6 patients were classified clinically as stage IVB, and 1 (16.7%) as stage IEA according to the Ann Arbor classification. The IPI score of patients were calculated, and the results revealed that 5 patients (83.3%) had a score of 3 while 1 patient (16.7%) had a score of 1. In addition, 1 (16.7%) patient had an ECOG performance status of 1, while 5 patients (83.3%) had an ECOG performance status of 0. Of the 6 patients, 3 (50%) had tumor located on the left side and 1 (16.3%) on the right side, whereas 2 (33.3%) on the bilateral sides. Besides testicular disease, 5 of the patients were identified to have lymph nodes or other distant metastases. All the patients have received treatment, of whom 6 (100%) had orchiectomy and chemotherapy, 2 patients (33.3%) had local radiotherapy, and 4 (66.7%) received prophylactic intrathecal injection in addition to their systemic chemotherapy. Adjunct laboratory and immunohistochemical results of the patients, such as Ki-67, β_2 microglobulin, and LDH, are also shown in Table 1.

Within the selected ROI, SUV_{max}, SUV_{mean}, SUV_{peak}, MTV, and TLG were measured. The mean SUV_{max} was 11.09 and varied between 7.20 and 19.75; mean SUV_{peak} was 9.56 and ranged between 6.79 and 14.39. In addition, mean MTV 42% was 18.4 mL and varied between 1.3 mL and 61.6 mL; mean MTV 2.5 was 34.7 mL and varied significantly between 1.6 mL and 141.9 mL. With regard to TLG, mean TLG 42% was 168.906 and ranged from 7.514 to 687.004, while mean TLG 2.5 was 253.972 and ranged from 8.400 to 1127.802 (Table 2).

The result of correlation analysis between functional parameters and survival time indicated that SUV_{max} and SUV_{peak} were not significantly associated with OS of the

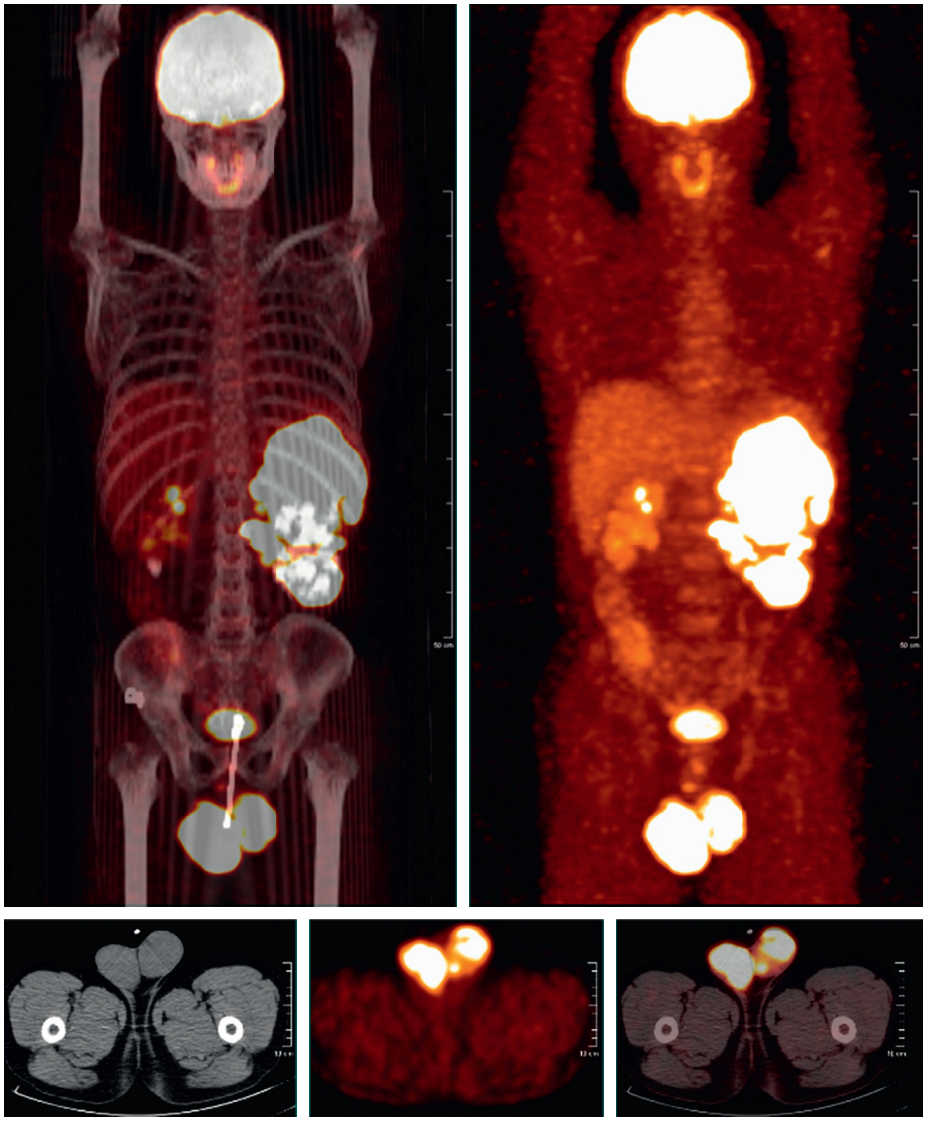

Figure 1: A 37-year-old patient was diagnosed with diffuse large B-cell lymphoma that involved with bilateral testes. The PET/CT showed asymmetrical increased uptake in the bilateral testes. He received orchiectomy, prophylactic intrathecal injection, and 6 cycles of chemotherapy with rituximab-etoposide, prednisone, oncovin (vincristine), cyclophosphamide, and hydroxydaunorubicin (doxorubicin) (R-DA-EPOCH). The duration from the time of diagnosis to the date when radiological findings suggested suspected pancreatic involvement was 9.3 months. The patient was alive till October 30, 2017, after a follow-up of 26 months.

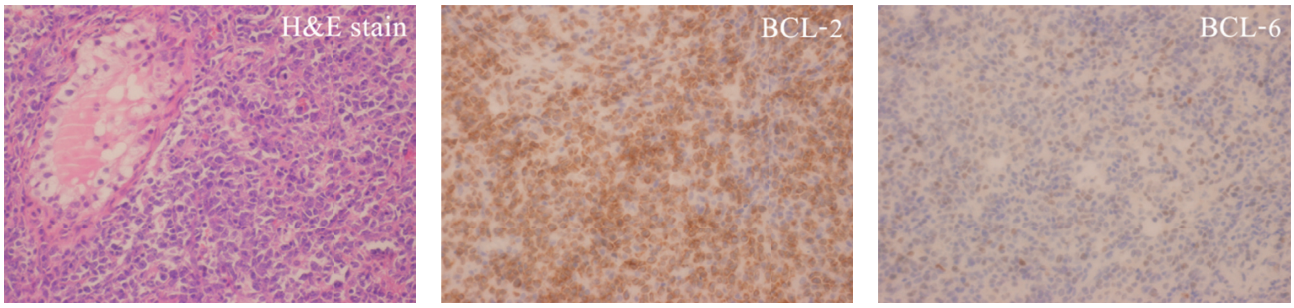

(a) (b) (c)

Figure 2: Continued.

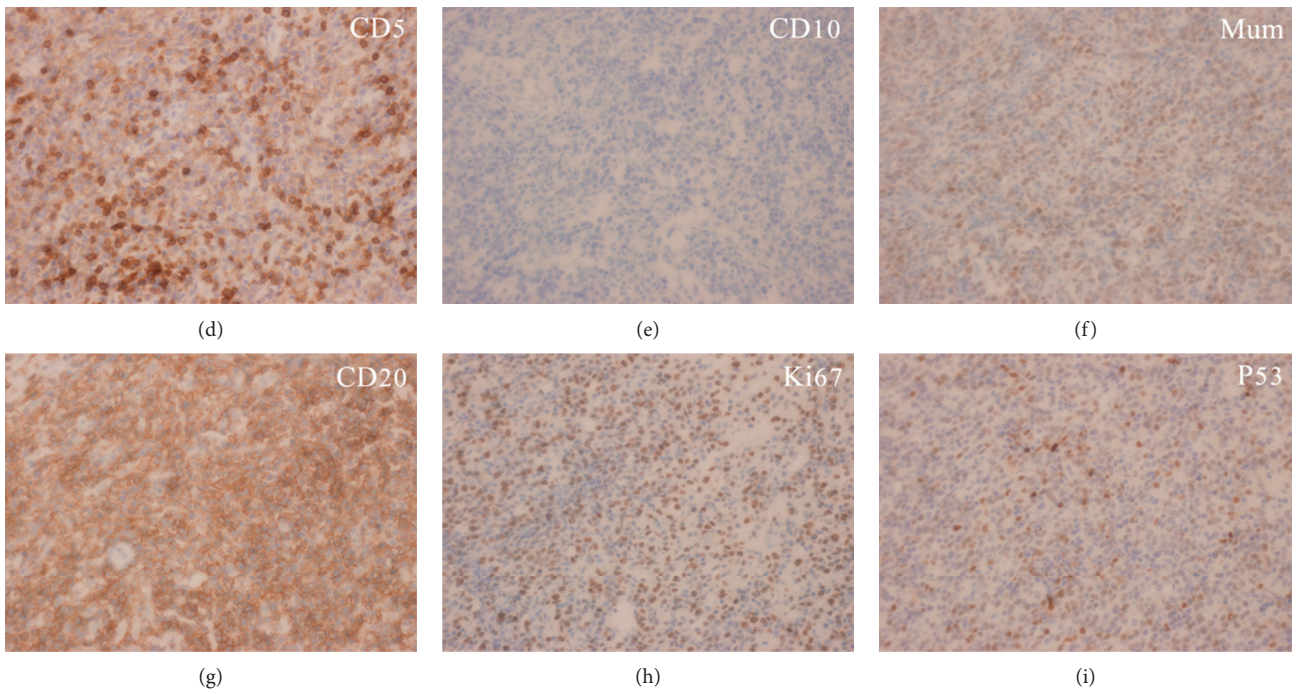

Figure 2: Histopathological (H&E stain (×400)) and immunohistochemical (×400) findings of the testicular lymphoma biopsy specimen of the 37-year-old patient: BCL-2 (+), BCL-6 (+), CD5 (+), CD10 (−), CD20 (+), Mum (+), Ki-67/MIB-1 (+, 80%), and P53 (+).

Table 1: Baseline characteristics of the patients.

No	Age	Ann Arbor stage	IPI score	ECOG performance status	Site	Nodal involvement	Exnodal involvement	Ki-67	β_2 microglobulin (mg/L)	LDH (IU/L)	Treatment
1	37	IVB	3	0	Bilateral	Para-aortic lymph node	Bilateral kidney, perirenal region, and spleen	80%	2.33	237	Orchiectomy, CT, and prophylactic intrathecal injection
2	73	IVB	3	0	Right	Abdominal lymph node	Lung and nasopharyngeal wall	40%	2.63	177	Orchiectomy, CT, RT, and prophylactic intrathecal injection
3	57	IVB	3	1	Left	Neck lymph node	Maxillary sinus, maxillary bone, orbital cavity, temporalis, multiple subcutaneous tissue, and bone of trunk	60%	2.82	301	Orchiectomy and CT
4	58	IEA	1	0	Left	—	—	N/A	N/A	223	Orchiectomy, CT, and RT
5	73	IVA	3	0	Bilateral	Cervical lymph nodes and hilar lymph node	Skin	50%	2.19	246	Orchiectomy, CT, and prophylactic intrathecal injection
6	58	IVB	3	0	Left	Multiple lymph nodes	Kidney, adrenal gland, and spermatic cord	90%	NA	367	Orchiectomy and CT + prophylactic intrathecal injection

IPI, International Prognostic Index; NCCN IPI, National Comprehensive Cancer Network International Prognostic Index; ECOG performance status, Eastern Cooperative Oncology Group performance status; LDH, lactic dehydrogenase; CT, chemotherapy; RT, radiotherapy; N/A, not applicable.

Table 2: SUV, MTV, TLG, and survival of the patients.

No.	SUV_{max}	SUV_{peak}	MTV 42%	MTV 2.5	TLG 42%	TLG 2.5	Overall survival (months)	Outcomes
1	19.75	14.39	61.6	141.9	687.004	1127.802	26	Alive
2	11.30	9.52	13.1	16.9	91.045	105.794	54	Death
3	7.98	6.99	3.8	4.8	20.786	23.808	17	Alive
4	11.90	11.56	20.7	31.7	168.912	209.537	22	Death
5	7.20	6.79	9.7	11.2	44.175	48.49	18	Alive
6	8.40	8.11	1.3	1.6	7.514	8.400	17	Alive

SUV_{max}, maximum standardized uptake values; SUV_{peak}, peak standardized uptake values; MTV, metabolic tumor volume; TLG, total lesion glycolysis.

Table 3: Spearman rank correlation for functional parameters and overall survival.

	SUV_{max}	SUV_{peak}	MTV 42%	MTV 2.5	TLG 42%	TLG 2.5
Spearman rank correlation coefficient	0.638	0.638	0.812	0.812	0.812	0.812
p value	0.1731	0.1731	0.0498	0.0498	0.0498	0.0498

SUV_{max}, maximum standardized uptake values; SUV_{peak}, peak standardized uptake values; MTV, metabolic tumor volume; TLG, total lesion glycolysis.

patients. However, MTV 42%, MTV 2.5, TLG 42%, and TLG 2.5 were revealed to be significantly correlated with OS of the patients, with Spearman's rank coefficients of 0.812 and $p = 0.04982$ (Table 3).

4. Discussion

^{18}F-FDG PET/CT is performed in combination with ^{18}FDG PET and CT scanners.^{18}F-FDG PET/CT has been reported to be a very useful tool with high sensitivity and specificity rates in evaluating most lymphoma subtypes, providing both metabolic and morphologic features of diseases [11]. Compared with contrast-enhanced CT (CECT), PET/CT shows a higher diagnostic value with sensitivity of 97% and specificity of 100%, especially for normal-sized lymph nodes and extranodal involvement [12–14]. Moreover, with the supplement of other examinations, ^{18}F-FDG PET/CT can not only make accurate diagnosis but also assess the treatment response as well as predict the outcomes [15–18]. However, as far as we know, the application of PET/CT in testicular DLBCL patients has not been well studied. In this study, we firstly focused on the use of ^{18}F-FDG PET/CT in the prognosis and staging of patients with testicular DLBCL and reported their SUV_{max}, SUV_{mean}, SUV_{peak}, MTV, and TLG.

Because of its aggressive clinical biological behavior, patients with testicular lymphoma usually present a poor prognosis. Timely and accurate diagnosis of testicular lymphoma is vital since early diagnosis was reported to be associated with better outcomes [19]. Imaging modalities that may be helpful in diagnosis include ultrasonography, magnetic resonance imaging, and CT, while unfortunately none of these methods shows satisfying specificity [3]. Fine-needle aspiration, testicular biopsy, and orchiectomy have been used for pathological diagnosis of testicular lymphoma. Nevertheless, these pathological diagnostic process may do harm to the testes' physiological functions as well as patients' mental health [3]. PET/CT is now widely used in the diagnosis and initial staging of high-grade lymphoma [20]. In this study, we also demonstrated the value of PET/CT in diagnosis and staging among patients with testicular DLBCL.

SUV_{max}, the most widely used parameter, is a reproducible measurement for disease evaluation in a quantitative way [21]. Previous studies have reported that the normal level of FDG uptake in the testis is relatively high and symmetrical in pattern and declines slightly with age [22]. A study involving 203 men has demonstrated that the normal SUV range from 1.23 to 3.85 with a mean value of 2.44 [23]. In addition, previous study including 53 patients has reported that a SUV_{max} of 3.75 is the optimal cut-off value for differentiating between benign and malignant testicular diseases [24]. As for the testicular lesions of our population, the mean SUV_{max} was 11.09, with a range of 7.20 to 19.75. SUV_{max} of all our patients were larger than 3.75. The results of this study revealed a high FDG uptake in testicular DLBCL patients; therefore, abnormal uptake of FDG in testis warranted further analysis. In addition, the value of SUV_{peak} was also shown in this study. However, to the best of our acknowledgement, no previous studies have reported these indexes of testicular DLBCL patients.

MTV and TLG can be measured by a fixed background SUV cut-off or a fixed percentage of the SUV_{max} [25–27]. Both MTV and TLG have been proposed to assess the burden of metabolically active tumors and are assumed to be reliable indicators of the tumor bulk [28]. In this study, we calculated MTV 42%, MTV 2.5, TLG 42%, and TLG 2.5 of each patient. The mean MTV 42% was 18.4 mL while the mean MTV 2.5 was 34.7 mL; meanwhile, both of them showed an apparent change. MTV of tumor burden has been recently found to be a useful prognostic factor in lymphoma [29]. TLG, which combined the volumetric and metabolic information of ^{18}F-FDG PET, was also calculated in this study. Elevated TLG has also been shown to be associated with poor survival in various types of cancer, but its prognostic value in testicular lymphoma has not been well established [30]. As a result, we demonstrated that MTV and TLG may greatly differ between different patients. The values of MTV and TLG in neither normal testes nor testicular lymphoma have been investigated; thus, further studies

are expected. To the best of our knowledge, we assessed the correlation between functional parameters of ^{18}F-FDG PET/CT and survival of patients with primary testicular DLBCL for the first time. MTV and TLG were shown to be correlated with survival with statistical significance, which indicated a potential prognostic value of MTV and TLG. However, further studies are needed to confirm these results.

The current study has several limitations. First, this is a retrospective analysis. Second, the number of patients is small. Although we identified 18 testicular DLBCL with PET/CT scan, 12 of them had undergone orchiectomy before PET/CT examination. As a result, testicular disease could not be identified in the scan. Third, population from a single center also limits the conclusions of our study. Thus, further prospective randomized studies using multicenter data are required to confirm our findings. The strength of this study includes that histological confirmation of testicular DLBCL was obtained in all the patients, and patients' data were complete.

5. Conclusions

In conclusion, PET/CT scan has the potential in evaluating patients with testicular DLBCL. SUV, MTV, and TLG may vary a lot in different patients. SUV_{max} of testicular DLBCL lesion is relative higher than that of normal testis. Also, we provided a set of MTV and TLG data and firstly showed their significant correlation with OS, which indicated a potential prognostic value of MTV and TLG. However, studies with a larger population are needed to confirm these findings.

Abbreviations

DLBCL: Diffuse large B-cell lymphoma
CT: Computed tomography
^{18}F-FDG: Fluorine-18 fluorodeoxyglucose
PET/CT: Positron-emission tomography/computed tomography
SUV_{max}: Maximum standardized uptake values
SUV_{peak}: Peak standardized uptake values
SUV_{mean}: Mean standardized uptake values
MTV: Metabolic tumor volume
TLG: Total lesion glycolysis
NCCN: National Comprehensive Cancer Network
IPI: International Prognostic Index
ROI: regions of interest
OS: Overall survival.

Data Availability

The data used to support the findings of this study are available from the corresponding author upon request.

Conflicts of Interest

The authors declare that they have no conflicts of interest.

Authors' Contributions

Jing Yang and Xuelei Ma contributed equally to this work.

References

[1] M. B. Moller, F. d'Amore, and B. E. Christensen, "Testicular lymphoma: a population-based study of incidence, clinicopathological correlations and prognosis, The Danish Lymphoma Study Group, LYFO," *European Journal of Cancer*, vol. 30, no. 12, pp. 1760–1764, 1994.

[2] J. D. Gundrum, M. A. Mathiason, D. B. Moore, and R. S. Go, "Primary testicular diffuse large B-cell lymphoma: a population-based study on the incidence, natural history, and survival comparison with primary nodal counterpart before and after the introduction of rituximab," *Journal of clinical oncology : official journal of the American Society of Clinical Oncology*, vol. 27, no. 31, pp. 5227–5232, 2009.

[3] C. Y. Cheah, A. Wirth, and J. F. Seymour, "Primary testicular lymphoma," *Blood*, vol. 123, no. 4, pp. 486–493, 2014.

[4] A. G. Lantz, N. Power, B. Hutton, and R. Gupta, "Malignant lymphoma of the testis: a study of 12 cases," *Canadian Urological Association Journal*, vol. 3, no. 5, pp. 393–398, 2009.

[5] N. Verma, J. Lazarchick, V. Gudena, J. Turner, and U. B. Chaudhary, "Testicular lymphoma: an update for clinicians," *American Journal of the Medical Sciences*, vol. 336, no. 4, pp. 336–341, 2008.

[6] D. Hernandez-Maraver, F. Hernandez-Navarro, N. Gomez-Leon et al., "Positron emission tomography/computed tomography: diagnostic accuracy in lymphoma," *British Journal of Haematology*, vol. 135, no. 3, pp. 293–302, 2006.

[7] L. Mansi, V. Cuccurullo, and R. Grassi, "Diagnostic imaging and pathology," in *Advanced Imaging Techniques in Clinical Pathology*, F. M. Sacerdoti, A. Giordano, and C. Cavaliere, Eds., pp. 107–111, Springer New York, New York, NY, USA, 2016.

[8] K. Pak, G. J. Cheon, K. W. Kang, J. K. Chung, E. E. Kim, and D. S. Lee, "Prognostic value of SUVmean in oropharyngeal and hypopharyngeal cancers: comparison with SUVmax and other volumetric parameters of 18F-FDG PET," *Clin Nucl Med*, vol. 40, no. 1, pp. 9–13, 2015.

[9] D. Rubello, P. Gordien, C. Morliere et al., "Variability of Hepatic 18F-FDG Uptake at Interim PET in Patients With Hodgkin Lymphoma," *Clinical Nuclear Medicine*, vol. 40, no. 8, pp. e405–e410, 2015.

[10] A. Sher, F. Lacoeuille, P. Fosse et al., "For avid glucose tumors, the SUV peak is the most reliable parameter for (18)FFDG-PET/CT quantification, regardless of acquisition time," *EJNMMI Research*, vol. 6, no. 1, pp. 016–0177, 2016.

[11] X. Wang, "PET/CT: appropriate application in lymphoma," *Chinese Clinical Oncology*, vol. 4, no. 1, pp. 2304–3865, 2015.

[12] N. G. Schaefer, T. F. Hany, C. Taverna et al., "Non-Hodgkin lymphoma and Hodgkin disease: coregistered FDG PET and CT at staging and restaging--do we need contrast-enhanced CT?," *Radiology*, vol. 232, no. 3, pp. 823–829, 2004.

[13] F. Moog, M. Bangerter, C. G. Diederichs et al., "Extranodal malignant lymphoma: detection with FDG PET versus CT," *Radiology*, vol. 206, no. 2, pp. 475–481, 1998.

[14] E. Bednaruk-Mlynski, J. Pienkowska, A. Skorzak et al., "Comparison of positron emission tomography/computed tomography with classical contrast-enhanced computed tomography in the initial staging of Hodgkin lymphoma," *Leukemia and Lymphoma*, vol. 56, no. 2, pp. 377–382, 2015.

[15] K. Ishiwata, M. Tomura, T. Ido, R. Iwata, J. Itoh, and M. Kameyama, "In vivo assessment of 6-deoxy-6-18Ffluoro-D-galactose as a PET tracer for studying galactose metabolism," *International Journal of Radiation Applications and Instrumentation. Part B. Nuclear Medicine and Biology*, vol. 16, no. 8, pp. 775–781, 1989.

[16] E. Mena, M. L. Lindenberg, B. I. Turkbey et al., "A pilot study of the value of 18F-fluoro-deoxy-thymidine PET/CT in predicting viable lymphoma in residual 18F-FDG avid masses after completion of therapy," *Clinical Nuclear Medicine*, vol. 39, no. 10, pp. 874–881, 2014.

[17] A. T. Ilica, K. Kocacelebi, R. Savas, and A. Ayan, "Imaging of extranodal lymphoma with PET/CT," *Clinical Nuclear Medicine*, vol. 36, no. 10, pp. e127–e138, 2011.

[18] S. Karunanithi, P. Sharma, S. G. Roy et al., "Use of 18F-FDG PET/CT imaging for evaluation of patients with primary splenic lymphoma," *Clinical Nuclear Medicine*, vol. 39, no. 9, pp. 772–776, 2014.

[19] S. J. Buskirk, R. G. Evans, P. M. Banks, M. J. O'Connell, and J. D. Earle, "Primary lymphoma of the testis," *International Journal of Radiation Oncology∗Biology∗Physics*, vol. 8, no. 10, pp. 1699–1703, 1982.

[20] S. S. Ahmad, S. F. Idris, G. A. Follows, and M. V. Williams, "Primary testicular lymphoma," *Clinical Oncology*, vol. 24, no. 5, pp. 358–365, 2012.

[21] H. Schoder, A. Noy, M. Gonen et al., "Intensity of 18fluorodeoxyglucose uptake in positron emission tomography distinguishes between indolent and aggressive non-Hodgkin's lymphoma," *Journal of Clinical Oncology*, vol. 23, no. 21, pp. 4643–4651, 2005.

[22] S. Kosuda, S. Fisher, P. V. Kison, R. L. Wahl, and H. B. Grossman, "Uptake of 2-deoxy-2-18Ffluoro-D-glucose in the normal testis: retrospective PET study and animal experiment," *Annals of Nuclear Medicine*, vol. 11, no. 3, pp. 195–199, 1997.

[23] K. Kitajima, Y. Nakamoto, M. Senda, Y. Onishi, H. Okizuka, and K. Sugimura, "Normal uptake of 18F-FDG in the testis: an assessment by PET/CT," *Annals of Nuclear Medicine*, vol. 21, no. 7, pp. 405–410, 2007.

[24] D. Shao, Q. Gao, X. W. Tian, S. Y. Wang, C. H. Liang, and S. X. Wang, "Differentiation and diagnosis of benign and malignant testicular lesions using 18F-FDG PET/CT," *European Journal of Radiology*, vol. 93, pp. 114–120, 2017.

[25] B. Khiewvan, P. Ziai, S. Houshmand, A. Salavati, P. Ziai, and A. Alavi, "The role of PET/CT as a prognosticator and outcome predictor in lung cancer," *Expert Review of Respiratory Medicine*, vol. 10, no. 3, pp. 317–330, 2016.

[26] S. H. Hwang, A. Cho, M. Yun, Y. D. Choi, S. Y. Rha, and W. J. Kang, "Prognostic value of pretreatment metabolic tumor volume and total lesion glycolysis using 18F-FDG PET/CT in patients with metastatic renal cell carcinoma treated with anti-vascular endothelial growth factor-targeted agents," *Clinical Nuclear Medicine*, vol. 42, no. 5, pp. e235–e241, 2017.

[27] J. Castelli, A. Depeursinge, B. de Bari et al., "Metabolic tumor volume and total lesion glycolysis in oropharyngeal cancer treated with definitive radiotherapy: which threshold is the best predictor of local control?," *Clin Nucl Med*, vol. 42, no. 6, pp. e281–e285, 2017.

[28] R. Lim, A. Eaton, N. Y. Lee et al., "18F-FDG PET/CT metabolic tumor volume and total lesion glycolysis predict outcome in oropharyngeal squamous cell carcinoma," *Journal of Nuclear Medicine*, vol. 53, no. 10, pp. 1506–1513, 2012.

[29] A. J. Moskowitz, H. Schoder, S. Gavane et al., "Prognostic significance of baseline metabolic tumor volume in relapsed and refractory Hodgkin lymphoma," *Blood*, vol. 130, no. 20, pp. 2196–2203, 2017.

[30] M. Xie, W. Zhai, S. Cheng, H. Zhang, Y. Xie, and W. He, "Predictive value of F-18 FDG PET/CT quantization parameters for progression-free survival in patients with diffuse large B-cell lymphoma," *Hematology*, vol. 21, no. 2, pp. 99–105, 2016.

Hindawi
Contrast Media & Molecular Imaging
Volume 2018, Article ID 3181258, 7 pages
https://doi.org/10.1155/2018/3181258

Research Article

Dynamic Contrast-Enhanced Imaging as a Prognostic Tool in Early Diagnosis of Prostate Cancer: Correlation with PSA and Clinical Stage

Xingchen Wu,[1,2,3] **Petri Reinikainen**,[1,2] **Mika Kapanen**,[1,4] **Tuula Vierikko**,[3] **Pertti Ryymin**,[3,4] **and Pirkko-Liisa Kellokumpu-Lehtinen**[1,2]

[1]*Department of Oncology, Tampere University Hospital, Tampere, Finland*
[2]*Faculty of Medicine and Life Sciences, University of Tampere, Tampere, Finland*
[3]*Department of Radiology, Medical Imaging Centre, Tampere University Hospital, Tampere, Finland*
[4]*Department of Medical Physics, Medical Imaging Centre, Tampere University Hospital, Tampere, Finland*

Correspondence should be addressed to Xingchen Wu; xingchen.wu@uta.fi

Received 10 April 2018; Accepted 22 July 2018; Published 19 September 2018

Academic Editor: Orazio Schillaci

Background and Purpose. Although several methods have been developed to predict the outcome of patients with prostate cancer, early diagnosis of individual patient remains challenging. The aim of the present study was to correlate tumor perfusion parameters derived from dynamic contrast-enhanced magnetic resonance imaging (DCE-MRI) and clinical prognostic factors and further to explore the diagnostic value of DCE-MRI parameters in early stage prostate cancer. *Patients and Methods*. Sixty-two newly diagnosed patients with histologically proven prostate adenocarcinoma were enrolled in our prospective study. Transrectal ultrasound-guided biopsy (12 cores, 6 on each lobe) was performed in each patient. Pathology was reviewed and graded according to the Gleason system. DCE-MRI was performed and analyzed using a two-compartmental model; quantitative parameters including volume transfer constant (K^{trans}), reflux constant (K_{ep}), and initial area under curve (iAUC) were calculated from the tumors and correlated with prostate-specific antigen (PSA), Gleason score, and clinical stage. *Results*. K^{trans} ($0.11 \pm 0.02\ min^{-1}$ versus $0.16 \pm 0.06\ min^{-1}$; $p < 0.05$), K_{ep} ($0.38 \pm 0.08\ min^{-1}$ versus $0.60 \pm 0.23\ min^{-1}$; $p < 0.01$), and iAUC (14.33 ± 2.66 mmoL/L/min versus 17.40 ± 5.97 mmoL/L/min; $p < 0.05$) were all lower in the clinical stage T1c tumors (tumor number, $n = 11$) than that of tumors in clinical stage T2 ($n = 58$). Serum PSA correlated with both tumor K^{trans} ($r = 0.304$, $p < 0.05$) and iAUC ($r = 0.258$, $p < 0.05$). *Conclusions*. Our study has confirmed that DCE-MRI is a promising biomarker that reflects the microcirculation of prostate cancer. DCE-MRI in combination with clinical prognostic factors may provide an effective new tool for the basis of early diagnosis and treatment decisions.

1. Introduction

Prostate cancer is the second leading cause of cancer-related death and the most frequently diagnosed male malignant disease in the Nordic countries [1]. Early detection of prostate cancer permits appropriate and timely management of the disease, and prognostic biomarkers can help clinicians to make a proper decision for treatment of individual patients and to avoid unnecessary treatments [2]. Although several methods have been developed to predict outcome of patients with prostate cancer, prognosis evaluation of individual patient remains challenging. Recent studies demonstrate that multiparametric magnetic resonance imaging (MP-MRI), consisting of T1-weighted, T2-weighted, diffusion-weighted imaging (DWI), and dynamic contrast-enhanced MRI (DCE-MRI), has emerged as a useful tool not only for localizing prostate cancer foci, but also for assessing tumor aggressiveness [3]. DWI allows to quantify the random motion of water molecules in tissue by means of apparent diffusion coefficient (ADC) measurements and provides information on tissue cellularity, tortuosity of extracellular space, and cell membrane integrity, thereby differentiating noncancerous and cancer lesions [4]. DCE-MRI is a relatively novel imaging modality that allows to

measure properties of tissue microvasculature resulting from tumor angiogenesis and improving tumor detection and response assessment [5]. The most commonly used DCE-MRI parameter that reflects vascular permeability is the volume transfer constant (K^{trans}) [6]. K^{trans} represents the rate at which the contrast agent transfers from the blood to the interstitial space, which indicates the tumor microcirculation and the surface infiltration area. In contrast, the reflux constant (K_{ep}) reflects the rate at which the contrast agent transfers from the extravascular extracellular space back to the blood. The extravascular extracellular leakage volume fraction ($Ve = K^{trans}/K_{ep}$) predominantly reflects the percentage of contrast agent in the extravascular extracellular space [6]. In addition, the semiquantitative parameter initial area under curve (iAUC) is associated with tumor blood influx, perfusion, and interstitial space and represents the general tumor blood flow, overall perfusion, and tumor interstitial space index [6].

The aim of the present study was to correlate tumor perfusion parameters derived from DCE-MRI and clinical prognostic factors and further to explore if we can separate very early tumors from relatively advanced ones with DCE-MRI-derived parameters for decision making in early stage prostate cancer.

2. Materials and Methods

2.1. Patients. Seventy-one consecutive patients with histologically proven prostate adenocarcinoma were enrolled in our prospective clinical trials to develop hypofractionated image-guided and intensity-modulated radical radiotherapy. The study identifier at www.ClinicalTrials.gov is NCT02319239. The inclusion and exclusion criteria have been described in details in our previous publication [7]. Briefly, newly diagnosed adult patients with one or two of the intermediate-risk features (Gleason score 7, staging T2b-T2c, PSA 10–20 ng/mL) according to the National Comprehensive Cancer Network (NCCN) criteria [8], and patients were suitable for MRI examination. No patients received neoadjuvant or adjuvant hormonal treatment. The study was approved by the Ethics Committee of Tampere University Hospital (Nr. R14009), and all patients gave written informed consent prior to study entry. Patients underwent physical examination, digital rectal examination, and standard laboratory tests including serum prostate-specific antigen (PSA).

2.2. Histological Analysis. Transrectal ultrasound-guided biopsy (12 cores, 6 on each lobe) was performed in each patient. Six biopsy cores were embedded in one paraffin block. Pathology was reviewed and graded according to the Gleason system. Major criteria include an infiltrative glandular growth pattern and an absence of basal cells and nuclear atypia in the form of nucleomegaly and nucleolomegaly. The diagnosis was based on the microscopic appearance of slides stained using haematoxylin and eosin. In difficult cases, basal cell absence has been confirmed by immunohistochemical stains for basal cell markers.

2.3. Multiparametric MRI Acquisition. Multiparametric MR imaging was acquired using a 3 Tesla MR System (Siemens Trio-Tim, Erlangen, Germany) with a combination of 6-channel body matrix coil and 6 elements of 24-channel spine matrix coil positioned around the pelvis to cover the prostate. Tri-planar T2-weighted turbo spin echo images from below the prostatic apex to above the seminal vesicles were obtained. DWI was acquired with a single-shot echoplanar sequence on the axial plane using three b values (50, 400, and 800 s/mm^2) and with the same orientation and location used to acquire axial T2-weighted images. DCE-MRI was performed with axial T1-weighted 3D volumetric interpolated breath-hold examination (VIBE) sequence that covers the entire prostate in consecutive sections. To determine the T1 relaxation time in the tissue before the arrival of contrast agent, the DCE-MRI included two precontrast 3D VIBE imaging sequences that had different flip angles (2° and 13°). These sequences were followed by a DCE series on the axial plane after gadolinium (Gd)-DOTA (0.2 ml/kg Dotarem®) injection, with a temporal resolution of 8 seconds and an acquisition time of 4 minutes 40 seconds. The contrast agent was administered using a power injector (Medrad Spectris Solaris EP, Bayer Medical Care Inc, PA, USA) followed by a 20 ml saline flush injection at a flow rate of 2.5 ml/s. To minimize postbiopsy artifact, MRI was performed 6–10 weeks after the prostate cancer confirmation by biopsy. For imaging parameters, see Table 1.

2.4. MR Image Analysis. All MR images were reviewed and analyzed on a syngo Multimodality Workplace (Siemens Healthcare). Voxelwise MRI signal enhancement time curves were fitted according to a pharmacokinetic model using Tissue 4D software (Siemens Healthcare). First, a motion correction has been performed, which registered all volumes of the time series to a user-selected reference volume to reduce the effect of patient and physiological motion during the DCE image acquisition. After the registration of the morphological image and the precontrast image, an oval-shaped or irregular-shaped region of interest (ROI) was drawn on the prostate cancer foci. ROIs were drawn in early enhancing region of DCE-MRI and with the DWI b800, ADC map, and T2-weighted image as references. T1 map calculation of precontrast was a prerequisite for pharmacokinetic modeling. T1 fitting was restricted to pixels with values above a noise level value (>20), and the respective values were automatically calculated by the system as a function of the entered contrast agents. For the Tofts modeling [6], Tissue 4D provides arterial input function (AIF) that are modeled using a biexponential function with three different modes (fast, intermediate, and slow). The AIF was chosen according to the fast sampling method to calculate kinetic parameters [9]. Parametric maps were calculated, and K^{trans}, K_{ep}, Ve, and iAUC of the selected ROI were automatically estimated by the software.

The ADC value of each identified tumor lesion was measured directly on the parametric ADC maps. The ADC map was reviewed simultaneously with the corresponding high b value DW images, T2-weighted images, and

Table 1: Sequence parameters for 3T multiparametric MRI with the body and spine matrix combination coil system.

Sequence	Pulse sequence	TR (msec)	TE (msec)	FA (°)	FOV (mm)	ACQmatrix	Slice/gap (mm)
Axial DWI, $b = 50$, 400, and 800 s/mm^2	SE-EPI	3800	77	90	221 × 260	102 × 160	3.6/0
Axial T2W	TSE	4000	100	90	200 × 200	288 × 320	3/0.6
Sagittal T2W	TSE	5000	100	90	200 × 200	288 × 320	3/0.6
Coronal T2W	TSE	5000	100	90	200 × 200	288 × 320	3/0.6
Axial 3D*	FLASH GRE	4.9	1.7	2 and 13	260 × 260	138 × 192	3/0
Axial 3D DCE	FLASH GRE	4.9	1.7	12	260 × 260	138 × 192	3.6/0

SE, spin echo; EPI, echo planar imaging; TSE, turbo spin echo; FLASH, fast low angle shot; GRE, gradient recalled echo; TR, repetition time; TE, echo time; FA, flip angle; ACQ matrix, acquisition matrix. *Sequence for the measurement of T1 relaxation time.

precontrast T1-weighted images. The slice of the ADC map containing the largest tumor extent was selected for analysis, and a ROI was drawn in the center of the tumor excluding the tumor edges. The mean ADC value and the size of the selected tumor area were generated at the workstation and recorded for analysis.

A prostate cancer was defined on each MRI as follows: a hypointense region relative to the adjacent parenchyma on T2-weighted image; a region with a low ADC value relative to the adjacent parenchyma on the ADC map; and a region with early wash-in and wash-out of contrast medium relative to the adjacent parenchyma on DCE-MRI. Precontrast T1-weighted images were used to identify postbiopsy hemorrhage (as an area with high signal intensity) to rule out false-positive findings.

2.5. Statistical Analysis. Statistical analysis was performed with SPSS (version 23.0, SPSS Inc., Chicago, Illinois, USA). A two-sided nonparametric Mann–Whitney U test was used to compare the patients age, PSA, tumor size, ADC, K^{trans}, K_{ep}, Ve, or iAUC between the peripheral and transitional zone tumor groups, between Gleason score 3 + 3 and 3 + 4 groups, and between different clinical stages. Spearman's correlation coefficient was used to evaluate the correlation between tumor size, ADC, K^{trans}, K_{ep}, Ve, iAUC, Gleason score, and serum PSA; p values less than 0.05 were considered significant.

3. Results

3.1. Patient Characteristics. No suspicious lesion was found on MRI in 7 out of the 71 patients with a biopsy proven prostate cancer; two patients had no DCE images due to allergy to the contrast agent. Sixty-nine lesions were detected in the prostate of the remaining 62 patients (age: mean ± SD: 70 ± 5 years, range from 60 to 79 years). Ten patients had clinical stage T1c and 52 had T2 (16 in T2a, 8 in T2b, and 28 in T2c) tumors according to TNM classification for prostate cancer. The serum PSA value (mean ± SD) was 9.5 ± 3.7 ng/mL, with the range from 3.4 to 19.1 ng/mL.

3.2. Pathological Results. There were 19 patients with a Gleason score 3 + 3, 41 with a Gleason score 3 + 4, and 2 with a Gleason score 4 + 3 tumor.

None of the measured parameters, including patients' age, serum PSA, and DWI- and DCE-MRI-derived parameters, were different between Gleason score 3 + 3 and 3 + 4 tumor groups.

3.3. Tumor Location. The majority of the tumors were in the peripheral zone (52, 75%), and the other 17 tumors were in the transitional zone.

There was no significant difference of the patients' age, serum PSA, tumor ADC, K^{trans}, or iAUC between the peripheral and transitional zone tumor groups (Table 2).

(a) The size of peripheral zone tumors (lesion number, $n = 52$) was smaller than that of the transitional zone tumors ($n = 17$) (0.68 ± 0.41 cm^2 versus 0.93 ± 0.59 cm^2; $p < 0.05$).

(b) K_{ep} was higher in the peripheral zone tumors (lesion number, $n = 52$) than that of the transitional zone tumors ($n = 17$) (0.59 ± 0.21 min^{-1} versus 0.49 ± 0.24 min^{-1}; $p < 0.05$).

(c) Ve was lower in the peripheral zone tumors (lesion number, $n = 52$) than that of the transitional zone tumors ($n = 17$) (0.27 ± 0.08 versus 0.32 ± 0.07; $p < 0.05$).

3.4. DCE-MRI-Derived Parameters. Prostate cancer showed earlier and more pronounced enhancement than surrounding normal prostate tissue (example Figure 1). Fifty-nine patients had perfusion MRI findings of at least one focal enhancing tumor in the prostate. In three patients, focal lesions were not obvious on the DCE images; all these 3 patients had clinical stage T2c tumors.

K^{trans} (0.11 ± 0.02 min^{-1} versus 0.16 ± 0.06 min^{-1}; $p < 0.05$), K_{ep} (0.38 ± 0.08 min^{-1} versus 0.60 ± 0.23 min^{-1}; $p < 0.01$), and iAUC (14.33 ± 2.66 mmoL/L/min versus 17.40 ± 5.97 mmoL/L/min; $p < 0.05$) were all lower in the clinical stage T1c tumors ($n = 11$) than that of the clinical stage T2 tumors ($n = 58$) (Figures 2(a)–2(c)).

3.5. Serum PSA Value. There were no significant differences of the serum PSA levels between clinical stage T1c ($n = 10$) and T2 patients ($n = 52$) (8.2 ± 4.5 ng/mL versus 9.8 ± 3.6 ng/mL; $p = 0.151$) (Figure 2(d)).

Table 2: Comparison of the 62 patients with peripheral and transitional zone prostate cancer (46 versus 16): age, tumor size, and DWI- and DCE-derived tumor parameters.

	Total $n = 69$ mean ± SD	Peripheral $n = 52$ mean ± SD	Transitional $n = 17$ mean ± SD	p value
Age (years)	70 ± 5	70 ± 5	70 ± 4	0.974
PSA (ng/mL)	9.5 ± 3.7	9.7 ± 3.9	9.1 ± 3.3	0.552
Area of tumor (cm^2)	0.74 ± 0.47	0.68 ± 0.41	0.93 ± 0.59	*0.037*
ADC ($\times 10^{-3}$ mm^2/s)	0.87 ± 0.16	0.89 ± 0.17	0.82 ± 0.13	0.259
K^{trans} (min^{-1})	0.15 ± 0.05	0.15 ± 0.05	0.14 ± 0.06	0.743
K_{ep} (min^{-1})	0.57 ± 0.22	0.59 ± 0.21	0.49 ± 0.24	*0.048*
Ve	0.28 ± 0.08	0.27 ± 0.08	0.32 ± 0.07	*0.026*
iAUC (mmoL/L/min)	16.70 ± 5.69	17.26 ± 5.51	15.86 ± 6.21	0.626

PSA, prostate-specific antigen; ADC, apparent diffusion coefficient; K^{trans}, volume transfer constant; K_{ep}, reflux constant; Ve, extravascular extracellular leakage volume fraction; iAUC, initial area under curve; n, number of tumors.

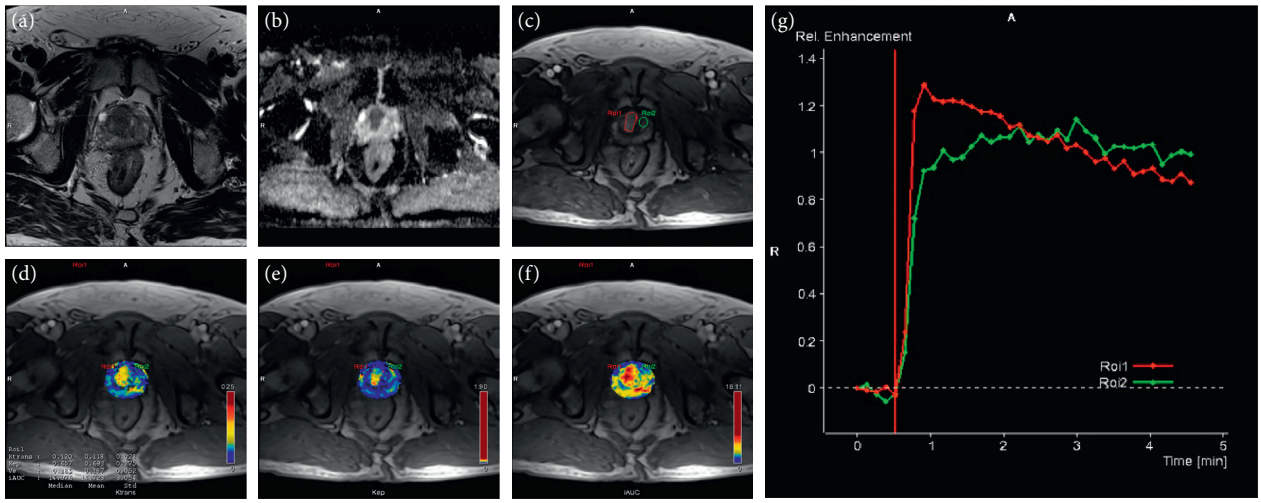

Figure 1: Transverse prostate MR images from a 69-year-old male patient with biopsy proven prostate cancer (Gleason score 3 + 4 and serum PSA 6.6 ng/mL): (a) T2-weighted image showing in the transitional zone a hypointense area without clear border; (b) ADC map: transitional zone hypointense region with a clear border, with ADC value of 0.75×10^{-3} mm^2/s; (c) T1-weighted image early enhancement map: the enhanced region of interest 1 (ROI1, red line) corresponds to the tumor, and ROI 2 (green line) was selected from normal prostate tissue as healthy control; (d) K^{trans} map: ROI 1 K^{trans} 0.120 min^{-1} and ROI 2 K^{trans} 0.048 min^{-1}; (e) K_{ep} map: ROI 1 K_{ep} 0.657 min^{-1} and ROI 2 K_{ep} 0.327 min^{-1}; (f) iAUC map: ROI 1 iAUC 14.976 mmoL/L/min and ROI 2 iAUC 6.871 mmoL/L/min; (g) enhancement kinetics pattern from the two ROIs: the time-intensity curves were obtained from dynamic contrast-enhanced MRI. ROI1 showing a higher peak enhancement and an early wash-in and wash-out of contrast medium compared with ROI 2.

3.6. The Correlations between PSA and MRI Parameters. Serum PSA correlated with both tumor K^{trans} ($r = 0.317$, $p = 0.012$) (Figure 3(a)) and tumor iAUC ($r = 0.258$, $p = 0.043$) (Figure 3(b)).

No correlation was found between serum PSA and tumor ADC value.

4. Discussion

A reliable diagnostic test should be able to provide an early prostate cancer diagnosis and minimize the amount of unnecessary biopsies or treatments. From this perspective, morphological MRI is a good candidate for prostate cancer investigation as it provides high-contrast and high-resolution images of the prostate. However, no single MRI sequence is sufficient to characterize prostate cancer. Each of the functional MR components has clinical advantages and limitations. Early promising data suggest that MP-MRI, which is performed concurrently with anatomical and functional techniques, is the most sensitive and specific imaging tool for lesion detection, characterization, and staging of prostate cancer [3]. Our study revealed a correlation between tumor K^{trans} and serum PSA in patients with early stage prostate cancer. This finding is consistent with previous publications [10, 11]. In addition, we detected a correlation between tumor iAUC and serum PSA. These may be explained by the altered vascular permeability of tumor microvessels and lymphatic system [12]. Neovascularity has been demonstrated to be a prerequisite for tumor growth and metastasis [13]. Abnormal angiogenesis in the tumor tissue lead to higher microvessel density, which is represented by leakage, twisted morphology, vascular wall expansion, and crosslinking [14]. Many scientists have suggested microvessel density as a prognostic and a predictive factor [15]. However, microvessel density measurement depends on the availability of postoperative tissue or biopsy materials, and it is a static assessment rather than information on vascular function. Therefore, there were

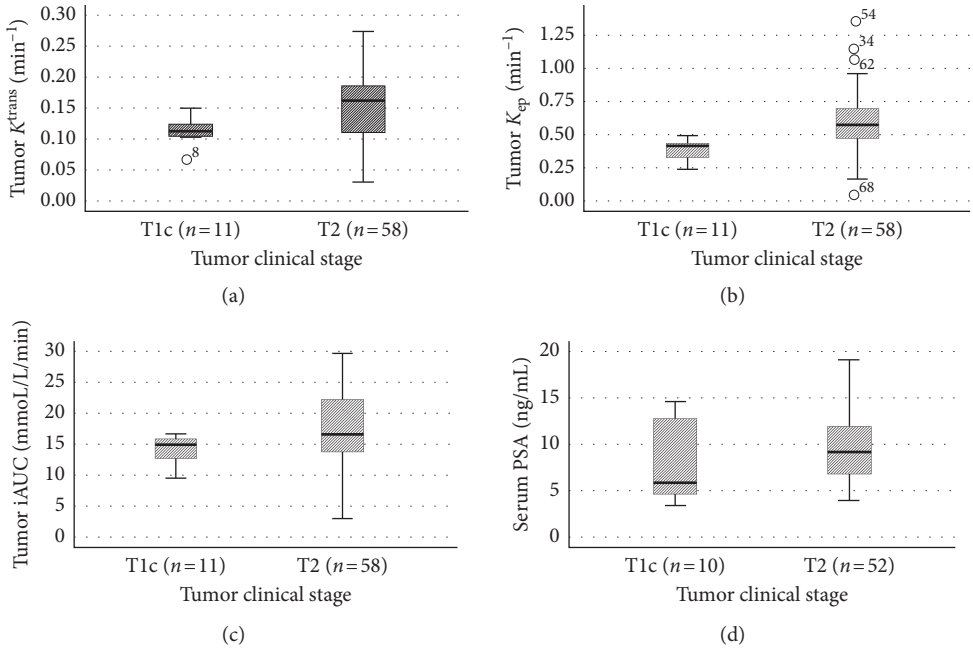

FIGURE 2: Comparison of tumor K^{trans}, K_{ep}, iAUC, and serum PSA level in patients with different clinical stages of prostate cancer. (a) K^{trans} ($0.11 \pm 0.02\,min^{-1}$ versus $0.16 \pm 0.06\,min^{-1}$; $p < 0.05$), (b) K_{ep} ($0.38 \pm 0.08\,min^{-1}$ versus $0.60 \pm 0.23\,min^{-1}$; $p < 0.01$), and (c) iAUC (14.33 ± 2.66 mmoL/L/min versus 17.40 ± 5.97 mmoL/L/min; $p < 0.05$) were all lower in clinical stage T1c tumors than that in clinical stage T2 tumors; (d) there was no significant difference of serum PSA between clinical stage T1c and T2 patients (8.2 ± 4.5 ng/mL versus 9.8 ± 3.6 ng/mL; $p = 0.151$).

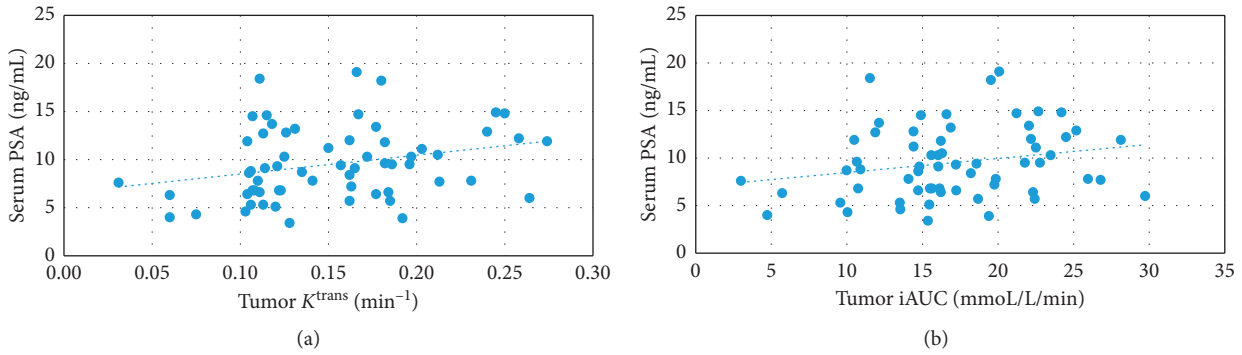

FIGURE 3: Correlations between serum PSA and DCE-MRI-derived tumor parameters in the 62 patients with prostate cancer. (a) Serum PSA correlated with tumor K^{trans} ($r = 0.317$, $p < 0.05$); (b) Serum PSA correlated with tumor iAUC ($r = 0.258$, $p < 0.05$).

controversial results between microvessel density and prostate cancer progression and grade [16]. In contrast, the distribution of Gd-DOTA in DCE-MRI is determined not only by microvessel density but also by vessel permeability and size of the extravascular extracellular space. DCE-MRI not only provides more details in tumor morphology but also allows to assess contrast agent kinetics and thus allows to improve detection and grading of prostate cancer.

DCE-MRI can be used to assess noninvasively the functional aspects of microcirculation of tissues. DCE-MRI relies on the fact that a bolus of contrast agent passing through the capillary bed is transiently confined within the vascular space before passing rapidly into the extravascular extracellular space at a rate determined by the permeability of the microvessels, their surface area, and blood flow [17, 18]. In DCE-MRI, the distribution of the contrast agent is repeatedly measured, allowing the evaluation of the tumor microcirculation in vivo and enabling the malignancy or benignancy of the tumor to be quantitatively distinguished [19]. Neoangiogenesis plays a vital role in the growth, progression, and metastasis process of prostate cancer [20, 21]. Microvessel density in prostatic carcinoma has also been shown to be an independent predictor of the pathological stage [13]. In consistent, we found that the tumor K^{trans}, K_{ep}, and iAUC were all lower in smaller tumors (T1c) than in larger local tumors (T2) in biopsy proven prostate cancer. To our knowledge, this is the first report that revealed DCE-MRI-derived parameters can separate very early stage tumors and relatively advanced tumors in clinically localized prostate cancer. Quantification of tumor angiogenesis by DCE-MRI may allow stratification of patients to type of treatment.

Serum PSA is elevated as a result of disruption of the prostatic architecture in the presence of prostate disease and injury, and PSA screening helps to diagnose prostate cancer earlier, at lower clinical stages and with lower Gleason score [22]. However, we did not find significant difference of the serum PSA levels between the tumors in clinical stage T1c and those with relatively extent diseases, for example, clinical stage T2. Serum PSA is not a specific marker for prostate cancer because of variable contribution to PSA from benign tissue and the nonlinear relationship between grade and PSA, which lead to overlap in PSA levels between different clinical stages as shown also in previous studies [23]. As a result, serum PSA level cannot be used alone to accurately predict disease extent for any individual patient. DCE-MRI play a role in conjunction with PSA for localizing suspicious lesions for biopsy, improving specificity, and identifying those tumors that are more likely to cause death if they are left untreated.

The Gleason score reflects the tumor aggressiveness and is an important predictor of outcome in patients with prostate cancer [2]. Correlation between the Gleason score and DCE-MRI-derived parameters may have been expected, because the Gleason scores have been shown to correlate with microvessel density measurements [13]. However, we did not detect any significant difference of the DCE-derived parameters between patients with Gleason score 3 + 3 and 3 + 4. The lack of differences may be explained by the heterogeneity of tumor tissues [24] and the histological sampling errors inherent in needle biopsy. Secondly, our patients were selected with one or two of the intermediate-risk features. Therefore, the differences of their disease extent/magnitude are relatively small compared with previous publications [10, 11].

Our study has a few limitations: firstly, the MRI was performed after biopsy. We were not sure, if the tumor ADC value and DCE parameters had been measured at the biopsy sites. Secondly, we were unable to evaluate the correlation between MRIs and histopathological features accurately because we did not obtain surgical specimens. There have been concerns about the probability of undergrading prostate cancer by biopsy due to tumor heterogeneity. Thirdly, all patients underwent needle biopsies before MRI examinations, implying that hemorrhagic or inflammatory changes caused by this procedure might have affected the MRIs. However, we excluded visible bleeding with the help of precontrast T1-weighted images, and the time interval between biopsy and MRI was long (6–10 weeks) enough for biopsy wound healing.

5. Conclusions

In conclusion, the present study has confirmed that DCE-MRI is a promising biomarker that reflects the microcirculation of prostate cancer. DCE-MRI-derived quantitative parameters in combination with clinical prognostic factors may provide an effective pretreatment diagnosis modality for early prostate cancer, especially for those with negative biopsy.

Data Availability

The data are available from the Medical Imaging Center of Tampere University Hospital.

Conflicts of Interest

The authors have no conflicts of interest to declare.

Acknowledgments

This project was supported by the Competitive State Research Financing of the Expert Responsibility Area of Tampere University Hospital, Seppo Nieminen Fund (Grant no. 150613), and Pirkko Kellokumpu-Lehtinen (Grant nos. 9R019 and 9S021). Xingchen Wu was supported by the Finnish Cultural Foundation, Pirkanmaa Regional Fund, and the Finnish Medical Foundation. The authors would like to thank research coordinator Irja Kolehmainen for her contributions.

References

[1] M. M. Center, A. Jemal, J. Lortet-Tieulent et al., "International variation in prostate cancer incidence and mortality rates," *European Urology*, vol. 61, no. 6, pp. 1079–1092, 2012.

[2] J. Cuzick, M. A. Thorat, G. Andriole et al., "Prevention and early detection of prostate cancer," *The Lancet Oncology*, vol. 15, no. 11, pp. e484–e492, 2014.

[3] L. Dickinson, H. U. Ahmed, C. Allen et al., "Magnetic resonance imaging for the detection, localisation, and characterisation of prostate cancer: recommendations from a European consensus meeting," *European Urology*, vol. 59, no. 4, pp. 477–494, 2011.

[4] C. Sato, S. Naganawa, T. Nakamura et al., "Differentiation of noncancerous tissue and cancer lesions by apparent diffusion coefficient values in transition and peripheral zones of the prostate," *Journal of Magnetic Resonance Imaging*, vol. 21, no. 3, pp. 258–262, 2005.

[5] N. Hylton, "Dynamic contrast-enhanced magnetic resonance imaging as an imaging biomarker," *Journal of Clinical Oncology*, vol. 24, no. 20, pp. 3293–3298, 2006.

[6] P. S. Tofts, G. Brix, D. L. Buckley et al., "Estimating kinetic parameters from dynamic contrast-enhanced T(1)-weighted MRI of a diffusable tracer: standardized quantities and symbols," *Journal of Magnetic Resonance Imaging*, vol. 10, no. 3, pp. 223–232, 1999.

[7] X. Wu, P. Reinikainen, A. Vanhanen et al., "Correlation between apparent diffusion coefficient value on diffusion-weighted MR imaging and Gleason score in prostate cancer," *Diagnostic and Interventional Imaging*, vol. 98, no. 1, pp. 63–71, 2017.

[8] NCCN, *National Comprehensive Cancer Network Clinical Practice Guidelines in Oncology: Prostate Cancer*, Version 1, NCCN, Fort Washington, PA, USA, 2014.

[9] M. R. Orton, J. A. d'Arcy, S. Walker-Samuel et al., "Computationally efficient vascular input function models for quantitative kinetic modelling using DCE-MRI," *Physics in Medicine and Biology*, vol. 53, no. 5, pp. 1225–1239, 2008.

[10] M. P. Chung, D. Margolis, S. Mesko, J. Wang, P. Kupelian, and M. Kamrava, "Correlation of quantitative diffusion-weighted and dynamic contrast-enhanced MRI parameters with prognostic factors in prostate cancer," *Journal of Medical*

Imaging and Radiation Oncology, vol. 58, no. 5, pp. 588–594, 2014.

[11] E. Cho, D. J. Chung, D. M. Yeo et al., "Optimal cut-off value of perfusion parameters for diagnosing prostate cancer and for assessing aggressiveness associated with Gleason score," *Clinical Imaging*, vol. 39, no. 5, pp. 834–840, 2015.

[12] S. Verma, B. Turkbey, N. Muradyan et al., "Overview of dynamic contrast-enhanced MRI in prostate cancer diagnosis and management," *American Journal of Roentgenology*, vol. 198, no. 6, pp. 1277–1288, 2012.

[13] M. K. Brawer, R. E. Deering, M. Brown, S. D. Preston, and S. A. Bigler, "Predictors of pathologic stage in prostatic carcinoma. The role of neovascularity," *Cancer*, vol. 73, no. 3, pp. 678–687, 1994.

[14] M. Furuya and Y. Yonemitsu, "Cancer neovascularization and proinflammatory microenvironments," *Current Cancer Drug Targets*, vol. 8, no. 4, pp. 253–265, 2008.

[15] S. Muhammadnejad, A. Muhammadnejad, M. Haddadi et al., "Correlation of microvessel density with nuclear pleomorphism, mitotic count and vascular invasion in breast and prostate cancers at preclinical and clinical levels," *Asian Pacific Journal of Cancer Prevention*, vol. 14, no. 1, pp. 63–68, 2013.

[16] P. Yuri, A. Z. Hendri, and R. Danarto, "Association between tumor-associated macrophages and microvessel density on prostate cancer progression," *Prostate International*, vol. 3, no. 3, pp. 93–98, 2015.

[17] J. Ren, Y. Huan, H. Wang et al., "Dynamic contrast-enhanced MRI of benign prostatic hyperplasia and prostatic carcinoma: correlation with angiogenesis," *Clinical Radiology*, vol. 63, no. 2, pp. 153–159, 2008.

[18] M. de Rooij, E. H. Hamoen, J. J. Futterer, J. O. Barentsz, and M. M. Rovers, "Accuracy of multiparametric MRI for prostate cancer detection: a meta-analysis," *American Journal of Roentgenology*, vol. 202, no. 2, pp. 343–351, 2014.

[19] A. Jackson, J. P. O'Connor, G. J. Parker, and G. C. Jayson, "Imaging tumor vascular heterogeneity and angiogenesis using dynamic contrast-enhanced magnetic resonance imaging," *Clinical Cancer Research*, vol. 13, no. 12, pp. 3449–3459, 2007.

[20] G. Russo, M. Mischi, W. Scheepens, J. J. De la Rosette, and H. Wijkstra, "Angiogenesis in prostate cancer: onset, progression and imaging," *BJU International*, vol. 110, no. 11c, pp. E794–E808, 2012.

[21] G. Bergers and L. E. Benjamin, "Tumorigenesis and the angiogenic switch," *Nature Reviews Cancer*, vol. 3, no. 6, pp. 401–410, 2003.

[22] H. B. Carter, "Differentiation of lethal and non lethal prostate cancer: PSA and PSA isoforms and kinetics," *Asian Journal of Andrology*, vol. 14, no. 3, pp. 355–360, 2012.

[23] S. Pentyala, T. Whyard, S. Pentyala et al., "Prostate cancer markers: an update," *Biomedical Reports*, vol. 4, no. 3, pp. 263–268, 2016.

[24] R. J. Gillies, P. A. Schornack, T. W. Secomb, and N. Raghunand, "Causes and effects of heterogeneous perfusion in tumors," *Neoplasia*, vol. 1, no. 3, pp. 197–207, 1999.

Hindawi
Contrast Media & Molecular Imaging
Volume 2018, Article ID 8271313, 7 pages
https://doi.org/10.1155/2018/8271313

Research Article

Comparison of ^{18}F-NaF PET/CT and ^{18}F-FDG PET/CT for Detection of Skull-Base Invasion and Osseous Metastases in Nasopharyngeal Carcinoma

Yin Zhang,[1] Yue Chen,[1,2] Zhanwen Huang,[1] Li Zhang,[1] Qiang Wan,[1] and Lei Lei[1]

[1]*Department of Nuclear Medicine, Affiliated Hospital of Southwest Medical University, Luzhou, China*
[2]*Nuclear Medicine and Molecular Imaging Key Laboratory of Sichuan Province, Luzhou, China*

Correspondence should be addressed to Yue Chen; chenyue5523@126.com

Received 3 April 2018; Accepted 9 August 2018; Published 5 September 2018

Academic Editor: Pietro Muto

Our study aimed at comparing the diagnostic value of ^{18}F-NaF positron emission tomography-computed tomography (PET/CT) and ^{18}F-fluorodeoxyglucose (FDG) PET/CT for detection of skull-base invasion and osseous metastases in patients with nasopharyngeal carcinoma (NPC). Our study retrospectively analyzed 45 patients with pathologically proven NPC. They all underwent both ^{18}F-NaF PET/CT and ^{18}F-FDG PET/CT within a 7-day interval. Bone metastases were confirmed by follow-up using PET/CT, enhance-contrast computed tomography (CT), and magnetic resonance image (MRI). These two examinations were compared using per-patient-based analysis and per-lesion-based analysis. ^{18}F-NaF PET/CT detected 27 patients with skull-base invasion, whereas ^{18}F-FDG PET/CT detected 17 patients. ^{18}F-NaF PET/CT and ^{18}F-FDG PET/CT differed significantly in diagnosing skull-base invasion ($p = 0.02$) and sensitivity ($p = 0.008$). The sensitivity, specificity, and agreement rate of ^{18}F-NaF PET/CT for detecting bone metastatic lesions were 98.3%, 65.7%, and 92.9%, respectively; these values were 42.9%, 97.1%, and 51.9%, respectively, for ^{18}F-FDG PET/CT. ^{18}F-NaF PET/CT and ^{18}F-FDG PET/CT differed significantly in the number of osseous metastases detected ($t = 2.45$, $p = 0.18$) sensitivity ($p < 0.0001$) and specificity ($p = 0.003$). In patients with nasopharyngeal carcinoma, ^{18}F-NaF PET/CT assessed invasion of the skull base better and detected more osseous metastases than ^{18}F-FDG PET/CT.

1. Introduction

Nasopharyngeal carcinoma (NPC) is an uncommon cancer worldwide but is prevalent in East and Southeast Asia [1]. NPC has a tendency to spread early to local sites, and regional nodal involvement is frequent (70–90%). Autopsy studies show that distant metastases are as frequent as 38–87% and that bone metastases occur in 70–80% of patients with distant metastases [2, 3]. The actual frequency of such metastases may be greater than the reported data owing to the low autopsy rate in Asia. Early and accurate NPC staging is important for improving both patient quality of life and therapeutic effects.

Prior to treating NPC, the presence of bone metastases or skull-base invasion should be evaluated. The management of patients with osseous metastases is quite different. If skull-base invasion is diagnosed, the T-stage is upgraded to T3, which has implications for changing therapeutic strategies, such as increasing the radiation dose and extending the therapeutic field [4].

^{99m}Tc-methylene diphosphonate (MDP) planar bone scan or single-photon emission computed tomography (SPECT) is widely used as noninvasive methods for detecting osseous metastases. However, these methods cannot obtain cross-sectional images of all the lesions, and they have lower resolution than other imaging techniques, such as positron emission tomography/computed tomography (PET/CT) [5].

As a molecular imaging technology, PET/CT can indicate the degree of metabolic function of a malignancy and the clinical stage, response to therapy, and tumour recurrence, whereas conventional imaging modalities can only reveal morphological and anatomical information [6, 7]. ^{18}F-fluorodeoxyglucose (FDG) has become a routine tracer

agent for PET/CT but detecting osseous metastases is a relative weakness of ^{18}F-FDG PET/CT compared with traditional bone scans and ^{18}F-NaF PET/CT.

^{18}F-NaF was approved by the U.S. Food and Drug Administration as a bone-seeking diagnostic molecular imaging agent in 1972 [8]. Because ^{18}F-NaF has better pharmacokinetic characteristics than ^{99m}Tc-MDP, ^{18}F-NaF regained clinical attention with the development of PET/CT. Many reports have compared the diagnostic value of ^{18}F-NaF PET/CT with that of ^{18}F-FDG PET/CT for detecting osseous metastases of lung, breast, and prostate cancer [9, 10]. However, to the best of our knowledge, no study has compared the clinical value of ^{18}F-NaF PET/CT with that of ^{18}F-FDG PET/CT for staging NPC.

2. Materials and Methods

2.1. Patients. We reviewed the medical records of patients with pathologically proven NPC from March 2013 to June 2015 who underwent both ^{18}F-NaF PET/CT and ^{18}F-FDG PET/CT within an interval of 7 days. The exclusion criteria were a history or the detection of another cancer type and an interval greater than 30 days between an imaging examination and chemotherapy or radiotherapy.

We obtained informed consent from patients before both examinations. Our retrospective review of imaging studies was approved by the institutional review board of the Affiliated Hospital of Southwest Medical University.

2.2. The ^{18}F-FDG PET/CT and ^{18}F-NaF PET/CT Protocols. ^{18}F-FDG and ^{18}F-NaF were produced by a Cyclotron (Siemens Eclipse RD) and an automatic synthesis module (Beijing PET Technology Co., Ltd., Beijing, China) in our centre. The radiochemical purity of ^{18}F-FDG was greater than 95%. Patients were requested to fast for at least 6 hours before ^{18}F-FDG was administered. The ^{18}F-FDG PET/CT procedure was delayed in patients with a blood glucose level >11 mmol/L (200 mg/dL) until the blood glucose level decreased to ≤11 mmol/L or these patients underwent the examination on another day [11, 12]. Before and after the injection, the patients rested and were kept quiet. The doses of ^{18}F-FDG and ^{18}F-NaF were 5.55 MBq/kg and 4.07 MBq/kg, respectively.

Approximately 1 hour after the injection, examinations began with a Philips Gemini TF/16 PET/CT scanner. For ^{18}F-FDG PET/CT, CT scanning was first performed with 120 kV, 80–250 mA, 0.81 pitch, and 0.5 rotation time from the mid-thigh to the skull base. For ^{18}F-NaF PET/CT, the scanned area ranged from the feet to the cranium. The emission image acquisition time was 70 seconds per bed position. PET image data were reconstructed by applying attenuation correction based on the CT data using the ordered subset expectation maximization algorithm.

2.3. Image Interpretation. Two experienced nuclear medicine physicians independently evaluated the ^{18}F-NaF PET/CT and ^{18}F-FDG PET/CT images in a random order for each patient. They were blinded to other imaging results and the final results of the lesions. For discrepant cases, the interpreters reached a consensus.

2.4. Definition of Skull-Base Invasion and Metastases. PET component: local foci of the radioindicator were targeted as malignancy. The maximal standardized uptake value (SUV_{max}) of the mediastinal blood pool was considered as the reference value for ^{18}F-FDG PET and the SUV_{max} of heterolateral or adjacent bone was the reference value for ^{18}F-NaF PET. Because of the heterogeneity of ^{18}F-NaF concentration in different bones, we could not establish a unified SUV_{max} standard to evaluate all skeletons [13].

CT component: bone destruction or osteoblastic manifestation of bone (local and asymmetric lesions with increased density) was targeted as malignancy. Differentiations between osteogenic metastases, degenerative disease, and changes after radiotherapy, such as osteoradionecrosis, were difficult only by CT images [14]. Although the uptake was associated with the end plates or joint surfaces, it was always representative of degeneration disease [15]. We combined the clinical history with PET/CT features to make diagnosis.

The examination range of ^{18}F-NaF PET/CT was from the feet to the cranium because of the clinical request of whole-body evaluation. But when we review the images, we only record the lesions located in the range from the mid-thigh to the skull base, which was same to ^{18}F-FDG PET/CT. The final diagnosis was based on the overall findings from both the PET and CT components.

Because the biopsy of all the skull-base invasion and bone metastases lesions were difficult to be obtained, whether the skull base of these patients were invaded was verified by MRI or contrast-enhanced CT within one week after the PET/CT examinations. Bone metastases were confirmed by enhance-contrast computed tomography (CT) or magnetic resonance image (MRI) and one year's follow-up. If lesions progressed in the period of follow-up or osteolytic lesion changed to osteoblastic lesion during treatment, they were determined as bone metastases [16]. Undetermined lesions and lesions without obvious changes during follow-up were considered benign lesions (verified negatives) in the analysis.

2.5. Biochemical Analysis. Biochemical markers such as alkaline phosphatase were reported to be correlated with bone metastases [17]. Test data of serum alkaline phosphatase were collected if the interval time between blood test and ^{18}F-NaF PET/CT was less than 7 days.

2.6. Statistical Analysis. The sensitivity, specificity, and positive and negative predictive values (PPVs and NPVs) of ^{18}F-NaF PET/CT and ^{18}F-FDG PET/CT were calculated for the diagnosis of skull-base invasion (per-patient analysis) and the detection of bone metastases (per-lesion analyses). The number of osseous metastases detected by ^{18}F-NaF PET/CT and ^{18}F-FDG PET/CT were compared using the paired-samples t test. McNemar's

chi-squared test for matched pairs was used to compare the diagnostic value of ^{18}F-NaF PET/CT with ^{18}F-FDG PET/CT for detecting skull-base invasion. Serum alkaline phosphatase of patients with bone metastases and patients without bone metastases were compared using independent samples t-test. Correlation between serum alkaline phosphatase and SUV_{max} of ^{18}F-NaF PET/CT had also been assessed by the Spearman analysis.

3. Results

In total, 45 patients were reviewed (Table 1). All 45 patients were evaluated during a 3-month follow-up visit. ^{18}F-NaF PET/CT detected skull-base invasion in the 26 patients with verified skull-base invasion. One additional patient who was diagnosed as having skull-base invasion according to ^{18}F-NaF PET/CT was considered a false positive based on the MRI evaluation. In contrast, ^{18}F-FDG PET/CT diagnosed only 17 of the 26 positively verified patients and did not detect any false-positive patients (Figure 1). Therefore, the sensitivity, specificity, accuracy, PPV, and NPV of ^{18}F-NaF PET/CT for detecting skull-base invasion were 100%, 94.7%, 97.8%, 96.3%, and 100%, respectively, whereas these diagnostic measures were 65.4%, 100%, 80%, 100%, and 67.9%, respectively, for ^{18}F-FDG PET/CT. ^{18}F-NaF PET/CT correctly diagnosed more patients than ^{18}F-FDG PET/CT ($p = 0.02$). Whereas the sensitivity of ^{18}F-NaF PET/CT was higher than that of ^{18}F-FDG PET/CT ($p = 0.008$), no significant difference in specificity was observed ($p = 1$).

Osseous metastases were detected in 26 patients using ^{18}F-NaF PET/CT or ^{18}F-FDG PET/CT. Using ^{18}F-NaF PET/CT, 208 lesions were identified as bone metastases in 26 patients (mean, 8). In contrast, using ^{18}F-FDG PET/CT, physicians diagnosed 81 lesions as osseous metastases (mean, 6.75). ^{18}F-NaF PET/CT detected more bone metastatic lesions than ^{18}F-FDG PET/CT did ($t = 2.45$, $p = 0.018$). The locations of these lesions are described in Table 2.

Over the course of more than one year's follow-up, 43 patients underwent chest and abdominal CT or MRI examinations. Six patients completed whole-spine MRI scans. Five patients completed pelvic cavity CT or MRI examinations. Seven patients underwent PET/CT reexaminations and 15 patients underwent ^{99m}Tc-MDP bone SPECT/CT scans. The final number of verified lesions was 212, among which 177 lesions were malignant and the other 35 lesions were benign. The osseous metastatic lesions that were diagnosed using ^{18}F-NaF PET/CT and ^{18}F-FDG PET/CT are presented in Table 3. Among the verified metastatic lesions, 12 lesions detected by ^{18}F-NaF PET/CT were false positives, whereas 3 lesions were false negatives. In contrast, one lesion diagnosed by ^{18}F-FDG PET/CT was a false positive, whereas 101 verified lesions were not detected by ^{18}F-FDG PET/CT (Figure 2). The sensitivity, specificity, PPV, and NPV of ^{18}F-NaF PET/CT and ^{18}F-FDG PET/CT for the diagnosis of osseous metastatic lesions are presented in Table 4. The differences between ^{18}F-NaF PET/CT and ^{18}F-FDG PET/CT in sensitivity and specificity were both significant ($p < 0.0001$ and $p = 0.003$, respectively). Combining ^{18}F-NaF PET/CT with ^{18}F-FDG PET/CT changed 13 of 45 (28.9%) management decisions made by ^{18}F-FDG PET/CT alone.

Table 1: Demographic and clinical characteristics of study patients.

Characteristics	Number of patients ($n = 45$)	%
Age		
Range (22–73 years)		
Median (52 years)		
Gender		
Male	36	80
Female	9	20
Histology		
Squamous carcinoma	38	84.4
Undifferentiated carcinoma	7	15.6
Pretreatment	35	77.8
Posttreatment	10	22.2

40 patients underwent the blood test of near the ^{18}F-NaF PET/CT examinations. The range of serum alkaline phosphatase was between 5.5 and 128 U/L (median was 82.1 U/L). SUV_{max} of ^{18}F-NaF PET/CT in these patients ranged from 8.16 to 68.8 (median was 16.9). T test showed there were no significant differences between patients with bone metastases and patients without bone metastases ($t = 1.575$, $p = 0.124$). There were no significant correlations between serum alkaline phosphatase and SUV_{max} of ^{18}F-NaF PET/CT of these patients (rs = 0.002, $p = 0.991$).

4. Discussion

As revealed by Löfgren's article [16], the pathological evidence of skull-base invasion and bone metastases was hard to be obtained even in the prospective study. It is mainly due to the impracticality of obtaining more than one, sometimes dozens of, biopsy specimens from one patient. Besides, the torture of patients and the difficulty of biopsy on skull-base invasion and bone metastases are other limitations to biopsy analyses. So the assessments of skull-base invasion and bone metastases are commonly accomplished by imaging methods.

Imaging methods commonly used in the clinical staging of NPC include ultrasound, plain film, CT, MRI, bone scans, and PET/CT. These examinations are generally regional, except for bone scans and PET/CT. A whole-body examination using multiple imaging modalities is superior to evaluating the clinical stage using only regional scan methods. Ultrasound is inaccurate for assessing osseous status. Whole-body CT examination is limited by the radiation exposure. As for MRI, its disadvantage is the long examination time required.

Among all imaging methods used for the management of cancer, the most specific one is radionuclide-labelled gene imaging. However, the target gene of NPC is under investigation [18, 19].

In clinical practice, we use ^{18}F-FDG PET/CT as the common method for tumour staging. However, in ^{18}F-FDG PET/CT, the uptake of radiotracer by brain and tumour tissue may disturb the estimation of whether the skull base is

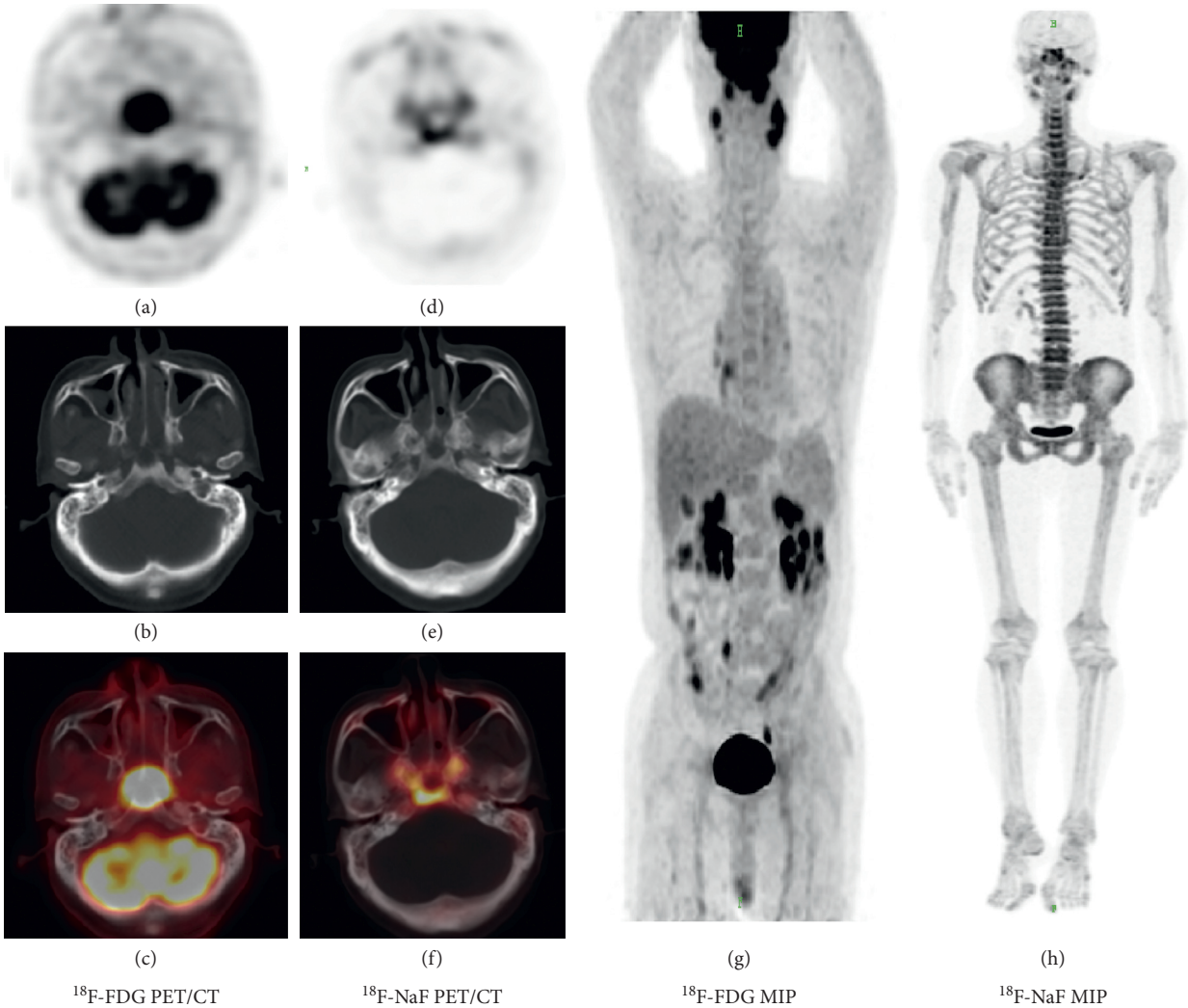

Figure 1: A 63-year-old man was diagnosed with nonkeratinizing nasopharyngeal carcinoma. (A–C) transverse sections of PET, CT, and fusion views in ^{18}F-FDG PET/CT, respectively. (D–F) transverse sections of PET, CT, and fusion views in ^{18}F-NaF PET/CT. (G and H) the maximum intensity projection (MIP) of ^{18}F-FDG PET/CT and ^{18}F-NaF PET/CT, respectively. Skull-base invasion was revealed on ^{18}F-NaF PET/CT but was hidden on ^{18}F-FDG PET/CT because of the interference from the tumor tissue. This was consistent with MRI two days before ^{18}F-NaF PET/CT.

Table 2: Description of osseous metastases detected in 26 patients: number of lesions by location, radiotracer, and follow-up status.

Location	NaF PET/CT	FDG PET/CT	Follow-up positive
Skull (except for skull base)	3	0	2
Sternum and ribs	52	17	46
Centrum	89	39	78
Ilium, pubis, and ischia	39	18	31
Limbs (include scapula and clavicle)	25	7	21
Total	208	81	177

Table 3: The proportion of confirmed osseous metastases that were detected by each radiotracer for each type of metastatic lesion.

	^{18}F-NaF PET/CT	^{18}F-FDG PET/CT
Osteoblastic	42/50	18/18
Osteolytic	49/57	27/28
Mixed	22/22	8/8
No obvious abnormality on CT	61/79	23/27
Total	174/208	76/81

invaded. The advantages of ^{11}C-choline PET/CT for T staging of NPC and other disease in skull base compared with ^{18}F-FDG PET/CT have been reported [20, 21]. However, the difficulty of producing ^{11}C-choline and the short half-life of the radionuclide are the limitations of its extension in clinical practice. These disadvantages are not applicable to ^{18}F-NaF PET/CT.

The uptake mechanism of ^{18}F-NaF is by chemisorption to hydroxyapatite, with resultant conversion into fluorapatite and a hydroxyl group. Regional blood flow and

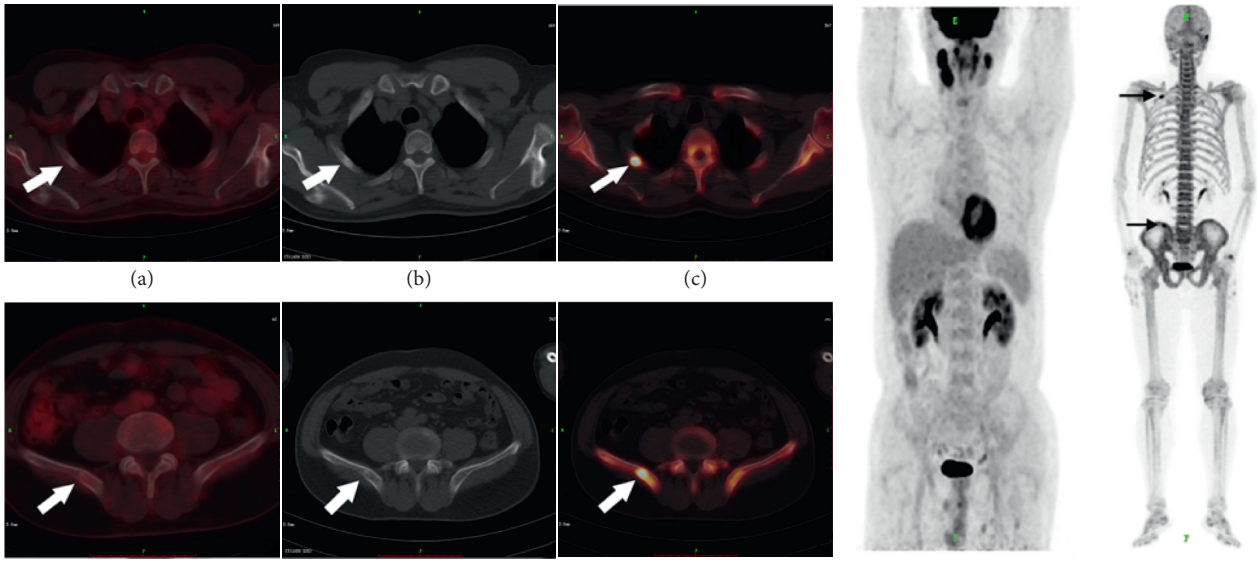

Figure 2: A, D, and G are parts of ^{18}F-FDG PET/CT and C, F, and H are parts of ^{18}F-NaF PET/CT. B and E are transverse sections of low-dose CT. Abnormal uptake of ^{18}F-NaF is shown at the right rib and right ilium, whereas no abnormal concentration of ^{18}F-FDG is found (arrows). The lesions are verified as osseous metastases by CT follow-up.

Table 4: Measures of diagnostic performance using ^{18}F-NaF PET/CT or ^{18}F-FDG PET/CT to detect osseous metastatic lesions of patients with nasopharyngeal carcinoma.

	TP	FP	TN	FN	Sensitivity (%)	Specificity (%)	PPV (%)	NPV (%)	Accuracy (%)
^{18}F-NaF PET/CT	174	12	23	3	98.3	65.7	93.4	88.5	92.9
^{18}F-FDG PET/CT	76	1	34	101	42.9	97.1	98.7	25.2	51.9

TP: true positive; FP: false positive; TN: true negative; FN: false negative.

osteoblastic activity are main factors that influence the ^{18}F-NaF uptake [15].

The overall accuracy and sensitivity of ^{18}F-NaF PET/CT are superior to those of ^{18}F-FDG PET/CT for diagnosing patients with skull-base invasion. Lau et al. previously reported that ^{18}F-NaF PET/CT was more sensitive than ^{18}F-FDG PET/CT for diagnosing skull-base invasion and could improve the diagnostic accuracy [4]. Our study revealed that ^{18}F-NaF PET/CT was more sensitive than ^{18}F-FDG PET/CT and exhibited a similar specificity. Owing to the better diagnostic performance of ^{18}F-NaF PET/CT for evaluating the skull base, it can more accurately determine the target volume for radiotherapy.

Although the reported false-positive rate of ^{18}F-NaF PET/CT is relatively high, our study demonstrated that the diagnostic accuracies of ^{18}F-NaF PET/CT are sufficiently high for detecting skull-base involvement in patients with NPC while compared with MRI. This finding is consistent with our previous study [22]. We consider that this finding may be related to the false-positive discoveries of MRI owing to common oedema and inflammation before and after radiotherapy. Although the uptake of ^{18}F-NaF is not specific to osseous malignancy, correlation of functional findings on ^{18}F-NaF PET with anatomic information on CT improves the specificity of this modality. Further studies should be performed to compare the accuracies of ^{18}F-NaF PET/CT, MRI, and true positive methods.

^{18}F-FDG PET/CT has advantages for evaluating systemic conditions. Liu et al. discovered that ^{18}F-FDG PET can replace conventional work-ups, including chest radiography, abdominal ultrasonography, and skeletal scintigraphy, in the primary M staging of nonkeratinizing NPC [23]. However, a retrospective study of 35 newly diagnosed NPC patients conducted by Yang et al. found no significant difference between ^{18}F-FDG PET/CT and planar bone scanning (PBS) in diagnosing one or more osseous metastases in NPC patients. They also reported that some bone metastases could be detected by PBS but not by ^{18}F-FDG PET/CT [3]. Many studies have reported the superiority of ^{18}F-NaF PET/CT for detecting bone metastases compared with ^{18}F-FDG PET/CT [24–26]. Our study showed that in patients with NPC, ^{18}F-NaF PET/CT detects more bone metastases with a higher sensitivity than ^{18}F-FDG PET/CT does. For osteoblastic lesions, ^{18}F-NaF PET/CT can show more sensitivity than ^{18}F-FDG PET/CT due to the imaging mechanism of these two tracers. ^{18}F-FDG PET/CT detects lesions owing to the abnormal metabolism of cancer cells, whereas ^{18}F-NaF PET/CT reveals abnormal blood perfusion and bone reconstruction. Previous studies have shown that ^{18}F-FDG PET/CT has modest sensitivity for detecting

osteoblastic lesions and that ^{18}F-NaF PET/CT detects both osteoblastic and osteolytic bone metastases well [10, 23]. In our study, ^{18}F-NaF PET/CT detected more osteoblastic, osteolytic, and mixed-type metastases and lesions without obvious changes on the CT images compared with ^{18}F-FDG PET/CT. These findings may be due to some osseous metastases having only abnormal blood perfusion or bone reconstruction without disordered glucose metabolism.

Because ^{18}F-NaF PET/CT and ^{18}F-FDG PET/CT each have unique advantages and disadvantages, medical management could be improved by using both methods in one combined examination [27]. Further study should be made to combine these two methods while keeping the radioexposure of patients low enough.

Serum alkaline phosphatase was proved to be uncorrelated with bone metastases and SUV_{max} of ^{18}F-NaF PET/CT in our study. It may be due to the small sample and the huge amount of influence factors on serum alkaline phosphatase such as age and living standard. Even so, ^{18}F-NaF PET/CT could still reflect the regional blood flow and osteoblastic activity in an noninvasive way, which could be an indicator for assessing treatment response [28].

Our study has several limitations. First, our study was performed retrospectively with a limited number of patients who were heterogeneous, which might have led to selection bias. Second, it was impossible for us to obtain pathological material from each patient, which potentially produced errors in the final diagnosis. Third, in the benign group, we included undetermined lesions and lesions without obvious changes during follow-up, which may have increased the rate of false negatives.

5. Conclusion

This retrospective study of NPC patients demonstrated that ^{18}F-NaF PET/CT detected more osseous metastases and more accurately assessed skull-base invasion than did ^{18}F-FDG PET/CT. Combining ^{18}F-NaF PET/CT with ^{18}F-FDG PET/CT could improve the stage evaluation of NPC compared with ^{18}F-FDG PET/CT alone.

Data Availability

The data used to support the findings of this study are included within the article.

Conflicts of Interest

The authors declare that there are no conflicts of interest regarding the publication of this article.

Acknowledgments

The authors would like to thank the patients who underwent the two examinations. The authors acknowledge the help of the staff members in the Department of Nuclear Medicine for the coordination of this study. The study was supported by the Luzhou City-Southwest Medical University Research Project on Nuclear Precision Medicine (grant number: 2016LZXNYD-G01).

References

[1] L. A. Torre, F. Bray, R. L. Siegel, J. Ferlay, J. Lortet-Tieulent, and A. Jemal, "Global cancer statistics," *CA: A Cancer Journal for Clinicians*, vol. 65, no. 2, pp. 87–108, 2015.

[2] F. Chiesa and F. De Paoli, "Distant metastases from nasopharyngeal cancer," *ORL*, vol. 63, no. 4, pp. 214–216, 2001.

[3] Z. Y. Yang, Y. Zhang, W. Shi et al., "Is ^{18}F-FDG PET/CT more reliable than ^{99m}Tc-MDP planar bone scintigraphy in detecting bone metastasis in nasopharyngeal carcinoma?," *Annals of Nuclear Medicine*, vol. 28, no. 5, pp. 411–416, 2014.

[4] Y. C. Lau, "The utility of ^{18}F-Fluoride PET/CT for the detection of skull base involvement in nasopharyngeal carcinoma," *SNM Annual Meeting Abstracts*, vol. 51, p. 460, 2010.

[5] L. Zhang, L. Chen, Q. Xie et al., "A comparative study of ^{18}F-fluorodeoxyglucose positron emission tomography/computed tomography and ^{99m}Tc-MDP whole-body bone scanning for imaging osteolytic bone metastases," *BMC Medical Imaging*, vol. 15, no. 1, 2015.

[6] J. Czernin, W. A. Weber, and H. R. Herschman, "Molecular imaging in the development of cancer therapeutics," *Annual Review of Medicine*, vol. 57, no. 1, pp. 99–118, 2006.

[7] P. L. Jager, M. A. de Korte, M. N. Lub-de Hooge et al., "Molecular imaging: what can be used today," *Cancer Imaging*, vol. 5, pp. S27–S32, 2005.

[8] G. Segall, D. Delbeke, M. G. Stabin et al., "SNM practice guideline for sodium ^{18}F-fluoride PET/CT bone scans 1.0," *Journal of Nuclear Medicine*, vol. 51, no. 11, pp. 1813–1820, 2010.

[9] U. Simoncic, S. Perlman, G. Liu et al., "Comparison of NaF and FDG PET/CT for assessment of treatment response in castration-resistant prostate cancers with osseous metastases," *Clinical Genitourinary Cancer*, vol. 13, no. 1, pp. e7–e17, 2015.

[10] N. A. Damle, C. Bal, G. P. Bandopadhyaya et al., "The role of ^{18}F-fluoride PET-CT in the detection of bone metastases in patients with breast, lung and prostate carcinoma: a comparison with FDG PET/CT and ^{99m}Tc-MDP bone scan," *Japanese Journal of Radiology*, vol. 31, no. 4, pp. 262–269, 2013.

[11] R. Boellaard, M. J. O'Doherty, A. Chiti, and B. J. Krause, "FDG PET and PET/CT: EANM procedure guidelines for tumour PET imaging: version 1.0," *European Journal of Nuclear Medicine and Molecular Imaging*, vol. 37, no. 7, pp. 1432-1433, 2010.

[12] D. Delbeke, R. E. Coleman, M. J. Guiberteau et al., "Procedure guideline for tumor imaging with ^{18}F-FDG PET/CT 1.0," *Journal of Nuclear Medicine*, vol. 47, no. 5, pp. 885–895, 2006.

[13] J. D. Oldan, A. S. Hawkins, and B. B. Chin, "^{18}F sodium fluoride PET/CT in patients with prostate cancer: quantification of normal tissues, benign degenerative lesions, and malignant lesions," *World Journal of Nuclear Medicine*, vol. 15, no. 2, pp. 102–108, 2016.

[14] L. A. Wu, H. M. Liu, C. W. Wang, Y. F. Chen, R. L. Hong, and J. Y. Ko, "Osteoradionecrosis of the upper cervical spine after radiation therapy for head and neck cancer: differentiation from recurrent or metastatic disease with MR imaging," *Radiology*, vol. 264, no. 1, pp. 136–145, 2012.

[15] M. Beheshti, A. Rezaee, H. Geinitz, W. Loidl, C. Pirich, and W. Langsteger, "Evaluation of prostate cancer bone metastases with ^{18}F-NaF and ^{18}F-fluorocholine PET/CT," *Journal of Nuclear Medicine*, vol. 57, no. S3, pp. 55S–60S, 2016.

[16] J. Löfgren, J. Mortensen, S. H. Rasmussen et al., "A prospective study comparing 99mTc-hydroxyethylene-diphosphonate planar bone scintigraphy and whole-body SPECT/CT with

^{18}F-fluoride PET/CT and ^{18}F-fluoride PET/MRI for diagnosing bone metastases," *Journal of Nuclear Medicine*, vol. 58, no. 11, pp. 1778–1785, 2017.

[17] Q. Huang and X. Ouyang, "Biochemical-markers for the diagnosis of bone metastasis: a clinical review," *Cancer Epidemiology*, vol. 36, no. 1, pp. 94–98, 2012.

[18] H. Wang, Z. Xu, M. Ma, N. Wang, and K. Wang, "Network analysis of microRNAs, transcription factors, target genes and host genes in nasopharyngeal carcinoma," *Oncology Letters*, vol. 11, no. 6, pp. 3821–3828, 2016.

[19] K. T. Lee, J. K. Tan, A. K. Lam, and S. Y. Gan, "MicroRNAs serving as potential biomarkers and therapeutic targets in nasopharyngeal carcinoma: a critical review," *Critical Reviews in Oncology/Hematology*, vol. 103, pp. 1–9, 2016.

[20] H. B. Wu, Q.-S. Wang, M.-F. Wang, X. Zhen, W.-L. Zhou, and H.-S. Li, "Preliminary study of 11C-choline PET/CT for T staging of locally advanced nasopharyngeal carcinoma: comparison with ^{18}F-FDG PET/CT," *Journal of Nuclear Medicine*, vol. 52, no. 3, pp. 341–346, 2011.

[21] C. Qin, F. Hu, M. M. R. Arnous, and X. Lan, "Detection of non-FDG-avid residual sinonasal malignant melanoma in the skull base with 11C-choline PET and contrast-enhanced MRI," *Clinical Nuclear Medicine*, vol. 42, no. 11, pp. 885-886, 2017.

[22] Y. Le, Y. Chen, F. Zhou, G. Liu, Z. Huang, and Y. Chen, "Comparative diagnostic value of ^{18}F-fluoride PET-CT versus MRI for skull-base bone invasion in nasopharyngeal carcinoma," *Nuclear Medicine Communications*, vol. 37, no. 10, pp. 1062–1068, 2016.

[23] F. Y. Liu, C.-Y. Lin, J. T. Chang et al., "^{18}F-FDG PET can replace conventional work-up in primary M staging of nonkeratinizing nasopharyngeal carcinoma," *Journal of Nuclear Medicine*, vol. 48, no. 10, pp. 1614–1619, 2007.

[24] S. Bastawrous, P. Bhargava, F. Behnia, D. S. Djang, and D. R. Haseley, "Newer PET application with an old tracer: role of ^{18}F-NaF skeletal PET/CT in oncologic practice," *Radiographics*, vol. 34, no. 5, pp. 1295–1316, 2014.

[25] C. T. Shen, Z. L. Qiu, T. T. Han, and Q. Y. Luo, "Performance of ^{18}F-fluoride PET or PET/CT for the detection of bone metastases: a meta-analysis," *Clinical Nuclear Medicine*, vol. 40, no. 2, pp. 103–110, 2015.

[26] C. G. Mick, T. James, J. D. Hill, P. Williams, and M. Perry, "Molecular imaging in oncology: (18)F-sodium fluoride PET imaging of osseous metastatic disease," *American Journal of Roentgenology*, vol. 203, no. 2, pp. 263–271, 2014.

[27] A. Iagaru, E. Mittra, C. Mosci et al., "Combined ^{18}F-fluoride and ^{18}F-FDG PET/CT scanning for evaluation of malignancy: results of an international multicenter trial," *Journal of Nuclear Medicine*, vol. 54, no. 2, pp. 176–183, 2013.

[28] M. Scimeca, N. Urbano, R. Bonfiglio, O. Schillaci, and E. Bonanno, "Management of oncological patients in the digital era: anatomic pathology and nuclear medicine teamwork," *Future Oncology*, vol. 14, no. 11, pp. 1013–1015, 2018.

Hindawi
Contrast Media & Molecular Imaging
Volume 2018, Article ID 5063285, 8 pages
https://doi.org/10.1155/2018/5063285

Research Article

Cervical Cancer: Associations between Metabolic Parameters and Whole Lesion Histogram Analysis Derived from Simultaneous ^{18}F-FDG-PET/MRI

Hans-Jonas Meyer,[1] **Sandra Purz**,[2] **Osama Sabri**,[2] **and Alexey Surov**[1]

[1]*Department of Diagnostic and Interventional Radiology, University of Leipzig, Leipzig, Germany*
[2]*Department of Nuclear Medicine, University of Leipzig, Leipzig, Germany*

Correspondence should be addressed to Hans-Jonas Meyer; jonas90.meyer@web.de

Received 17 April 2018; Revised 12 June 2018; Accepted 25 June 2018; Published 30 July 2018

Academic Editor: Elena Bonanno

Multimodal imaging has been increasingly used in oncology, especially in cervical cancer. By using a simultaneous positron emission (PET) and magnetic resonance imaging (MRI, PET/MRI) approach, PET and MRI can be obtained at the same time which minimizes motion artefacts and allows an exact imaging fusion, which is especially important in anatomically complex regions like the pelvis. The associations between functional parameters from MRI and ^{18}F-FDG-PET reflecting different tumor aspects are complex with inconclusive results in cervical cancer. The present study correlates histogram analysis and ^{18}F-FDG-PET parameters derived from simultaneous FDG-PET/MRI in cervical cancer. Overall, 18 female patients (age range: 32–79 years) with histopathologically confirmed squamous cell cervical carcinoma were retrospectively enrolled. All 18 patients underwent a whole-body simultaneous ^{18}F-FDG-PET/MRI, including diffusion-weighted imaging (DWI) using b-values 0 and 1000 s/mm^2. Apparent diffusion coefficient (ADC) histogram parameters included several percentiles, mean, min, max, mode, median, skewness, kurtosis, and entropy. Furthermore, mean and maximum standardized uptake values (SUV_{mean} and SUV_{max}), metabolic tumor volume (MTV), and total lesion glycolysis (TLG) were estimated. No statistically significant correlations were observed between SUV_{max} or SUV_{mean} and ADC histogram parameters. TLG correlated inversely with p25 ($r = -0.486$, $P = 0.041$), p75 ($r = -0.490$, $P = 0.039$), p90 ($r = -0.513$, $P = 0.029$), ADC median ($r = -0.497$, $P = 0.036$), and ADC mode ($r = -0.546$, $P = 0.019$). MTV also showed significant correlations with several ADC parameters: mean ($r = -0.546$, $P = 0.019$), p10 ($r = -0.473$, $P = 0.047$), p25 ($r = -0.569$, $P = 0.014$), p75 ($r = -0.576$, $P = 0.012$), p90 ($r = -0.585$, $P = 0.011$), ADC median ($r = -0.577$, $P = 0.012$), and ADC mode ($r = -0.597$, $P = 0.009$). ADC histogram analysis and volume-based metabolic 18F-FDG-PET parameters are related to each other in cervical cancer.

1. Introduction

Cervical cancer is the third most commonly diagnosed cancer and the fourth leading cause of cancer death in females worldwide [1].

Magnetic resonance imaging (MRI) has been established as the best imaging modality for staging of cervical cancers due to its excellent soft tissue contrast [2]. Furthermore, MRI can provide information regarding tumor microstructure by diffusion-weighted imaging (DWI). The principle hypothesis is that DWI can quantify the free movement of protons (Brownian molecular movement) by using apparent diffusion coefficients (ADC) [3]. This movement is hindered predominantly by cell membranes. In fact, previous studies showed that ADC inversely correlated with cell count in several malignant and benign lesions [4].

Another clinically important functional imaging modality is ^{18}F-fluorodeoxyglucose positron emission tomography (FDG-PET), which reflects tumor glucose-metabolism [5]. The FDG-uptake in tumor tissue is associated with the increased expression of glucose transporters (GLUT), mainly subtype GLUT-1 [6]. Clinically, ^{18}F-FDG-uptake is semiquantified by standardized uptake values (SUV). Moreover, it has been shown that volume-based metabolic PET parameters, such as metabolic tumor volume (MTV) and total lesion glycolysis (TLG), might provide additional information

Table 1: Overview about published literature regarding correlation analysis between DWI and FDG-PET.

Author	Number of patients	Analyzed parameters	Correlation
Ho et al. [15]	33	$ADC_{min,\ mean}$, $SUV_{max,\ mean}$	No statistically significant correlations
Sun et al. [16]	35	$ADC_{min,\ mean}$, $SUV_{max,\ mean}$	No significant correlation between SUV_{max} and ADC_{min} ($r = -0.074, P = 0.501$) or between SUV_{mean} and ADC_{mean} ($r = -0.505, P = 0.201$) across all 35 primary tumors; for the 28 squamous cell carcinomas, there was also no significant correlation between SUV_{max} and ADC_{min} ($r = -0.363, P = 0.342$) or between SUV_{mean} and ADC_{mean} ($r = -0.354, P = 0.150$)
Wang et al. [35]	30	$ADC_{min,\ mean}$, $SUV_{max,\ mean}$	No statistically significant correlations between ADC and SUV fractions
Brandmaier et al. [10]	31 (14 primary, 17 recurrence)	$ADC_{min,\ mean}$, $SUV_{max,\ mean}$	SUV_{max} versus ADC_{min} ($r = -0.532, P = 0.05$) in primary tumors. Primary metastasis showed weak inverse correlations for SUV_{max} and ADC_{min} ($r = -0.362, P = 0.05$) and moderate correlations for SUV_{mean} and ADC_{min} ($r = -0.403, P = 0.03$)
Pinker et al. [36]	11	ADC_{mean}, SUV_{max}	No significant correlations
Surov et al. [14]	21	$ADC_{min,\ mean,\ max}$, $SUV_{max,\ mean}$	No significant correlations between ADC and SUV fractions
Lai et al. [37]	29	MTV, functional diffusion volume	Significant differences regarding MTV and functional diffusion volume derived from ADC maps

regarding tumor behavior [7]. MTV and TLG have been reported as possible prognostic factors, for example, for lung cancer or laryngeal carcinoma. In cervical cancer, for example, MTV was the only parameter to be of prognostic relevance in a multivariate analysis performed by Hong et al. [8].

Presumably, functional parameter derived from PET and from MRI, albeit reflecting slightly different tumor aspects, might be linked to each other [9]. As a hypothesis, a cell-rich tumor might also express more GLUT-transporters within their cell membranes, and hence, an association between ADC and SUV values might exist.

In fact, this was studied by various investigations in several different tumor entities like esophageal or breast cancer [9–13]. However, in a recent meta-analysis, comprising 35 studies, only a weak inverse correlation coefficient of $r = -0.30$ was identified over all various investigated tumors [9].

Regarding cervical cancer, there are inconclusive results [10, 14–16]. Table 1 summarizes the published data about reported correlations between ADC and SUV values. So, Brandmaier et al. identified an inverse correlation between SUV_{max} and ADC_{min} ($r = -0.532, P = 0.05$) [10], whereas most authors did not [14–16].

An emergent imaging analysis, namely, ADC histogram analysis, which is based on pixel distribution, is used to improve tumor heterogeneity in DWI-MRI assessment. Every voxel of a region of interest is issued into a histogram and thusly statistically information about the tumor is provided. Typically parameters are percentiles, median, mode, skewness, kurtosis, and entropy [17]. It is acknowledged that heterogeneity displayed by the histogram might be reflected by tumor microstructure heterogeneity, and therefore, a better reflection of tumor biology may be possible [17]. The histogram analysis approach has been applied in other tumors, for example, in prostate cancer. For example, Liu et al. characterized histogram variables of ADC as predictors for the aggressiveness of prostate cancer [18]. In a study of Shindo et al., ADC histogram analysis has been described as helpful in differentiating pancreatic adenocarcinomas from neuroendocrine tumors [19]. Regarding cervical cancer, there are only few reports compared metabolic parameters of ^{18}F-FDG-PET and ADC histogram analysis. For instance, Ueno et al. evaluated the prognostic value of SUV, MTV and TLG, and ADC histogram analysis for tumor response to therapy and event-free survival in patients with cervical cancer [20]. It has been shown that pretreatment volume-based metabolic ^{18}F-FDG-PET parameters may have better potential than ADC histogram analysis for predicting treatment response and survival in these patients [20]. The main drawback of this study was that data from PET and MRI were obtained sequentially and not simultaneously; thus, the results of this study may have been influenced by this fact.

The aim of our study was to elucidate possible associations between ADC histogram-based parameters and ^{18}F-FDG-PET parameters derived from simultaneous PET/MRI in cervical cancer.

2. Materials and Methods

This prospective study was approved by the local research ethics committee.

2.1. Patients. Overall, 18 female patients (age range: 32–79 years; mean age: 55.4 years) with histopathologically confirmed squamous cell cervical carcinoma were enrolled. Inclusion criteria were a staging investigating with a body simultaneous ^{18}F-FDG-PET/MRI before any form of treatment.

Table 2 gives an overview about the patients and the different clinical pathological stages.

Table 2: Clinical data of the investigated patients.

Case	Age	Tumor grade	T stage	N stage	M stage
1	63	G2	2b	1	0
2	76	G3	4	0	0
3	65	G2	2b	0	0
4	63	G3	4	1	1
5	34	G3	2b	1	0
6	57	G2	4	1	1
7	53	G3	2b	0	0
8	32	G2	4	1	0
9	32	G2	2b	0	0
10	54	G2	3a	2	0
11	79	G3	4	1	0
12	52	G1	4	0	0
13	37	G3	2b	1	1
14	72	G3	4	0	0
15	46	G2	2b	1	1
16	71	G2	4	1	1
17	50	G2	2b	1	1
18	61	G2	4	1	0

2.2. PET/MRI. All 18 patients underwent a whole-body simultaneous ^{18}F-FDG-PET/MRI (Biograph mMR-Biograph, Siemens Healthcare Sector, Erlangen, Germany) which was performed from the upper thigh to the skull for 4 minutes per bed position. PET images were reconstructed using the iterative ordered subset expectation maximization algorithm with 3 iterations and 21 subsets, a Gaussian filter with 4 mm full width at half maximum (FWHM), and a 256×256 image matrix. Attenuation correction of the PET data was performed using a four-tissue (fat, soft tissue, air, and background) model attenuation map, which was generated from a Dixon-Vibe MR sequence according to previous description.

Radiotracer administration was performed intravenously after a fasting period of at least 6 hours with a body weight-adapted dose of ^{18}F-FDG (4 MBq/kg; range: 152–442 MBq; mean ± std: 285 ± 70 MBq). PET/MRI image acquisition started on average 122 minutes after ^{18}F-FDG application. Due to radiotracer elimination via the urinary tract, which may influence evaluation of pelvic PET images, all patients received a bladder catheter prior to PET/MRI examination.

Image analysis was performed on the dedicated workstation of Hermes Medical Solutions, Sweden. For each tumor, maximum and mean SUV (SUV_{max} and SUV_{mean}), total lesion glycolysis (TLG), and metabolic tumor volume (MTV) were determined on PET images. MTV was defined as total tumor volume with an SUV ≥ 2.5 and was calculated automatically. TLG was also calculated automatically by multiplying the MTV of the primary tumor by its SUV_{mean}.

In all cases, pelvic MRI was performed. Our investigation protocol included the following sequences: transverse T2 turbo spin echo (TSE) sequence (TR/TE: 5590/105), sagittal T2 TSE sequence (TR/TE: 4110/131), transverse T1 TSE sequence (TR/TE:1310/12), transverse T1 TSE after intravenous application of contrast medium (0.1 mmol/kg body weight Gadobutrol, Bayer Healthcare, Germany) (TR/TE: 912/12), and sagittal postcontrast T1 TSE (TR/TE: 593/12). Additionally, diffusion-weighted imaging was performed using an echo-planar imaging (EPI) sequence (b0 and b1000 s/mm^2, TR/TE: 4900/105). Figure 1 shows an exemplary patient of our patient sample.

2.3. Histogram Analysis of ADC Values. Automatically generated ADC maps were transferred in DICOM format and processed offline with custom-made Matlab-based application (The Mathworks, Natick, MA) on a standard windows-operated system. The ADC maps were displayed within a graphical user interface (GUI), which enables the reader to scroll through the slices and draw a volume of interest (VOI) at the tumor's boundary (whole-lesion measure). All measurements were performed by two authors blinded to each other (AS, HJM, 15 and 2 years of radiological experience). The ROIs were modified in the GUI and saved (in Matlab-specific format) for later processing. After setting the ROIs, following parameters were calculated and written in a spreadsheet format: ROI volume (cm^3), mean (ADC_{mean}), maximum (ADC_{max}), minimum (ADC_{min}), ADC median, 10th (p10 ADC), 25th (p25 ADC), 75th (p75 ADC), 90th (p90 ADC) percentile, and mode (ADC mode). Additionally, histogram-based characteristics of the ROI—kurtosis, skewness, and entropy—were calculated.

2.4. Statistical Analysis. Statistical analysis was performed using SPSS 23.0 (SPSS Inc, Chicago, IL). Collected data were evaluated by means of descriptive statistics. The data were not normally distributed according to Kolmogorow–Smirnow test. Therefore, Spearman's correlation coefficient (p) was used to analyze associations between investigated parameters. Interreader variability was assessed with intraclass coefficients. P values < 0.05 were taken to indicate statistical significance.

3. Results

The investigated ADC histogram showed a good interreader variability, ranging from ICC = 0.705 for entropy to ICC = 0.959 for ADC median (Table 3).

Table 4 shows results of correlation analysis between the investigated PET and ADC parameters. No statistically significant correlations were observed between SUV_{max} or SUV_{mean} and ADC histogram parameters.

TLG correlated inversely with p25 ($r = -0.486$, $P = 0.041$), p75 ($r = -0.490$, $P = 0.039$), p90 ($r = -0.513$, $P = 0.029$), ADC median ($r = -0.497$, $P = 0.036$), and ADC mode ($r = -0.546$, $P = 0.019$). MTV also showed significant correlations with several ADC parameters as follows: mean ($r = -0.546$, $P = 0.019$), p10 ($r = -0.473$, $P = 0.047$), p25 ($r = -0.569$, $P = 0.014$), p75 ($r = -0.576$, $P = 0.012$), p90 ($r = -0.585$, $P = 0.011$), ADC median ($r = -0.577$, $P = 0.012$), and ADC mode ($r = -0.597$, $P = 0.009$). Finally, histogram-based parameters—skewness, kurtosis and entropy—did not correlate with PET parameters.

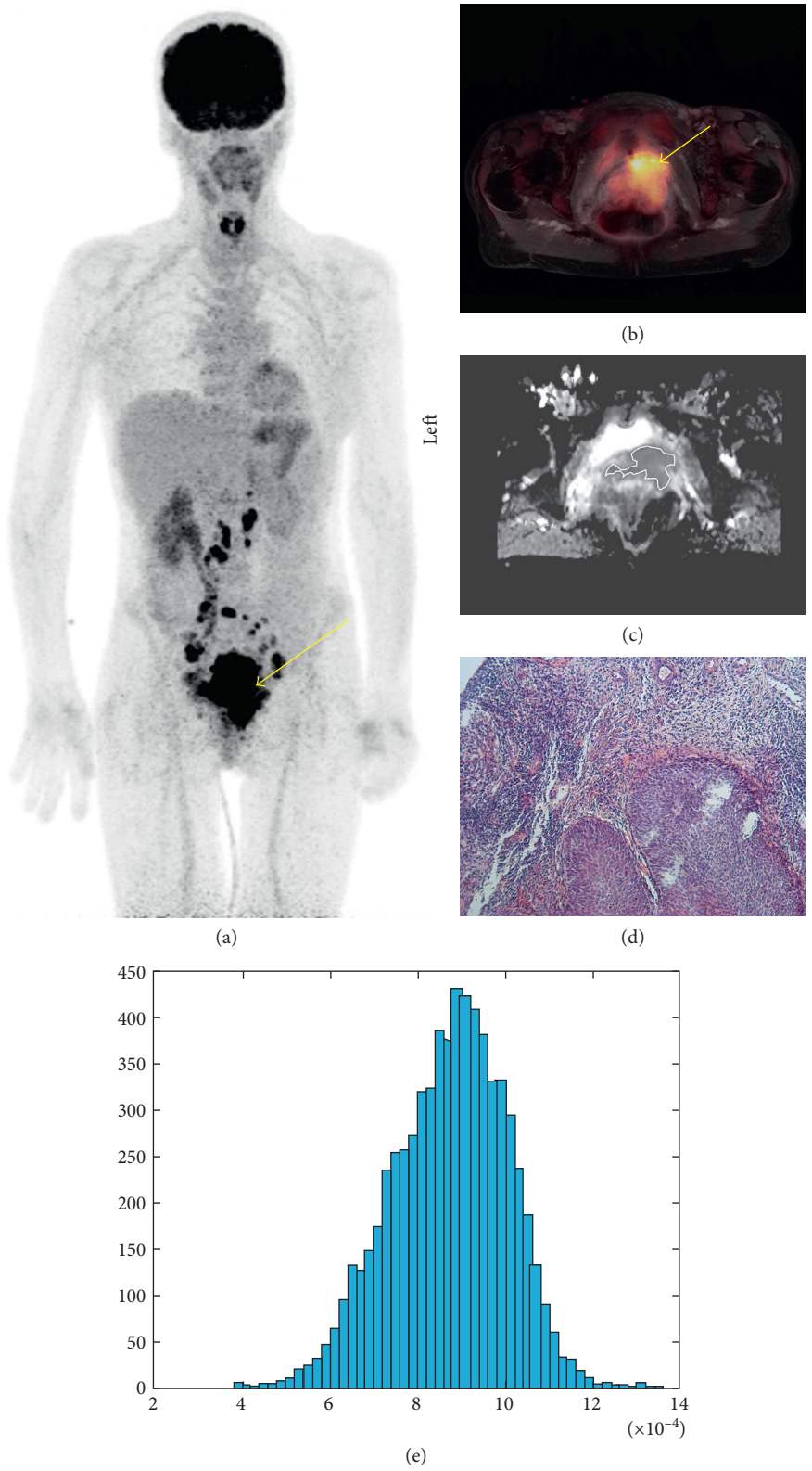

FIGURE 1: Imaging and histopathological findings in a case of cervical cancer. (a) ^{18}F-FDG-PET of a 57-year-old woman with locally advanced cervical cancer (arrow). (b) Fused ^{18}F-FDG-PET/MRI image demonstration of the metabolic active uterine cervical cancer (arrow). Calculated ^{18}F-FDG-PET parameters are as follows: $SUV_{max} = 8.77$, $SUV_{mean} = 4.66$, SUV median = 4.32, TLG = 92.91, and MTV = 19.96. (c) ADC map of the tumor with a ROI. (e) ADC histogram. The histogram analysis parameters ($\times 10^{-3}$ mm^2·s^{-1}) are as follows: $ADC_{min} = 0.36$, $ADC_{mean} = 0.87$, $ADC_{max} = 1.36$, p10 = 0.7, p25 = 0.78, p75 = 0.96, p90 = 1.03, median = 0.88, and mode = 0.93. Histogram-based characteristics are as follows: kurtosis = 2.96, skewness = −028, and entropy = 4.72. (d) Histopathological examination (hematoxylin and eosin-stained specimen) after tumor biopsy reveals a G2 cervical cancer.

Table 3: Interreader variability with intraclass coefficients of the investigated ADC parameters.

Parameter	ICC
ADC_{mean}	0.870
ADC_{min}	0.947
ADC_{max}	0.920
ADC P10	0.727
ADC P25	0.844
ADC P75	0.804
ADC P90	0.803
ADC median	0.959
ADC mode	0.917
Kurtosis	0.859
Skewness	0.792
Entropy	0.705

ICC, intraclass coefficient.

4. Discussion

To the best of our knowledge, this is the first study elucidating possible correlations between ADC histogram analysis and complex ^{18}F-FDG-PET parameters derived from simultaneous PET/MRI in cervical cancer.

Pretherapeutic tumor staging in cervical cancer is of great importance. MRI is the best imaging modality to estimate regional tumor extent, with identification of tumor infiltration into the adjacent organs/tissues within the female pelvis [2]. Hybrid imaging, in terms of PET/CT, has been shown to be superior to other conventional imaging modalities (MRI, CT) for the identification of nodal or distant metastatic spread [21]. Consequently, the combination of both, namely, a simultaneous PET/MRI, has been described as valuable imaging modality for whole-body tumor staging of cervical cancer patients providing improved treatment planning when compared to MRI alone [22]. Furthermore, our own preliminary data show that simultaneous PET/MRI is a valuable imaging modality to reflect histopathologic parameters like cellularity and proliferation index in cervical cancer [14].

Additionally, functional MRI, as well as ^{18}F-FDG-PET can provide information about tumor biology in a different fashion. ADC values derived from DWI are mainly influenced by cellularity, whereas SUV values derived from FDG-PET are mainly influenced by GLUT-1 overexpression within cell membranes and enhanced activity of tumor hexokinase [4, 14, 23].

Presumably, parameters from PET and MRI might be associated with each other due to the fact that a more cell-dense tumor also might express more GLUT-1 or may have an increased enzymatic activity [9]. However, a recent meta-analysis identified only a weak inverse correlation ($r = -0.30$) between SUV and ADC values pooling various tumors in oncologic imaging [9]. Regarding cervical cancer, the studies, which investigated associations between ADC and SUV values, showed inconclusive results [10, 14–16]. Only one study found an inverse correlation between SUV_{max} and ADC_{min} ($r = -0.532$) [10], whereas most authors could not identify linear correlations between these parameters, indicating that they might reflect different tumor aspects [14–16].

The present study identified that several ADC histogram parameters were associated with volume-based metabolic PET parameters, namely, MTV and TLG. In good agreement with the literature, there were no correlations between ADC parameters and SUV values in the current patient sample. Therefore, our results suggest that ADC histogram analysis parameters and TLG and MTV are more sensitive to reflect relationships between ^{18}F-FDG-PET and DWI than the widely used SUV and "conventional" ADC values. Furthermore, our study may explain negative results of the previous investigations. Moreover, in the present study, ADC values were obtained as a whole-lesion measurement, whereas in most studies [10, 14–16], only one slice was used for calculation and might therefore not be representative for the whole tumor. According to Kyriazi et al., whole-lesion measurement might be more beneficial than the conventional one slide approach since pixel-by-pixel ADC histograms through the entire tumor volume include different microenvironments of diffusivity, which may be masked by mean ADC analysis [24].

Furthermore, histogram-based analysis has been evaluated to have an excellent interobserver agreement [25, 26]. Additionally, it could clearly discriminate between tissue affected with cancer and physiological cervical tissue [25]. Finally, it could distinguish different FIGO stages: with increasing skewness, kurtosis, and entropy in the advanced stages indicating higher tumor heterogeneity in those lesions [26].

Interestingly, ADC histogram analysis parameters correlated with some histopathological features in cervical cancer. For example, entropy was associated with p53 expression [27]. Moreover, Meng et al. identified that ADC histogram parameters can predict tumor recurrence after radiochemotherapy with an area under the curve 0.85 [28]. In another study, it was identified that skewness and several percentiles derived from ADC maps were significantly different between squamous cell and adenocarcinomas of the uterine cervix and, therefore, ADC histogram analysis might aid in discrimination of the entities [29]. In fact, as reported previously, skewness was significantly higher for squamous cell carcinomas than adenocarcinomas and was higher in poorly differentiated tumors [29].

Regarding ^{18}F-FDG-PET, pretreatment SUV_{max} and MTV have been reported to be associated with tumor prognosis [30, 31]. So MTV had a hazard ratio of 3.15 for disease-free survival [31], and SUV_{max} of the primary tumor was the only identified prognostic factor in a multivariate analysis [30]. Furthermore, TLG was also associated with the overall survival in locally advanced cervical cancer [32]. However, it might be of limited use for primary diagnosis in early stage carcinomas since ^{18}F-FDG-PET only has little value in the routine pretreatment assessment in patients with early FIGO stages [33]. However, there are promising histopathological methods to better understand underlying microstructure changes, which can be displayed with PET imaging [34].

Table 4: Correlation between ADC histogram parameters and ^{18}F-FDG-PET parameters in cervical cancer. Spearman's rho correlation coefficient was used.

		SUV_{max}	SUV_{mean}	SUV_{median}	TLG	MTV
Mean ADC	p (rho)	−0.134	−0.215	−0.336	−0.461	**−0.546**
	P	0.595	0.392	0.173	0.054	**0.019**
Min ADC	p (rho)	−0.218	−0.213	−0.282	−0.219	−0.257
	P	0.385	0.396	0.257	0.382	0.303
Max ADC	p (rho)	−0.044	−0.166	−0.176	0.166	0.162
	P	0.861	0.510	0.484	0.510	0.521
P10 ADC	p (rho)	−0.183	−0.223	−0.332	−0.413	**−0.473**
	P	0.468	0.373	0.179	0.088	**0.047**
P25 ADC	p (rho)	−0.150	−0.214	−0.329	**−0.486**	**−0.569**
	P	0.553	0.395	0.182	**0.041**	**0.014**
P75 ADC	p (rho)	−0.142	−0.244	−0.354	**−0.490**	**−0.576**
	P	0.575	0.329	0.150	**0.039**	**0.012**
P90 ADC	p (rho)	−0.215	−0.275	−0.361	**−0.513**	**−0.585**
	P	0.392	0.270	0.142	**0.029**	**0.011**
Median ADC	p (rho)	−0.153	−0.244	−0.368	**−0.497**	**−0.577**
	P	0.544	0.329	0.133	**0.036**	**0.012**
Mode ADC	p (rho)	−0.225	−0.157	−0.261	**−0.546**	**−0.597**
	P	0.370	0.533	0.296	**0.019**	**0.009**
Kurtosis	p (rho)	−0.150	−0.148	−0.117	0.288	0.284
	P	0.553	0.559	0.645	0.247	0.254
Skewness	p (rho)	−0.095	−0.054	−0.004	0.149	0.142
	P	0.708	0.832	0.987	0.556	0.573
Entropy	p (rho)	0.071	−0.036	−0.049	0.084	0.172
	P	0.779	0.887	0.848	0.742	0.494

Significant correlations are highlighted in bold.

Overall, our report indicates that for further analyses about associations between DWI and PET and as well between PET, DWI, and histopathology in several tumors, ADC histogram analysis and volume-based metabolic PET parameters like TLG/MTV should be obtained.

There are several limitations of the present study to address. Firstly, it is a retrospective study with possible known bias. However, MRI and ^{18}F-FDG-PET were measured by two different readers, blinded to each other. Secondly, the patient sample is relatively small. Thirdly, only squamous cell carcinomas were evaluated.

In conclusion, the present study shows that ADC histogram analysis and volume-based metabolic ^{18}F-FDG-PET parameters are related to each other and might, therefore, reflect similar tumor behavior of cervical cancer. The next step would be to assess the value of these simultaneous PET/MRI parameters for predicting treatment response and survival in cervical cancer patients.

Abbreviations

MRI: Magnetic resonance imaging
DWI: Diffusion-weighted imaging
ADC: Apparent diffusion coefficient
FDG-PET: ^{18}F-fluorodeoxyglucose positron emission tomography
TLG: Total lesion glycolysis
MTV: Mean tumor volume
GLUT: Glucose transporters
SUV: Standardized uptake value.

Data Availability

The anonymous patient data used to support the findings of this study are available from the corresponding author upon request.

Conflicts of Interest

The authors declare no conflicts of interest.

Authors' Contributions

Hans-Jonas Meyer, Alexey Surov, and Sandra Purz wrote the manuscript. Hans-Jonas Meyer and Alexey Surov performed histogram analysis. Sandra Purz and Osama Sabri performed PET analysis. Hans-Jonas Meyer performed the statistical analysis. All authors contributed equally to this work.

References

[1] A. Jemal, F. Bray, M. M. Center et al., "Global cancer statistics," *Cancer Journal for Clinician*, vol. 61, no. 2, pp. 69–90, 2011.

[2] E. Sala, S. Wakely, E. Senior, and D. Lomas, "MRI of malignant neoplasms of the uterine corpus and cervix," *American Journal of Roentgenology*, vol. 188, no. 6, pp. 1577–1587, 2007.

[3] A. R. Padhani, G. Liu, D. M. Koh et al., "Diffusion-weighted magnetic resonance imaging as a cancer biomarker: consensus and recommendations," *Neoplasia: an International Journal for Oncology Research*, vol. 11, no. 2, pp. 102–125, 2009.

[4] A. Surov, H. J. Meyer, and A. Wienke, "Correlation between apparent diffusion coefficient (ADC) and cellularity is different in several tumors: a meta-analysis," *Oncotarget*, vol. 8, no. 35, pp. 59492–59499, 2017.

[5] H. H. Chung, S. Y. Kang, S. Ha et al., "Prognostic value of preoperative intratumoral FDG uptake heterogeneity in early stage uterine cervical cancer," *Journal of Gynecologic Oncology*, vol. 27, no. 2, p. e15, 2016.

[6] M. S. Jo, O. H. Choi, D. S. Suh et al., "Correlation between expression of biological markers and Ffluorodeoxyglucose uptake in endometrial cancer," *Oncology Research and Treatment*, vol. 37, no. 1-2, pp. 30–34, 2014.

[7] H. J. Im, T. Bradshaw, M. Solaiyappan, and S. Y. Cho, "Current methods to define metabolic tumor volume in positron emission tomography: which one is better," *Nuclear Medicine and Molecular Imaging*, vol. 52, no. 1, pp. 5–15, 2018.

[8] J. H. Hong, K. J. Min, J. K. Lee et al., "Prognostic value of the sum of metabolic tumor volume of primary tumor and lymph nodes using 18F-FDG PET/CT in patients with cervical cancer," *Medicine*, vol. 95, no. 9, article e2992, 2016.

[9] G. Shen, H. Ma, B. Liu et al., "Correlation of the apparent diffusion coefficient and the standardized uptake value in neoplastic lesions: a meta-analysis," *Nuclear Medicine Communications*, vol. 38, no. 12, pp. 1076–1084, 2017.

[10] P. Brandmaier, S. Purz, K. Bremicker et al., "Simultaneous [18F]FDG-PET/MRI: correlation of apparent diffusion coefficient (ADC) and standardized uptake value (SUV) in primary and recurrent cervical cancer," *PLoS One*, vol. 10, no. 11, Article ID e0141684, 2015.

[11] L. Goense, S. E. Heethuis, P. S. N. van Rossum et al., "Correlation between functional imaging markers derived from diffusion-weighted MRI and 18F-FDG PET/CT in esophageal cancer," *Nuclear Medicine Communications*, vol. 39, no. 1, pp. 60–67, 2018.

[12] K. A. Zukotynski, S. Vajapeyam, F. H. Fahey et al., "Correlation of 18F-FDG PET and MRI apparent diffusion coefficient histogram metrics with survival in diffuse intrinsic pontine glioma: a report from the pediatric brain tumor consortium," *Journal of Nuclear Medicine*, vol. 58, no. 8, pp. 1264–1269, 2017.

[13] K. Kitajima, T. Yamano, K. Fukushima et al., "Correlation of the SUVmax of FDG-PET and ADC values of diffusion-weighted MR imaging with pathologic prognostic factors in breast carcinoma," *European Journal of Radiology*, vol. 85, no. 5, pp. 943–949, 2016.

[14] A. Surov, H. J. Meyer, S. Schob et al., "Parameters of simultaneous 18F-FDG-PET/MRI predict tumor stage and several histopathological features in uterine cervical cancer," *Oncotarget*, vol. 8, no. 27, pp. 28285–28296, 2017.

[15] K. C. Ho, G. Lin, J. J. Wang et al., "Correlation of apparent diffusion coefficients measured by 3T diffusion-weighted MRI and SUV from FDG PET/CT in primary cervical cancer," *European Journal of Nuclear Medicine and Molecular Imaging*, vol. 36, no. 2, pp. 200–208, 2009.

[16] H. Sun, J. Xin, S. Zhang et al., "Anatomical and functional volume concordance between FDG PET, and T2 and diffusion-weighted MRI for cervical cancer: a hybrid PET/MR study," *European Journal of Nuclear Medicine and Molecular Imaging*, vol. 41, no. 5, pp. 898–905, 2014.

[17] N. Just, "Improving tumour heterogeneity MRI assessment with histograms," *British Journal of Cancer*, vol. 111, no. 12, pp. 2205–2213, 2014.

[18] W. Liu, X. H. Liu, W. Tang et al., "Histogram analysis of stretched-exponential and monoexponential diffusion-weighted imaging models for distinguishing low and intermediate/high gleason scores in prostate carcinoma," *Journal of Magnetic Resonance Imaging*, 2018, In press.

[19] T. Shindo, Y. Fukukura, T. Umanodan et al., "Histogram analysis of apparent diffusion coefficient in differentiating pancreatic adenocarcinoma and neuroendocrine tumor," *Medicine*, vol. 95, no. 4, article e2574, 2016.

[20] Y. Ueno, R. Lisbona, T. Tamada et al., "Comparison of FDG PET metabolic tumour volume versus ADC histogram: prognostic value of tumour treatment response and survival in patients with locally advanced uterine cervical cancer," *British Journal of Radiology*, vol. 90, no. 1075, article 20170035, 2017.

[21] H. J. Choi, J. W. Roh, S. S. Seo et al., "Comparison of the accuracy of magnetic resonance imaging and positron emission tomography/computed tomography in the presurgical detection of lymph node metastases in patients with uterine cervical carcinoma: a prospective study," *Cancer*, vol. 106, no. 4, pp. 914–922, 2006.

[22] T. Sarabhai, B. M. Schaarschmidt, A. Wetter et al., "Comparison of 18F-FDG PET/MRI and MRI for pre-therapeutic tumor staging of patients with primary cancer of the uterine cervix," *European Journal of Nuclear Medicine and Molecular Imaging*, vol. 45, no. 1, pp. 67–76, 2018.

[23] H. J. Yang, W. J. Xu, Y. H. Guan et al., "Expression of Glut-1 and HK-II in pancreatic cancer and their impact on prognosis and FDG accumulation," *Translational Oncology*, vol. 9, no. 6, pp. 583–591, 2016.

[24] S. Kyriazi, D. J. Collins, C. Messiou et al., "Metastatic ovarian and primary peritoneal cancer: assessing chemotherapy response with diffusion-weighted MR imaging–value of histogram analysis of apparent diffusion coefficients," *Radiology*, vol. 261, no. 1, pp. 182–192, 2011.

[25] Y. Guan, W. Li, Z. Jiang et al., "Whole-lesion apparent diffusion coefficient-based entropy-related parameters for characterizing cervical cancers: initial findings," *Academic Radiology*, vol. 23, no. 12, pp. 1559–1567, 2016.

[26] Y. Guan, W. Li, Z. Jiang et al., "Value of whole-lesion apparent diffusion coefficient (ADC) first-order statistics and texture features in clinical staging of cervical cancers," *Clinical Radiology*, vol. 72, no. 11, pp. 951–958, 2017.

[27] S. Schob, H. J. Meyer, N. Pazaitis et al., "ADC histogram analysis of cervical cancer aids detecting lymphatic metastases-a preliminary study," *Molecular Imaging and Biology*, vol. 19, no. 6, pp. 953–962, 2017.

[28] J. Meng, L. Zhu, L. Zhu et al., "Whole-lesion ADC histogram and texture analysis in predicting recurrence of cervical cancer treated with CCRT," *Oncotarget*, vol. 8, no. 54, pp. 92442–92453, 2017.

[29] Y. Lin, H. Li, Z. Chen et al., "Correlation of histogram analysis of apparent diffusion coefficient with uterine cervical pathologic finding," *American Journal of Roentgenology*, vol. 204, no. 5, pp. 1125–1131, 2015.

[30] S. Cima, A. M. Perrone, P. Castellucci et al., "Prognostic impact of pretreatment fluorodeoxyglucose positron emission tomography/computed tomography SUV_{max} in patients with locally advanced cervical cancer," *International Journal of Gynecological Cancer*, vol. 28, no. 3, pp. 575–580, 2018.

[31] G. O. Chong, W. K. Lee, S. Y. Jeong et al., "Prognostic value of intratumoral metabolic heterogeneity on F-18 fluorodeoxyglucose positron emission tomography/computed tomography in locally advanced cervical cancer patients treated with concurrent chemoradiotherapy," *Oncotarget*, vol. 8, no. 52, pp. 90402–90412, 2017.

[32] Y. Liang, X. Li, H. Wan et al., "Prognostic value of volume-based metabolic parameters obtained by 18F-FDG-PET/CT in patients with locally advanced squamous cell cervical carcinoma," *Journal of Computer Assisted Tomography*, vol. 42, no. 3, pp. 429–434, 2018.

[33] D. O. Driscoll, D. Halpenny, C. Johnston et al., "18F-FDG-PET/CT is of limited value in primary staging of early stage cervical cancer," *Abdominal Imaging*, vol. 40, no. 1, pp. 127–133, 2015.

[34] M. Scimeca, N. Urbano, R. Bonfiglio et al., "Management of oncological patients in the digital era: anatomic pathology and nuclear medicine teamwork," *Future Oncology*, vol. 14, no. 11, pp. 1013–1015, 2018.

[35] P. Y. Wang, J. Xin, H. Z. Sun et al., "Observation on correlation of ADC value and SUV in primary squamous cell cervical cancer with hybrid 18F-FDG PET/MR," *Chinese Journal of Medical Imaging Technology*, vol. 30, pp. 603–607, 2014.

[36] K. Pinker, P. Andrzejewski, P. Baltzer et al., "Multiparametric [18F]fluorodeoxyglucose/[18F]fluoromisonidazole positron emission tomography/magnetic resonance imaging of locally advanced cervical cancer for the non-invasive detection of tumor heterogeneity: a pilot study," *PLoS One*, vol. 11, no. 5, Article ID e0155333, 2016.

[37] A. Y. T. Lai, J. A. U. Perucho, X. Xu et al., "Concordance of FDG PET/CT metabolic tumour volume versus DW-MRI functional tumour volume with T2-weighted anatomical tumour volume in cervical cancer," *BMC Cancer*, vol. 17, no. 1, p. 825, 2017.

Hindawi
Contrast Media & Molecular Imaging
Volume 2018, Article ID 2601281, 8 pages
https://doi.org/10.1155/2018/2601281

Research Article

Use of 18F-FDG-PET/CT for Retroperitoneal/Intra-Abdominal Soft Tissue Sarcomas

Dao-ning Liu,[1] **Zhong-wu Li**,[2] **Hai-yue Wang**,[2] **Min Zhao**,[2] **Wei Zhao**,[3] **and Chun-yi Hao**[1]

[1]*Sarcoma Center, Peking University Cancer Hospital & Institute, Beijing, China*
[2]*Department of Pathology, Peking University Cancer Hospital & Institute, Beijing, China*
[3]*Department of Nuclear Medicine, Peking University Cancer Hospital & Institute, Beijing, China*

Correspondence should be addressed to Chun-yi Hao; haochunyi@bjmu.edu.cn

Received 22 March 2018; Accepted 24 May 2018; Published 2 July 2018

Academic Editor: Elena Bonanno

Rationale. To assess the diagnostic value of 18F-FDG-PET/CT for different retroperitoneal soft tissue sarcomas (STS) and other similar tumors. To analyze the predictive value of 18F-FDG-PET/CT for histological grade and main prognostic factors. *Methods*. 195 patients with 44 different diseases have been included. Relationship between SUVmax, Clinical, pathological, and prognostic information has been analyzed. *Results*. Malignant tumors do not show higher SUVmax than benign ones ($P = 0.443$). We divided all 44 different diseases into two groups; SUVmax of group 1 is significantly higher than group 2 ($P \leq 0.001$). The ROC curve suggests 4.35 is the cutoff value to distinguish groups 1 and 2 (sensitivity = 0.789; specificity = 0.736). SUVmax correlates with Ki-67 index, mitotic count, vascular resection, histological grade, and recurrent STS without considering pathological diagnosis ($P = 0.001$, $P = 0.012$, $P = 0.002$, $P \leq 0.001$, and $P = 0.037$, resp.). *Conclusion*. 18F-FDG-PET/CT cannot simply distinguish malignant and benign tumors in retroperitoneal/intra-abdominal cavity; however, the SUVmax of malignant tumors, inflammatory pseudotumor, and PPGL group is higher than the SUVmax of benign tumors, lymph node metastasis, hematoma, and low malignant STS group. Guidance of "SUVmax location" may be helpful for biopsy and pathology dissection.

1. Introduction

Retroperitoneal and intra-abdominal sarcomas contain various soft tissue tumors and a wide prognostic range. Precise diagnosis of these sarcomas always plays a key role in treatment selection, especially in the application of compartment resection [1]. As STS are generally cured by adequate surgical resection, inaccurate diagnosis may cause unnecessary resection of innocent organs and extra risks. Judgment of malignancy is not accurate even using biopsy [2]. Moreover, some researchers resort to other preoperative examinations such as 18F-Fluoro-2-deoxy-D-glucose (18F-FDG) positron emission tomography (PET); however, the effort of 18F-FDG-PET/CT to distinguish extremity low-grade sarcomas and benign lesions is not fully paid off [3]. Unlike extremity STS, the special anatomical cavity contains many different pathological types that can mimic STS. There is yet no such comprehensive study regarding the use of 18F-FDG-PET/CT in retroperitoneal and intra-abdominal STS, considering the limitation of low incidence of STS [4]. As the establishment of the only sarcoma center in China, the abundant resource provides us an opportunity to afford such an analysis.

The use of 18F-FDG-PET/CT in oncology is based on the FDG accumulation in malignant tumor cells. 18F-FDG-PET/CT is initially used for diagnosis, staging, and therapy monitoring. The value for prediction of tumor biology and even prognosis has been found in recent researches [5, 6]. To evaluate the use of 18F-FDG-PET/CT in precise diagnosis and prognosis prediction, we try to correlate maximum standardized uptake value (SUVmax) with different pathologic diagnosis and prognostic factors. In recent researches, common STS prognostic factors are histological grade, tumor size, age, location, vascular resection, number of resected organs, Ki-67 index, and multifocality [7–9]. Among them, Ki-67 is a nuclear protein associated with

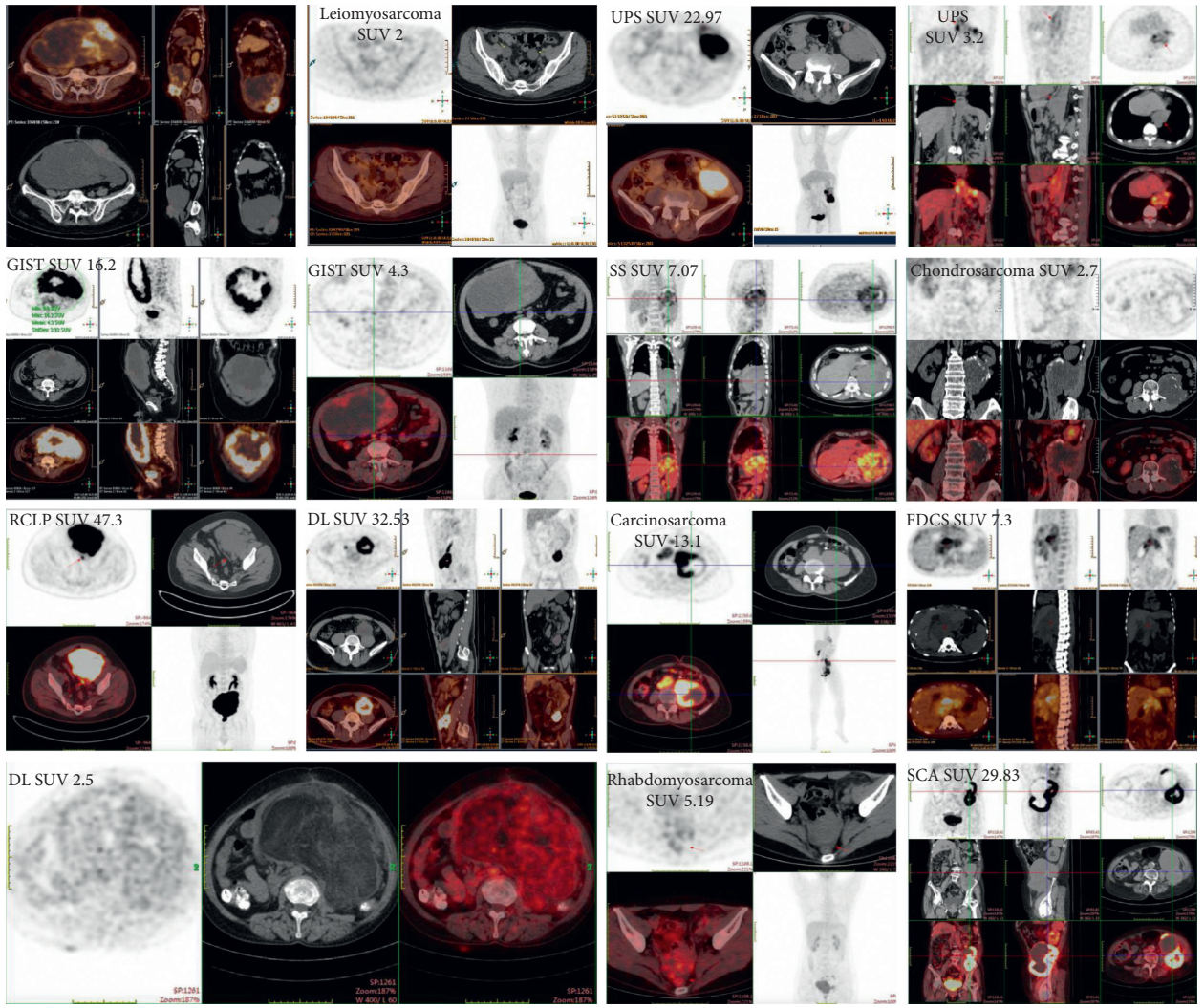

(a)

Figure 1: Continued.

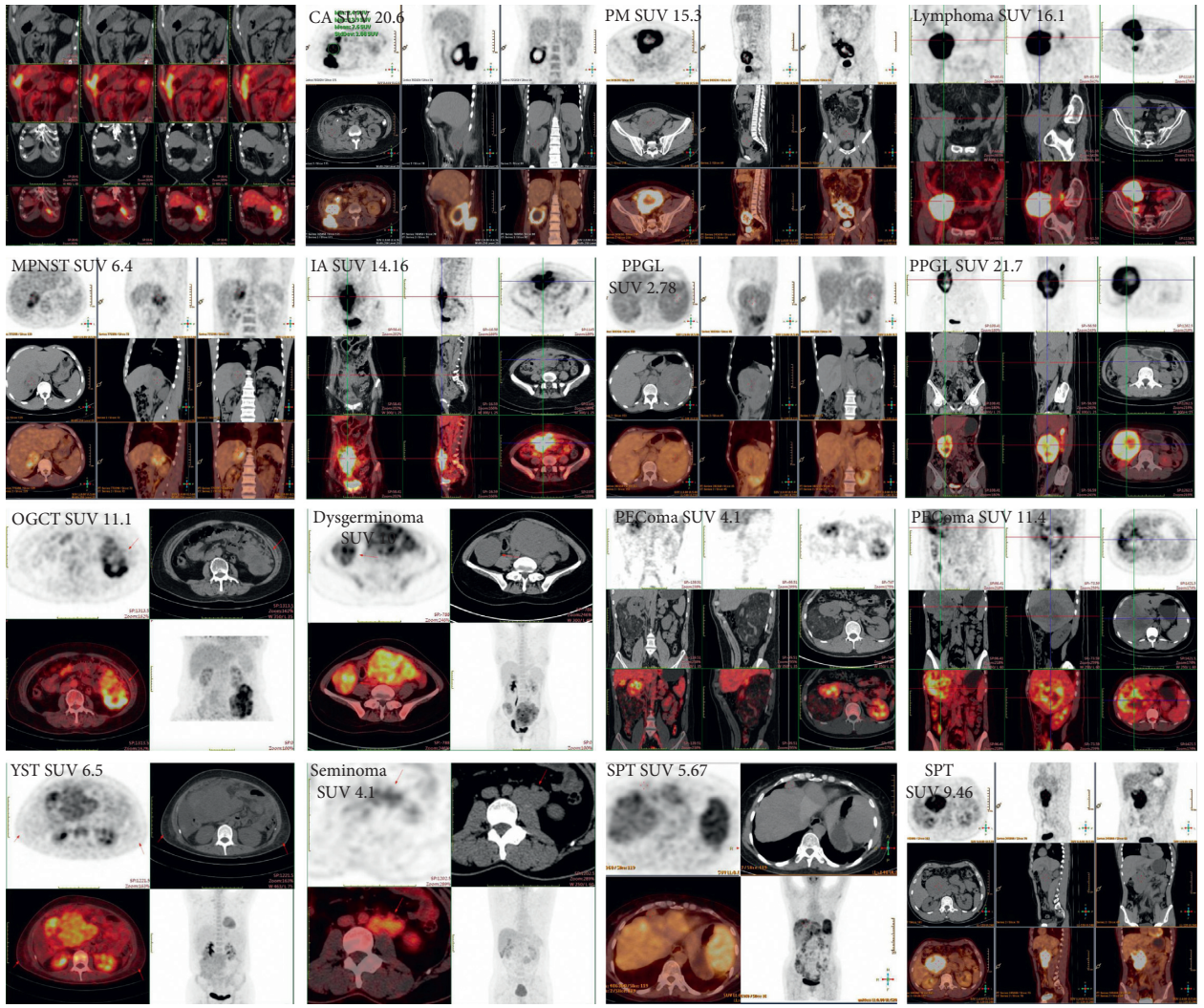

(b)

Figure 1: Representative cases in group 1. STS in group 1 are listed in (a). Other tumors in group 1 are listed in (b).

cellular proliferation. Histological grade of the FNCLCC system has been widely used in prognostic prediction for most STS [10]. They will be perfect representative histological data for us to evaluate 18F-FDG-PET/CT.

2. Materials and Methods

2.1. Patients. 195 patients with 44 different pathological diagnosis have been enrolled. All patients accepted surgical treatment and 18F-FDG-PET/CT in retroperitoneal and intra-abdominal soft tissue sarcoma center, Peking University Cancer Hospital, during a 4-year period (November, 2013, to December, 2017). All patients did not receive any antitumor treatment before the performance of 18F-FDG-PET/CT. Ethical approval and written informed consent have been obtained. Clinical, pathological, and prognostic information have been collected. Histological grade of STS cases without GIST has been reassessed by two experienced pathologists in accordance with the FNCLCC system [10]; the two pathologists were blinded to the findings of clinical and prognostic information.

These patients were divided into two different parts. The first part included 154 retroperitoneal/intra-abdominal STS patients, for whom the relationship among SUVmax, pathological diagnosis, tumor biology, and clinical characters would be analyzed. Then, 32 patients were excluded as per the inclusion and exclusion criteria listed below. The remaining 121 patients would be used to analyze the relationship between SUVmax and prognosis. The second part included 41 patients with benign tumors, psuedotumors, reproductive tumors, and other tumors. They are excellent cases for differentiation.

2.2. Inclusion and Exclusion Criteria

(1) Patients whose preoperative diagnosis and postoperative pathology are soft tissue sarcoma will be included; others will not be included for survival analysis.

(2) Patients do not receive any antitumor treatment before 18F-FDG-PET/CT examination.

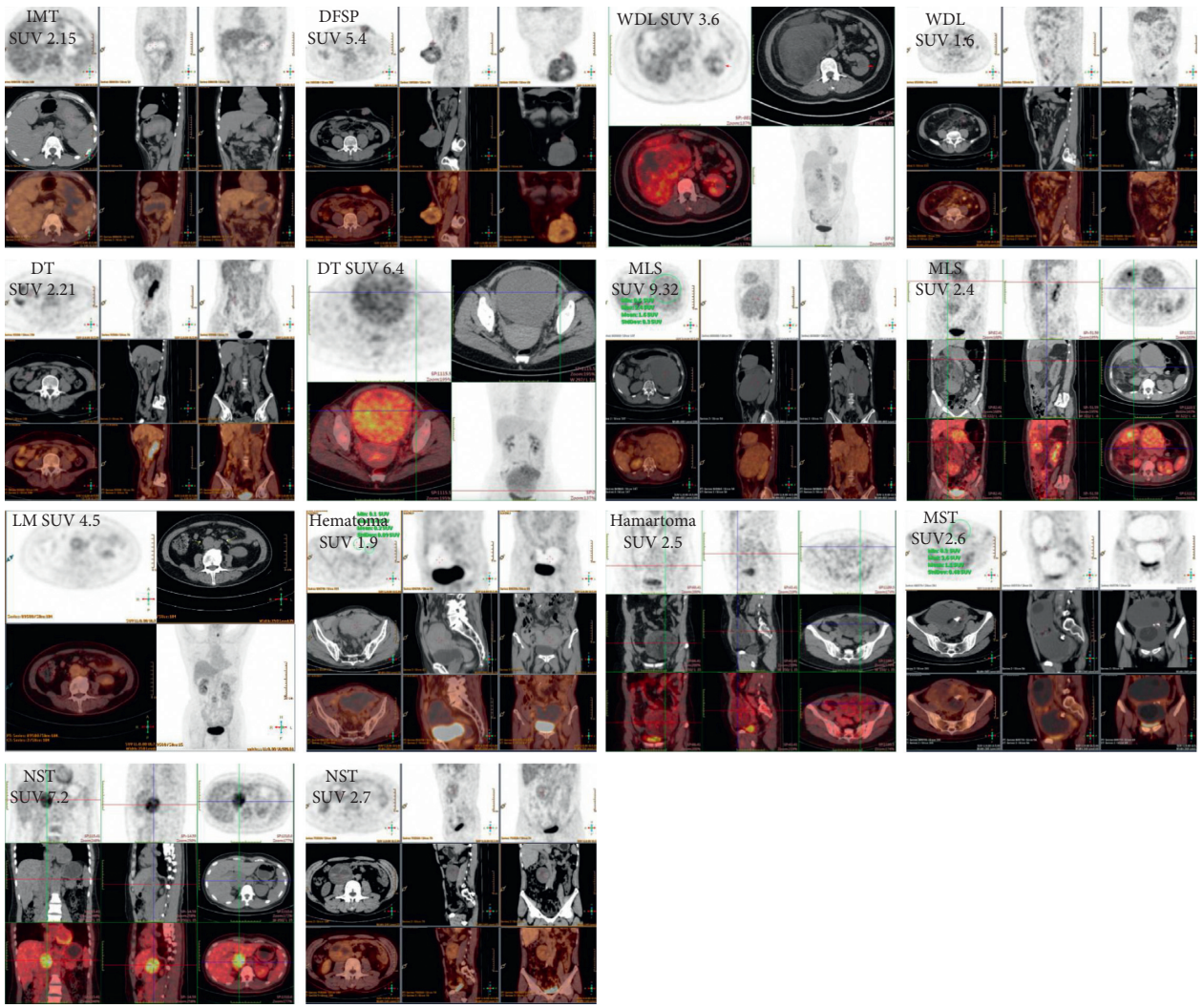

Figure 2: Representative cases in group 2.

(3) All patients accept R0/R1 resection, and those who accept R2 resection will be excluded.

(4) Expect for GIST, no distant metastasis is found before/during the operation.

(5) All patients have signed the informed consent and agreed to participate in this study.

(6) Those patients who died of perioperative complications or other noncancer-related causes will be excluded.

2.3. 18F-FDG-PET/CT Acquisition. Patients fasted for at least 6 h before the 18F-FDG-PET/CT scan. Images were acquired 1 h after injection of 3.7 MBq/kg 18F-FDG. Awhole-body scan (brain to midthigh) was performed with the patient in the supine position. CT exposure factors for all scans were 120 kV and 100 mAs. 18F-FDG-PET/CT images were reported in consensus by two experienced nuclear medicine physicians, who were blinded to the findings of clinical and prognostic information. At the same time, CT imaging was used to differentiate lesions from physiological uptake. The SUVmax of lesions were calculated. The SUVmax generated from each patient was used in the final analysis.

2.4. Statistics. Data collection and statistical analysis were performed with IBM SPSS Version 20 (SPSS Inc., Chicago, IL, USA). Enumeration data were expressed as mean and standard deviation, ranked data by cross-tabulation and percentages, and survival data by the Kaplan–Meier method. The ROC curve was used to find appropriate cutoff SUVmax for differentiation. For statistical analysis, T test, linear regression, ANOVA, nonparametric test, chi-square test, and log-rank test were employed. All tests were performed two-sided at a significance level of $P = 0.05$.

3. Results

3.1. Diagnosis. For all cases included, SUVmax correlates with Ki-67 index and mitotic count ($P = 0.001$, and $P = 0.012$,

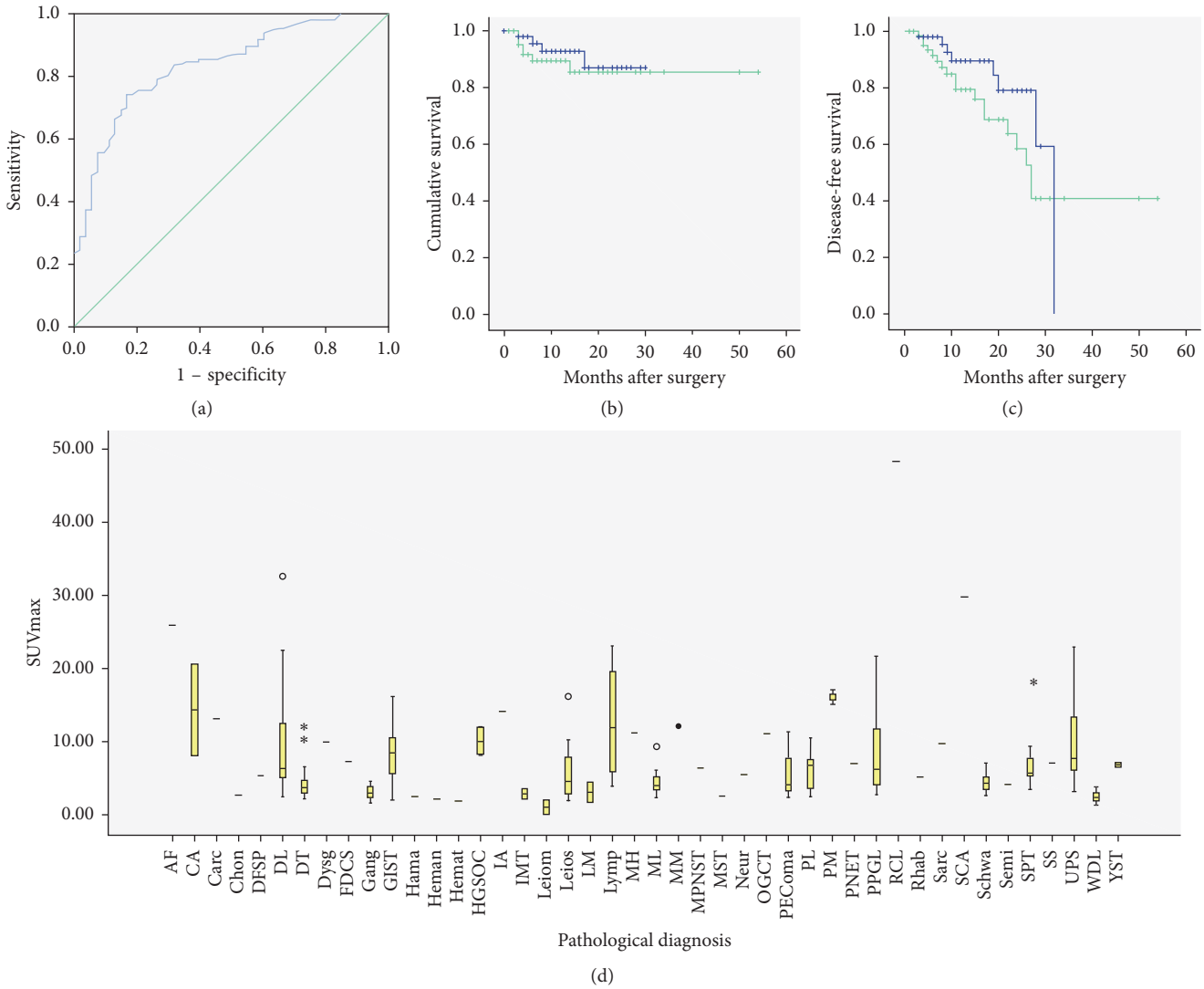

FIGURE 3: (a) The ROC curve for SUVmax to distinguish group 1 from group 2. (b, c) SUVmax (cutoff at 4.35) does not correlate with OS and DFS using Kaplan–Meier survival curves. (d) The box plot for SUVmax of all cases.

Group 1	Retroperitoneal and intra-abdominal STS	UPS, DL, GIST, SS, PL, leiomyosarcoma, RCL, AF, MH, FDCS, PNET, MPNST, rhabdomyosarcoma, chondrosarcoma
	Benign tumors	PPGL
	Pseudotumor	CA, IA, sarcoidosis
	Reproductive tumors	HGSOC, YST, OGCT, dysgerminoma, seminoma
	Others	PM, lymphoma,MM, SPT, PEComa, carcinosarcoma, SCA
Group 2	Retroperitoneal and intra-abdominal STS (mainly G1)	ML,IMT, WDL, DT, DFSP
	Benign tumors	Swchannoma, ganglioneuroma, leiomyoma, neurofibroma, MST, hamartoma, hemangioma
	Pseudotumor	Hematoma
	Others	LM

FIGURE 4: Specific pathological types for groups 1 and 2.

resp.). Malignant tumors do not show higher SUVmax than benign ones ($P = 0.443$). They have been divided into two groups according to the box plot, and literature review, representative images, and pathological types of each group have been shown in Figures 1–4. SUVmax of group 2 is significantly higher than group 1 ($P \leq 0.001$). The ROC curve suggests 4.35 is an appropriate cutoff value to distinguish group 1 from group 2 (sensitivity = 0.789;

specificity = 0.736, Figure 3). SUVmax of all diseases are listed in Table 1.

3.2. Treatment. For all STS cases, SUVmax correlates with vascular resection ($P = 0.002$) but has no relationship with combined organs resection (cutoff at 3 organs, $P = 0.453$). SUVmax does not correlate with pathological invasion of adjacent organs ($P = 0.085$). SUVmax shows no relationship with operative time and blood loss ($P = 0.252$ *and* $P = 0.592$, resp.).

3.3. Prognosis. Recurrent STS show higher SUVmax than primitive STS ($P = 0.037$). SUVmax correlates with histological grade ($P \leq 0.001$), grade 1 is the lowest and grade 3 is the highest. SUVmax for grade 1, 2 and 3 are 4.03 ± 2.28, 6.31 ± 4.78 and 10.09 ± 12.02, respectively. SUVmax also significantly correlates with tumor differentiation scores and tumor necrosis scores of the FNCLCC system ($P = 0.006$ and $P \leq 0.001$, resp.). SUVmax for tumor differentiation scores 1, 2, and 3 are 3.51 ± 1.99, 5.47 ± 3.84, and 9.63 ± 7.89, respectively. SUVmax for tumor necrosis scores 0, 1, and 2 are 5.81 ± 3.94, 9.73 ± 8.57, and 11.28 ± 4.44. SUVmax shows no significant difference between multifocal and unifocal tumors ($P = 0.279$). SUVmax does not correlate with tumor size ($P = 0.279$). SUVmax shows no relationship with death or postoperative recurrence ($P = 0.081$ and $P = 0.162$, resp.). Using 4.35 as the cutoff value, SUVmax does not correlate with DFS or OS by the Kaplan–Meier method ($P = 0.168$ and $P = 0.491$, resp., Figure 3).

Table 1: SUVmax for all diseases.

Pathological diagnosis	*N*	SUVmax
Retroperitoneal and intra-abdominal STS		
Undifferentiated pleomorphic sarcoma (UPS)	9	10.78 ± 6.72
Dedifferentiated liposarcoma (DL)	32	8.93 ± 6.42
Gastrointestinal stromal tumor (GIST)	23	8.51 ± 3.73
Synovial sarcoma (SS)	2	7.09 ± 0.02
Pleomorphic liposarcoma (PL)	6	5.90 ± 3.20
Leiomyosarcoma	14	5.77 ± 3.98
Desmoid tumors (DT)	19	5.76 ± 5.54
Myxoid liposarcoma (ML)	7	4.70 ± 2.33
Inflammatory myofibroblastic tumor (IMT)	2	2.83 ± 0.95
Well-differentiated liposarcoma (WDL)	9	2.48 ± 0.88
Round cell liposarcoma (RCL)	1	47.3
Adult fibrosarcoma (AF)	1	25.94
Malignant hemangiopericytoma (MH)	1	11.21
Follicular dendritic cell sarcoma (FDCS)	1	7.3
Primitive neuroectodermal tumor (PNET)	1	7
Malignant peripheral nerve sheath tumor (MPNST)	1	6.4
Dermatofibrosarcoma protuberans (DFSP)	1	5.4
Rhabdomyosarcoma	1	5.19
Chondrosarcoma	1	2.7
Benign tumors		
Pheochromocytoma and paraganglioma (PPGL)	13	7.87 ± 5.26
Schwannoma	6	4.56 ± 1.59
Ganglioneuroma	3	3.13 ± 1.53
Leiomyoma	2	1.05 ± 1.48
Neurofibroma	1	5.5
Mature cystic teratoma (MST)	1	2.6
Hamartoma	1	2.5
Hemangioma	1	2.2
Psuedotumor		
Chronic abscess (CA)	2	14.4 ± 8.77
Infection of actinomyces (IA)	1	14.16
Sarcoidosis	1	9.75
Hematoma	1	1.9
Reproductive tumors		
High-grade serous ovarian carcinoma (HGSOC)	2	10.1 ± 2.68
Yolk sac tumor (YST)	2	6.8 ± 0.42
Ovarian granulosa cell tumor (OGCT)	1	11.1
Dysgerminoma	1	10
Seminoma	1	4.1
Others		
Peritoneal mesothelioma (PM)	3	16.06 ± 0.92
Lymphoma	4	12.75 ± 8.56
Malignant melanoma (MM)	2	12.05 ± 0.35
Solid pseudopapillary tumor (SPT)	7	7.58 ± 4.93
Perivascular epithelioid cell tumor (PEComa)	3	5.97 ± 4.78
Lymph node metastasis (LM)	2	3.10 ± 1.98
Carcinosarcoma	1	13.1
Sarcomatoid carcinoma (SCA)	1	29.83

4. Discussion

Precise preoperative diagnosis of retroperitoneal and intra-abdominal sarcomas is always a vital problem, since different pathological diagnosis would lead to completely different treatment and prognosis. In former studies, the intermediate and high-grade malignant lesions have significantly higher FDG-uptake than the low-grade and benign lesions, but 18F-FDG-PET/CT offered inadequate discrimination between the latter two groups [3, 11]. Some researchers also tried to find a cutoff to differentiate malignant from benign tumors; the sensitivity and specificity of 18F-FDG-PET/CT for detecting malignant versus benign lesions were 79% and 77% using SUV ≥ 2.0 and 60% and 86% using SUV ≥ 3.0, respectively [4].

In our study, we included 44 different diseases for differentiation. Unlike STS elsewhere, we found that 18F-FDG-PET/CT cannot simply distinguish benign and malignant tumors in retroperitoneal and intra-abdominal cavity. To solve this problem, we divided them into 2 different groups. With this method, we found that sensitivity and specificity for distinguishing 2 different groups are 0.789 and 0.736 using SUVmax ≥ 4.35. Group 1 stands for malignant tumors, inflammatory pseudotumor, and pheochromocytoma and paraganglioma (PPGL). Group 2 stands for benign tumors, relatively low malignant STS, lymph node metastasis, and hematoma. The theory behind this system is that some STS with relatively low malignancy including desmoid tumor, myxoid liposarcoma, and well-differentiated liposarcoma often show lower SUVmax [12, 13]. STS in group 2 are all assessed as FNCLCC grade 1 sarcoma, except for 1 myxoid liposarcoma patient (G2) and 1 desmoid tumor patient (G2). The SUVmax of the special myxoid liposarcoma and

desmoid tumor are 4.3 and 6.47, respectively. We also have a special pleomorphic liposarcoma case assessed as grade 1, and its SUVmax is 2.5. We do not get enough proof to conclude dermatofibrosarcoma protuberans (DFSPs) and inflammatory myofibroblastic tumor (IMT) as the members of group 2, because we only have a bit G1 cases. In Aisheng Dong's study, the SUVmax of IMT was 10.9 ± 5.5, with a high variability of SUVmax among tumors ranging from 3.3 to 20.8 [14]. DFSP can also present high SUVmax [15]. Most reports about hematoma and lymph node metastasis focus on detection of lesions but not on differentiation with other diseases, so they did not list data of SUVmax [16, 17]. SUVmax of hematoma and lymph node metastasis has been reported as 3.4 and 6.3, but we still need more evidence [18, 19]. We just temporarily regard them as group 2 members. On the other side, the range of PPGL SUVmax is from 2.5 to 62.3 [20]. Combined with our data, we list it as the only benign tumor in group 1.

In the future, we think that the members of different groups may vary with the accumulation of cases. If we can establish such a mature system, it could be very helpful for the clinical use of 18F-FDG-PET/CT in retroperitoneal and intra-abdominal sarcomas. There will be 2 possibilities of this system. One is 2 different groups with certain diseases. The other is G1 sarcoma in one group, and rest sarcomas in another one. For now, we prefer the combination of these 2 possibilities, as certain disease is more likely to be of certain grade. If we can make the system mature, this differentiation must be very helpful for preoperative diagnosis combined with other examinations. For example, with exclusion of fat-containing lesions using MRI, we should be very careful to perform compartment resection for group 2 diseases without liposarcoma.

For diagnostic aspect, SUVmax correlates with the Ki-67 index, mitotic count, and histological grade without considering different pathological types, which is the same as extremity STS [21]. This result suggests that 18F-FDG-PET/CT may be helpful for preoperative biopsy and pathology dissection. For retroperitoneal sarcomas, it is reliable for core biopsy to determine the presence of a sarcoma, but it is difficult to correctly identify sarcoma subtype and grade [2, 22]. Reason for this difficulty is the heterogeneity of sarcoma, which can be solved by multiple site sampling after resection. However, even sequential biopsies before resection cannot offer precise diagnosis for STS. The relationship of anatomic pathology and nuclear medicine mentioned in Manuel Scimeca's study has drawn our attention [23]. With the guidance of "SUVmax location," it may be helpful for core biopsy and pathology dissection to find the most representative part of a tumor. It is also possible to build a map of histological grade and different cell types. If the hypothesis is proved, it will reduce the number of biopsy and increase the accuracy of diagnosis and grade. The chaotic circumstance for STS diagnosis means that STS diagnosis and grade may vary with different biopsies, different samplings, or different pathologists. Even pathology of primary tumor and recurrent tumor in one patient could be different. Some relations may exist between different STS, like one STS changes into another one after several recurrences. However, we must know that any further studies or hypothesis must be established on accurate diagnosis and histological grade. With development of imaging fusion, we are convinced that the fusion of 18F-FDG-PET/CT and ultrasound will greatly enhance the accuracy of core biopsy and pathology dissection. This is also the aim for our further study.

For therapeutic aspect, SUVmax correlates with vascular resection but not with combined organ resection. This is because of our aggressive operative decisions. As there is high risk of thrombosis or bleeding, vascular resection is relatively passive. However, we will perform compartment resection even though some organs are "not really infiltrated" by tumors. At the same time, SUVmax does not correlate with pathological invasion of adjacent organs ($P = 0.085$), but the relationship is more significant than organ resection ($P = 0.453$). To some extent, we think SUVmax may be helpful to predict tumor infiltration and operative risks.

In prognostic aspect, SUVmax does correlate with STS prognostic factors including histological grade and recurrent tumors. However, we do not find the relationship among SUVmax, OS, DFS, death, and postoperative recurrence. This is because our follow-up is relatively short, and the median survival of STS is 103 months for R0 resection [24]. Our median follow-up is 10 months overall, with a range of 1 through 54 months. As SUVmax correlates with STS prognostic factors, we are convinced that we can get a positive result with enough follow-up in the future. For instance, G3 and recurrent sarcomas have higher SUVmax than G1 and primary sarcomas. G3 and recurrent sarcomas always leads to bad prognosis.

5. Conclusion

From our observation of retroperitoneal/intra-abdominal tumors, we draw the conclusion that 18F-FDG-PET/CT cannot simply distinguish malignant and benign tumors. We find that the SUVmax of malignant tumors, inflammatory pseudotumor, and PPGL group is higher than the SUVmax of benign tumors, lymph node metastasis, hematoma, and low malignant STS group. Guidance of "SUVmax location" may be helpful for biopsy and pathology dissection.

Data Availability

The data used to support the findings of this study are available from the corresponding author upon request.

Conflicts of Interest

The authors declare that they have no conflicts of interest.

Acknowledgments

This work was supported by the Beijing Municipal Administration of Hospital's Ascent Plan (Approval no. DFL20181104), Beijing Municipal Administration of Hospital's Clinical Medicine Development of Special Funding Support (Approval no. XMLX201708), Capital Health

Research and Development of Special Funds (Approval no. 2016-2-2151), and National Natural Science Fund (Approval no. 31770836). The authors thank Si-meng Zou's support in drafting the manuscript.

References

[1] A. Kirane and A. M. Crago, "The importance of surgical margins in retroperitoneal sarcoma," *Journal of Surgical Oncology*, vol. 113, no. 3, pp. 270–276, 2016.

[2] S. Y. Hwang, S. Warrier, S. Thompson, T. Davidson, J. L. Yang, and P. Crowe, "Safety and accuracy of core biopsy in retroperitoneal sarcomas," *Asia-Pacific Journal of Clinical Oncology*, vol. 12, no. 1, pp. e174–e178, 2016.

[3] J. P. A. Ioannidis and J. Lau, "18F-FDG PET for the diagnosis and grading of soft-tissue sarcoma: a meta-analysis," *Journal of Nuclear Medicine Official Publication Society of Nuclear Medicine*, vol. 44, pp. 717–724, 2003.

[4] Z. Németh, K. Boér, and K. Borbély, "Advantages of (18)F FDG-PET/CT over conventional staging for sarcoma patients," *Pathology & Oncology Research*, vol. 4, pp. 1–6, 2017.

[5] T. C. Kwee, S. Basu, B. Saboury, V. Ambrosini, D. A. Torigian, and A. Alavi, "A new dimension of FDG-PET interpretation: assessment of tumor biology," *European Journal of Nuclear Medicine and Molecular Imaging*, vol. 38, no. 6, pp. 1158–1170, 2011.

[6] Y. Yamamoto, Y. Ono, F. Aga, N. Kawai, N. Kudomi, and Y. Nishiyama, "Correlation of 18F-FLT uptake with tumor grade and Ki-67 immunohistochemistry in patients with newly diagnosed and recurrent gliomas," *Journal of Nuclear Medicine*, vol. 53, no. 12, pp. 1911–1915, 2012.

[7] D. Callegaro, R. Miceli, and R. Gladdy, "Prognostic models for RPS patients-attempting to predict patient outcomes," *Journal of Surgical Oncology*, vol. 117, no. 1, pp. 69–78, 2017.

[8] Y. Zhou, W. Hu, P. Chen et al., "Ki67 is a biological marker of malignant risk of gastrointestinal stromal tumors: a systematic review and meta-analysis," *Medicine*, vol. 96, no. 34, article e7911, 2017.

[9] M. C. Tan, M. F. Brennan, D. Kuk et al., "Histology-based classification predicts pattern of recurrence and improves risk stratification in primary retroperitoneal sarcoma," *Annals of Surgery*, vol. 263, no. 3, pp. 593–600, 2016.

[10] M. M. Von, R. L. Randall, R. S. Benjamin et al., "Soft tissue sarcoma, version 2.2016, NCCN clinical practice guidelines in oncology," *Journal of the National Comprehensive Cancer Network*, vol. 14, pp. 758–786, 2016.

[11] M. H. M. Schwarzbach, A. Dimitrakopoulou-Strauss, F. Willeke et al., "Clinical value of [18-F] fluorodeoxyglucose positron emission tomography imaging in soft tissue sarcomas," *Annals of Surgery*, vol. 231, no. 3, pp. 380–386, 2000.

[12] W. Brenner, J. F. Eary, W. Hwang, C. Vernon, and E. U. Conrad, "Risk assessment in liposarcoma patients based on FDG PET imaging," *European Journal of Nuclear Medicine and Molecular Imaging*, vol. 33, no. 11, pp. 1290–1295, 2006.

[13] H. Xu, H. J. Koo, S. Lim et al., "Desmoid-type fibromatosis of the thorax: CT, MRI, and FDG PET characteristics in a large series from a tertiary referral center," *Medicine*, vol. 94, no. 38, article e1547, 2015.

[14] A. Dong, Y. Wang, H. Dong et al., "Inflammatory myofibroblastic tumor: FDG PET/CT findings with pathologic correlation," *Clinical Nuclear Medicine*, vol. 39, no. 2, pp. 113–121, 2014.

[15] S. Basu and F. Goliwale, "18F-FDG PET/CT prediction of an aggressive clinical course for dermatofibrosarcoma protuberans," *Journal of Nuclear Medicine Technology*, vol. 44, no. 2, pp. 88-89, 2015.

[16] M. Atri, Z. Zhang, F. Dehdashti et al., "Utility of PET-CT to evaluate retroperitoneal lymph node metastasis in advanced cervical cancer: results of ACRIN6671/GOG0233 trial," *Gynecologic Oncology*, vol. 142, no. 3, pp. 413–419, 2016.

[17] A. Toriihara, E. Yamaga, M. Nakadate, J. Oyama, and U. Tateishi, "Detection of unexpected emergency diseases using FDG-PET/CT in oncology patients," *Japanese Journal of Radiology*, vol. 35, no. 9, pp. 539–545, 2017.

[18] G. Schaiberger, D. Pucar, V. Patel, B. Bateson, H. Williams, and W. Bates, "Para-atrial non-acute mediastinal hematoma after left atrial maze procedure mimicking tumor in a patient with treated melanoma," *Journal of Nuclear Cardiology*, vol. 4, pp. 1–3, 2017.

[19] Y. Tsunoda, M. Ito, H. Fujii, H. Kuwano, and N. Saito, "Preoperative diagnosis of lymph node metastases of colorectal cancer by FDG-PET/CT," *Japanese Journal of Clinical Oncology*, vol. 38, no. 5, pp. 347–353, 2008.

[20] T. H. Tan, Z. Hussein, F. F. Saad, and I. L. Shuaib, "Diagnostic performance of (68)Ga-DOTATATE PET/CT, (18)F-FDG PET/CT and (131)I-MIBG scintigraphy in mapping metastatic pheochromocytoma and paraganglioma," *Nuclear Medicine and Molecular Imaging*, vol. 49, no. 2, pp. 143–151, 2015.

[21] L. P. Adler, H. F. Blair, J. T. Makley et al., "Noninvasive grading of musculoskeletal tumors using PET," *Journal of Nuclear Medicine Official Publication Society of Nuclear Medicine*, vol. 32, no. 8, pp. 1508–1512, 1991.

[22] D. Berger-Richardson and C. J. Swallow, "Needle tract seeding after percutaneous biopsy of sarcoma: risk/benefit considerations," *Cancer*, vol. 123, no. 4, pp. 560–567, 2017.

[23] M. Scimeca, N. Urbano, R. Bonfiglio, O. Schillaci, and E. Bonanno, "Management of oncological patients in the digital era: anatomic pathology and nuclear medicine teamwork," *Future Oncology*, vol. 14, no. 11, pp. 1013–1015, 2018.

[24] J. J. Lewis, D. Leung, J. M. Woodruff, and M. F. Brennan, "Retroperitoneal soft-tissue sarcoma: analysis of 500 patients treated and followed at a single institution," *Annals of Surgery*, vol. 228, no. 3, pp. 355–365, 1998.

Hindawi
Contrast Media & Molecular Imaging
Volume 2018, Article ID 9257929, 10 pages
https://doi.org/10.1155/2018/9257929

Research Article

Standardized Uptake Values Derived from ^{18}F-FDG PET May Predict Lung Cancer Microvessel Density and Expression of KI 67, VEGF, and HIF-1α but Not Expression of Cyclin D1, PCNA, EGFR, PD L1, and p53

Alexey Surov,[1] **Hans Jonas Meyer**,[1] **and Andreas Wienke**[2]

[1]*Department of Diagnostic and Interventional Radiology, University of Leipzig, Leipzig, Germany*
[2]*Institute of Medical Epidemiology, Biostatistics, and Informatics, Martin-Luther-University Halle-Wittenberg, Halle, Germany*

Correspondence should be addressed to Alexey Surov; alexey.surov@medizin.uni-leipzig.de

Received 2 March 2018; Accepted 26 April 2018; Published 6 June 2018

Academic Editor: Elena Bonanno

Background. Our purpose was to provide data regarding relationships between ^{18}F-FDG PET and histopathological parameters in lung cancer. *Methods*. MEDLINE library was screened for associations between PET parameters and histopathological features in lung cancer up to December 2017. Only papers containing correlation coefficients between PET parameters and histopathological findings were acquired for the analysis. Overall, 40 publications were identified. *Results*. Associations between SUV and KI 67 were reported in 23 studies (1362 patients). The pooled correlation coefficient was 0.44. In 2 studies (180 patients), relationships between SUV and expression of cyclin D1 were analyzed (pooled correlation coefficient = 0.05). Correlation between SUV and HIF-1α was investigated in 3 studies (288 patients), and the pooled correlation coefficient was 0.42. In 5 studies (310 patients), associations between SUV and MVD were investigated (pooled correlation coefficient = 0.54). In 6 studies (305 patients), relationships between SUV and p53 were analyzed (pooled correlation coefficient = 0.30). In 6 studies (415 patients), associations between SUV and VEGF expression were investigated (pooled correlation coefficient = 0.44). In 5 studies (202 patients), associations between SUV and PCNA were investigated (pooled correlation coefficient = 0.32). In 3 studies (718 patients), associations between SUV and expression of PD L1 were analyzed (pooled correlation coefficient = 0.36). Finally, in 5 studies (409 patients), associations between SUV and EGFR were investigated (pooled correlation coefficient = 0.38). *Conclusion*. SUV may predict microvessel density and expression of VEGF, KI 67, and HIF-1α in lung cancer.

1. Introduction

Lung cancer is one of the most frequent malignancies in humans [1]. It is the largest cause of cancer deaths in the United States [1].

Multiple histopathological factors influence tumor biology in lung cancer. According to the literature, different molecular markers play a key role here [2]. Previous reports investigated numerous biomarkers and suggested that some histopathological parameters can predict tumor behavior in lung cancer [2–5]. It has been shown that they provide information about tumor proliferation, aggressiveness, prognosis, and therapy response [2–5]. According to the literature, following biomarkers are relevant in lung cancer: proliferation index KI 67, hypoxia-inducible factor- (HIF-) 1α, tumor suppressor protein p53, vascular endothelial growth factor (VEGF), epidermal growth factor receptor (EGFR), proliferating cell nuclear antigen (PCNA), PD L1, and several cyclins [2–10]. For instance, it has been shown that tumors with high expression of KI 67 and/or VEGF were associated with a worse prognosis [3, 4]. Similar results were also reported for expression of HIF-1α and p53 [5–7].

Furthermore, some reports analyzed associations between imaging parameters and histopathological features in lung cancer [11–14]. Especially parameters of positron emission tomography (PET) like standardized uptake values

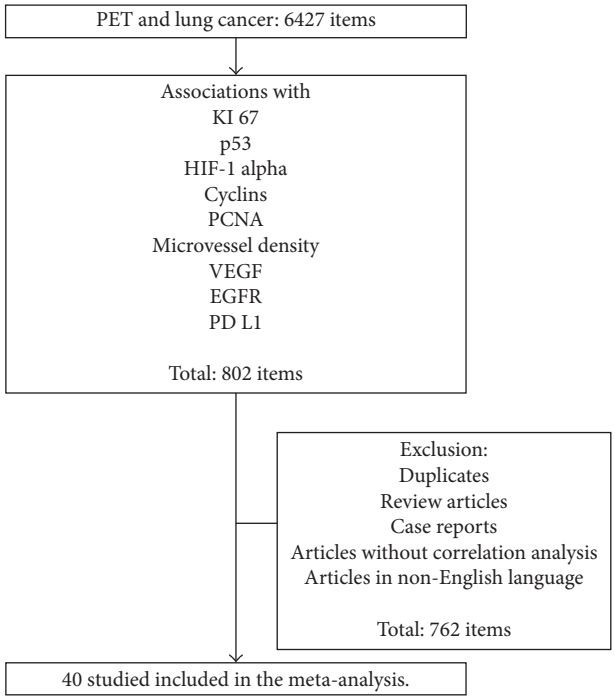

Figure 1: Flowchart of the data acquisition.

(SUV) were in focus of the studies. However, the reported data were inconsistent. While some authors found such significant relationships, others did not. Therefore, it is unclear whether SUV can be used as a surrogate parameter reflecting histopathological features in lung cancer or not.

The purpose of this meta-analysis was to provide evident data about associations between SUV and histopathological parameters in lung cancer.

2. Materials and Methods

2.1. Data Acquisition. The strategy of data acquisition is shown in Figure 1. MEDLINE library was screened for associations between PET parameters and histopathological findings in lung cancer up to December 2017.

For associations between PET and different biomarkers, the following search words were used:

(i) *PET and KI 67*: "lung cancer AND PET OR positron emission tomography AND KI 67 OR KI67 OR ki67 OR ki-67 OR mitotic index OR proliferation index OR MIB 1 OR MIB-1 OR mitosis index" (192 items)

(ii) *PET and expression of p53*: "lung cancer AND PET or positron emission tomography AND p53 OR tumor suppressor protein" (51 items)

(iii) *PET and expression of VEGF*: "lung cancer AND PET or positron emission tomography AND VEGF OR vascular endothelial growth factor" (82 items)

(iv) *PET and expression of EGFR*: "lung cancer AND PET or positron emission tomography AND EGFR OR epidermal growth factor receptor" (345 items)

Table 1: Methodological quality of the involved 40 studies according to the QUADAS criteria.

QUADAS criteria	Yes (%)	No (%)	Unclear (%)
Patient spectrum	38 (95.0)	—	2 (5.0)
Selection criteria	28 (70.0)	1 (2.50)	11 (27.5)
Reference standard	40 (100)	—	—
Disease progression bias	40 (100)	—	—
Partial verification bias	40 (100)	—	—
Differential verification bias	40 (100)	—	—
Incorporation bias	40 (100)	—	—
Text details	40 (100)	—	—
Reference standard details	40 (100)	—	—
Text review details	16 (40.0)	4 (10.0)	20 (50.0)
Diagnostic review bias	17 (42.5)	4 (10.0)	19 (47.5)
Clinical review bias	39 (97.5)	—	1 (2.5)
Uninterpretable results	39 (97.5)	—	1 (2.5)
Withdrawal explained	38 (95.0)	1 (2.5)	1 (2.5)

(v) *PET and expression of HIF-1α*: "lung cancer AND PET or positron emission tomography AND HIF-1α OR HIF1α OR HIF-1 alpha OR HIF1 alpha OR hypoxia-inducible factor" (38 items)

(vi) *PET and expression of PCNA*: "lung cancer AND PET or positron emission tomography AND PCNA OR proliferating cell nuclear antigen" (23 items)

(vii) *PET and expression of cyclins*: "lung cancer AND PET or positron emission tomography AND cyclin" (22 items)

(viii) *PET and microvessel density*: "lung cancer AND PET or positron emission tomography AND microvessel density OR MVD" (34 items)

(ix) *PET and expression of PD L1*: "lung cancer AND PET or positron emission tomography AND programmed cell death-ligand 1 OR PD L1" (15 items).

Secondary references were also recruited. Overall, 802 records were identified. After exclusion of doublets, review articles, case reports, non-English publications, and articles, which not contain correlation coefficients between PET and histopathological parameters, there were 40 articles [11–50].

The following data were extracted from the literature: authors, year of publication, number of patients, histopathological parameters, and correlation coefficients, according to our previous descriptions [51–53].

The Preferred Reporting Items for Systematic Reviews and Meta-Analyses statement (PRISMA) was used for the research [54].

2.2. Meta-Analysis. The methodological quality of the acquired 40 studies was independently checked by two observers (Alexey Surov and Hans Jonas Meyer) using the Quality Assessment of Diagnostic Studies (QUADAS) instrument according to previous descriptions [55]. Table 1 shows the results of QUADAS proving.

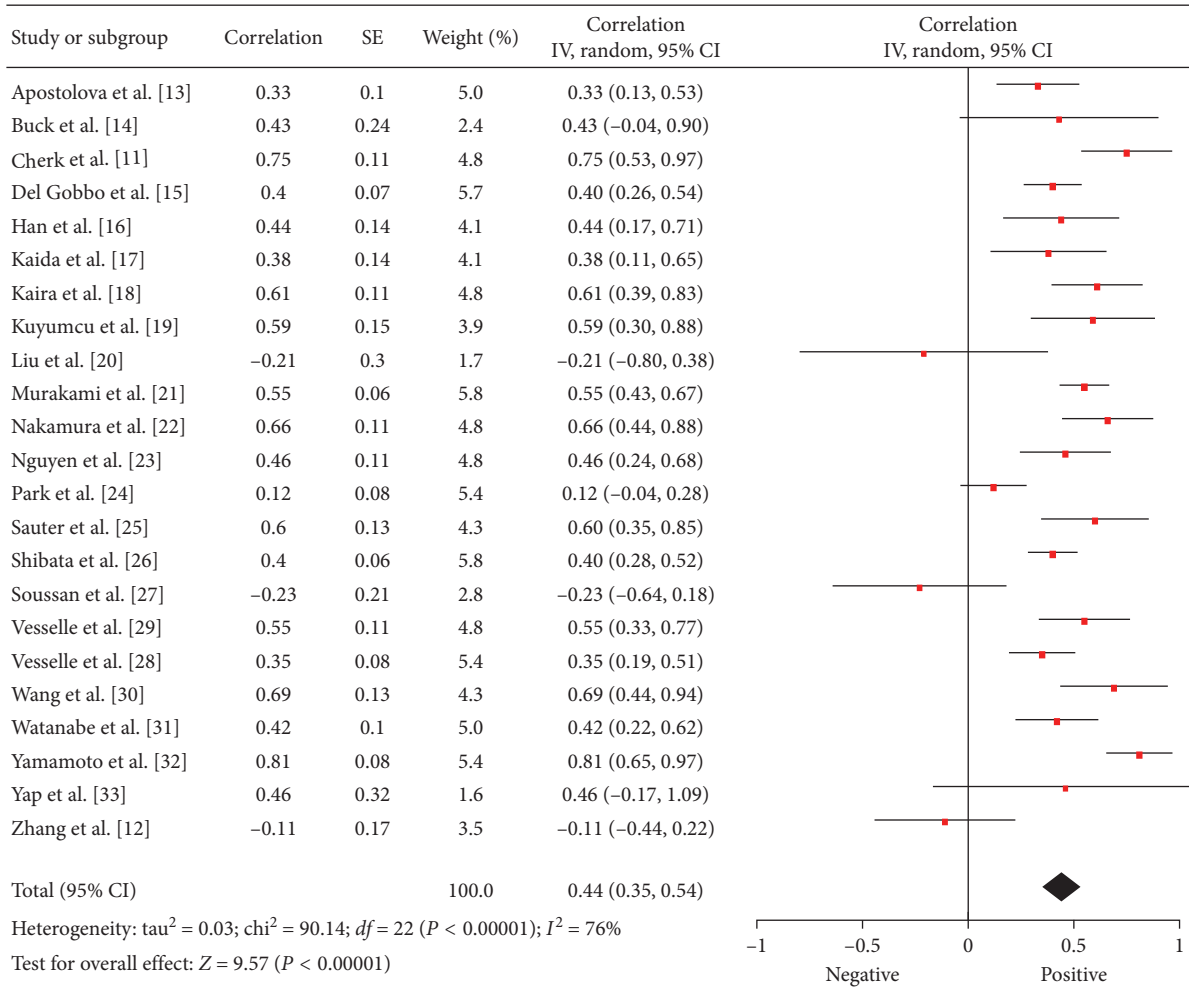

Figure 2: Forest plots of correlation coefficients between SUV_{max} and KI 67 in patients with lung cancer.

Associations between PET and histopathological findings were analyzed by Spearman's correlation coefficient. The reported Pearson's correlation coefficients in some studies were converted into Spearman's correlation coefficients according to the previous description [56].

Furthermore, the meta-analysis was undertaken by using RevMan 5.3 (Computer Program, version 5.3, The Cochrane Collaboration, 2014, The Nordic Cochrane Centre, Copenhagen). Heterogeneity was calculated by means of the inconsistency index I^2 [57, 58]. Additionally, DerSimonian and Laird random-effects models with inverse-variance weights were used without any further correction [59].

3. Results

3.1. KI 67. Associations between ^{18}F-FDG PET and KI 67 were reported in 23 studies (1362 patients) [11–33]. The calculated correlation coefficients between SUV_{max} and KI 67 ranged from −0.23 to 0.81 (Figure 2). The pooled correlation coefficient was 0.44 (95% CI = (0.35; 0.54)).

3.2. Cyclin D1. In 2 studies (180 patients), relationships between 18F-FDG PET and expression of cyclin D1 were analyzed [34, 35]. The pooled correlation coefficient between these parameters was 0.05 (95% CI = (−0.36; 0.46)) (Figure 3).

3.3. HIF-1α. Associations between ^{18}F-FDG PET and HIF-1α were investigated in 3 studies (288 patients) [36–38]. The reported correlation coefficients ranged from −0.19 to 0.99 (Figure 4). The pooled correlation coefficient was 0.42 (95% CI = (0.06; 0.78)).

3.4. Microvessel Density (MVD). Associations between ^{18}F-FDG PET and MVD were investigated in 5 studies (310 patients) [25,37–40]. The reported correlation coefficients ranged from −0.23 to 0.91 (Figure 5). The pooled correlation coefficient was 0.54 (95% CI = (0.29; 0.80)).

3.5. P53. In 6 studies (305 patients), relationships between ^{18}F-FDG PET and p53 were analyzed [13,22,34,41–43]. The pooled correlation coefficient between these parameters was 0.30 (95% CI = (0.13; 0.47)) (Figure 6).

Study or subgroup	Correlation	SE	Weight (%)	Correlation IV, random, 95% CI
Taylor et al. [34]	−0.13	0.08	56.4	−0.13 (−0.29, 0.03)
Yang et al. [35]	0.29	0.17	43.6	0.29 (−0.04, 0.62)
Total (95% CI)			100.0	0.05 (−0.36, 0.46)

Heterogeneity: tau^2 = 0.07; chi^2 = 5.00; df = 1 (P = 0.03); I^2 = 80%

Test for overall effect: Z = 0.26 (P = 0.80)

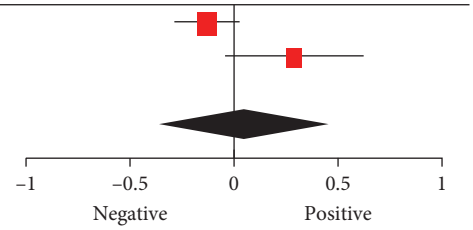

Figure 3: Forest plots of correlation coefficients between SUV_{max} and expression of cyclin D1.

Study or subgroup	Correlation	SE	Weight (%)	Correlation IV, random, 95% CI
Furukawa et al. [36]	0.31	0.09	37.3	0.31 (0.13, 0.49)
Kaira et al. [37]	0.09	0.26	22.5	0.09 (−0.42, 0.60)
Kaira et al. [38]	0.71	0.04	40.2	0.71 (0.63, 0.79)
Total (95% CI)			100.0	0.42 (0.06, 0.78)

Heterogeneity: tau^2 = 0.08; chi^2 = 20.95; df = 2 (P < 0.0001); I^2 = 90%

Test for overall effect: Z = 2.30 (P = 0.02)

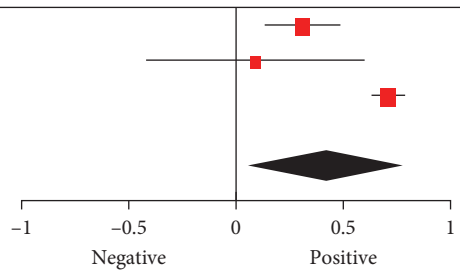

Figure 4: Forest plots of correlation coefficients between SUV_{max} and expression of HIF-1α in lung cancer.

Study or subgroup	Correlation	SE	Weight (%)	Correlation IV, random, 95% CI
Kaira et al. [37]	0.82	0.09	20.7	0.82 (0.64, 1.00)
Kaira et al. [38]	0.67	0.05	22.3	0.67 (0.57, 0.77)
Sauter et al. [25]	−0.23	0.21	14.5	−0.23 (−0.64, 0.18)
Xing et al. [39]	0.91	0.05	22.3	0.91 (0.81, 1.01)
Zhang et al. [40]	0.27	0.1	20.3	0.27 (0.07, 0.47)
Total (95% CI)			100.0	0.54 (0.29, 0.80)

Heterogeneity: tau^2 = 0.07; chi^2 = 57.39; df = 4 (P < 0.00001); I^2 = 93%

Test for overall effect: Z = 4.15 (P < 0.0001)

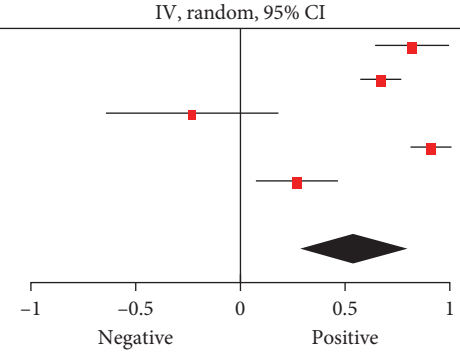

Figure 5: Forest plots of correlation coefficients between SUV_{max} and microvessel density.

Study or subgroup	Correlation	SE	Weight (%)	Correlation IV, random, 95% CI
Apostolova et al. [13]	0.01	0.15	14.4	0.01 (−0.28, 0.30)
Araz et al. [41]	0.36	0.15	14.4	0.36 (0.07, 0.65)
Bai et al. [42]	0.46	0.12	17.2	0.46 (0.22, 0.70)
Duan et al. [43]	0.49	0.1	19.2	0.49 (0.29, 0.69)
Nakamura et al. [22]	0.36	0.16	13.6	0.36 (0.05, 0.67)
Taylor et al. [34]	0.11	0.08	21.2	0.11 (−0.05, 0.27)
Total (95% CI)			100.0	0.30 (0.13, 0.47)

Heterogeneity: tau^2 = 0.03; chi^2 = 14.94; df = 5 (P = 0.01); I^2 = 67%

Test for overall effect: Z = 3.50 (P = 0.0005)

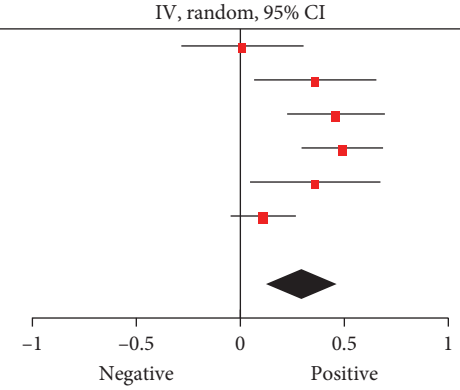

Figure 6: Forest plots of correlation coefficients between SUV_{max} and expression of p53.

Study or subgroup	Correlation	SE	Weight (%)	Correlation IV, random, 95% CI
Apostolova et al. [13]	−0.13	0.15	15.4	−0.13 (−0.42, 0.16)
Kaira et al. [18]	0.37	0.14	15.7	0.37 (0.10, 0.64)
Kaira et al. [37]	0.69	0.14	15.7	0.69 (0.42, 0.96)
Kaira et al. [38]	0.71	0.04	18.0	0.71 (0.63, 0.79)
Liu et al. [44]	0.87	0.05	17.9	0.87 (0.77, 0.97)
Taylor et al. [34]	0.03	0.08	17.3	0.03 (−0.13, 0.19)
Total (95% CI)			100.0	0.44 (0.14, 0.73)

Heterogeneity: tau^2 = 0.12; chi^2 = 112.54; df = 5 (P < 0.00001); I^2 = 96%

Test for overall effect: Z = 2.93 (P = 0.003)

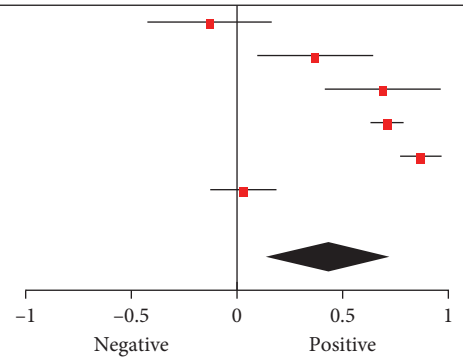

Figure 7: Forest plots of correlation coefficients between SUV_{max} and VEGF expression.

Study or subgroup	Correlation	SE	Weight (%)	Correlation IV, random, 95% CI
Higashi et al. [45]	0.72	0.09	23.4	0.72 (0.54, 0.90)
Khandani et al. [46]	−0.11	0.24	14.8	−0.11 (−0.58, 0.36)
Mamede et al. [47]	0.42	0.13	21.2	0.42 (0.17, 0.67)
Nakamura et al. [22]	0.21	0.18	18.2	0.21 (−0.14, 0.56)
Zhang et al. [40]	0.2	0.11	22.4	0.20 (−0.02, 0.42)
Total (95% CI)			100.0	0.32 (0.05, 0.60)

Heterogeneity: tau^2 = 0.08; chi^2 = 21.32; df = 4 (P = 0.0003); I^2 = 81%

Test for overall effect: Z = 2.31 (P = 0.02)

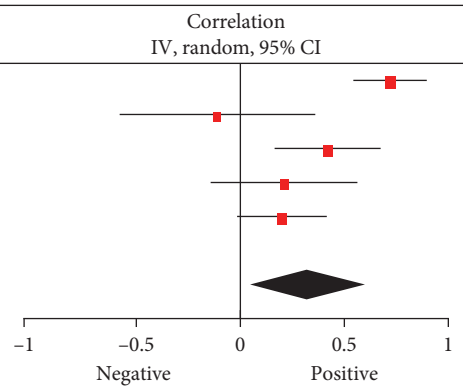

Figure 8: Forest plots of correlation coefficients between SUV_{max} and PCNA.

Study or subgroup	Correlation	SE	Weight (%)	Correlation IV, random, 95% CI
Apostolova et al. [13]	0.34	0.13	18.8	0.34 (0.09, 0.59)
Bai et al. [42]	0.04	0.15	17.9	0.04 (−0.25, 0.33)
Kaira et al. [38]	0.38	0.07	21.1	0.38 (0.24, 0.52)
Liu et al. [44]	0.83	0.06	21.4	0.83 (0.71, 0.95)
Taylor et al. [34]	0.24	0.08	20.8	0.24 (0.08, 0.40)
Total (95% CI)			100.0	0.38 (0.10, 0.66)

Heterogeneity: tau^2 = 0.09; chi^2 = 54.66; df = 4 (P < 0.00001); I^2 = 93%

Test for overall effect: Z = 2.63 (P = 0.009)

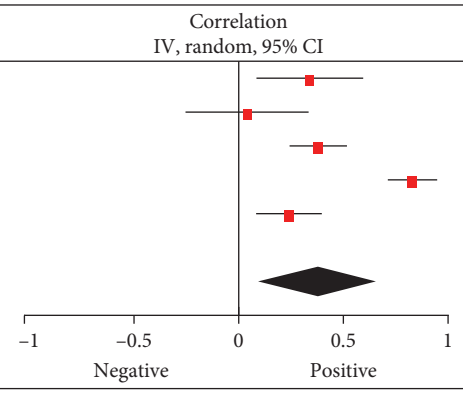

Figure 9: Forest plots of correlation coefficients between SUV_{max} and EGFR expression.

3.6. VEGF. There were 6 studies (415 patients) which investigated associations between SUV and expression of VEGF in lung cancer [13, 18, 34, 37, 38, 44]. The reported correlation coefficients ranged from −0.13 to 0.77 (Figure 7). The pooled correlation coefficient was 0.44 (95% CI = (0.14; 0.73)).

3.7. PCNA. There were 5 studies (202 patients) which investigated associations between ^{18}F-FDG PET and PCNA in lung cancer [22,40,45–47]. The reported correlation coefficients ranged from 0.04 to 0.83 (Figure 8). The pooled correlation coefficient was 0.32 (95% CI = (0.05; 0.60)).

3.8. EGFR. There were 5 studies (409 patients) which investigated associations between ^{18}F-FDG PET and expression of EGFR in lung cancer [13, 34, 38, 42, 44]. The reported correlation coefficients ranged from 0.04 to 0.83 (Figure 9). The pooled correlation coefficient was 0.38 (95% CI = (0.10; 0.66)).

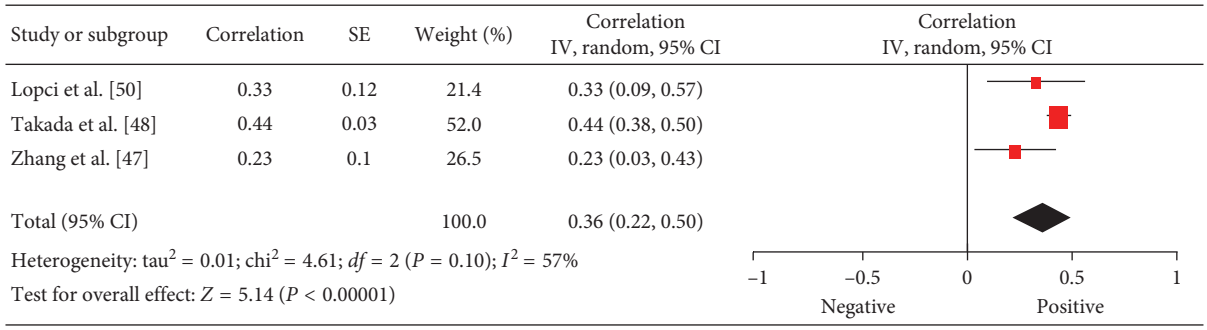

Figure 10: Forest plots of correlation coefficients between SUV_{max} and EGFR expression.

3.9. PD L1. In 3 studies (718 patients), relationships between ^{18}F-FDG PET and expression of PD L1 were analyzed [48–50]. The pooled correlation coefficient between these parameters was 0.36 (95% CI = (0.22; 0.50)) (Figure 10).

4. Discussion

Analysis of interactions between imaging findings, in particular, between PET and histopathology can significantly improve oncologic diagnostics [60]. The possibility to characterize histological tissues by imaging can also personalize anticancer treatment [60]. Although PET is an established investigation of lung cancer in clinical practice, only few reports analyzed the question if there are relationships between PET findings and different histopathological parameters. However, this is a key question. In fact, if PET parameters do correlate with several histopathological findings reflecting proliferation or other features of lung cancer, then PET values can also be used as biomarkers.

Our meta-analysis showed that SUV can reflect different histopathological parameters in lung cancer. As shown, SUV correlated moderately with KI 67. This finding is not surprisingly. KI 67 is a nonhistone, nuclear protein synthesized throughout the whole cell cycle except the G0 phase and has been shown to be responsible for cell proliferation [61]. It is an established biomarker in lung cancer for prediction of tumor behavior. Our data are in agreement with those of previous investigations and also analyzed relationships between expression of KI 67 and SUV in lung cancer [62, 63]. However, we found weak correlations between SUV_{max} and other proliferation markers, namely, PCNA (0.32). This finding is difficult to explain. Theoretically, SUV reflects metabolic activity and, therefore, might correlate stronger with several proliferation biomarkers. Obviously, metabolic activity and proliferation are not associated directly.

Similarly, our analysis found only slight correlation between SUV_{max} and expression of EGFR (0.38). EGFR is a cell membrane tyrosine kinase receptor [64, 65]. As reported previously, EGFR signaling is critical in development and cellular homeostasis, proliferation, and growth [64–66]. EGFR is overexpressed in most lung cancers [64–66]. Overexpression of EGFR is associated with a poor prognosis in non-small-cell lung cancer [66]. In addition, EGFR overexpression is also associated with chemoresistance in non-small-cell lung cancer [64, 66]. The present meta-analysis showed that SUV_{max} cannot be used as a surrogate marker for EGFR expression in lung cancer.

Furthermore, we analyzed associations between SUV_{max} and expression of p53. As seen, these parameters correlate weakly (0.30). According to the literature, p53 is a protein encoded by the TP53 gene and plays a key role in tumor suppression and in the cellular response to DNA damage [2, 5]. Some authors indicated that high expression of p53 can be used as a predictor for better overall survival [2]. However, in the study of Tsao et al., p53 protein overexpression was a significant prognostic marker of shortened survival [5]. Relationships between SUV_{max} and p53 were analyzed in 6 previous studies with divergent results [13,22,34,41–43]. Our data suggest that SUV cannot be used as a surrogate marker for expression of p53.

Programmed cell death-ligand 1 or PD L1 is another very important biomarker in lung cancer [67]. PD L1 is an immune modulator that promotes immunosuppression by binding to PD-1 receptor [68]. PD L1 on the surface of tumor cells inhibits an immune-mediated attack by binding to PD-1 on cytotoxic T-cells [68, 69]. According to the literature, high expression of PD L1 is associated with shorter overall survival in patients with non-small cell lung cancer [70]. Therefore, prediction of PD L1 expression by imaging may be of interest in clinical practice. Our analysis identified only a slightly correlation (0.36) between SUV_{max} and PD L1 expression in lung cancer; that is, SUV_{max} cannot be used as a surrogate marker for PD L1 status.

Our analysis also showed that SUV_{max} cannot predict expression of cyclin D1 in lung cancer. As reported previously, data of the role of this protein are inconsequent. For example, Gautschi et al. found a strong pathological role for cyclin D1 deregulation in bronchial neoplasia [71]. However, Zhang et al. suggested in their meta-analysis that the expression of cyclin D1 is unlikely to be useful as a prognostic marker for NSCLC in clinical practice from current evidence [72].

The present meta-analysis identified a moderate pooled correlation between SUV_{max} and hypoxia-inducible factor-1 alpha (HIF-1α). According to the literature, HIF-1α characterizes cellular responses to hypoxic stress [6, 7]. It has been reported that patients with lung cancer and positive HIF-1α expression in tumor tissues had lower overall survival rate than patients with negative HIF-1α expression [6, 7]. Furthermore, in a recent meta-analysis, it was suggested that HIF-1α expression may be a prognostic

biomarker for lung cancer [6]. In addition, it is discussed that HIF-1α might be a target for therapy in lung cancer [7]. Therefore, associations between PET parameters and HIF-1α may be also of clinical importance.

Similarly, we calculated a moderate pooled correlation between SUV_{max} and expression of VEGF. Previous reports indicated that VEGF overexpression is associated with poor prognosis for NSCLC patients [3]. Furthermore, VEGF plays an important role in sustaining the development and progression of lung cancer [73]. Notably, some reports indicated a great potential of anti-VEGF agents in therapy of lung cancer [74]. Therefore, possible relationships between VEGF expression and SUV in lung cancer may play a significant role to plane chemotherapy. In fact, if SUV or other PET parameters may predict VEGF expression and tumors with overexpression, respectively, then PET may also be used for therapy control with anti-VEGF agents.

Finally, the strongest correlation was found between SUV_{max} and microvessel density (0.54). This finding seems to be logical. In fact, high metabolic activity may induce a high perfusion, which is associated with more vessels. SUV may identify hypervascularized tumor areas. Therefore, SUV may be used for evaluation of response to therapy with angiogenesis inhibitors.

The present meta-analysis also identified several other problems. Overall, most analyzed biomarkers are associated with SUV. This finding suggests that SUV_{max} may reflect different histopathological features in lung cancer. However, as mentioned above, the calculated pooled correlations are slightly-to-moderate. Therefore, our analysis showed that SUV_{max} cannot be used as an ultimate one-to-one surrogate marker for different receptor expressions in lung cancer.

Some reports suggested that other PET parameters like metabolic tumor volume or total lesion glycolysis are more sensitive than SUV_{max} [75]. In fact, pretreatment SUV is commonly used as a relative measure of ^{18}FDG uptake and is considered a prognostic factor for risk stratification in different malignancies. However, as suggested previously, it does not reflect the heterogeneity of a tumor [76]. Therefore, to overcome this drawback of SUV, other PET parameters, such as metabolic tumor volume and total lesion glycolysis that reflect metabolic volume and activity, have been proposed as quantitative indexes of tumor metabolism [76, 77]. According to the literature, these parameters can be used as prognostic factors for survival in several malignant diseases like non-small lung cancer, pleural mesothelioma, and ovarian cancer [77–79]. Clearly, further researches are needed to investigate possible associations between several PET parameters and histopathology in lung cancer.

Furthermore, lung cancer involves several carcinomas with different histopathological features and behavior. Presumably, different subtypes of lung cancer may have also different associations between PET and histopathology. This question should also be analyzed by further investigations.

There were also other problems. Only 40 reports with small number of patients investigated associations between PET parameters and histopathological features in lung cancer. Furthermore, most of the acquired studies were retrospective. Finally, according the QUADAS criteria, all involved studies showed partial verification bias, differential verification bias, and incorporation bias. Also, most of the studies had clinical review bias and diagnostic review bias. Clearly, further prospective studies with more patients are needed to investigate associations between PET and histopathology in lung cancer.

Some recent reports indicated that other histopathological markers like tumor-infiltrating CD8-positive T lymphocytes, cyclooxygenase-2, and survivin play also a great role in lung cancer [3, 4]. However, there were either no data or in each case only one report about relationships between PET and these histopathological factors. This should be also the purpose for further investigations.

In conclusion, our meta-analysis showed that SUV_{max} may predict microvessel density and expression of VEGF, KI 67, and HIF-1α in lung cancer. There were no significant associations between SUV_{max} and expression of cyclin D1, EGFR, PD L1, PCNA, and p53.

Data Availability

The data used to support the findings of this study are available from the corresponding author upon request.

Ethical Approval

The study was approved by the institutional review board of the University of Leipzig. All procedures performed in the study were in accordance with the ethical standards of the institutional research committee and with the 1964 Helsinki Declaration and its later amendments or comparable ethical standards.

Conflicts of Interest

There are no conflicts of interest.

Authors' Contributions

Alexey Surov conceptualized the data. Alexey Surov, Hans Jonas Meyer, and Andreas Wienke performed data curation. Alexey Surov, Hans Jonas Meyer, and Andreas Wienke did formal analysis. Alexey Surov, Hans Jonas Meyer, and Andreas Wienke investigated the data. Alexey Surov, Hans Jonas Meyer, and Andreas Wienke designed the methodology. Alexey Surov administered the project. Alexey Surov, Hans Jonas Meyer, and Andreas Wienke collected resources. Alexey Surov, Hans Jonas Meyer, and Andreas Wienke designed the software. Alexey Surov helped in supervision. Alexey Surov validated the data. Alexey Surov, Hans Jonas Meyer, and Andreas Wienke visualized the data. Alexey Surov wrote the original draft. Alexey Surov, Hans Jonas Meyer, and Andreas Wienke wrote, reviewed, and edited the data. All authors contributed equally to this work.

References

[1] R. Siegel, D. Naishadham, and A. Jemal, "Cancer statistics," *CA: A Cancer Journal for Clinicians*, vol. 62, no. 1, pp. 10–29, 2012.

[2] S. Wallerek and J. B. Sørensen, "Biomarkers for efficacy of adjuvant chemotherapy following complete resection in NSCLC stages I-IIIA," *European Respiratory Review*, vol. 24, no. 136, pp. 340–355, 2015.

[3] H. Jiang, W. Shao, and W. Zhao, "VEGF-C in non-small cell lung cancer: meta-analysis," *Clinica Chimica Acta*, vol. 427, pp. 94–99, 2014.

[4] B. Martin, M. Paesmans, C. Mascaux et al., "Ki-67 expression and patients survival in lung cancer: systematic review of the literature with meta-analysis," *British Journal of Cancer*, vol. 91, no. 12, pp. 2018–2025, 2004.

[5] M. S. Tsao, S. Aviel-Ronen, K. Ding et al., "Prognostic and predictive importance of p53 and RAS for adjuvant chemotherapy in non small-cell lung cancer," *Journal of Clinical Oncology*, vol. 25, no. 33, pp. 5240–5247, 2007.

[6] S. L. Yang, Q. G. Ren, L. Wen, and J. L. Hu, "Clinicopathological and prognostic significance of hypoxia-inducible factor-1 alpha in lung cancer: a systematic review with meta-analysis," *Journal of Huazhong University of Science and Technology*, vol. 36, no. 3, pp. 321–327, 2016.

[7] W. Ren, D. Mi, K. Yang et al., "The expression of hypoxia-inducible factor-1α and its clinical significance in lung cancer: a systematic review and meta-analysis," *Swiss Medical Weekly*, vol. 143, p. w13855, 2013.

[8] R. T. Adamson, "Biomarkers and molecular profiling in non-small cell lung cancer: an expanding role and its managed care implications," *American Journal of Managed Care*, vol. 19, no. 19, pp. s398–s404, 2013.

[9] X. Li, X. Liu, D. Cui, X. Wu, and R. Qian, "Clinical significance of nucleostemin and proliferating cell nuclear antigen protein expression in non-small cell lung cancer," *Journal of B.U.ON.: Official Journal of the Balkan Union of Oncology*, vol. 20, no. 4, pp. 1088–1093, 2015.

[10] S. Singhal, A. Vachani, D. Antin-Ozerkis, L. R. Kaiser, and S. M. Albelda, "Prognostic implications of cell cycle, apoptosis, and angiogenesis biomarkers in non-small cell lung cancer: a review," *Clinical Cancer Research*, vol. 11, no. 11, pp. 3974–3986, 2005.

[11] M. H. Cherk, S. S. Foo, A. M. Poon et al., "Lack of correlation of hypoxic cell fraction and angiogenesis with glucose metabolic rate in non-small cell lung cancer assessed by 18F-fluoromisonidazole and 18F-FDG PET," *Journal of Nuclear Medicine*, vol. 47, no. 12, pp. 1921–1926, 2006.

[12] J. Zhang, L. B. Cui, X. Tang et al., "DW MRI at 3.0 T versus FDG PET/CT for detection of malignant pulmonary tumors," *International Journal of Cancer*, vol. 134, no. 3, pp. 606–611, 2014.

[13] I. Apostolova, K. Ego, I. G. Steffen et al., "The asphericity of the metabolic tumour volume in NSCLC: correlation with histopathology and molecular markers," *European Journal of Nuclear Medicine and Molecular Imaging*, vol. 43, no. 13, pp. 2360–2373, 2016.

[14] A. K. Buck, G. Halter, H. Schirrmeister et al., "Imaging proliferation in lung tumors with PET: 18F-FLT versus 18F-FDG," *Journal of Nuclear Medicine*, vol. 44, no. 9, pp. 1426–1431, 2003.

[15] A. Del Gobbo, A. Pellegrinelli, G. Gaudioso et al., "Analysis of NSCLC tumour heterogeneity, proliferative and 18F-FDG PET indices reveals Ki67 prognostic role in adenocarcinomas," *Histopathology*, vol. 68, no. 5, pp. 746–751, 2016.

[16] B. Han, S. Lin, L. J. Yu, R. Z. Wang, and Y. Y. Wang, "Correlation of ^{18}F-FDG PET activity with expressions of survivin, Ki67, and CD34 in non-small-cell lung cancer," *Nuclear Medicine Communications*, vol. 30, no. 11, pp. 831–837, 2009.

[17] H. Kaida, A. Kawahara, M. Hayakawa et al., "The difference in relationship between ^{18}F-FDG uptake and clinicopathological factors on thyroid, esophageal, and lung cancers," *Nuclear Medicine Communications*, vol. 35, no. 1, pp. 36–43, 2014.

[18] K. Kaira, N. Oriuchi, K. Shimizu et al., "Correlation of angiogenesis with ^{18}F-FMT and ^{18}F-FDG uptake in non-small cell lung cancer," *Cancer Science*, vol. 100, no. 4, pp. 753–758, 2009.

[19] S. Kuyumcu, I. Adalet, Y. Sanli, C. Turkmen, Z. G. Ozkan, and D. Yilmazbayhan, "Somatostatin receptor scintigraphy with 111In-octreotide in pulmonary carcinoid tumours correlated with pathological and 18FDG PET/CT findings," *Annals of Nuclear Medicine*, vol. 26, no. 9, pp. 689–697, 2012.

[20] L. P. Liu, X. X. Zhang, L. B. Cui et al., "Preliminary comparison of diffusion-weighted MRI and PET/CT in predicting histological type and malignancy of lung cancer," *Clinical Respiratory Journal*, vol. 11, no. 2, pp. 151–158, 2017.

[21] S. Murakami, H. Saito, Y. Sakuma et al., "Correlation of 18F-fluorodeoxyglucose uptake on positron emission tomography with Ki-67 index and pathological invasive area in lung adenocarcinomas 30 mm or less in size," *European Journal of Radiology*, vol. 75, no. 2, pp. e62–e66, 2010.

[22] H. Nakamura, T. Hirata, H. Kitamura, and J. Nishikawa, "Correlation of the standardized uptake value in FDG-PET with the expression level of cell-cycle-related molecular biomarkers in resected non-small cell lung cancers," *Annals of Thoracic and Cardiovascular Surgery*, vol. 15, no. 3, pp. 304–310, 2009.

[23] X. C. Nguyen, W. W. Lee, J. H. Chung et al., "FDG uptake, glucose transporter type 1, and Ki-67 expressions in non-small-cell lung cancer: correlations and prognostic values," *European Journal of Radiology*, vol. 62, no. 2, pp. 214–219, 2007.

[24] S. Park, E. Lee, S. Rhee et al., "Correlation between semi-quantitative (18)F-FDG PET/CT parameters and Ki-67 expression in small cell lung cancer," *Nuclear Medicine and Molecular Imaging*, vol. 50, no. 1, pp. 24–30, 2016.

[25] A. W. Sauter, S. Winterstein, D. Spira et al., "Multifunctional profiling of non-small cell lung cancer using 18F-FDG PET/CT and volume perfusion CT.," *Journal of Nuclear Medicine*, vol. 53, no. 4, pp. 521–529, 2012.

[26] H. Shibata, H. Nomori, K. Uno et al., "11C-acetate for positron emission tomography imaging of clinical stage IA lung adenocarcinoma: comparison with ^{18}F-fluorodeoxyglucose for imaging and evaluation of tumor aggressiveness," *Annals of Nuclear Medicine*, vol. 23, no. 7, pp. 609–616, 2009.

[27] M. Soussan, J. Cyrta, C. Pouliquen et al., "Fluorine 18 fluorodeoxyglucose PET/CT volume-based indices in locally advanced non-small cell lung cancer: prediction of residual viable tumor after induction chemotherapy," *Radiology*, vol. 272, no. 3, pp. 875–884, 2014.

[28] H. Vesselle, A. Salskov, E. Turcotte et al., "Relationship between non-small cell lung cancer FDG uptake at PET, tumor histology, and Ki-67 proliferation index," *Journal of Thoracic Oncology*, vol. 3, no. 9, pp. 971–978, 2008.

[29] H. Vesselle, R. A. Schmidt, J. M. Pugsley et al., "Lung cancer proliferation correlates with [F-18]fluorodeoxyglucose uptake by positron emission tomography," *Clinical Cancer Research*, vol. 6, no. 10, pp. 3837–3844, 2000.

[30] F. L. Wang, Y. Y. Tan, X. M. Gu et al., "Comparison of positron emission tomography using 2-[18F]-fluoro-2-deoxy-D-glucose and 3-deoxy-3-[18F]-fluorothymidine in lung cancer imaging," *Chinese Medical Journal*, vol. 129, no. 24, pp. 2926–2935, 2016.

[31] K. Watanabe, H. Nomori, T. Ohtsuka et al., "[F-18] Fluorodeoxyglucose positron emission tomography can predict pathological tumor stage and proliferative activity determined by Ki-67 in clinical stage IA lung adenocarcinomas," *Japanese Journal of Clinical Oncology*, vol. 36, no. 7, pp. 403–409, 2006.

[32] Y. Yamamoto, Y. Nishiyama, S. Ishikawa et al., "Correlation of ^{18}F-FLT and ^{18}F-FDG uptake on PET with Ki-67 immunohistochemistry in non-small cell lung cancer," *European Journal of Nuclear Medicine and Molecular Imaging*, vol. 34, no. 10, pp. 1610–1616, 2007.

[33] C. S. Yap, J Czernin, M. C. Fishbein et al., "Evaluation of thoracic tumors with ^{18}F-fluorothymidine and ^{18}F-fluorodeoxyglucose-positron emission tomography," *Chest*, vol. 129, no. 2, pp. 393–401, 2006.

[34] M. D. Taylor, P. W. Smith, W. K. Brix et al., "Fluorodeoxyglucose positron emission tomography and tumor marker expression in non-small cell lung cancer," *Journal of Thoracic and Cardiovascular Surgery*, vol. 137, no. 1, pp. 43–48, 2009.

[35] W. Yang, Y. Zhang, Z. Fu et al., "Imaging of proliferation with ^{18}F-FLT PET/CT versus ^{18}F-FDG PET/CT in non-small-cell lung cancer," *European J Nuclear Medicine and Molecular Imaging*, vol. 37, no. 7, pp. 1291–1299, 2010.

[36] T. Furukawa, Y. Miyata, K. Kushitani et al., "Association between [^{18}F]-fluoro-2-deoxyglucose uptake and expressions of hypoxia-induced factor 1α and glucose transporter 1 in non-small cell lung cancer," *Japanese Journal of Clinical Oncology*, vol. 45, no. 12, pp. 1154–1161, 2015.

[37] K. Kaira, M. Endo, M. Abe et al., "Biologic correlates of ^{18}F-FDG uptake on PET in pulmonary pleomorphic carcinoma," *Lung Cancer*, vol. 71, no. 2, pp. 144–150, 2011.

[38] K. Kaira, M. Serizawa, Y. Koh et al., "Biological significance of 18F-FDG uptake on PET in patients with non-small-cell lung cancer," *Lung Cancer*, vol. 83, no. 2, pp. 197–204, 2014.

[39] N. Xing, Z. L. Cai, S. H. Zhao, L. Yang, B. X. Xu, and F. L. Wang, "The use of CT perfusion to determine microvessel density in lung cancer: comparison with FDG-PET and pathology," *Chinese Journal of Cancer Research*, vol. 23, no. 2, pp. 118–122, 2011.

[40] Z. J. Zhang, J. H. Chen, L. Meng et al., "^{18}F-FDG uptake as a biologic factor predicting outcome in patients with resected non-small-cell lung cancer," *Chinese Medical Journal*, vol. 120, no. 2, pp. 125–131, 2007.

[41] O. Araz, E. Demirci, E. Y. Ucar et al., "Roles of Ki-67, p53, transforming growth factor-β and lysyl oxidase in the metastasis of lung cancer," *Respirology*, vol. 19, no. 7, pp. 1034–1039, 2014.

[42] L. Bai, C. Guo, J. Wang et al., "^{18}F-fludrodeoxyglucose maximal standardized uptake value and metabolic tumor burden are associated with major chemotherapy-related tumor markers in NSCLC patients," *OncoTargets and Therapy*, vol. 9, pp. 6315–6324, 2016.

[43] X. Y. Duan, W. Wang, J. S. Wang, J Shang, J. G. Gao, and Y. M. Guo, "Fluorodeoxyglucose positron emission tomography and chemotherapy-related tumor marker expression in non-small cell lung cancer," *BMC Cancer*, vol. 13, no. 1, p. 546, 2013.

[44] X. Liu, H. Zhang, X. Yu et al., "The correlation of expression of VEGF and EGFR with SUV of (18)FDG-PET-CT in non-small cell lung cancer," *Contemporary Oncology*, vol. 18, no. 5, pp. 334–339, 2014.

[45] K. Higashi, Y. Ueda, A. Sakurai et al., "Correlation of Glut-1 glucose transporter expression with [(18)F]FDG uptake in non-small cell lung cancer," *European Journal of Nuclear Medicine*, vol. 27, no. 12, pp. 1778–1785, 2000.

[46] A. H. Khandani, K. D. Whitney, S. M. Keller, C. R. Isasi, and M. Donald Blaufox, "Sensitivity of FDG PET, GLUT1 expression and proliferative index in bronchioloalveolar lung cancer," *Nuclear Medicine Communications*, vol. 28, no. 3, pp. 173–177, 2007.

[47] M. Mamede, T. Higashi, M. Kitaichi et al., "[18F]FDG uptake and PCNA, Glut-1, and Hexokinase-II expressions in cancers and inflammatory lesions of the lung," *Neoplasia*, vol. 7, no. 4, pp. 369–379, 2005.

[48] K. Takada, G. Toyokawa, T. Okamoto et al., "Metabolic characteristics of programmed cell death-ligand 1-expressing lung cancer on ^{18}F-fluorodeoxyglucose positron emission tomography/computed tomography," *Cancer Medicine*, vol. 6, no. 11, pp. 2552–2561, 2017.

[49] M. Zhang, D. Wang, Q. Sun et al., "Prognostic significance of PD-L1 expression and ^{18}F-FDG PET/CT in surgical pulmonary squamous cell carcinoma," *Oncotarget*, vol. 8, no. 31, pp. 51630–51640, 2017.

[50] E. Lopci, L. Toschi, F. Grizzi et al., "Correlation of metabolic information on FDG-PET with tissue expression of immune markers in patients with non-small cell lung cancer (NSCLC) who are candidates for upfront surgery," *European Journal of Nuclear Medicine and Molecular Imaging*, vol. 43, no. 11, pp. 1954–1961, 2016.

[51] A. Surov, H. J. Meyer, and A. Wienke, "Can imaging parameters provide information regarding histopathology in head and neck squamous cell carcinoma? A meta-analysis," *Translational Oncology*, vol. 11, no. 2, pp. 498–503, 2018.

[52] A. Surov, H. J. Meyer, and A. Wienke, "Correlation between apparent diffusion coefficient (ADC) and KI 67 in different tumors: a meta-analysis. Part 1: ADC_{mean}," *Oncotarget*, vol. 8, no. 43, pp. 75434–75444, 2017.

[53] A. Surov, H. J. Meyer, and A. Wienke, "Correlation between apparent diffusion coefficient (ADC) and cellularity is different in several tumors: a meta-analysis," *Oncotarget*, vol. 8, no. 35, pp. 59492–59499, 2017.

[54] D. Moher, A. Liberati, J. Tetzlaff, and D. G. Altman, "Preferred reporting items for systematic reviews and meta-analyses: the PRISMA statement," *PLoS Medicine*, vol. 6, no. 7, article e1000097, 2009.

[55] P. Whiting, A. W. Rutjes, J. B. Reitsma, P. M. Bossuyt, and J. Kleijnen, "The development of QUADAS: a tool for the quality assessment of studies of diagnostic accuracy included in systematic reviews," *BMC Medical Research Methodology*, vol. 3, no. 1, p. 25, 2003.

[56] A. Chalkidou, D. B. Landau, E. W. Odell, V. R. Cornelius, M. J. O'Doherty, and P. K. Marsden, "Correlation between Ki-67 immunohistochemistry and ^{18}F-fluorothymidine uptake in patients with cancer: a systematic review and meta-analysis," *European Journal of Cancer*, vol. 48, no. 18, pp. 3499–3513, 2012.

[57] M. M. Leeflang, J. J. Deeks, C. Gatsonis, and P. M. Bossuyt, "Systematic reviews of diagnostic test accuracy," *Annals of Internal Medicine*, vol. 149, no. 12, pp. 889–897, 2008.

[58] J. Zamora, V. Abraira, A. Muriel, K. Khan, and A. Coomarasamy, "Meta-DiSc: a software for meta-analysis of test accuracy data," *BMC Medical Research Methodology*, vol. 6, no. 1, p. 31, 2006.

[59] R. DerSimonian and N. Laird, "Meta-analysis in clinical trials," *Controlled Clinical Trials*, vol. 7, no. 3, pp. 177–188, 1986.

[60] M. Scimeca, N. Urbano, R. Bonfiglio, O. Schillaci, and E. Bonanno, "Management of oncological patients in the digital era: anatomic pathology and nuclear medicine teamwork," *Future Oncology* vol. 14, no. 11, pp. 1013–1015, 2018.

[61] C. Schlüter, M. Duchrow, C. Wohlenberg et al., "The cell proliferation-associated antigen of antibody Ki-67: a very large, ubiquitous nuclear protein with numerous repeated elements, representing a new kind of cell cycle-maintaining proteins," *Journal of Cell Biology*, vol. 123, no. 3, pp. 513–522, 1993.

[62] S. M. Deng, W. Zhang, B. Zhang, Y. Y. Chen, J. H. Li, and Y. W. Wu, "Correlation between the uptake of ^{18}F-fluorodeoxyglucose (18F-FDG) and the expression of proliferation-associated antigen Ki-67 in cancer patients: a meta-analysis," *PLoS One*, vol. 10, no. 6, article e0129028, 2015.

[63] G. Shen, H. Ma, F. Pang, P. Ren, and A. Kuang, "Correlations of ^{18}F-FDG and ^{18}F-FLT uptake on PET with Ki-67 expression in patients with lung cancer: a meta-analysis," *Acta Radiologica*, vol. 59, no. 2, pp. 188–195, 2018.

[64] L. M. Sholl, "Biomarkers in lung adenocarcinoma: a decade of progress," *Archives of Pathology & Laboratory Medicine*, vol. 139, no. 4, pp. 469–480, 2015.

[65] S. V. Sharma, D. W. Bell, J. Settleman, and D. A. Haber, "Epidermal growth factor receptor mutations in lung cancer," *Nature Reviews Cancer*, vol. 7, no. 3, pp. 169–181, 2007.

[66] M. Tateishi, T. Ishida, T. Mitsudomi, S. Kaneko, and K. Sugimachi, "Immunohistochemical evidence of autocrine growth factors in adenocarcinoma of the human lung," *Cancer Research*, vol. 50, no. 21, pp. 7077–7080, 1990.

[67] K. Inamura, "Update on immunohistochemistry for the diagnosis of lung cancer," *Cancers,* vol. 10, no. 3, pii E72, 2018.

[68] P. C. Tumeh, C. L. Harview, J. H. Yearley et al., "PD-1 blockade induces responses by inhibiting adaptive immune resistance," *Nature*, vol. 515, no. 7528, pp. 568–571, 2014.

[69] S. Simon and N. Labarriere, "PD-1 expression on tumor-specific T cells: friend or foe for immunotherapy?," *Oncoimmunology*, vol. 7, p. e1364828, 2017.

[70] R. Brody, Y. Zhang, M. Ballas et al., "PD-L1 expression in advanced NSCLC: insights into risk stratification and treatment selection from a systematic literature review," *Lung Cancer*, vol. 112, pp. 200–215, 2017.

[71] O. Gautschi, D. Ratschiller, M. Gugger, D. C. Betticher, and J. Heighway, "Cyclin D1 in non-small cell lung cancer: a key driver of malignant transformation," *Lung Cancer*, vol. 55, no. 1, pp. 1–14, 2007.

[72] L. Q. Zhang, F. Jiang, L. Xu et al., "The role of cyclin D1 expression and patient's survival in non-small-cell lung cancer: a systematic review with meta-analysis," *Clinical Lung Cancer*, vol. 13, no. 3, pp. 188–195, 2012.

[73] V. M. Villaflor and R. Salgia, "Targeted agents in non-small cell lung cancer therapy: what is there on the horizon?," *Journal of Carcinogenesis*, vol. 12, p. 7, 2013.

[74] D. Frezzetti, M. Gallo, M. R. Maiello et al., "VEGF as a potential target in lung cancer," *Expert Opinion on Therapeutic Targets*, vol. 21, no. 10, pp. 959–966, 2017.

[75] A. Sharma, A. Mohan, A. S. Bhalla et al., "Role of various metabolic parameters derived from baseline ^{18}F-FDG PET/CT as prognostic markers in non-small cell lung cancer patients undergoing platinum-based chemotherapy," *Clinical Nuclear Medicine*, vol. 43, no. 1, pp. e8–e17, 2018.

[76] J. H. Hong, H. H. Kim, E. J. Han et al., "Total lesion glycolysis using ^{18}F-FDG PET/CT as a prognostic factor for locally advanced esophageal cancer," *Journal of Korean Medical Science*, vol. 31, no. 1, pp. 39–46, 2016.

[77] S. Liao, B. C. Penney, K. Wroblewski et al., "Prognostic value of metabolic tumor burden on ^{18}F-FDG PET in nonsurgical patients with non-small cell lung cancer," *European Journal of Nuclear Medicine and Molecular Imaging*, vol. 39, no. 1, pp. 27–38, 2012.

[78] H. Y. Lee, S. H. Hyun, K. S. Lee et al., "Volume-based parameter of ^{18}F-FDG PET/CT in malignant pleural mesothelioma: prediction of therapeutic response and prognostic implications," *Annals of Surgical Oncology*, vol. 17, no. 10, pp. 2787–2794, 2010.

[79] H. H. Chung, H. W. Kwon, K. W. Kang et al., "Prognostic value of preoperative metabolic tumor volume and total lesion glycolysis in patients with epithelial ovarian cancer," *Annals of Surgical Oncology*, vol. 19, no. 6, pp. 1966–1972, 2012.